RATIONAL DESIGN OF ARCHITECTURED AMPHIPHILIC BLOCK COPOLYMERS AND POLYMER-LIGATED NANOCRYSTALS FOR ENERGY STORAGE AND DRUG DELIVERY

A Dissertation
Presented to
The Academic Faculty

by

Zewei Wang

In Partial Fulfillment
of the Requirements for the Degree
DOCTOR OF PHILOSOPHY in the
SCHOOL OF MATERIALS SCIENCE AND ENGINEERING

Georgia Institute of Technology
December 2019

RATIONAL DESIGN OF ARCHITECTURED AMPHIPHILIC BLOCK COPOLYMERS AND POLYMER-LIGATED NANOCRYSTALS FOR ENERGY STORAGE AND DRUG DELIVERY

Approved by:

Dr. Zhiqun Lin, Advisor
School of Materials Science and Engineering
Georgia Institute of Technology

Dr. Younan Xia
School of Chemical and Biomolecular Engineering
Georgia Institute of Technology

Dr. Vladimir Tsukruk
School of Materials Science and Engineering
Georgia Institute of Technology

Dr. Yulin Deng
School of Chemical and Biomolecular Engineering
Georgia Institute of Technology

Dr. Dong Qin
School of Materials Science and Engineering
Georgia Institute of Technology

Date Approved: [October 29, 2019]

ACKNOWLEDGEMENTS

I want to give my special thanks to my advisor Prof. Zhiqun Lin, who has been very supportive and patient with me. The Janus project I worked with is really difficult and I suffered a lot during the first several years. It is Prof. Lin who constantly encourages and helps me get through the difficult time. Not only does he work hard as an already accomplished professor, but he is also very kind and generous to his students even in personal lives. It is no doubt that I wouldn't have the accomplishment today without him. I'll always be inspired by his passion for science and research. I'd also like to thank all my committee members, Prof. Vladimir Tsukruk, Prof. Dong Qin, Prof. Younan Xia, Prof. Yulin Deng for their kindness to serve on my committee and provide me with lots of constructive suggestions and opinions on my research, leading to the successful completion of my PhD dissertation.

Over the six years of PhD study in Prof. Lin's group, I've got enormous helps from all group members and made a lot of friends. When I first joined the group, I received countless guidance and advice from several senior members, Prof. Xinchang Pang, Prof. Hefeng Zhang, Dr. Yanjie He, Dr. James Iocozzia, all of whom act like mentors to me in some sense and teach me the basic knowledge and experimental techniques so I am capable of carrying out my own project. I would also like to thank three long-time group members, also my dearest friends, Dr. Yihuang Chen, Dr. Shiqiang Zhao, and Yeu Wei Harn, who has been my companion throughout my PhD life in Georgia Tech and shared valuable memories. Together, we have collaboratively worked on so many novel projects with tremendous outcomes. Finally, I want to thank all other groups members, current and

former, for their helps and supports during my PhD study all over the past several years, including Prof. Ming He, Prof. Yupeng Yuan, Prof. Shuguang Zhang, Prof. Yijiang Liu, Prof. Bing Wang, Prof. Meng Zhang, Dr. Bo Li, Dr. Beibei Jiang, Dr. Chaowei Feng, Dr. Young Jun Yoon, Dr. Han Miao, Dr. Cheng-Hsin Lu, Dr. Zili Li, Dr. Shuang Pan, Dr. Xun Cui, Dr. Xueqin Liu, Dr. Xiao Li, Dr. Wei Wang, Xiangtong Meng, Yajing Chang, Kunjie Yuan, Qianqian Fan, Hanyin Zhang, Jiwoo Yu, Aurelia Wang, Gill Biesold-Mcgee, Shuang Liang, Mingyue Zhang, Chris Sewell, Likun Gao, Chuntao Lan, Dingfeng Shen, Jiabin Qi, and Songru Jia.

I am also extremely grateful for the support from all my friends at Georgia Tech, Dr. Guanghui Zhu, Xueting Liu, Dr. Xu Du, Dr. Songcheng Wang. Most important of all, I wouldn't be able to finish my PhD without the mental and financial support from my family including my significant other Wenqin You. She is part of the motivations that drive me to move forward and get through obstacles for creating a better future.

TABLE OF CONTENTS

LIST OF TABLES

LIST OF FIGURES

LIST OF SYMBOLS AND ABBREVIATIONS

^{1}H-NMR	Proton nuclear magnetic resonance imaging
4VP	4-vinylpyridine
AFM	Atomic force microscopy
AIBN	Azobisisobutyronitrile
ALD	Atomic layer deposition
AN	Acrylonitrile
ANPs	Aggregated nanoparticles
ATRP	Atom-transfer radical polymerization
BA	Benzyl alcohol
BBCP	Bottlebrush block copolymer
BIBB	2-bromo-2-methylpropionyl bromide
BIBA	2-bromo-2-methylpropionic acid
BMBB	4-bromomethylbenzoyl bromide
BTBA	Borane *tert*-butylamine complex
CV	Cyclic voltammetry
CVD	Chemical vapor deposition
CuAAC	Copper-catalyzed azide-alkyne cycloaddition
DDMAT	2-(Dodecylthiocarbonothioylthio)-2-methylpropionic acid
DLS	Dynamic light scattering
DMF	Dimethylformamide
EDS	Energy dispersive X-ray spectrometry
EIS	Electrochemical impedance spectroscopy
EtOH	Ethanol
FT-IR	Fourier transform infrared spectroscopy
GPC	Gel permeation chromatography
HEMA	2-Hydroxyethyl methacrylate
HRTEM	High-resolution transmission electron microscopy
L7	Left 7-arm
LIB	Lithium ion battery
Me6TREN	Tris[2-(dimethylamino)ethyl]amine
MeOH	Methanol

MEK	Methyl ethyl ketone
MRI	Magnetic resonance imaging
M_n	Number average molecular weight
MW	Molecular weight
NMP	Nitroxide mediated polymerization
NC	Nanocrystal
NP	Nanoparticle
NR	Nanorod
P3HT	Poly(3-hexylthiophene)
P4VP	Poly(4-vinyl pyridine)
PAA	Poly(acrylic acid)
PCL	Polycaprolactone
PDI	Polydispersity index
PEDOT	Poly(3,4-ethylenedioxythiophene) polystyrene sulfonate
PEO	Poly(ethylene oxide)
PEG	Polyethylene glycol
PHEMA	Poly(2-hydroxyethyl methacrylate)
PL	Photoluminescence
PMDETA	N,N,N',N'',N''-pentamethyldiethylenetriamine
PVDF	Polyvinylidene fluoride
PS	Polystyrene
PSAN	Poly(styrene-co-acrylonitrile)
P*t*BA	Poly(*tert*-butyl acrylate)
R8	Right 8-arm
RAFT	Reversible addition fragmentation chain transfer polymerization
ROP	Ring opening polymerization
ROMP	Ring-opening metathesis polymerization
SEM	Scanning electron microscopy
SIB	Sodium ion battery
St	Styrene
STEM	Scanning transmission electron microscopy
*t*BA	*Tert*-butyl acrylate

TEM	Transmission electron microscopy
TFA	Trifluoroacetic acid
TGA	Thermogravimetric analysis
THF	Tetrahydrofuran
UV-vis	Ultraviolet-visible spectroscopy
XPS	X-ray photoelectron spectroscopy
XRD	X-ray diffraction
β-CD	Beta-cyclodextrin

SUMMARY

Architectured amphiphilic block copolymers with complex molecular structures have garnered much attention in recent years due to their distinct chemical and physical properties compared to the linear counterparts. The amphiphilic chemical environment provides a robust platform for site selective functionalization as well as molecular interactions. Notably, architectured amphiphilic block copolymers can be employed as nanoreactors for crafting polymer-ligated nanocrystals. Specifically, the hydrophilic blocks of architectured amphiphilic block copolymers can be selectively loaded with metal precursors to achieve confined growth of inorganic nanocrystals. The size and shape of as-synthesized polymer-ligated nanocrystals can be precisely tailored via architectural design and controlling the reaction time of architectured amphiphilic block copolymers.

With fast advancement in controlled living polymerization technique, such as the development of atom-transfer radical polymerization (ATRP) and reversible addition-fragmentation chain transfer polymerization (RAFT), novel synthesis of monodisperse polymers with complex architectures has become possible. In addition, by post-polymerization reactions, specific functionalities can be incorporate to desired domains of the polymer structure. In this thesis work, three different architectured amphiphilic block copolymers (star-shaped, bottlebrush-shaped, and Janus star- shaped) are rationally designed and synthesized by capitalizing on multifunctional glucose-based biomolecules, either β-cyclodextrin (β-CD) as the core (for star- and Janus star-shaped) or cellulose as the backbone (for bottlebrush-shaped). These architectured amphiphilic block copolymers are synthesized through ATRP and/or RAFT, thereby possessing precisely controlled

molecular weight and low polydispersity (PDI). These characteristics render them perfect polymeric nanoreactors for synthesis of plain nanoparticles, nanorods, and spherical Janus nanoparticles. More importantly, as-synthesized nanocrystals are permanently capped with artificially designed polymer hairs rendering superior crystal stability as well as practical surface properties, which carry tremendous advantages in energy and biomedical related applications.

First, MFe_2O_4 (M = Mn, Co, Ni, Cu, Zn) and MO_x (M = Mn, Co, Fe) nanoparticles with a desired size were precisely crafted by capitalizing on star-like polyacrylic acid-*block*-poly(styrene-acrylonitrile) (star-like PAA-*b*-PSAN) copolymers as nanoreactors, which was then uniformly anchored on reduced graphene oxide nanosheets induced by the π-π stacking interaction between PSAN and rGO (denoted MFe_2O_4/PAA@PSAN-rGO and MO_x/PAA@PSAN-rGO). As anodes of LIBs/SIBs, the MFe_2O_4/PAA@PSAN-rGO expressed outstanding cycling stabilities at various current rates. In stark contrast, Li^+ storage capacities of MO_x/PAA@PSAN-rGO decreased initially and then raised while Na^+ storage capacities continued to decay. According to the HRTEM observations of cycled Fe_2O_3/PAA@PSAN-rGO electrodes, the coarsening of small Fe nanoparticles into larger domains led to the decrease of specific contact areas of Fe with Li_2O/Na_2O, finally resulting in the reduction of conversion reaction reversibility. Notably, the $CoFe_2O_4$/PAA@PSAN nanoparticles randomly phase-separated into CoO and Fe_2O_3 domains after the first cycle creating abundant heterophase interfaces within the cycled $CoFe_2O_4$/PAA@PSAN-rGO nanocomposites. The heterophase interfaces together with physical barriers provided by rGO and PSAN hairs inhibited the large-scale homophase coarsening of Co and Fe nanoparticles, thereby stabilizing the electrochemical reaction reversibility. Therefore, two

key strategies to inhibit homophase metal coarsening are proposed and verified, which are essential for the enhancement of cycling stability of MO_x as anode of LIBs/SIBs: (1) establishing robust physical barriers on the surfaces of MO_x nanoparticles by homogeneously coating carbonaceous materials or polymers; (2) introducing abundant heterophase interfaces in the cycled MO_x electrodes by fabricating polymetallic oxides (e.g., MFe_2O_4) or uniform mixture of different MO_x nanoparticles.

Second, a robust route to unimolecular organic bottle-brush cocoons with crosslinked shell was developed where the interior was occupied by judiciously designed polymer chains (i.e., poly(acrylic acid)) to provide preferential anchoring points for organic molecules and inorganic precursors. The azide-functionalized outer block of the bottle-brush polymer can be readily crosslinked upon UV irradiation, presenting an efficient and robust route for post-loading encapsulation. As a result, the polymeric cocoons showed excellent encapsulation and delivery properties with 3-fold encapsulation amount and 3-fold total delivery period over uncrosslinked bottle-brush polymers. Different from previous approaches for making worm-like bottle-brush polymers, cellulose was used as the backbone, affording the cocoons a straight nanorod morphology. This type of bottle-brush cocoons can be directly capitalized as nanoreactors to produce monodisperse inorganic nanorod with controlled size and composition. The crosslinked outer layer on the nanorod surface provides additional barrier protection to enhance its stability. $CsPbBr_3$ nanorods as a promising perovskite material has been known to have extremely poor stability. However, the $CsPbBr_3$ nanorods synthesized from the polymeric cocoons exhibited much enhanced UV, water, and thermal stabilities when the outer polymer block was crosslinked after nanorods synthesis, rendering them with great potential for

applications in optoelectronics. This unique cocoon strategy provides an innovating approach towards the development of new-generation nanocarrier for drug delivery and nanoreactor for the synthesis of nanocrystals with superior stabilities.

Third, an innovative synthetic strategy for star-shaped Janus block polymers was developed by employing bifunctional β-CD as the macroinitiator. The bowl shaped β-CD is composed of 7 primary -OH groups on one side of the bowl and 14 secondary -OH groups on the other, which can be selectively functionalized based on the difference in reactivity and steric hindrance. 7 -COOH terminated RAFT agent (DDMAT) was first coupled to the primary alcohols by esterification with the other 8 out of 14 secondary alcohols esterified by bromination agent, producing a multifunctional macroinitiator with 7 RAFT initiating sites and 8 ATRP initiating sites on different side of the bowl-shaped β-CD to generate a symmetric amphiphilic structure. After sequential 4-step polymerization (2-steps RAFT of 4VP and St, 2-steps ATRP of *t*BA and St), star-shaped Janus core-shell polymers were synthesized with an amphiphilic core and hydrophobic PS shell. Strictly biphasic Janus nanoparticles can be synthesized using the above Janus polymer as the nanoreactor. The amphiphilic core consists of an activated P4VP half, which can be incorporated with Au precursors for the synthesis of Au hemisphere, and a deactivated P*t*BA half which can be hydrolyzed into PAA to coordinate with TiO_2 precursor for the synthesis of the other TiO_2 hemisphere, together yielding a spherical Au/TiO_2 Janus nanoparticle with two hemispheres comprising different materials. So far, Au hemispheres have been synthesized with undergoing effort for synthesis of the other TiO_2 hemisphere.

CHAPTER 1. INTRODUCTION

1.1 Synthesis of architectured block copolymers (star-like and bottlebrush-like) by controlled polymerization

Architectured (branched) polymers represent a set of polymers with sophisticated architectures which have complete different physical properties from linear block copolymers and have been widely used in advanced materials applications. Common architectured polymer architectures include tadpole-like, mop-like, star-like (including dendrimer), Necklace-like, bottlebrush-like, cyclic, asymmetric (Janus), crosslinked network.[1] The synthesis of these highly ordered structures is usually achieved through controlled living polymerization on specially designed initiator with multiple initiating site. Controlled living polymerization such as atom transfer radical polymerization (ATRP),[2] reversible addition fragmentation chain-transfer polymerization (RAFT),[3] anionic polymerization,[4] ring-opening metathesis polymerization (ROMP)[5] can produce polymer with controlled molecular weight (MW) and low dispersity (PDI). In other word, the morphology of the architectured polymer can be precisely controlled. Because of the livingness of these polymerization techniques, architectured block copolymer can be easily created via sequential polymerization of two different monomers. Additionally, the well-established click chemistry such as azide-alkyne cycloaddition, thiol-ene addition, Diels-Alder cycloaddition provides an alternative for crafting block copolymers that is otherwise hard to synthesize by single polymerization pathway. Due to the anisotropic nature of block copolymers, architectured block copolymers are widely used in the self-assembly of highly hierarchical structures. For example, Janus bottlebrush block copolymers have emerged to

be the mostly promising materials for photonic crystal.[6] On the other hand, core-shell architectured block copolymers have numerous application in biomedical separation, sensing, and drug delivery as well as nanocrystal synthesis due to significant difference in the chemical environment of core and shell. In the following sections, the synthetic strategies of two most heavily studied architectured block copolymers will be discussed: star-like polymer, bottlebrush (comb) polymer.

1.1.1 Synthesis of star-like block copolymers

1.1.1.1 Star-like polymers

There are numerous strategies for synthesizing star-like polymers which can be generally categorized into three approaches: core-first, arm-first, and grafting-onto approaches (**Figure 1.1**).[7]

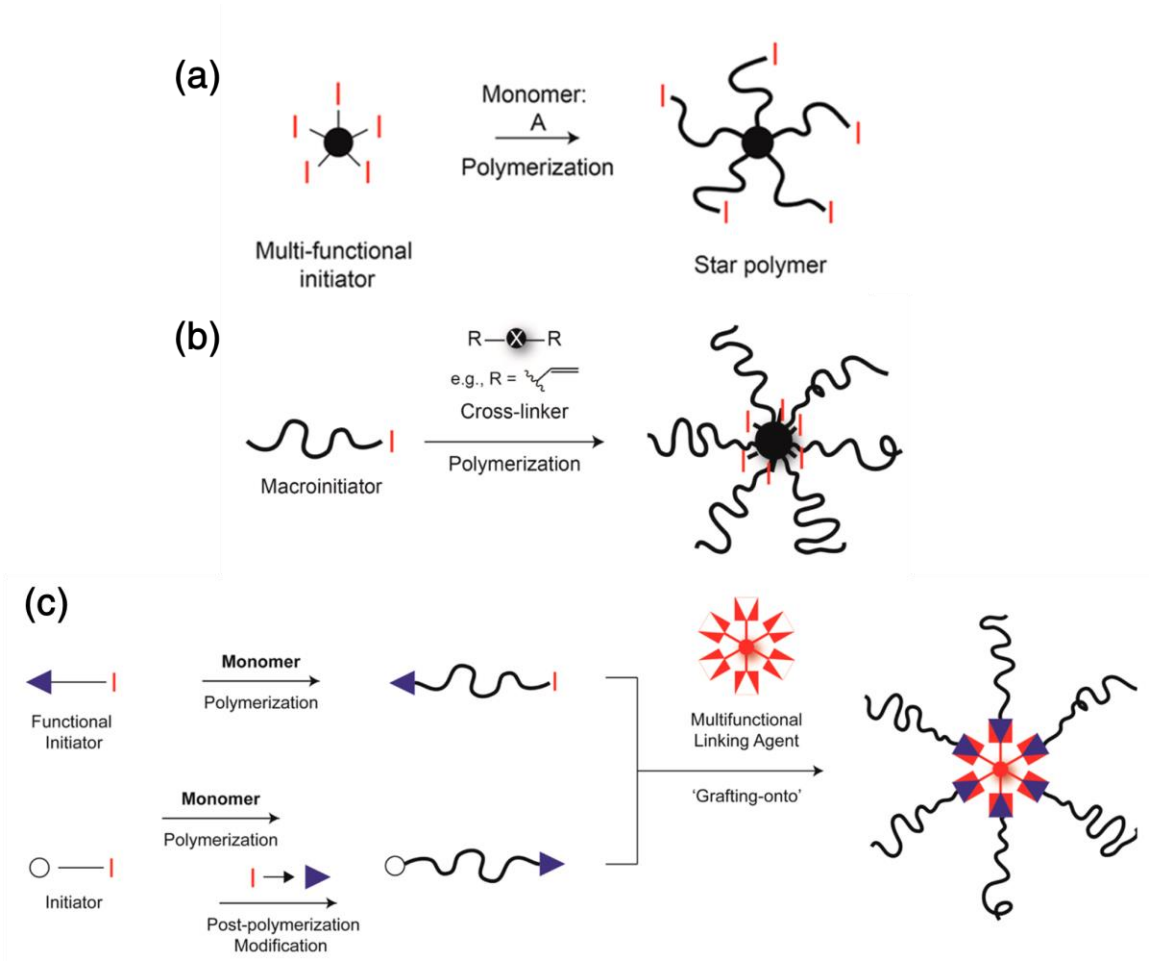

Figure 1.1. Schematic illustration of star synthesis via (a) core-first, (b) arm first, (c) grafting-onto approach. Reproduced from Ren et al.[7] Copyright 2016 American Chemical Society.

The core-first approach requires synthetic or natural multifunctional initiator. Functionality can be tuned to suit different polymerization techniques, for example, halogen end groups for ATRP, -OH end groups for anionic polymerization, RAFT end groups for RAFT polymerization. A critical value in the core-first approach is the number of arms which is strictly limited by the number of initiator site on the core. Theoretically, more arms will result in better-defined spherical structure because each arm is fully stretch due to steric hindrance. The size of the star-like polymer can be directly predicted from the

molecular weight of each arm. However, it is also because of strong steric hindrance between neighboring chains, uniform growth on each initiating site is rather hard to achieve. The active chain end can be easily buried inside the jungle of polymers and stop growing. Nevertheless, commonly used cores all have low arm numbers and a much smaller core domain size. To overcome this limitation, functionalized hyperbranched polymers[8-10] as well as dendritic polymers[11-12] have been developed as the multifunctional macroinitiator which will provide significantly larger arm numbers. Up to now, the most promising multifunctional core for crafting star-like polymer is β-cyclodextrin (β-CD) which is a natural compound with 21 -OH groups that can be easily functionalized for ATRP and RAFT. Other molecular initiator with such high arm numbers are all dendritic structures that require sophisticated synthetic procedures. The synthesis of β-CD initiated star-like block copolymer will be further discussed in sections 1.1.1.2.

The arm-first approach, on the other hand, forms star-like polymers by crosslinking through the end of linear polymers by polymerization or coupling reactions. Based on different crosslinking mechanisms, it can be further divided into three categories: macroinitiator (MI), macromonomer (MM), and self-assembly crosslinking (SC). The arms are usually synthesized through living polymerization with functional end groups. If the end is initiating site, it is macroinitiator. The core of the star-like polymer will then be formed via arm-end initiated polymerization of multifunctional monomer (crosslinker). If the end group has monomer unit, it is macromonomer, which will be copolymerized with crosslinker by external initiator. If the end group has crosslinkable segment such as -Cl which can undergo atom transfer radical coupling (ATRC) reactions, it is self-assembly crosslinking. The linear block copolymers (arm) first have to self-assemble into micelle

structure before subsequently crosslinking of the core blocks to form a unimolecular star-like polymer. In the arm-first approach, the MW of arms can be uniformly controlled because it is pre-synthesized. The number of arms in one star-like polymer usually has a broad distribution since it is influence by multiple synthesis condition as well as feed ratio. However, the average number is typically greater than 100, much higher than core-first approach. Such high population is also a result of large core size. Therefore, this approach is not suitable for synthesized of star-like polymers below 10 nm.

In grafting-onto approach, both core and arms are pre-synthesized providing the highest level of molecular control. Polydispersity of the star-like polymer can be reduced to the minimum. Typically, the functional core and arms are linked together through coupling reactions such as azide-alkyne cycloaddition. A drawback of this approach is the limited arm number (typically 4-8) as well as high MW arm. The huge steric hindrance within high density and high MW arm will lead to incomplete conjugation between core and arm, in other words, low coupling efficiency. Excess arms are often needed to reach high grafting ratio of arms, which makes it harder to remove during purification of the star-like polymers. Another weakness of the grafting-onto approach is the extremely low reaction rate due to the low concentration of functional groups both on arm-end and core. Thus, this approach is rarely used for attaching long arms on a small core.

1.1.1.2 Star-like block copolymers

Among three general approaches for making star-like polymers, the core-first and grafting-onto approach has been mostly adopted for the synthesis of star-like block copolymers with core-shell structures. One the other hand, the synthesis of the arms in the

star-like diblock copolymers show some analog to linear diblock copolymers, either by continuous polymerization or by click chemistry with a pre-synthesized second block. For continuous polymerization, in most cases, the two blocks are polymerized via same polymerization mechanism (ATRP or RAFT). However, if the inner block is polyester which is typically polymerized by ring-opening polymerization (ROP) terminated with -OH groups, and the outer block needs to be polyacrylate or polystyrene which is polymerized by radical polymerization. The -OH groups have to be post-functionalized into either -Br for ATRP or -DDMAT for RAFT.

A unique advantage of star-like block copolymers is that each block can be functionalized for specific applications. Functionalities can be incorporated by polymerization of pre-functionalized monomers or direct reactions on as-synthesized polymers. The difference in the core and shell functionalities will lead significant difference in their chemical environment, which facilitates selective incorporation of materials such as drugs or metallic compound into core or shell. For example, Liu et al. synthesized PCL-PEG star-like polymer as novel anticancer theragnostic vehicles shown in **Figure 1.2**.[13] The core initiator used is hyperbranched polymer (*Bolton H40*) which possesses abundant surface -OH groups as the initiator for ROP of ε-caprolactone. Then, end -OH groups was brominated by BIBB to introduce ATRP initiating groups. ATRP of $OEGMA_{475}$ and AzPMA forms the outer block with both PEG functionality to provide good water solubility and azide functionality which undergoes click reactions with alkyne functionalized cancer cell-targeting targeting moiety and MRI contrast agent via Cu catalyzed azide-alkyne cycloaddition. It was demonstrated that the drug-loaded star-like polymer has extended blood circulation duration and exhibits both cancer targeting and

high-contrast MRI properties. In the meantime, high drug (paclitaxel) loading as well as controlled release is observed in in-vitro drug release test. These star-like polymers represent a promising candidate for theragnostic platform.

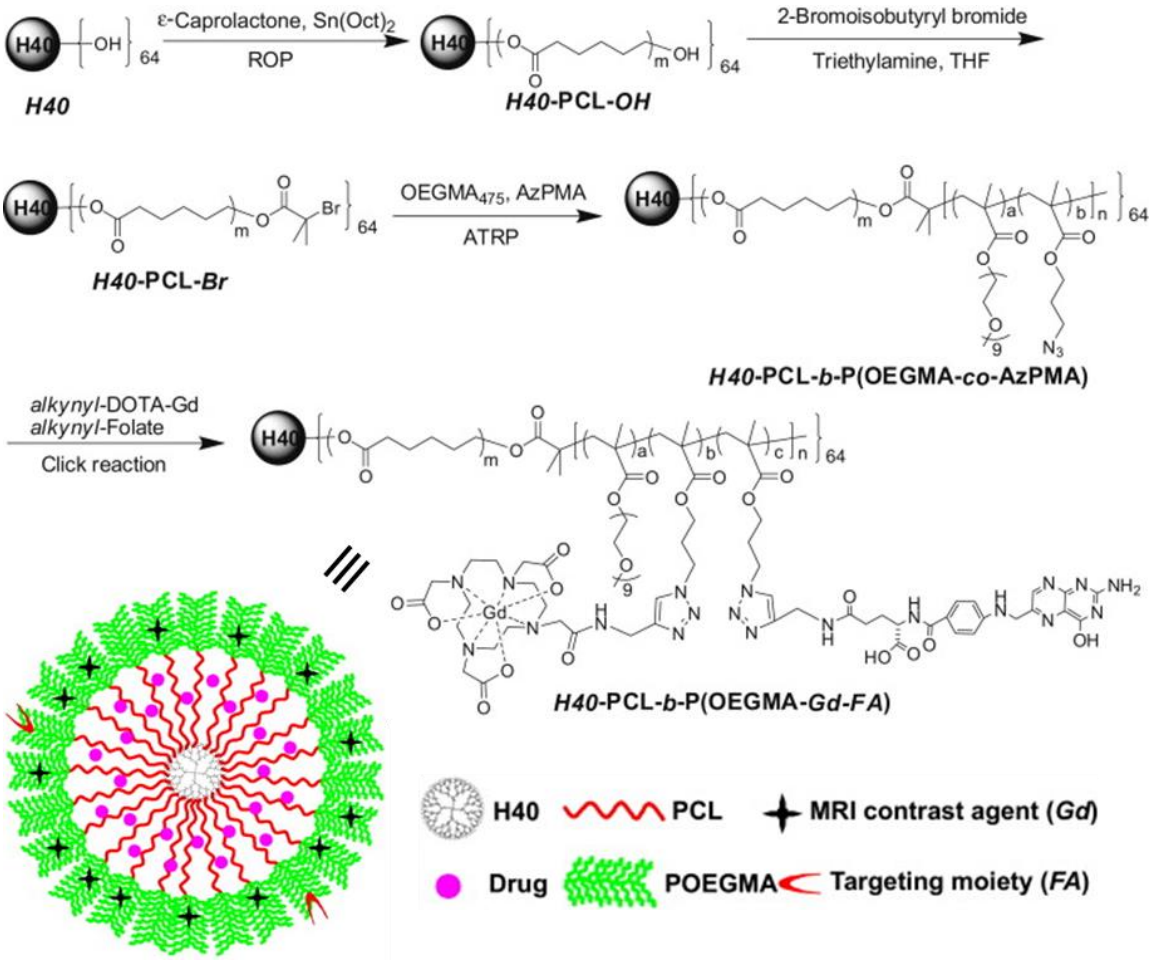

Figure 1.2. Schematic illustration of the synthetic route employed for the preparation of the amphiphilic multiarm star block copolymer, H40-PCL-*b*-P(OEGMA-Gd-FA). Reproduced from Liu et al.[13] Copyright 2011 Elsevier.

The core of the star-like block copolymer can also be functionalized with drugs for anti-cancer treatment. Prabaharan et al. used the same core (*Bolton H40*) to synthesis star-like block copolymer by grafting-onto approach shown in **Figure 1.3**.[14] The arms were first synthesized by ROP of BLA-NCA from NH_2 end-functionalized PEG to yield linear

PBLA-*b*-PEG-OH, which was then anchored to *Bolton H40* surface by DCC coupling esterification. Folate was coupled to the end of each arm which will specific target cancel drugs. After further polymer reactions of the PBLA block, doxorubicin hydrochloride (DOX, an anti-cancer drug) molecules were conjugated to the hydrophobic inner arm of the polymer by pH-sensitive hydrazone linkage. The unique chemical structure and amphiphilic nature of H40-P(LA-DOX)-*b*-PEG-OH/FA result in stable unimolecular micelles in aqueous solutions. FA-conjugated micelles can be directed to the cancer cells and subsequently immobilized in the target cell. Conjugation of DOX to the inner core of the amphiphilic star-like block copolymer is expected to improve the drug loading level and reduce the chance of premature drug release outside targeted cancer cells. Furthermore, hydrazone linkage between the DOX and polymer can be hydrolyzed in acidic conditions, leading to the increased release rate of DOX from the micelles in the acidic environment of the endosomal intracellular compartments, thereby providing a sufficient concentration of DOX in the tumor cells within a short period of time.

In summary, functionalization of the star-like block copolymers is versatile and serves as a general platform to endue different properties to star-like polymer for a variety of applications.

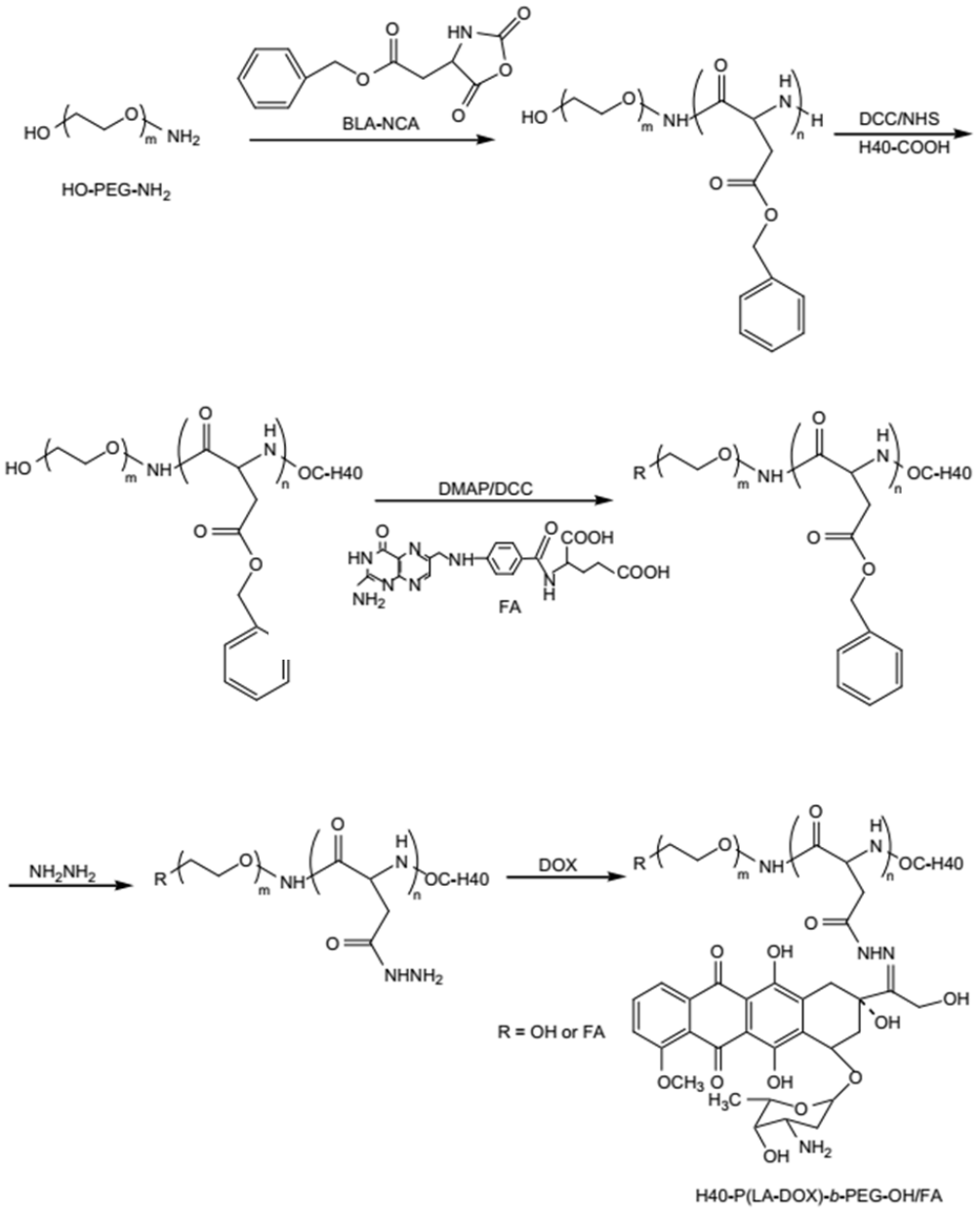
HO-PEG-NH2
BLA-NCA
DCC/NHS
H40-COOH
DMAP/DCC
FA
NH2NH2
DOX
R = OH or FA
H40-P(LA-DOX)-b-PEG-OH/FA
DOX conjugated via
a pH-sensitive hydrazone
bond
H40 core
Hydrophobic poly(L-aspartate) segment
Hydrophilic PEG segment
DOX conjugated by hydrazone bond
FA ligand

Figure 1.3. Reaction scheme for synthetic of amphiphilic H40-P(LA-DOX)-*b*-PEG-OH/FA star-like block copolymer. Reproduced from Prabaharan et al.[14] Copyright 2009 Elsevier.

1.1.1.3 β-CD initiated star-like block copolymer

β-CD has recently been a hot choice for synthesis of star-like polymer due to its high population of -OH functionality. It is also abundant in nature that doesn't require sophisticated synthesis. The 21 -OH groups distribute uniformly around the core minimizing any steric hindrance during polymer initiation while maintaining high arm number. At the same time, -OH groups can be readily used as the imitator for ring-opening polymerization to make polyesters. It can also be converted into halogen groups as well as RAFT end groups in a one-step reaction pathway giving it ability to initiate ATRP and RAFT polymerization. Several star-like polymers, including star-like PMCDMA (methyl chloride quaternized poly(2-(dimethylamino)ethyl methacrylate)),[15] star-like P*t*BA, and star-like PMMA-*b*-PBMA,[16-17] have been synthesized by ATRP with a β-CD initiator. Pang et al. has developed a novel strategy for synthesizing amphiphilic multi-arm, star-like block copolymers as unimolecular micelles with β-CD as the macroinitiator (**Figure 1.4**).[18]

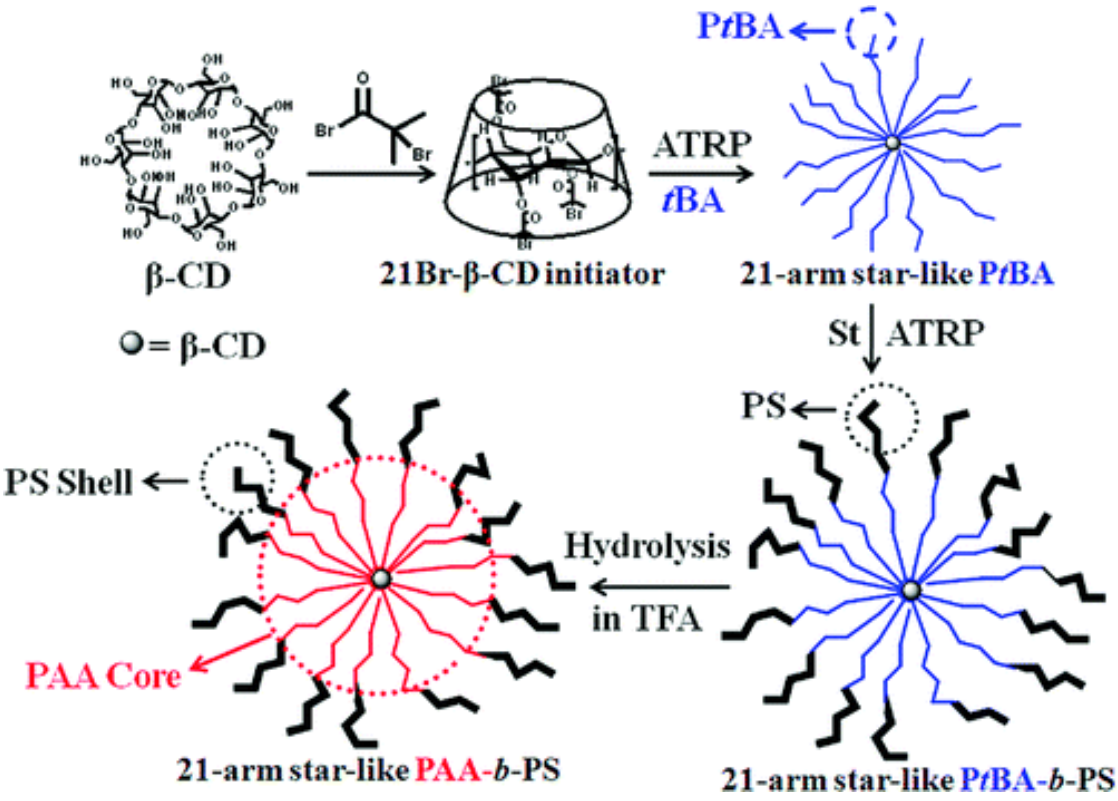

Figure 1.4. Schematic representation of the synthetic route to a novel amphiphilic 21-Arm, star-like PAA-*b*-PS, by sequential ATRP. Reproduced from Pang et al.[18] Copyright 2011 American Chemical Society.

Sequential ATRP of *tert*-butyl acrylate (*t*BA) and styrene (St) was carried out on brominated β-CD to yield 21-arm, star-like diblock (P*t*BA-*b*-PS) copolymers. Lastly, the P*t*BA block in star-like P*t*BA-*b*-PS were selectively hydrolyzed by trifluoroacetic acid (TFA) into polyacrylate acid (PAA) creating amphiphilic 21-arm, star-like PAA-*b*-PS with narrow molecular weight distribution. Because of the limited use of ATRP for certain types of monomers such as monomers with halogen moieties, RAFT can be applied for a broader range of polymers thus substituting ATRP in some cases to polymerize one block. For example, Feng at al. used β-CD to grow star-like poly(caprolactone)-*b*-poly(4-chloromethylstyrene) (PCL-*b*-P(S-Cl)).[19] In this case, β-CD was used as a macroinitiator to grow PCL by ring-opening polymerization. Next, the -OH group at the end of PCL

blocks was coupled with a small-molecule RAFT agent (DDMAT), followed by RAFT polymerization of 4-chloromethylstyrene. The -Cl on P(S-Cl) block was further functionalized into azide groups to create photo-crosslinkable star-like polymers serving as the template for soft nanocapsules. Nevertheless, β-CD derived star-like block copolymers templates purely by RAFT polymerization have not yet been reported. Click chemistry has also been widely used in the synthesis of β-CD derived star-like block copolymers due to the incompatibility of radical polymerization with lots of novel polymers with specific properties. The most commonly used click chemistry is the copper-catalyzed azide-alkyne cycloaddition (CuAAC). It enabled the preparation of 21-arm star-like PNIPAM. After bromination of all-21 -OH groups into -Br, the -Br groups were subsequently nucleophilic substituted with $-N_3$. Then, alkyne-functionalized PNIPAM was grafted onto the β-CD core via CuAAC.[20] Star-like coil-rod PS-*b*-P3HT with an inner coil PS and an outer rod P3HT was obtained by a combination of ATRP and CuAAC.[21] In this example, PS was first grafted onto brominated β-CD macroinitiator by ATRP. Next, the -Br end groups were converted into $-N_3$ similar to previously discussed examples. Finally, pre-synthesized alkyne-terminated P3HT was clicked onto the PS chains by CuAAC. In a similar fashion, PEO, PVDF, PEDOT were also grafted onto the star-like polymers.[22-25]

1.1.2 Synthesis of bottlebrush block copolymers

1.1.2.1 Bottlebrush-like polymers

Bottlebrush-like polymers, which are composed of a linear backbone and densely grafted side chains[26] have gained increasing attention and found to be useful in various fields, including photonics,[27-35] lithography resistances,[36-38] molecular pressure sensors,[39]

pH-sensitive molecular probes,[40] templates for generating nanowires,[41-46] therapeutic delivery vehicles,[47-54] etc., because of their unique properties, such as remarkable spatial dimensions, controllable architectures and compositions, as well as notable chain end effects.

Methods for synthesizing bottlebrush polymers are generally categorized into "grafting-to", "grafting-through", and "grafting-from".[55-60] (shown in **Figure 1.5a**). And different types of bottlebrush polymers (shown in **Figure 1.5b**) can be produced by choosing different method even reaction sequences.

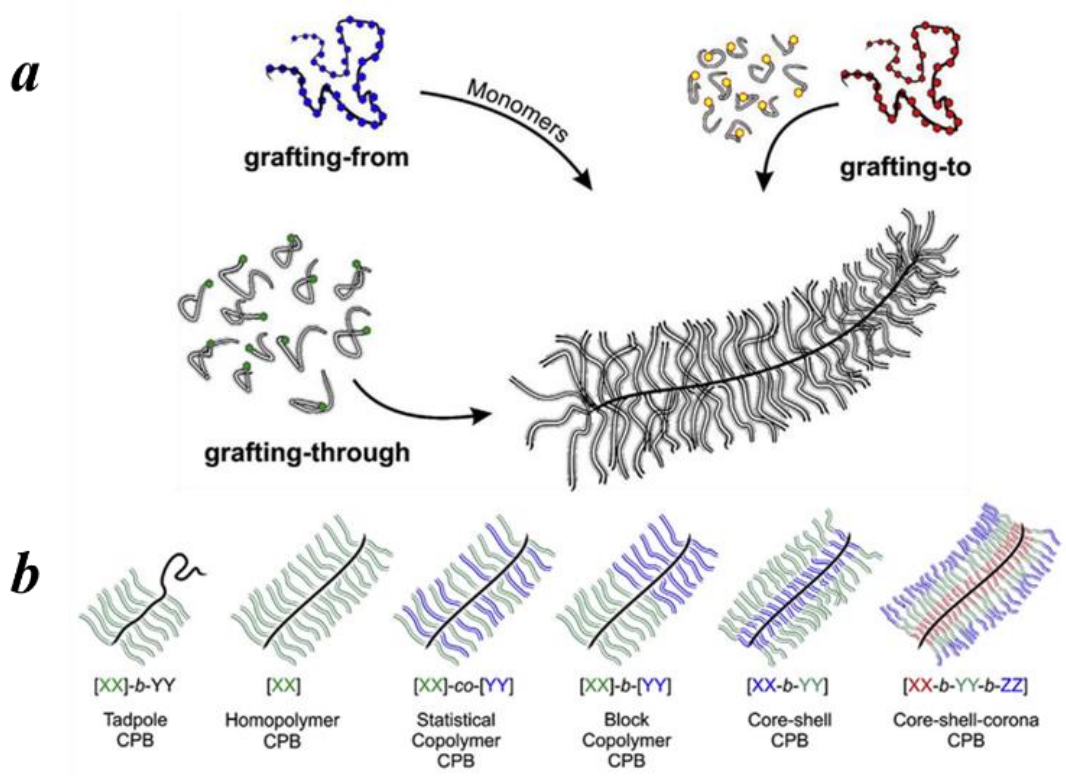

Figure 1.5. (a) An illustration of the three grafting strategies to produce bottlebrush polymers and (b) some of their many compositions. Reproduced from Mullner et al.[61] Copyright 2016 Elsevier.

The "grafting to"[62-67] method is to synthesize polymeric backbone and side chains separately, then attach them together by chemical coupling reactions, such as click

reactions. Difficult removal of unreacted side chains and lower grafting density[68-72] due to steric hindrance from the side groups are the major issues of this method. The "grafting-through"[26, 73-88] method is to polymerize the pre-synthesized polymeric side chains to form bottlebrush polymers by radical polymerization[41, 89-91] or controlled ring-opening metathesis polymerization (ROMP).[92-101] Although more uniform side chain length can be guaranteed, poorer backbone length control and lower degree of polymerization of backbone can be observed with this method.[102] Compared to those two polymerization tools, the "grafting-from"[103-110] method, synthesizing and functionalizing backbone first, then grafting side chains from the backbone, can adjust the dimension and grafting density more precisely, thus particularly suitable for synthesizing well-defined functional molecular bottlebrush copolymers.[111-113]

Aided by recent advances in polymerization techniques, a variety of chemical structures, including bottlebrush homopolymer,[109, 113-116] mikto (or statistic)[68, 107, 114-115, 117] bottlebrush copolymer, core-shell bottlebrush copolymer,[74, 111-112] etc., can be successfully synthesized. Bottlebrush homopolymer simply consist of side chains with only one composition, whereas mikto and core-shell bottlebrush copolymers consist of side chains with at least two monomeric units. The main distinction between the latter two bottlebrushes is that side chains of mikto copolymers graft randomly whereas side chains of core-shell copolymers graft in the core and shell compartment separately. Core-shell bottlebrush copolymers are especially interesting because the core and shell have different chemical environment which is considered to an ideal building block for non-spherical nano-objects[46, 118].

Bottlebrush homopolymer can be synthesized by all the approaches mentioned. For example, norbornenyl-grafted polystyrene (PS) and poly (ethylene oxide) (PEO) molecular brushes with high yield and narrow distribution of molar masses were successfully synthesized by ROMP via "grafting-through" method.[95] By employing atom transfer radical polymerization (ATRP) with "grafting from" technique, well-defined homopolymer and core-shell cylindrical copolymer brushes with various composition were prepared.[74]

The relative reactivity of the two monomers, affected by the identity of the side chains and the presence of additives can significantly influence the distribution of the side chains along the backbone, thus the type of bottlebrush copolymers. A versatile synthetic protocol for synthesizing mikto terpolymers with wide range of block lengths, compositions, and molar masses was proposed by first preparing three end-functionalized homopolymers then combining them with alternating controlled radical copolymerization.[119] Core-shell bottlebrush copolymers typically gain a great deal of interest because of their respectively tunable chemical environments in core and shell. Among the "grafting-to" method, click reactions have been one of the most widely used approaches for the synthesis of functional monomers, functional polymers, and polymers with complex topologies.[68] Many researches also employed ATRP by "grafting-from" method. By properly adjusting the reaction parameters, reactant, etc., one can synthesize bottlebrush polymers with more sophisticated morphologies, including triblock, gradient, or hollow. For instance, core-shell bottlebrush copolymers composed of an etchable inner block and a functional outer block were synthesized then hollow organic nanotubes formed by crosslinking the outer layer and removing the inner core.[48] In another research, architecturally-complex comb tri-

and tetrablock copolymers were obtained by applying highly active oxanorbornene as monomers.[120]

1.1.2.2 Cellulose initiated bottlebrush block copolymers

Huge breakthrough has been made for synthesizing core-shell bottlebrush block copolymers with cellulose as the macroinitiator. Cellulose is chosen as the desired backbone for cylindrical bottlebrush polymers because each repeating unit of cellulose can provide three hydroxyl groups for modification, which enable the backbone to be densely grafted by polymer side chains. Natural cellulose has a large length distribution and is hard to be dissolved in common solvent. To obtain single cellulose chain with certain length, they were first brominated in a mixed solvent of ionic liquid, anhydrous 1-methyl-2-pyrrolidione (NMP), and DMF, followed by fractional precipitation to divide the cellulose into a series of size each with low dispersity. It is worth mentioning that fractionation of cellulose backbone is performed via preparative GPC, which allows the collection of elute at different time intervals. The polydispersity (PDI) of each fractional collected was ensured to be within 1.05. It is essential that BBCPs with rather low PDI are used for self-assembly to avoid any defect or variation in the domain size, which may jeopardize their physical properties. Each core-shell bottlebrush block copolymer was synthesized from the backbone of distinct size by either sequential ATRP (for cellulose-*g*-(P*t*BA-*b*-PS)) or ATRP followed by click reaction (for cellulose-*g*-(P*t*BA-*b*-PEO)). All P*t*BA blocks were later converted into PAA by the same hydrolysis process as star-like block copolymers. The dimension of core and shell of the bottlebrush block copolymers can be precisely controlled by tuning the molecular weight of the inner and outer block. ATRP is one type of controlled radical polymerization technique where each polymer chain is going at the

same rate and the MW can be precisely controlled by reaction time. Therefore, uniform brushes were able to be grown onto the cellulose backbone maintaining the rod-like shape. Meanwhile, due to the helical structure of cellulose with -OH situated all over the surface, the synthesized bottlebrush copolymers will have their side chains uniformly distributed on the backbone. The bromide end group from ATRP can be further substituted with azide ($-N_3$) to enable the "click" reaction with pre-synthesized linear polymer which has an alkyne end group. This strategy was employed to make water-soluble BBCPs (cellulose-*g*-(P*t*BA-*b*-PEO)) since PEO cannot be synthesized by ATRP method.

1.2 Janus nanoparticles: synthesis, property, and application

1.2.1 Janus Particles, Properties, and Application

Janus particles are particles consisting of two different kinds of materials with distinct boundary between them as well as particles whose surface can be characterized by two distinct physical properties. It's a representative kind of asymmetric structure, which is widely adopted by nature for self-assembly into different types of hierarchical architecture (e.g. cell membranes). The word Janus comes from the name of a Roman god who has two faces, one looking to the future and one looking to the fast. The first well-recognized Janus particle was made by C. Casagrande and M. Veyssie which was brought into attention by P. G. de Gennes in his 1991 Nobel lecture[121]. Since then there has been great progress in the development of Janus particles both in synthetic strategies and application.

1.2.1.1 Types of Janus particles

Janus particles were first recognized as spherical particles composed of two different hemispheres. However, with decades' development in synthetic methods and more broadened application, a number of biphasic structures are cataloged under Janus particles. In some occasions, a more technical term is used, which is heterodimer. To date, besides spherical Janus particle, there are 10 more types of Janus particles that have been thoroughly studied including cylinders, disks, various dumbbell-shaped, and vesicles, all of which shown in **Figure 1.6**.[122] These types of Janus structures have varied degrees of anisotropy. Due to their specific architecture, each of them has its own unique properties that are preferred in certain applications. For example, Au and Ag metal with spherical, cylindrical and disk shape has different optical properties. They can also self-assemble into different hierarchical structures. On the other hand, dumbbell-shaped nanoparticles are easier to synthesis due to incompatibility of different materials and the nature of crystal growth.

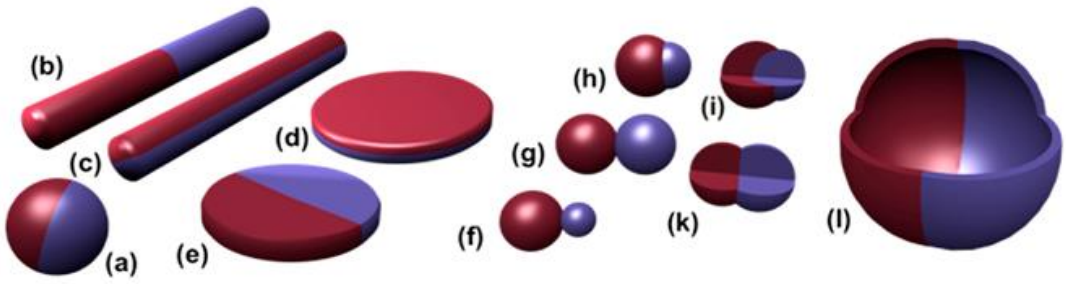

Figure 1.6. Types of Janus particles in active research. Reprinted from Walther et al.[122] Copyright 2013 American Chemical Society.

It is also worth mentioning that the focus of almost all research on Janus particles lies in microscale and nanoscale, which has been the hotspot in material science for decades. Among them, inorganic hybrids are most intriguing since they can combine the physical properties from two different inorganic materials, which themselves are of great

importance. Sometimes inorganic Janus particles are also referred to as nanocrystalline heterodimers. Although micro-sized and sub-micro inorganic Janus particles with well-defined structure and uniformity can be already synthesis in large scale via rational methods such as surface deposition[123-124] and emulsion[125] approach, few literatures have reported the formation of uniform Janus nanoparticles below 100 nm with good morphology. The focus of this project will be on the new strategy for making monodisperse spherical Janus nanoparticles.

1.2.1.2 Properties of Janus nanoparticles

The unique structure of Janus nanoparticle gives it superior properties compared with homogeneous nanoparticles. It combines the properties from both sides of JPs and even exhibit improvement in certain cases. The most superficial character of JPs is their surface anisotropy. The different materials on each side of the surface possess distinct physical and chemical properties which can be further functionalized separately. This amphiphilicity provide the JPs with largely improved stability in interfacial assembly to form higher ordered structures. Meanwhile, they can also serve as effective a surfactant or stabilizer at phase boundaries between two materials. Krausch[126] and Muller[127] has demonstrated that Janus nanoparticles and cylinders comprising two different materials (hard or soft) show an evidently lowered interfacial tension than the ones comprising only single material (as shown in **Figure 1.7**).

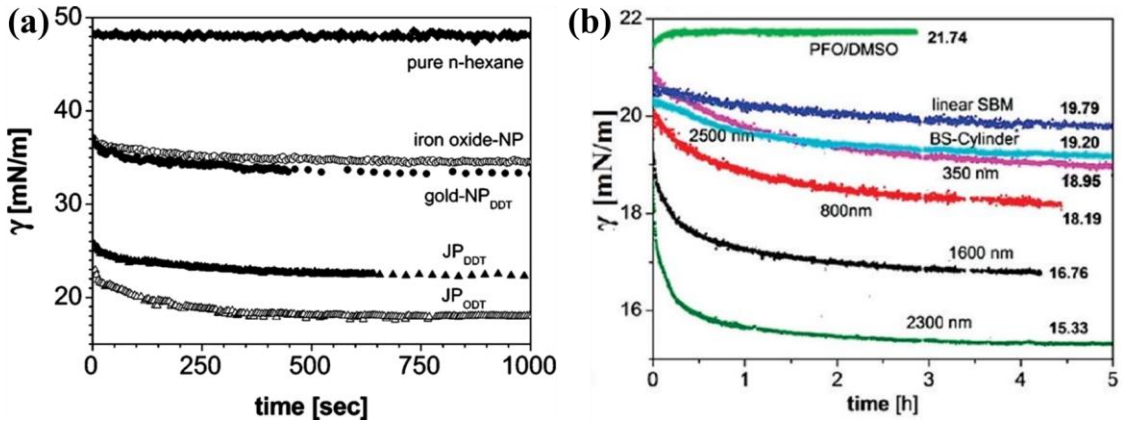

Figure 1.7. Interfacial tension isotherms in (a) Janus particle and (b) Janus cylinder system: (a) Comparison of pristine Fe_3O_4 NPs, DDT-coated Au NPs, and dumbbell Au-Fe_3O_4 JPs in hexane/water interface. Reprinted from Glaser et al.[126] Copyright 2006 American Chemical Society. (b) Comparison of linear SBM terpolymer and homogeneous BS core-shell cylinders in PFO/DMSO interface. Reprinted from Ruhland et al.[127] Copyright 2011 American Chemical Society.

Despite the superior interfacial activity JPs have, they also exhibit the physical properties from both sides of the particle. In other words, JPs are dual-functional materials. For example, as reported by Sun et al[128], Au/Fe_3O_4 Janus nanoparticles are partly superparamagnetic and partly optical plasmonic, which is highly efficient as imaging probes. In essence, any combination of physical or chemical properties can be achieved by incorporating two kinds of material into one Janus structure.

Another important property of JPs is controlled self-assembly and controlled rotation arising from the anisotropic nature. Hatton[129]'s group has prepared both pH responsive and thermoresponsive Janus nanoparticles (**Figure 1.8a**). When pH-dependent poly(acrylic acid) (PAA) and pH-independent polystyrene sodium sulfonate (PSSNa) are coated on each side of a magnetic nanoparticle, the nanoparticle shows a pH-reversible self-assembly behaviour. After substituting PSSNa with temperature-dependant poly(N-isopropyl acrylamide) (PNIPAM), the nanoparticles, in turn, shows temperature- reversible self-

assembly. Similarly, inorganic Janus nanoparticles can also present self-assembly behavior in electrical[130] or magnetic[131] field. On the other hand, Kopelman[132-133]'s group developed a type of Janus magnetic microparticles that can align and rotate in magnetic field (**Figure 1.8b,c**).

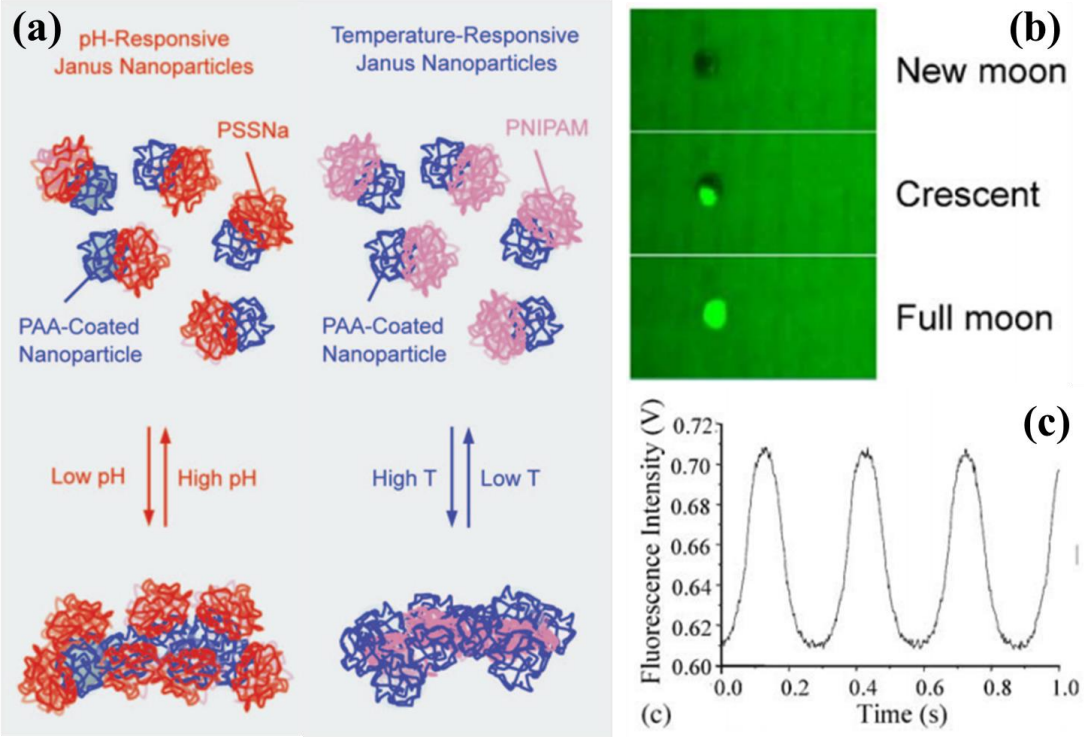

Figure 1.8. (a) Scheme for pH and temperature responsive Janus nanoparticles. Reprinted from Isojima et al.[129] Copyright 2008 American Chemical Society. (b) Aluminum-capped 4.4 μm paramagnetic JPs in three orientation. (c) Intensity oscillation due to rotation of paramagnetic JPs in magnetic field. Reprinted from Anker et al.[133] Copyright 2005 Elsevier.

1.2.1.3 Application of Janus nanoparticles

The unique properties of Janus nanoparticles arising from their anisotropic nature grants them with a wide variety of advanced applications. Although the interesting behaviours of Janus nanoparticles have only been discovered no more than 10 years ago

and explored for application in a limited time and rage, the performance of these Janus NPs is already found to transcend any other type of nanoparticles.

For purely polymeric Janus particles, usually amphiphilic nanoparticles, the application for single Janus particle is mainly limited in surfactant or stabilizer for emulsion[134] or between solid interface to increase surface compatibility[135]. However, due to the self-assembly behaviour of these Janus nanoparticles, micelles or vesicles of different size and shape can be obtained, which serves as excellent materials for drug encapsulation and delivery.

One standout application of inorganic Janus nanoparticles is nanomotors. This phenomenon is also called self-propulsion. Owing to the particle's anisotropic surface, local heating or electrochemical reactions can take place on only half the surface, which triggers the movement of nanoparticles. Xuan[136-137] et al. has prepared Au-nanoshell functionalized Janus mesoporous silica nanoparticles by surface deposition of Au on silica particle monolayer. Under near infrared (NIR), Au nanoshell will generate local heat causing a thermal gradient around the nanoparticles. This self-thermophoresis effect creates a net force suppressing Brownian force, resulting in swift motion of these nanoparticles. The same group also replaced Au with Pt. The Pt shell catalyses the deposition of H_2O_2 and produces O_2, which propelled the nanoparticles. On the other hand, Dong[138] et al. demonstrated rapid motion of Au-TiO_2 Janus microparticles under UV light by self-electrophoresis (i.e. water splitting). These new types of self-propelling nanoparticles can make significant contributions as delivering vehicles for biomedical applications.

Metal oxide nanoparticles is well-recognized as active components in photocatalysis. The efficiency is further enhanced by coupling with metallic materials such as Au, which reduces charge recombination. Pradhan[139] and Seh[140] successfully synthesized Au-TiO_2 heterodimers that have superior photocatalytic performance compared with novel Au-TiO_2 core-shell nanocomposites. The asymmetric structure leads to strong localized-surface-plasmon-resonance (LSPR) at Au-TiO_2 interface, where enhanced optical absorption and electron-hole generation is observed.

Inorganic Janus nanoparticles combined two different materials (i.e. two different properties) in one body which gives it dual-functionality. This dual-functionality is of great importance in the application in bioimaging and targeting. For example, Au-Fe_3O_4 dumbbell-shaped Janus NPs synthesized by Sun et al.[128] exhibit both superparamagnetic property from Fe_3O_4 and surface plasmon resonance from Au. Consequently, this type of nanoparticles is capable of simultaneous optical and magnetic detection in biomedical imaging. Moreover, different functional groups can be attached to the anisotropic Au-Fe_3O_4 surface for targeted imaging and delivery. It offers significant improvement in kinetic studies of cell targeting and drug release. Meanwhile, Hu and Gao[125] developed a type of organic-inorganic hybrid Janus nanoparticles with organic phase loaded by fluorescent dye and inorganic being superparamagnetic. These nanoparticles combine fluorescent imaging with magnetolytic therapy (killing cells by mechanical destruction of cell wall under spinning magnetic field).

Overall, the application of Janus nanoparticles is still in its developing stage with lots of potentials yet to be explored. On the other hand, in order to achieve better performance

or to be applied in more high-end field, a versatile synthetic strategy towards Janus nanoparticles with well-defined structure and small size distribution is in great need.

1.2.2 Synthetic Strategies of Janus Nanoparticles

Over recent decades, much effort has been put into developing synthetic methods for nano-sized structures due to their distinct properties which bulk materials don't have. Therefore, this part of the introduction only focuses on the synthesis of Janus Nanoparticles whose sizes are below hundreds of nanometers.

There are 3 types of widely adopted methods for making Janus NPs including self-assembly from block copolymer, masking in which one side of the particle is exposed for modification, and phase separation of two inorganic components (see **Figure 1.9**). However, due to thermal dynamic instability for self-assembly and phase separation, as well as limited size of mask, it is so far difficult to make monodisperse Janus nanoparticles with well-defined structure below 100 nm. A bottom-up approach with confined structure in each step of synthesis is needed to achieve this goal, which will be discussed in section 1.3.2.2.

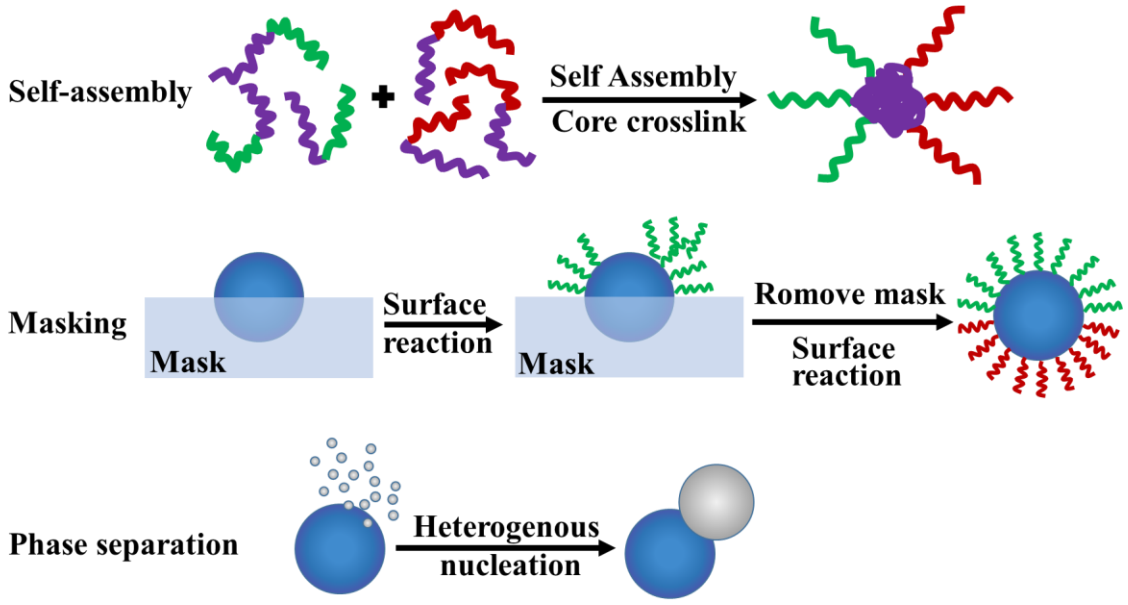

Figure 1.9. Three types of synthetic strategy for making Janus nanoparticles.

1.2.2.1 Self-Assembly

Self-assembly is a characteristic behavior of block copolymer. Polymers of the same type in several copolymers will tend to form one domain due to less interface energy between them. Depending on the ratio of different blocks, they will form spherical, cylindrical, lamellae structures, etc. This versatile assembly of almost any kinds of block copolymer makes it widely used for making nanoparticles, nanocylinders and nanosheets. The first polymeric Janus nanoparticle synthesized by self-assembly was published by Muller's group, who used polystyrene-block-polybutadiene-block-poly(methyl methacrylate) terpolymer to form PS/PMMA alternating lamellae structure with PB spheres locating at the interface[141]. After crosslinking the PB domain followed by dissolution, polymeric Janus nanoparticles with PS and PMMA on the opposite side of the PB core is generated. Another approach for polymeric Janus nanoparticles is through the co-assembly of two different block copolymers in which only one block is the same (as

shown in Figure 4). For example, in Ma's report, poly(2-vinyl pyridine)(P2VP)-block-poly(ethylene oxide)(PEO) is self-assembled with P2VP-block-PNIPAm, after which P2VP from two polymers is crosslinked by divalent sulfate ions[142]. Interestingly, in another work published by Zubarev[143], PS-*b*-PEO block copolymer is self-assembled on the surface of Au nanoparticle enabled by the strong binding between carboxyl group (-COOH) and Au. These Au nanoparticles with Janus (amphiphilic) ligand will then self-assemble into nanorods in water.

While asymmetric capping of inorganic nanocrystals can be achieved by the above approach, a more versatile strategy by assembly of two incompatible ligands on NPs' surface is also widely used[144-147].

In summary, since self-assembly behavior mainly exist in polymers or long-chain ligands, the Janus nanoparticles that can be formed through self-assembly are usually polymeric. On the other hand, it is worth mentioning that Janus polymer can potentially serve as template for crystal growth of inorganic materials as a result of the specific binding between the functionality on polymer and metal.

1.2.2.2 Masking

The principle of masking is to cover or protect one hemisphere of the as-formed nanoparticles by solid or liquid substrate and expose the surface of the other hemisphere for chemical modification. The simplest way is to cast the NPs onto a solid substrate or trap them at oil-water/air-water interface. It is a versatile method for surface modification that can be applied to both inorganic and organic particles. For example, it can be used to make metallic nanoparticles with Janus ligands[148-150], hard-soft hybrid Janus

nanoparticles[151-153], dumbbell-shaped heterodimers[154-155], strictly spherical metallic-ceramic Janus nanoparticles[136, 156-157].

Mask can exist in different forms. The most common used mask is a hard substrate such as glass or silicon wafer. A monolayer of nanoparticles is first deposited on the substrate followed by surface coating with another material. Then the nude surface on the substrate side is further modified with other functionalities. However, another approach with pre-treated surface may also be applied, in which Janus character can be generated in a single step. Wang et al.[155] drop casted a layer of PEO-SH crystal onto an inert substrate before depositing Au NPs afterwards, in which situation the Au surface contacting the substrate is immediately tethered with PEO chain. In a similar fashion, soft flat substrate (polymer matrix) was also used as mask[158]. Other masking techniques including particle dispersion[148, 159], droplet and Pickering emulsion[160-162], air-water interface[139, 163], and oil-water interface[164-165] utilize the self-assembly behaviour of nanoparticles at interface for selective modification within each phase.

Masking is obviously the most flexible and versatile method in the preparation of Janus nanoparticles covering all types of Janus structures from all-soft, all-hard to soft-hard hybrid materials. However, it has its own limitations. On the one hand, it required monodisperse nanoparticles made beforehand with remaining ligands attached, which have to be removed in many circumstances. On the other hand, there is a size limitation for the nanoparticles that are compatible with masking approach, usually above 100 nm.

1.2.2.3 Phase separation

Phase separation will be the focus of discussion in this section since it is the most widely used and rational strategy for making inorganic Janus nanoparticles (i.e. nanocrystalline heterodimers). Polymeric Janus particles and polymer-inorganic hybrids synthesized by phase separation will not be discussed here since it's not the focus of the proposal. Four different growing mechanisms of inorganic heterojunction are proposed by Casavola[166] and slightly modified by Carbone[167] are shown in **Figure 1.10** including (a) direct heterogeneous nucleation; (b-c) nonepitaxial deposition followed by thermally driven coalescence-crystallization and/or solid-state atomic diffusion; (d) reactions at liquid/liquid interfaces; (e-f) self-regulated homogeneous-heterogeneous nucleation. The formation of heterogeneous structure in Janus nanoparticles is a thermodynamically driven process. The energy gain from release of interfacial tension between two materials is large enough to compensate increased surface energy during heterodimer formation. It is more favorable for the combination of two inorganic crystals with large lattice mismatch (i.e. more incompatible). Overall, the process is a result of minimized Gibbs free energy.

Although Janus NPs synthesis by phase separation is the most commonly used strategy. This seed-mediated growth is predominately a thermally driven process with little kinetic control. The ultimate structure is largely dependent on precursor concentration, capping ligand, temperature, solvent, and reaction time. Consequently, it is difficult to achieve high uniformity with this method. The interfacial interaction of the two phases is extremely hard to predict and control, which usually leads to an undefined interfacial area and coverage. Additionally, since the formed nanocrystals tend to form thermodynamically more stabled spherical structure at the meantime minimize interfacial tension, the second material often grows into a nanoparticle decorated on the original seed, ending up with

dumbbell-shaped Janus nanoparticles. Sharp phase boundary is prohibited in the formation process. Although unique as it already is, it still lacks certain properties that will be otherwise provided by spherical nanoparticles composed of two distinct hemispheres. For example, spherical shape can be subjected to rapid rotation as well as directed motion based on fluid dynamics. On the other hand, self-assembly behavior varies a lot between spherical Janus particle and dumbbell shaped Janus particle where spherical structures are more likely to form more closely packed superlattice as well as self-assembled monolayer (SAM) at interface. Thus, a rational method for preparing well-defined spherical Janus nanocrystals is of urgent need.

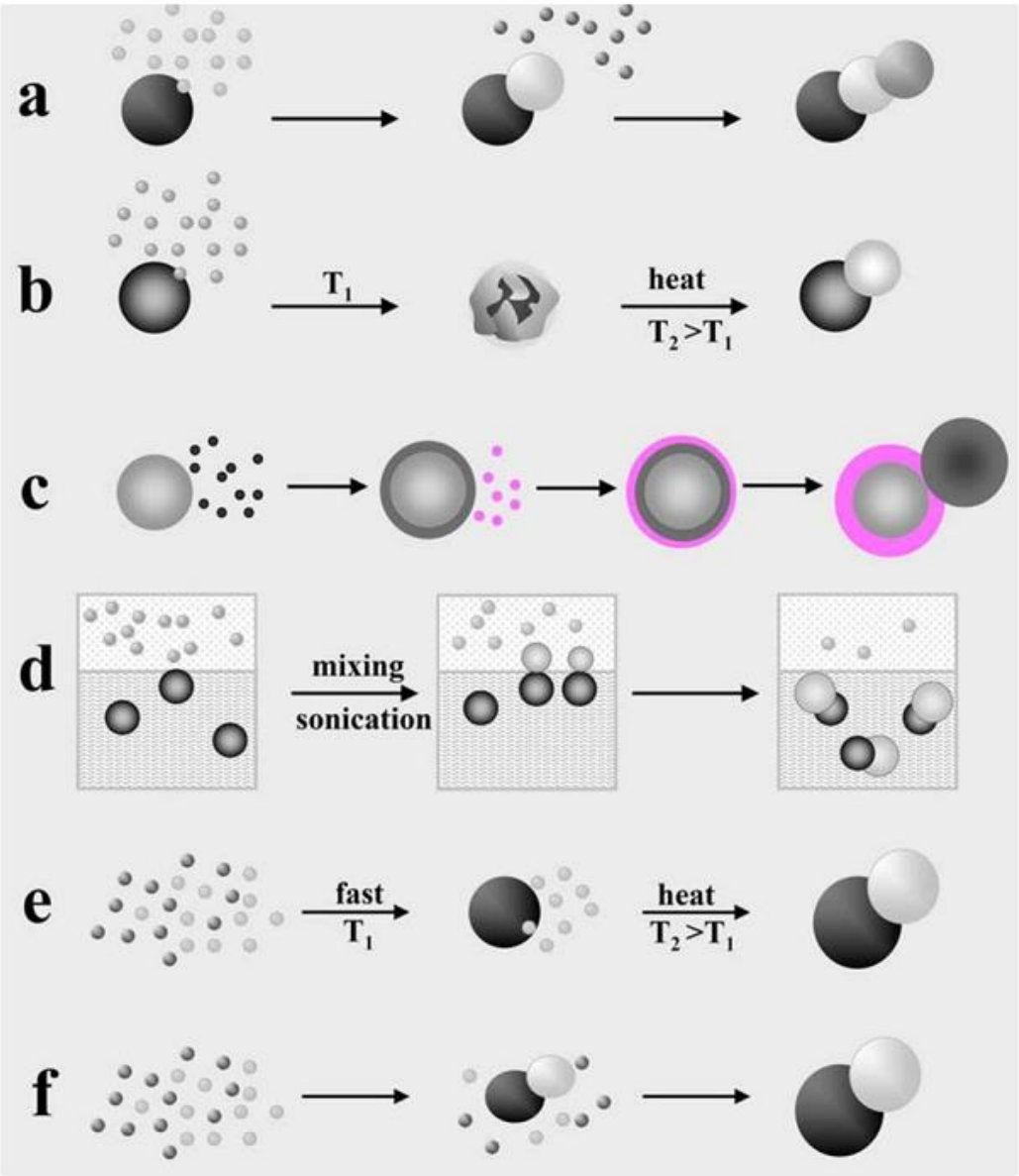

Figure 1.10. Sketch of mechanisms underlying the formation of Janus inorganic heterodimers: (a) direct heterogeneous nucleation; (b-c) nonepitaxial deposition followed by thermally driven coalescence-crystallization and/or solid-state atomic diffusion; (d) reactions at liquid/liquid interfaces; (e-f) self-regulated homogeneous-heterogeneous nucleation. Reprinted from Carbone et al.[167] Copyright 2010 Elsevier.

(1) Direct heterogeneous nucleation

Direct heterogeneous nucleation also known as epitaxial growth is the most well-understood and implemented method for nanoparticle growth where one particle nuclear

and grow on the surface of another crystalline particle (**Figure 1.10a**). Heterodimer formation is favored due to the intrinsic lattice incompatibility of two different materials, the orientation of which driven by minimized strain at interface.

Most common materials made through this approach is noble metal-metal oxide heterodimer among which Au-Fe_3O_4 is thoroughly investigated for its formation mechanism. Solvent plays an essential role in controlling the morphology of formed nanocrystal by modulating nucleation sites on Au seeds[168-169]. There is a charge polarization effect near Au-Fe_3O_4 interface. In nonpolar solvent, electrons on the entire surface of Au is accumulated on the first nucleation site of Fe_3O_4, renders elsewhere electron deficient and incapable of forming another nucleation site, thus creating heterodimer. However, in polar electron-donor solvent, such electron deficiency is compensated, therefore, providing availability for multiple nucleation sites, which end up with flower-like or even complete core-shell structures.

The steric conformation of Janus nanoparticles can be tuned by varying seed to metal-ion precursor concentration ratio as well as temperature, which is demonstrated in Au-$CoPt_3$[170] and Ag-Fe_3O_4[171] synthesis. Furthermore, hetero-oligomers could be synthesized simply by repetition of epitaxial growth of a third material onto the heterodimers and so forth.

(2) Post-deposition coalescence-crystallization and/or solid-state diffusion

This nonepitaxial growth defers from direct heterogeneous growth due to larger lattice mismatch which inhibits epitaxial growth. It is mostly observed in FePt or γ-Fe_2O_3 and metal chalcogenides (MeX) system. Initially, with the addition of organometallic

precursors at low temperature, an amorphous MeX shell is formed onto the seed particle. During the crystallization at high temperature, strain is gradually built up at seed-MeX interface leading to the final coalescence and segregation of the MeX shell into heterojunction (**Figure 1.10b**). The driving force for this post phase separation fully comes from the reduction of interfacial energy between two materials.

Coincident Site Lattice Theory (CSLT)[172] explains the degree of lattice matching between two different crystal structures. It can be generalized by the frequency of a correspondence existing in two lattices along the grain boundary, which dominates the average number of MeX domains presented on FePt or γ-Fe_2O_3 seed. It is also discovered recently that transformation between core-shell structure and heterojunction can occur by aging[173]. More interestingly, Yang et al.[174] discovered that the Au middle shell in a Pt@Au@Ag_2S core-double shell structure was able to diffuse through the Ag_2S outer shell and eventually formed a heterogeneous dimer crystal in which Pt and Au was completed phase separated (**Figure 1.10c**). A substitutional-interstitial mechanism[175] was proposed for explanation where electron transfer from Auto semiconductor facilitates Au ion penetration through semiconductor lattice. Meanwhile, as mentioned above, only material combinations with certain degree of lattice matching are capable of coalescence into heterogeneous structures with just two domains (heterodimers), which as a result limits the extension of this method into other varieties of materials.

(3) Reactions at liquid/liquid interfaces

This interfacial reaction technique is developed to fabricate magnetic-noble metal heterodimers[154]. Typically carried out in water-oil emulsion, the reaction takes advantage

of the different solubility of magnetic seeds capped with hydrophobic ligand and noble metal precursor which is usually hydrophilic. During heterodimer synthesis, Ag^+ or $AuCl_4^-$ ions are reduced on the catalytic sites (e.g. Fe(II)) of the seed nanoparticles. Since only one face of the seed is exposed to hydrophilic precursor solution at the liquid-liquid interface, heterogeneous growth only takes place on the exposed site forming single domains on each seed (**Figure 1.10d**). However, this method is not widely used since catalytic behavior is required from the seed. At the same time, crystal growth is not well controlled in emulsion preventing the formation of uniform structure.

(4) Self-regulated homogeneous-heterogeneous nucleation

Both direct heterogeneous nucleation and post-deposition coalescence-crystallization require using pre-synthesized nanoparticle seeds, which involve another synthetic step. In order to simplify the procedure for making Janus nanoparticles, self-regulated homogeneous-heterogeneous nucleation is developed as a one-pot synthetic method where precursors for two different materials are mixed with the same surfactant in the beginning. Homogeneous nucleation of the first particles and heterogeneous nucleation of the second crystal are both self-regulated.

Depending on the nature of reactions, the growth of two counterparts of the heterodimer can be either sequentially (**Figure 1.10e**) or simultaneously (**Figure 1.10f**). For example, Au-Ni heterodimer is synthesis by Wang et al.[176] using $HAuCl_4$ and $Ni(NO_3)_2$ as precursors. Au seeds were initially formed at 120 ºC, which afterward catalyzed the reduction of Ni at Au surface. It is worth mentioning that Ni^{2+} reduction is kinetically unfavorable and can only take place with Au catalysis during the reactions. In another case,

Saunders and coworkers successfully made Ag-AgBr heterodimers by simultaneous nucleation and growth of Ag and AgBr. The precursors used are $AgNO_3$ and alkylammonium bromide complex which can reduce Ag^+ to Ag and precipitate AgBr at the same time. Detailed characterization showed constant size ratio between two domains in the heterodimer.

Convenient and fast as it may seem, this method demands delicate and sophisticated design of chemical reaction to achieve self-regulated nucleation and growth for two different materials, for which its implementation and generalization remains challenging.

1.3 Polymer-templated synthesis of inorganic nanocrystals

Conventional colloidal synthesis of inorganic nanocrystals is mostly by bottom-up approach starting from inorganic precursors. By controlling the nucleation and growth of the nanocrystals, the size and shape of the nanocrystals can be tuned through different strategies. The first control step is the nucleation step, according to LaMer, it is important to ensure as much nuclei are produced in a short time as possible in order to obtain uniform particle size. Typically, higher temperature will increase nucleation and growth speed by driving molecular diffusion, lower temperature gives less and smaller nucleus. In case of two precursor system, instant nucleation is achieved by fast injection of one precursor into the dilute solution of the other precursor. Surfactant is always needed to reduce surface tension between nuclei and solution therefore preventing bulk formation. Secondly, the crystal growth step can be controlled by the addition of capping agent, which will be absorbed on particles surface to limit crystal growth. It provides steric hindrance between the particles to prevent aggregation.[177] In some case, a facet-selective ligand or surfactant

is used to selective bind to specific facets and inhibit the growth in that crystal plane with stronger interaction to the ligand. This strategy has been widely adopted for the production of anisotropic nanocrystals such as nanocubes, nanorods, nanowires, nanoplatelets.[178] However, in all the above cases, the finally synthesized nanocrystals are capped with organic ligand or surfactant via non-covalent interactions between the functional groups on the ligand (e.g. carboxylic acid or amine) with metal moieties. Therefore, these weak linkages are extremely vulnerable and can be easily broke under extensive washing or harsh conditions such as high temperature. Additionally, crystal growth is typically very fast, sometimes in a matter of seconds. Ligand or surfactant do not possess any confinement effect on crystal growth. Therefore, the nanocrystals can growth to infinitely large if the growth is not stopped or quenched. In this situation, the reaction condition and time have to be precisely controlled to product nanocrystals with desired size and shape, which jeopardize the reproducibility. Finally, ligand selection is crucial in the synthesis of anisotropic nanocrystals and it takes enormous effect find the right ligand that exhibit stronger interaction with one facet of a specific crystal type. There hasn't been any versatile ligand that can be used to produce a specific anisotropic crystal structure of any inorganic materials.

In order to have confined growth of nanocrystals where growth is only limited in space, templated assisted nanocrystal synthesis has been extensively researched in recently decades.[179-180] The nucleation and growth of nanocrystals can only take place inside the template (sometimes called nanoreactor). The size and shape of the nanocrystals is controlled by the nano-space inside the nanoreactor. For inorganic template such as activated carbon or porous silica[181], the crystal growth is confined by the nano-pores. For

organic template (mostly polymer template), the growth is confined within certain polymer domains where there is specific interaction between polymer functionality with inorganic precursors. The polymer template approach can be generally divided into two categories: polymer matrix and polymer micelle, which will be discussed individually in the following sections.

1.3.1 Polymer matrix template

In-situ synthesis of inorganic nanocrystals within polymer matrix has been an efficient way to produce polymer/nanocrystals nanocomposite. The nanocrystals are grown inside the polymeric domains therefore having extended surface polymer protection. Certain functionality as well as responsiveness can also be incorporated into the nanocomposite through design of polymer matrix. More importantly, no ligand or surfactant is required in the synthesis of nanocrystals simplifying the reaction systems.

Polymer microgel has been widely adopted as the template for the synthesis of dispersed inorganic nanoparticles embedded in polymer matrix. Jia et al.[182] reported a facile strategy for the fabrication of α-cyclodextrin (α-CD) modified poly(N-vinylcaprolactam) (PVCL) microgels decorated with Au nanoparticles with enhanced catalytic activities. Au nanoparticles were grown in the free space created by the swelling of microgel and immobilized inside the hybrid gel due to strong coordination between cyclodextrin molecules and the surface of Au nanoparticles. Selectively absorption and reduction of 4-nitrophenol (NIP) on surface of Au is observed which is attributed to the complexation of NIP with α-CD that is coordinated with Au nanoparticles. Other inorganic materials such as Bi_2O_3, Ag, CdS nanoparticles have also been incorporated into the

polymer microgel by introducing -OH, -COOH functional groups onto the polymer chains which can coordinate with metal precursors.[183-184] An advantage of using polymer microgel as the template to support nanoparticles is that stimuli-responsive polymer can be used to introduce responsiveness into the nanocomposite. For example, Suzuki et al.[185] synthesized thermoresponsive cationic microgel by aqueous free radical precipitation polymerization which was used as the template to grow Au nanoparticles. The cationic sites in the microgel directed the nucleation and growth of particles. The size of Au nanoparticles was able to be tuned through variation of temperature or types of reducing agents. Shi et al.[186] fabricated multiple stimuli-responsive hybrid microgel with triblock copolymers containing thermoresponsive PNIPAM, pH-responsive PMAA, and a thiol functionalized block to coordinate with Au (**Figure 1.11a**). The hybrid microgels had a unique structure with the majority of Au nanoparticles situated in the interior of the microgel with a fluff-like surface. More significantly, the plasmonic properties and catalysis activity can be regulated via external stimuli such as temperature and pH. Akamatsu et al.[187] used crosslinked poly(2-vinylpyridine) latex particles to deposit Au nanoparticles with tunable size over a range of 10-30 nm simply by varying reduction rate. It is found that Au nanoparticles only formed on the surface of the microgel due to diffusion of precursors from the interior onto the surface during reduction. The pH-responsiveness of the polymer was well maintained in the hybrid microgel which had the ability to modulate plasmon coupling between Au nanoparticles.

In addition to polymer microgels, other polymeric microstructures have also been used as the templates for nanoparticles synthesis. Han et al.[188] reported a novel method to synthesize gold nanoparticles on both inner and outer surfaces of poly(o-phenylenediamine)

(PoPD) hollow microspheres, which act as both reductant and template/stabilizer. More importantly, with seed-growth strategy, Au nanorods can also be fabricated on the shells of PoPD hollow microspheres, indicating the diversity of the proposed method. Ding et al.[189] grew Pd nanoparticles of 4-7 nm inside a nanostructured lyotropic liquid crystal network by ion exchange of Pd(II) followed by hydrogen reduction (**Figure 1.11b**). The Pd nanoparticle composite exhibits excellent catalytic properties.

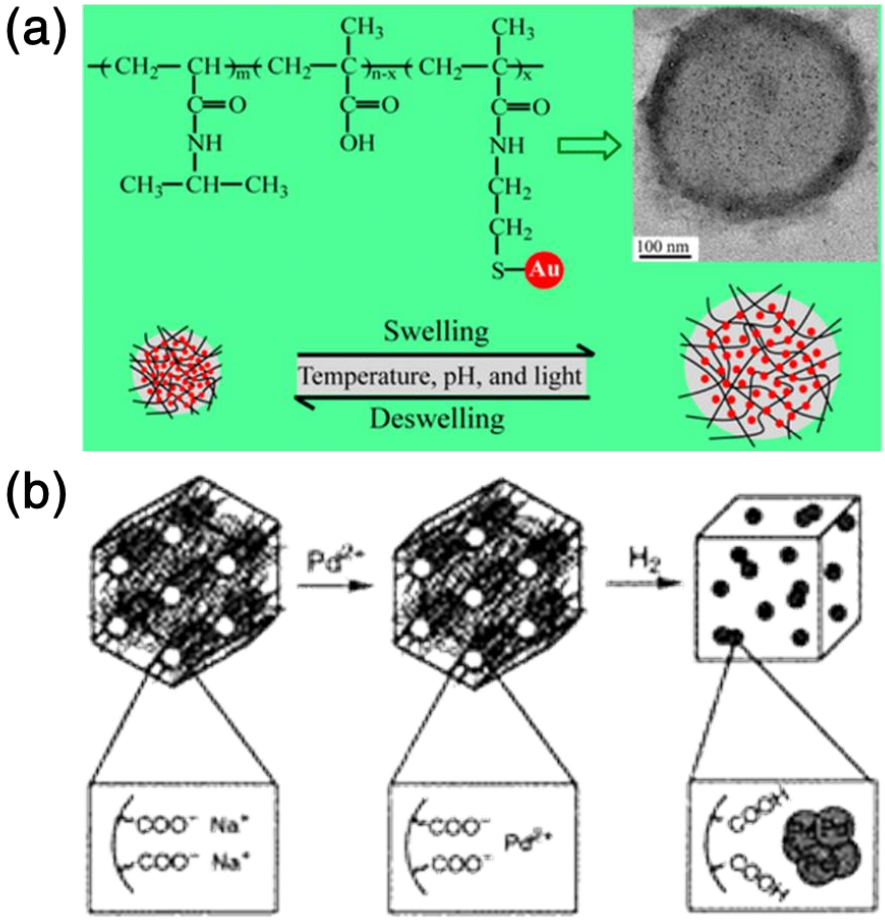

Figure 1.11. (a) Thermo-, pH-, and light-responsive poly(N-isopropylacrylamide-co-methacrylic acid)–Au hybrid microgels prepared by the in situ reduction method based on Au-thiol chemistry. Reproduced from Shi et al.[186] Copyright 2014 American Chemical Society. (b) Catalytic Pd nanoparticles synthesized using a lyotropic liquid crystal polymer template. Reproduced from Ding et al.[189] Copyright 2000 American Chemical Society.

Despite the good shaped confinement and excellent stability of polymer matrix for growth of inorganic nanocrystals, there are several non-negligible drawbacks. First, the nanoparticles will lose their surface protection when they are isolated from the polymer matrix due to the lack of capping agents. Thus, they cannot be dispersed in solutions. Second and most importantly, the growth of nanocrystals is highly dependent on the distribution of precursors in the matrix which is rather random. The size and shape of nanocrystals cannot be precisely controlled due to poorly confined nanostructures inside the matrix. Therefore, the nanocrystals synthesized in the polymer matrix is not suitable for investigation of their size or shaped dependent physical/chemical properties.

1.3.2 Block copolymer template (polymer micelle)

Surface passivation of nanoparticles is crucial to prevent nanoparticles aggregation due to their high surface energy. Although it can be achieved by chemical treatment on nanoparticles via grafting onto or grafting from methods, no size and shape control can be achieved by post surface passivation since the growth is not limited during particle formation stage. Therefore, in order to synthesize nanocrystals with existing surface passivation, block copolymer (polymer micelle) strategy has been exploited.

1.3.2.1 Self-assembled polymer micelle

Polymer micelles of different architectures including spherical, tubular, worm-like with distinct core-shell structures can be formed by self-assembly of block copolymers.[190-192] Typically, the one polymer block situated in the core of polymer micelle carries specific functional groups to provide coordination sites for metal precursors and direct the nucleation and growth of nanoparticles., while the other block in the shell serves as the

capping ligand to passivation nanoparticle surface and prevent aggregation. Block copolymer template strategy is advantageous since the outer polymer blocks are permanently tethered on the particle surface providing superior colloidal stability. Additionally, the size and shape of the nanoparticles can be easily tuned by changing the molecular weight of each block.

Different types of block copolymers are utilized for the self-assembly of polymer micelles to synthesize nanoparticles that are soluble in either organic or aqueous solution. To make organic solvent soluble nanoparticles, amphiphilic block copolymers are self-assembled into micelles with a hydrophilic core and hydrophobic shell. Typical amphiphilic block copolymers include PS-*b*-P4VP[193], PS-*b*-P2VP[194], PS-*b*-PAA[195-196], PS-*b*-PMA[197], where PS served as the outer block to provide solubility in common organic solvents such as toluene, THF, $CHCl_3$. To make water-soluble nanoparticles, double hydrophilic block copolymers such as P2VP-*b*-PEO[198], PEO-*b*-PEI[199-200], PAA-*b*-PAM[201] are used.

The most critical step in this synthetic strategy of nanocrystals is the self-assembly of block copolymers. Eisenberg et al.[202] have extensively summarized the self-assembly principles of block copolymers. A large variety of morphologies can be obtained by self-assembly of linear block copolymers in solution including spherical micelles, rods, discontinuous structures, lamellae, vesicles, large compound micelles, large compound vesicles, tubules, ‘‘onions’’, ‘‘eggshells’’, baroclinic tubules, pincushions, etc. The self-assembly is governed by three free energy contributions: the degree of stretching of the core-forming blocks, the interfacial tension between the micelle core and the solvent outside the core, and the repulsive interactions among corona-forming chains. Therefore,

the morphology is strictly controlled by factors affecting these contributions including copolymer composition, copolymer concentration, water content, nature of common solvent, and the presence of additives. In practice, the assembly condition for spherical micelle is much milder than other morphologies and easier to control. It is also more likely to tolerate the inorganic synthesis conditions. Therefore, spherical micelles are mostly used among all self-assembly structures as the nanoreactors for nanocrystal synthesis, which exclusively produces spherical nanoparticles. The next step is precursor loading into the inner core of polymer micelle. The selective incorporation is typically based on electrostatic coordination between the metal precursors and the functional groups in the core blocks such as pyridine or carboxylic acid. After precursor loading, nucleation and growth of nanoparticles are initiated by different types of chemical reactions depending on the inorganic materials synthesized. For example, noble metals such as Au, Ag, Pt are synthesized by reduction, semiconducting materials such as CdS are synthesized by coprecipitation, transition metal oxides such as Fe_3O_4 can be synthesized by either precipitation or thermo-decomposition depending on the precursor used, silicon and titanium oxides are usually synthesized by sol-gel process.

Although the growth is confined within the inner spherical domain of the polymer micelles, nanoclusters rather than nanoparticles that occupy the entire interior are mostly synthesized due to fast nucleation and growth.[193, 203] In terms of noble metal nanoparticle synthesis, choice of reductant is also important because the reduction speed is closely related to the synthesized nanoparticle morphology. Both Antonietti et al.[193] and Moller et al.[204] have discovered that raspberry-like Au nanoparticles formed when strong homogeneous reductant such as $NaBH_4$ was used while cherry-like Au nanoparticles

formed with hydrazine, a weaker reductant. It indicated that single nanoparticles tend to form with slower nucleation rate. A similar phenomenon was also observed in Pd nanoparticle synthesis.[203]

Evidently, the size of the nanoparticles is supposed to be increasing linearly with core size of the micelle (i.e. the length of the inner block). However, as observed in the synthesis of CdS nanoparticles shown in **Figure 1.12**, such relationship only exists in a certain range when single crystal formation is favoured.[195] When micelle core diameter increased beyond 10 nm, no change is observed in the size of CdS nanoparticles due to the formation of multiple CdS particles in one micelle.

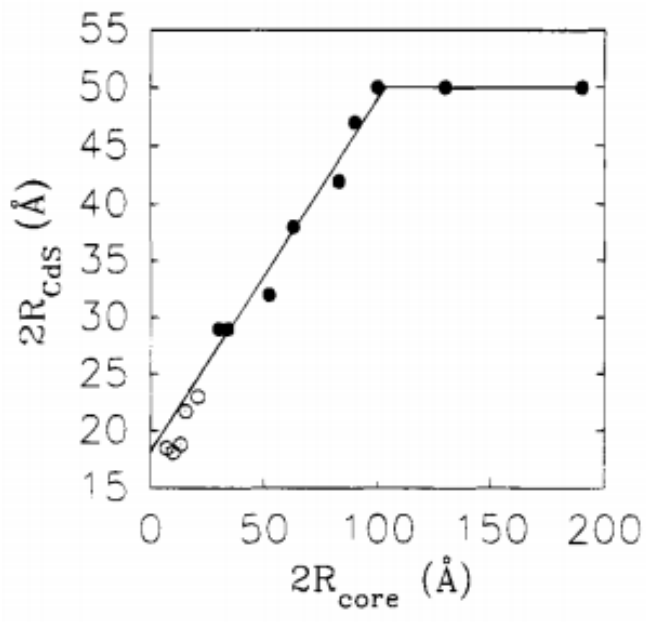

Figure 1.12. Plot of CdS cluster diameters versus the diameter of the original ionic core calculated from scaling relation. Dotted circles are cluster sizes obtained in random ionomers. Reprinted from Moffitt et al.[195] Copyright 1995 American Chemical Society.

Aside from plain nanoparticles, hollow nanoparticles can also be synthesized by polymer micelle templated method. Conventionally, hollow nanoparticles are extremely

hard to make and can only be achieved by growth inorganic crystals on a hard sacrificial template to form a core-shell structure first followed by removal of the inner template by dissolution or calcination.[205] However, the hollow structure is not stable after template removal. Soft templates such as emulsion or surfactant micelles are also used but with poorly defined structures due to deformability of soft materials.[206] In contrast, block copolymer micelles can provide a more rigid platform for hollow structure formation. Few have used diblock copolymer micelles to make hollow nanoparticles through loading precursors into the micelle core because external capping ligand is required. Instead, triblock copolymers are typically used to form a cores-shell-corona micelle where precursors are loaded into the intermediate shell block with corona block providing solubility and colloidal stability. The most commonly applied core and corona polymers are PS and PEO respectively with functional intermediate shell block such as PVP, PAA. Similar to plain nanoparticles, the size and thickness of the hollow nanoparticles can be tuned by varying the molecular weight core and shell block (**Figure 1.13**).[207]

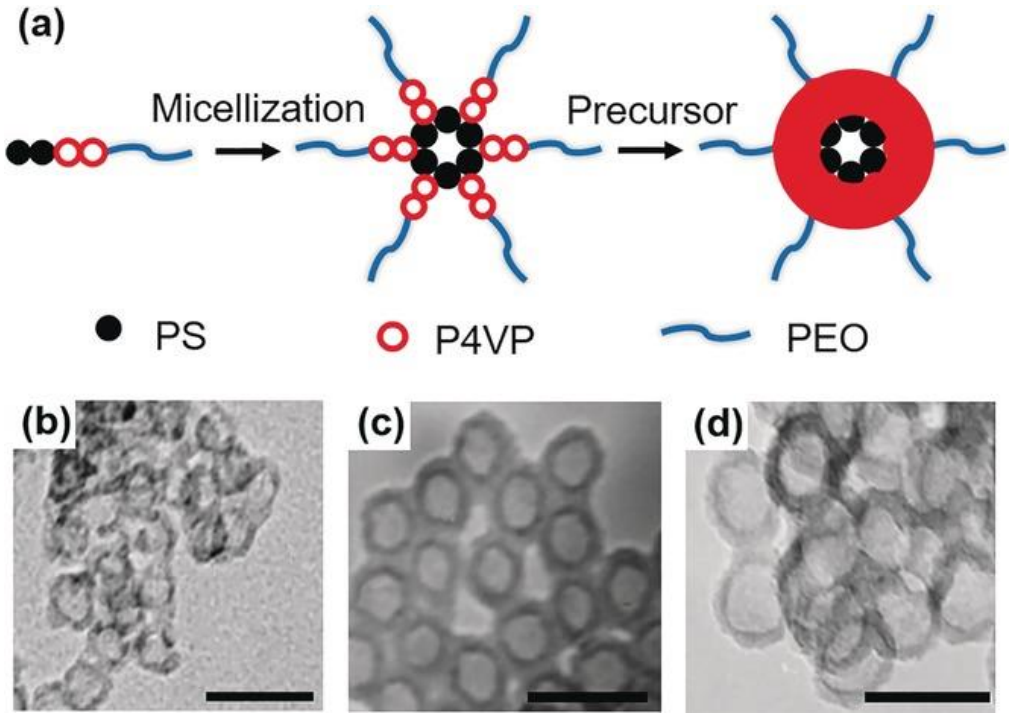

Figure 1.13. (a) Synthetic route to hollow inorganic nanoparticles with linear triblock copolymer template. TEM images of hollow silica nanospheres produced by triblock copolymers of different molecular weights: (b) PS(14.1k)-PVP(12.3k)-PEO(35k), (c) PS(20.1k)-PVP(14.2k)-PEO(26k), (d) PS(45k)-PVP(16k)-PEO(8.5k). Scale bar: 50 nm. Reprinted from Sasidharan et al.[207] Copyright 2011 Royal Society of Chemistry.

Similarly, the triblock copolymer micelles can also be utilized as template to synthesis all inorganic core-shell nanoparticles by different design of each block. Aizawa et al.[208] reported the application of PS-*b*-P2VP-*b*-PEO triblock copolymer with two functional blocks, P2VP and PEO for the synthesis of noble-metal Au@Ag core–shell nanoparticles. Anionic gold precursors were selectively coordinated with the P2VP block while the cationic silver precursors prefer the PEO block. Russell et al.[209] synthesized concentric Pt@Au spheres from PS-*b*-P2VP-*b*-PEO triblock copolymers by sequentially loading P2VP with H_2PtCl_6 and PEO with $LiAuCl_4$. Nevertheless, there is still limited reports on polymer micelle templated synthesis of core-shell nanoparticles due to the complicated

process and weaker control of growth. There isn't significant selectively in the loading of two different precursors in two active blocks leading to weakly confined growth.

1.3.2.2 Unimolecular block copolymer micelle

Although self-assembled micelles of linear block copolymers provide good size and shape control for nanoparticle synthesis, such control is only dynamically stable. The assembly can potentially be destroyed by sudden environmental change such as polymer concentration, solution pH and composition, and temperature. Therefore, unimolecular block copolymer micelles are much better templates for nanocrystal synthesis due to superior stability in all chemical environments.

Recently, a robust and general strategy has been developed to synthesis 21-arm unimolecular star-like block copolymers, which were successfully capitalized into nanoreactors for crafting monodisperse nanoparticles of different compositions.[210] As illustrated in **Figure 1.14a**, β-CD with 21 hydroxy (-OH) groups was first brominated to convert all the hydroxy groups into alkyl bromide, which is a commonly used initiating site for ATRP. Then this brominated β-CD with 21 -Br end-groups was used as the macroinitiator for sequential polymerization of tert-butyl acrylate and styrene to form star-like core-shell diblock copolymers. The inner poly(*tert*-butyl acylate) can be readily hydrolyzed into polyacrylic acid (PAA) which selectively interact with metal precursors through coordination between -COOH groups on PAA block and metal moieties. In this way, metal precursor is preferentially loaded into the inner PAA domain of the star-like block copolymer. After in-situ growth of inorganic crystals within the nanoreactor, monodispersed nanoparticles are produced with outer PS chains permanently attached to

the surface. By varying the metal precursor together with corresponding crystal formation method, nanoparticles of different compositions but same morphology can be successfully synthesized with the same star-like polymer nanoreactor as demonstrated in **Figure 1.14b**. The advantage of this nanoreactor facilitated nanocrystal synthesis compared with traditional colloidal synthesis lies in three aspects. First, due to confinement effect of the PAA block on precursors, the size of the nanoparticles strictly follows the size of PAA domain. Therefore, the size and shape of synthesized nanoparticles can be precisely controlled by tuning the molecular weight the corresponding PAA block.[211] Second, compared with conventional organic ligand used for nanoparticles synthesis such as oleic acid and oleic amine, the nanoparticles synthesized from nanoreactors have polymer chain (e.g. PS) permanently tethered on the surface providing exceptional solubility as well as long-term stability. Organic ligand, which is attached on the surface by non-covalent bonding through post-synthesis surface passivation, can easily be peeled off under high temperature, UV exposure, or in electrochemical environment. Third, the outer block of the star-like block copolymer can be substituted with functional polymers to endow nanoparticles with more advanced properties. For example, the nanoparticles will be water-solution if the outer block is changed to poly(ethylene oxide) (PEO).[212] Conductive polymers such as PEDOT were used for making semiconducting nanoparticles which facilitate electron transfer.[22, 24] Thermal responsive and pH responsive polymers have also been incorporated into the outer block of the nanoreactor so that the synthesized nanoparticles exhibit reversible stimuli-responsive properties.[213-214]

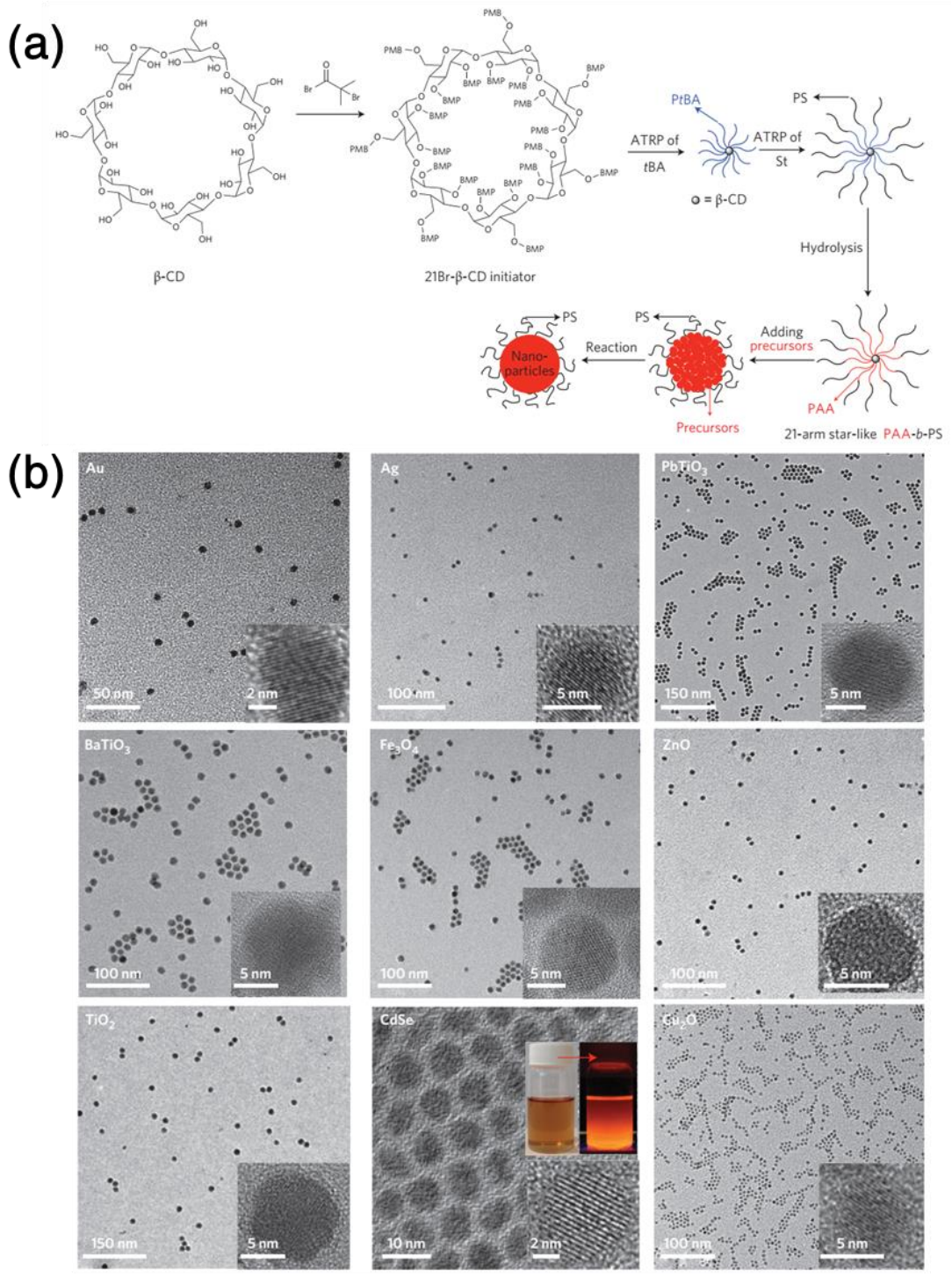

Figure 1.14. (a) Schematic representation of nanoparticle synthesis using amphiphilic star-like block co-polymers as nanoreactors. (b) TEM images of a variety of inorganic nanoparticles templated by star-like PAA-*b*-PS. Reprinted from Pang et al.[210] Copyright 2013 Macmillan Publishers Limited.

Similar to linear triblock copolymer micelle template, this β-CD based unimolecular triblock copolymer can also be capitalized on as nanoreactor for the synthesis of hollow and core-shell nanoparticle via rational polymer design. For example, hollow Au nanoparticles have been directly synthesized from star-like PS-*b*-PAA-*b*-PS triblock copolymers where Au precursors were loaded into the middle PAA block.[215] The polymer template allows precise control of the hollow cavity size and shell thickness, which strongly affect the surface plasmon resonance frequency of hollow Au nanoparticles. At the same time, core-shell nanoparticles were prepared with star-like P4VP-*b*-P*t*BA-*b*-PS or P4VP-*b*-P*t*BA-*b*-PEO triblock copolymers to be soluble in either organic or aqueous solution. Water solution high quality magnetic/plasmonic Fe_3O_4/Au core/shell nanoparticles were synthesized from P4VP-*b*-P*t*BA-*b*-PEO triblock copolymers, whose optical properties can be readily tuned by precise control of the core diameter and shell thickness.[25] It was discovered that the absorption peak of Fe_3O_4/Au core/shell nanoparticles red shifted compared with pure Au nanoparticles, and this red shift became more pronounced when the diameter of the Fe_3O_4 core increased. Whereas the absorption peak blue shifted when the thickness of the Au shell increased. The advantage of this triblock composition design is that only P4VP is active for precursor loading in the beginning where core is first synthesized, after which P*t*BA was hydrolyzed into PAA for loading shell precursor to synthesize the shell. This allow the synthesis of core-shell separately in well-confined domains preventing mutual intervention.

Generally speaking, star-like unimolecular template is much more advantageous over linear block copolymer assembly in the preparation of hollow and core-shell nanoparticles. In the meantime, because of precise control of crystal structure, the monodisperse

nanoparticles obtained from star-like block copolymer templates are the best materials for understanding structure–property relationships.

In addition to spherical morphologies, due to stable unimolecular structure, bottlebrush polymers in worm-like or rod-like morphologies can also serve as the template for nanocrystal synthesis which is otherwise different to achieve through linear block copolymer assembly. Zhang et al.[118] fabricated wire-like assemblies of cadmium sulfide nanoparticles with core-shell cylindrical polymer brushes. The original chemical structure and morphology of the bottlebrush polymer was resumed after CdS nanoparticle formation. Theoretically, such robust reaction strategy is applicable to various metal, metal oxides, metal chalcogenides materials. However, the drawback of traditional bottlebrush polymer is its flexible chains leading to mostly worm-like morphology. To overcome this limitation, Pang et al.[216] developed a new type of bottlebrush polymers based on cellulose backbone, which provide much higher grafting density to yield a rigid rod morphology. The rod-like bottlebrush polymers can be readily capitalized on as nanoreactors to synthesize inorganic nanorods as demonstrated in **Figure 1.15a**. There are three hydroxy groups in one repeating unit of cellulose which can be brominated in ionic liquid leading to high population of radical initiation sites. After sequential ATRP polymerization of *t*BA and PS, a core-shell bottlebrush block copolymer with rigid conformation was formed, which was then capitalized as nanoreactor to synthesis inorganic nanorod. This synthetic strategy is versatile in that by simply varying the precursor used, monodisperse nanorods of different compositions can be produced (**Figure 1.15b**). The longitudinal and lateral dimension of the nanorod can be precisely tuned by controlling the molecular weight of cellulose as well as the grafted P*t*BA block. Similarly, by substituting PS with PEO, water-soluble nanorods

were created. More complex structures such as core-shell nanorods and nanotubes were also synthesized by designing bottlebrush triblock copolymers.

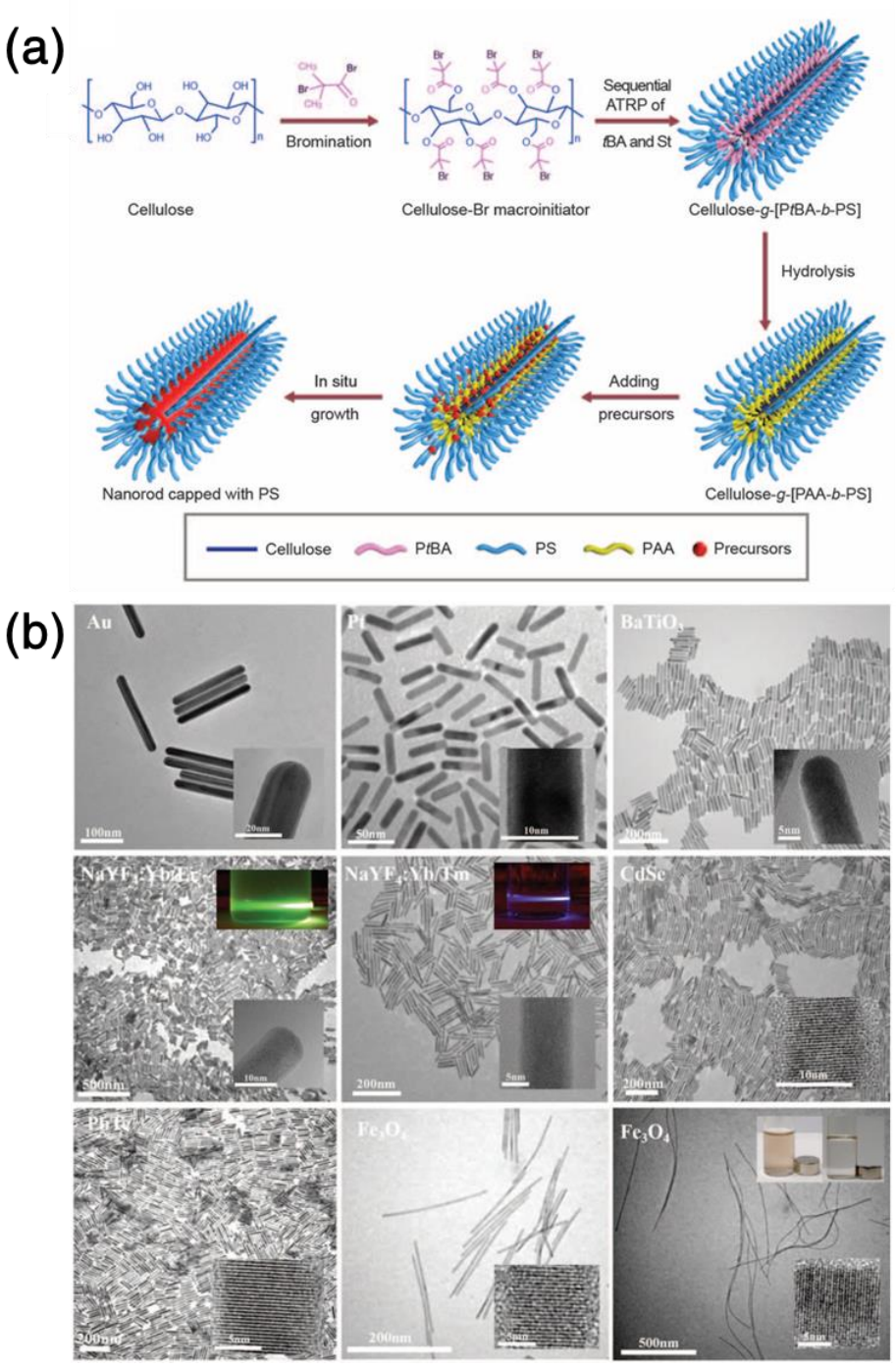

Figure 1.15. (a) Schematic representation of plain nanorods synthesis using amphiphilic bottlebrush block co-polymers as nanoreactors. (b) TEM images of a

variety of plain nanorods templated by cellulose-*g*-(PAA-*b*-PS). Reprinted from Pang et al.[216] Copyright 2016 AAAS.

In summary, unimolecular block copolymer templated method provides a promising way to produce nanoparticles with well-defined sizes and morphologies that enabled a series of investigations into their specific size- and shape-dependent properties. Their applications in catalysis, solar cells, and lithium ion batteries have also been explored exhibiting excellent performances due to well-defined nanocomposite structures. However, the property and application investigation of hollow, core-shell nanoparticles as well as all types of nanorods are still limited. The incorporation of the monodisperse nanocrystals with different functional polymers hairs is also a rising research direction. Great potential can be found in the applications of emerging functional materials such as perovskite, thermoelectric, and ferroelectric nanoparticles. Additionally, strictly biphasic Janus nanoparticles have never been realized via conventional method, however approachable by block copolymer nanoreactor strategy. The integration of two dissimilar functional materials into one nanostructure provides new opportunity for discovering cutting-edge properties and applications.

CHAPTER 2. MOTIVATION AND OBJECTVES

2.1 Motivations

Inorganic nanocrystals (NCs) display unique properties compared to the bulk counterpart due to high surface volume ratio in the nano-region as well as quantum confinement effect. The intriguing properties of NCs such as plasmonic effect in noble metal (Au, Ag, Pt) NCs, superparamagnetic effect in magnetic nanoparticles, size-dependent optoelectronic properties in semiconducting quantum dots make them attractive for applications in energy, environment, biomedical, aerospace, etc. Colloidal NC synthesis has been well-developed in recent decades. To acquire small NCs within 10s of nanometers, bottom up approach is mostly used with the assistance of external ligand to stabilize the nanoparticles. However, the dissociation of surface ligand after NCs synthesis leads to their poor colloidal stability under high temperature, UV irradiation, and electrochemical environment. Polymer/carbon template has been used to provide superior stability by permanent surface protection. Nevertheless, poor structural and size control is presented in NC synthesis in polymer matrix or 1D/2D graphene. Conversely, polymeric micelles have been shown to act as perfect template for the synthesis of inorganic NCs of precisely controlled size and shape with surface polymer protection/functionalization. In stark contrast to polymer micelles assembled from linear block copolymers which are highly sensitive to chemical environment, unimolecular micelles created from non-linear block copolymers is suitable for the synthesis of a variety of monodisperse inorganic NCs in wide synthesis conditions. By rational design of architectured block copolymers (i.e.,

non-linear), the size and structure of the inorganic NCs can be easily manipulated to suit different applications.

*The **goal** of this thesis work is to develop a general yet robust strategy for the synthesis of monodisperse polymer-ligated nanomaterials with precisely controlled size, composition, architecture and surface chemistry that renders nanomaterials with a set of intriguing properties for use in energy storage, drug delivery, etc.* Three different non-linear polymeric architectures have been investigated, including star-shaped polymer (CHAPTER III), bottlebrush-shaped polymer (CHAPTER IV), and Janus star-shaped polymer (CHAPTER V). The motivations for each of the three projects are detailed as follows:

CHAPTER 3: Star-like polymers and MFe_2O_4 nanoparticles. With a fast advancement in electronic devices, most importantly, electric vehicles nowadays, there is great demand for lithium-ion battery (LIB) with much higher capacity. One approach to increase the overall capacity is to substitute current graphene anode by materials with much higher theoretical capacity such as silicon, transition metal oxide, lithium-alloy oxide. Moreover, nanostructures are essential to reach theoretical capacity due to high surface to volume ratio which enables the complete lithium insertion. Conventional metal oxide nanoparticles used in LIB suffer from low cycling stability and unstable performance. The major cause of poor stability is phasing coarsening during the lithium insertion-desertion process. The volume expansion of nanoparticles after lithium insertion leads to the phase aggregation of adjacent particles to form much larger particles which hinders the complete reaction in anode material. Traditional small organic ligand cannot tolerate the extreme electrochemical environment within the electrolyte, thereby providing no barrier protection.

In order to prevent the phase coarsening during battery reaction by introducing additional spacer between nanoparticles, star-like block copolymers were capitalized on as nanoreactors for the synthesis of ferrite nanoparticles with PSAN permanently capped on the surface. Furthermore, due to the poor electrical conductivity of metal oxide materials which hinders electron transport within anode, graphene has been incorporated in previous works to connect the nanoparticles and boost conductivity. Intriguingly, the PSAN-capped nanoparticles can potentially be tethered strongly to graphene surface because of the strong π-π interaction between the benzene rings on PS and in graphene. Therefore, this PSAN-capped ferrite nanoparticles-graphene nanocomposite is expected to exhibit exceptionally high capacity and cycling stability in LIB.

CHAPTER 4: Bottlebrush cocoons and perovskite nanorods. Recently, there is enormous research to apply cylindrical bottlebrush polymers as nanocarriers for drug encapsulation and delivery because the cylindrical structure is advantageous for molecular retention and uptake as well as targeting of specific cells or tissues. However, most of the nanocarrier function is achieved by covalently attaching the effective drug moieties onto the polymer chains and triggering the breakage through external stimuli, which limits the drug loading level. Polymeric cocoons derived from crosslinked bottlebrush polymers is of great advantage to serve as unimolecular drug carriers. Up to now, there are several polymeric cocoons that have been prepared through post-polymerization crosslinking of the outer block of bottlebrush polymers with additional crosslinker. However, none of them have demonstrated the encapsulation properties of the cocoons and the external crosslinkers are usually bio-toxic which are not feasible as drug delivery material. The cellulose-based bottlebrush polymer with photo-crosslinkable shell is therefore developed

here to resolve these issues, thus creating a perfect candidate as nanocarrier for drug delivery. Additionally, these polymeric cocoons can also be employed as nanoreactors for inorganic nanorods synthesis. $CsPbBr_3$ nanorods has been recently discovered to possess excellent properties in optoelectronic applications. However, the few reported synthesis strategies for monodisperse $CsPbBr_3$ nanorods all involve the usage of aliphatic ligands as the capping agents that are non-covalently bonded to the surface, which renders the nanorods with poor water, UV, thermal stabilities. The cocoon nanoreactor strategy can significantly improve the stability of $CsPbBr_3$ nanorods by permanent surface capping of crosslinked polymers.

CHAPTER 5: Janus star-shaped polymers and Janus Au/TiO_2 nanoparticles. Janus type NCs have been a rising field in the field of nanoscience and nanotechnology. The anisotropic structure of Janus NCs grants them with unique properties that couldn't be replicated otherwise. Therefore, a great potential for applications in advanced materials and technology can be foreseen for Janus NCs.

There has been a rapid and extensive development of synthetic strategies for Janus nanoparticles in this century, especially inorganic heterodimers. The most commonly used methods are masking and phase-separation techniques. Masking selectively protects half of the pre-synthesized spherical particles and decorates the other half either by surface deposition or direct heterogeneous nucleation, while phase-separation prepared Janus nanoparticles by epitaxial or nonepitaxial growth of another material on an existing nanoparticle driven by Gibbs free energy. Both have their limitations. Masking usually cannot use particle size within 100 nm while phase-separation mostly ends up with dumbbell shaped heterodimer with poor structural confinement.

So far, few efforts have been made to prepare spherical Janus nanoparticles within tenth of nm size and the only viable technique, in which half of the inorganic nanoparticle is coated with a layer of noble metal or metal oxide through sputtering, chemical vapor deposition (CVD) or atomic layer deposition (ALD), can only form a shell on a particle rather than a hemisphere. Therefore, a general method for crafting monodisperse Janus inorganic nanoparticles strictly consisting of two hemispheres with well-confined size and composition is proposed here by using unimolecular polymer micelle as nanoreactor for in-situ nanocrystal growth. In terms of photocatalysis of Au/TiO_2 Janus nanoparticles, the performance is influenced by interfacial interaction between Au and TiO_2 domain. The planar interface crafted from the Janus nanoreactor which has never been studied before will help us better understand such influence and direct the future design of Janus morphology for photocatalysis.

2.2 Objectives

CHAPTER 3:

(1) Rationally design and synthesize star-shaped block copolymers with PSAN as the outer block via ATRP

(2) Capitalize on star-shaped block copolymers as nanoreactors to craft monodisperse polymer-ligated MFe_2O_4 nanoparticles (M= Ni, Co, Fe, Mn, etc.) and in-situ incorporate them with graphene to yield NPs/graphene nanocomposites

(3) Employ NPs/graphene nanocomposite as anode materials for lithium/sodium ion batteries and scrutinize the resulting battery performance, including capacity, rate performance, and cycling stability

(4) Investigate the battery reaction mechanism by comparing the nanoscale morphology and phase-change with and without surface polymer protection or bimetallic compositions

CHAPTER 4:

(1) Rationally design and synthesize cellulose-based bottlebrush-shaped polymeric cocoons with heavily crosslinked outer shell

(2) Investigate encapsulation and controlled delivery properties of the polymeric cocoons

(3) Capitalize on bottlebrush block copolymers and cocoons as nanoreactors to craft $CsPbBr_3$ nanorods with different types of surface polymer capping

(4) Explore the influence of surface capped polymer on the water, UV, thermal stabilities of $CsPbBr_3$ nanorods

CHAPTER 5:

(1) Rationally design and synthesize star-shaped Janus block copolymers composed of amphiphilic arms grafted from dual-functional core

(2) Capitalize on star-shaped Janus block copolymers as nanoreactors to craft Au hemispheres

2.3 Content overview

CHAPTER 1 is the background introduction for architectured polymers and nanocrystal synthesis. The recent progress in the design and synthesis of star-shaped and bottlebrush-shaped polymers were present including the use of well-develop controlling

living polymerization technique in the synthesis of polymer with complex structure. The limitation of current synthetic strategy of Janus nanoparticles were also discussed. More importantly, the advancements in polymer-templated nanocrystal synthesis were explored, specifically the advantages and drawbacks of polymer micelle system in the synthesis of nanoparticles.

CHAPTER 2 describes the motivations and objectives of the three projects involved in the dissertation listed in 3 chapters. Generally, the motivation for this work is to overcome the limitation and disadvantages of conventional nanomaterial synthesis by developing a general strategy for synthesis of monodisperse organic/inorganic nanomaterials with precisely defined structure and functionalized surface capping polymer that will exhibit superior performance than traditional materials in specific applications. To this end, the 3 projects aim to rationally designed and synthesis three different types of unimolecular block copolymers to be capitalized on as nanoreactors for the production of monodispersed nanoparticles, nanorods, Janus nanoparticles with functional polymer capping.

CHAPTER 3 details the synthesis of β-CD-based star-like block copolymer (PAA-*b*-PSAN) with precisely controlled size by sequential ATRP. The star-like polymers were capitalized as nanoreactors to synthesize a variety of MFe_2O_4 nanoparticles with different composition. By in-situ incorporation with graphene oxide, MFe_2O_4 nanoparticles were self-assembled into monolayer on the graphene sheets, which was then used as the anode materials to assemble lithium/sodium ion batteries. The polymer capping as well as metallic composition is discovered to greatly enhance the cycling performance of LIB. The

detailed reaction mechanism for such improvement was extensively characterized by a combination of techniques such as HRTEM, STEM, Raman, XPS.

CHAPTER 4 details the synthesis of a type of cellulose-based bottlebrush block copolymer (cellulose-*g*-(PAA-*b*-P(HEMA-N_3))) with crosslinkable shell. The bottlebrush polymer was synthesized by sequential ATRP of *t*BA and HEMA, followed by two-step functionalization of the -OH groups on PHEMA into -N_3, which is subjected to photo-crosslink under UV irradiation. Drug delivery properties of the bottlebrush polymers were demonstrated by loading with fluorescent dye and readily crosslinking the surface by UV for encapsulation to form cocoons. The total encapsulation level and the release profile were tracked by PL measurement to verify the improved drug delivery performance induced by surface crosslinking. Additionally, such bottlebrush polymers and cocoons were also used as nanoreactors to synthesize $CsPbBr_3$ nanorods which is hard to make by conventional strategies. Water, UV, thermal stabilities of $CsPbBr_3$ nanorods capped with different polymers (crosslinked and uncrosslinked PHEMA, PS) were tested to investigate how $CsPbBr_3$ stability is influenced by the properties of surface capped polymers such as crosslink and hydrophobicity.

CHAPTER 5 details the synthesize of Janus star-shaped tetrablock copolymer with bifunctional β-CD as the initiator. The primary and secondary hydroxy groups in β-CD were functionalized sequentially by selective esterification with RAFT agent and brominating agent, creating a macroinitiator capable of carrying out 2 different types of polymerization on each side the bowl-shaped initiator. Sequential 4-step polymerization include 2 RAFT following by 2 ATRP was implemented and characterized by NMR and GPC. Janus star-shaped block polymers can be capitalized as nanoreactors to synthesis

strict biphasic Janus nanoparticles comprising two distinct hemispheres, which has never been reported before.

CHAPTER 6 summarizes the general conclusions and broader impacts of this work. this dissertation aims to establish a universal methodology for the design and synthesis of block copolymers with complex architectures and use it as nanoreactors to produce NCs of interest with precisely confined size and shape. Branching out from the star-shaped, bottlebrush-shaped, and Janus star-shaped morphologies that were investigated here, much more sophisticated structures (both polymeric and inorganic) could be developed via combinations of modern polymer synthesis technique such as living polymerization, click chemistry, host-guest interaction, and polymer functionalization, even ionic or hydrogen bonding. In the meantime, nanoreactor strategy for nanocrystal synthesis has enabled the possibility of precision synthesis of artificially designed nanostructures with no limitation.

CHAPTER 3. TAILORING HOMOPHASE COARSENING BY SURFACE AND COMPOSITION ENGINEERING OF METAL OXIDE NANOPARTICLES IN LITHIUM/SODIUM ION BATTERIES

This work will be published as: S. Zhao†, Z. Wang†, H. Zhang, Y. Harn, and Z. Lin*, Homophase Metal Coarsening: An Essential Reason for the Capacity Decay of Conversion Type Metal Oxide Anodes for Lithium/Sodium Ion Batteries. (In preparation)

3.1 Introduction

Continuously increasing contribution of renewable energy sources (e.g., wind, wave, solar, etc.) and rapidly evolving demand for electric vehicles has witnessed rapid development of high-efficiency energy storage devices.[217,218,219,220] Currently, lithium-ion batteries (LIBs) are the most widely used energy storage devices especially in cellphones and laptops, yet the low theoretical capacity of commercial anode material (i.e., graphite; 372 mAh g^{-1}) cannot satisfy the needs for high energy demand equipment (e.g., electric vehicles and smart power grids).[221,222,223] In recent years, in view of the lower price and higher reserves of sodium (Na) than lithium (Li), much attention has been focused on developing sodium ion batteries (SIBs) as a substitution of LIBs for cost-effective and large-scale electrical energy storage applications.[224,225,226] Learning from the cathode materials of LIBs, various sodium-containing transition-metal oxides and polyanions have been explored as promising cathodes of SIBs. Nevertheless the anodic graphite for LIBs also has poor sodium storage capability.[227,228,229,230] In addition, the limited Li^+/Na^+ content in the cathode materials of LIBs/SIBs is detrimental in improving their specific capacities

over large scale. Therefore, developing high-capacity anode materials has been identified as an imperative approach to prominently increase the energy densities of LIBs and SIBs.[231,232,233,234,235]

A rich variety of transition metal oxides (MO_x, M = Mn, Fe, Co, Ni, etc.) have been explored as promising anode materials for LIBs/SIBs, which enables the Li^+/Na^+ storage via the conversion reaction of $MO_x + 2xA^+ + 2xe^- \leftrightarrow xA_2O + M$ (A = Li^+ or Na^+) with high theoretical capacities in the range of ~700-1000 mAh g^{-1}.[236, 237,238] As widely recognized in literature, the low conductivity and poor structural stability are the major causes of low capacity and poor cycling stability of MO_x-based electrodes. The intrinsic low electronic conductivities of MO_x results in low electrochemical reaction kinetics, leading to low Li^+/Na^+ storage capacities especially at high current rates. The volume expansion/contraction of conventionally structured MO_x particles induced by Li^+/Na^+ insertion/extraction will lead to their pulverization and subsequent falling off from the substrate ending up with poor cycling stabilities. Based on these understandings, the following strategies are normally adopted to improve the performances of MO_x anodes: (1) synthesizing nanostructured MO_x particles with short Li^+/Na^+ and e^- transfer distances to improve the electrochemical reactivities for high capacities[237,238]; (2) constructing porous or hollow structured MO_x particles with abundant void spaces for accommodating the volume changes to stabilize the particle structures for high cycling stabilities[239,240]; (3) compositing MO_x particles with conductive polymers or carbonaceous materials (e.g., graphene (Gr), carbon nanotube, and amorphous carbon, etc.) for concurrently promoting the electron transfer and buffering the volume changes to enhance the conductivities and structural stabilities for high capacities and cycling stabilities[241,242,243,244]. However, even

though the above strategies can effectively improve the Li^+/Na^+ storage performances of MO_x, the underlying mechanism for the capacity decay of conversion-type MO_x anodes along with long-term cycling remain elusive in all cases.

Among all the above performance enhancement strategies, fabricating MO_x nanoparticles-graphene nanocomposites has been demonstrated as the most efficient and versatile method for both LIBs and SIBs due to short Li^+/Na^+ transfer distances of MO_x nanoparticles, high electronic conductivity of graphene and high structural stability of the MO_x nanoparticles-graphene nanocomposites[242,243]. In previous studies, graphene was usually *in-situ* presented in the formation system of MO_x nanoparticles, which served as both the matrix to load MO_x nanoparticles and a separator to prevent aggregation of MO_x nanoparticles. However, this method is not universally applicable to various MO_x. It also has poor control over particle size, dispersion uniformity, and loading density of MOx nanoparticles, all of which are key aspects affecting the battery performance.

In recent years, block copolymer nanoreactor strategy has been exploited as an exceptional technology for precisely controllable synthesis of various nanoparticles with designed sizes and morphologies (e.g., sphere, hollow, core-shell, and rod).[216,210,25,245] The basic concept of this strategy is that the functional groups (e.g., carboxyl) in the inner polymer block can be selectively incorporated with metal precursors, providing well-confined domain for the nucleation and growth of nanocrystals, while the outer polymer blocks act as the capping ligand to limit the size and prevent the aggregation of nanoparticles. Herein, star-like poly(acrylic acid)-*block*-poly(styrene-co-acrylonitrile) (PAA-*b*-PSAN) copolymers were rationally designed and synthesized, which were then employed as robust polymeric nanoreactors to craft a series of monodispersed metal oxides

nanoparticles (MOx/PAA@PSAN) including bimetallic ferrites MFe_2O_4 (M = Mn, Co, Ni, Cu, and Zn) and monometallic oxides MO_x (e.g., CoO, Fe_2O_3, Fe_3O_4, and Mn_3O_4) nanoparticles with a designed diameter of ~8 nm. The PSAN capped MOs/PAA@PSAN nanoparticles could be individually dispersed in N, N-dimethylformamide (DMF) solution containing graphene oxide (GO) nanosheets. The π-π stacking interaction between benzene rings on PSAN hairs and GO nanosheets guided the uniform and compact absorption of MOs/PAA@PSAN nanoparticles on GO. After heat treatment, the removal of oxygen-containing functional groups on GO induces the reduction of GO into rGO along with the layer-by-layer self-assembly of MOx/PAA@PSAN nanoparticles-loaded rGO for the generation of micronized MOx/PAA@PSAN-rGO nanocomposites with a graphite-like macrostructure. All the MFe_2O_4/PAA@PSAN-rGO nanocomposites exhibit remarkable cycling stabilities at different current rates as both anodes of LIBs and SIBs, while MO_x/PAA@PSAN-rGO delivered unsatisfactory cycling stabilities with first declined then raised Li^+ storage capacities but continuously decayed Na^+ storage capacities. Fundamental mechanism study revealed that such phenomenon can be attributed to the random distribution of two different metal oxide domains after phase-separation of MFe_2O_4 during battery discharge process, thereby providing abundant heterophase interfaces, which prevented the large-scale homophase coarsening of M or Fe nanoparticles inside the nanospheres and among different nanoparticles, ultimately leading to excellent reaction reversibility.

3.2 Experimental Section

3.2.1 Materials

Anhydrous N,N-dimethylformamide (DMF, 99.9%), benzyl alcohol (BA, 99%), 2-bromoisobutyryl bromide (BIBB, 98%), N,N,N′,N″,N″-pentamethyldiethylenetriamine (PMDETA, 99%), methyl ethyl ketone (MEK, 99.9%), anhydrous 1-methyl-2-pyrrolidinone (NMP, 99.5%), trifluoroacetic acid (TFA, 99.9%), iron(III) 2,4-pentanedionate ($Fe(acac)_3$), copper(II) acetate ($Cu(ac)_2$, 98%), cobalt(II) acetate tetrahydrate ($Co(ac)_2 \cdot 4H_2O$, 98%), manganese(II) acetate tetrahydrate ($Mn(ac)_2 \cdot 4H_2O$, Mn ~ 22%), nickel acetate tetrahydrate ($Ni(ac)_2 \cdot 4H_2O$, ≥98%), zinc acetate dihydrate ($Zn(ac)_2 \cdot 2H_2O$, ≥97%). graphite flake (~325 mesh, 99.8%), sodium nitrate ($NaNO_3$, 99%), potassium permanganate ($KMnO_4$, 99%), concentrated sulfur acid (H_2SO_4, 95-98%), hydrogen peroxide (H_2O_2, 30%), acetylene black (99.9%), sodium alginate ($(C_6H_7O_6Na)_n$, 99%). All above chemicals were used as received. β-Cyclodextrin (β-CD, Sigma-Aldrich) was dried in a vacuum oven at 80 °C overnight prior to use. CuBr (98%, Sigma-Aldrich) was stirred in acetic acid for 24 h, washed with ethanol and diethyl ether, and dried in a vacuum oven at room temperature. Acrylonitrile (AN, Alfa Aesar, ≥99%), Styrene (St, Alfa Aesar, ≥99%), and *tert*-butyl acrylate (*t*BA, Alfa Aesar, 98%) were distilled over CaH_2 under reduced pressure prior to use.

3.2.2 Characterizations

3.2.2.1 Structural Characterization

Gel permeation chromatography (GPC) equipped with an LC20AD HPLC pump and a refractive index detector (RID-10A, 120 V) was used measure the number-average molecular weight (Mn) and dispersity (PDI) of star-like polymers. Calibration was built from monodisperse polystyrenes as standards. THF was used as the eluent with a flow rate

of 1.0 mL/min and operation temperature of 35 °C. Proton nuclear magnetic resonance (1H NMR) spectra of organic samples were recorded on Varian VXR-300 spectroscope. The morphology of all samples was measured by transmission electron microscope (TEM, JEOL 100 CX-II; operated at 100 kV), high-resolution transmission electron microscope (HRTEM, FEI Tecnai F30; operated at 300 kV), and scanning transmission electron microscope (STEM, Hitachi HD-2700; operated at 200 kV). TEM, HRTEM, STEM samples were prepared by dropping product solution in ethanol or DMF onto a carbon-coated copper TEM grid (300 mesh) and dried at room temperature. The TEM grids deposited with $CoFe_2O_4$ nanoparticles were also stained with uranium tetroxide vapor for 30 min prior to the TEM imaging. Phosphotungstic acid were used for staining of PAA blocks of the nanoreactors. Scanning electron microscopy (SEM) measurements were performed using a field emission source operated at an accelerating voltage of 15 kV by JEOL JSM-6700F. The elemental mapping was recorded using energy dispersive X-ray spectrometry (EDS) with the abovementioned STEM and SEM. Atomic force microscope (AFM) imaging was conducting using Bruker Dimension Icon operated in the tapping mode at the scanning rate of 0.5 Hz. The SEM and AFM samples were prepared by dispersing products of interest in ethanol via ultrasonication, followed by the deposition and dry on a silicon substrate. Powder X-ray diffraction (XRD, Rigaku D/max-2400) measurements were conducted using Cu-Kα radiation (40 kV, 120 mA) with a 2θ range of 10-80°. Raman spectroscopy characterizations were performed on a Renishaw InVia Raman spectrometer equipped with a 532 nm laser. Fourier transform infrared (FTIR) spectra were collected by JASCO FTIR 6300. X-ray photoelectron spectroscopy (XPS) measurements were carried out on a Thermo K-alpha electron spectrometer with Al Kα

radiation. Thermogravimetric analysis (TGA) was done using a Perkin Elmer DAIMOND TG/DTA instrument in air atmosphere at a heating rate of 10 ºC/min from room temperature to 600 ºC. Brunauer-Emmet-Teller (BET) isotherms and specific surface area were obtained using a Micromeritics ASAP 2020 sorptometer.

3.2.2.2 Electrochemical Measurements

To make working electrodes, after dispersing the synthesized active material (AM), acetylene black (AB) and sodium alginate (SA) at a weight ratio of 7:2:1 in ultrapure water, the resulting homogeneous slurry was pasted onto a copper foil (CF) and dried at 80°C for 12 h. The foil was then cut into discs (10 mm in diameter). The average loading density of active materials in working electrodes is 1.5 ± 0.2 mg cm^{-2}. The self-supported working electrodes were prepared by dropwise adding the ethanol-dispersed samples on battery cases and drying at 80°C for 12 h. For assembling lithium coin cells, lithium foil, polypropylene (Celgard 2500, Celgard Inc., USA) and 1 mol L^{-1} $LiPF_6$ in ethylene carbonate (EC)/dimethyl carbonate (DMC) (volume ratio, 1:1) with 5 wt.% fluoroethylene carbonate (FEC) were used as counter electrode, separator and electrolyte, respectively. For assembling sodium coin cells, the sodium foil, glass fiber and 1 mol L^{-1} $NaClO_4$ in ethylene carbonate (EC)/dimethyl carbonate (DMC) (volume ratio, 1:1) with 5 wt.% fluoroethylene carbonate (FEC) were used as counter electrode, separator and electrolyte, respectively. The CR2032-type coin cells were assembled in an argon-filled glove box (MBraun).

Galvanostatic cycling tests were conducted using an Arbin battery testing system (BT2043) over the voltage range of 0.01-3.0 V (vs. Li^+/Li or Na^+/Na). Prior to each

galvanostatic cycling test at the high current rates of 1000 and 2000 mA g^{-1} for LIBs and 500 mA g^{-1} for SIBs, the cells were first activated at 100 mA g^{-1} (for LIBs) and 50 mA g^{-1} (for SIBs) for three cycles, respectively. Cyclic voltammetry (CV) curves were collected on an IM6ex electrochemical workstation at a scan rate of 0.2 mV s^{-1} in the voltage window of 0.01-3.0 V (vs. Li^+/Li). The electrochemical impedance spectroscopy (EIS) measurements were also performed using the IM6ex electrochemical workstation over a frequency range of 10^{-2}-10^5 Hz by applying a perturbation of 0.005 V. After the cycling performance test, the cycled cells were disassembled, rinsed by dimethyl carbonate (DMC), dried in the argon-filled glove box, and sealed in glass vials for subsequent HRTEM, TEM, STEM, SEM, XPS and Raman characterizations.

3.2.3 Synthesis procedures

Synthesis of 21-arm Star-like Poly(*tert*-Butyl Acrylate) (P*t*BA) by ATRP. Heptakis[2,3,6-tri-O-(2-bromo-2-methylpropionyl]-β-cyclodextrin) (denoted 21Br-β-CD) was synthesized according to previous published work in the group.[18] 21Br-β-CD was used as the macroinitiator for ATRP of *tert*-butyl acrylate (*t*BA) to synthesize 21-arm star-like P*t*BA-Br. In a typical procedure, CuBr (35.0 mg), PMDETA (85.0 mg), 21Br-β-CD (50 mg), *t*BA (21 mL), and MEK (21 mL) were mixed in a pressure vessel, degassed by three freeze-pump-thaw cycles, and charged with argon. The vessel was sealed and immerged into oil bath at 60 ºC for a desired period. Then the reaction was quenched by dipping the vessel into liquid N_2, diluted with THF, and passed through a column of neutral alumina to remove the catalyst. After removing the solvent, the product was precipitated with methanol/water (v/v = 1/1) as the precipitator to yield a white semitransparent solid.

Synthesis of 21-arm Star-like Poly(*tert*-Butyl Acrylate)-block-Poly(styrene-co-acrylonitrile) (P*t*BA-*b*-PSAN) by ATRP. Star-like P*t*BA-Br was used as the macroinitiator for second ATRP of styrene and acrylonitrile mixture. In a typical procedure, A reaction mixture at star-like P*t*BA-Br: CuBr: PMDETA: styrene: acrylonitrile = 1: 1: 2: 800: 200 was placed in a pressure vessel, degassed by three freeze-pump-thaw cycles and charged with argon. The vessel was sealed and immerged into oil bath at 90 ºC for a desired period. Then the reaction was quenched by dipping the vessel into liquid N_2, diluted with THF, and passed through a column of neutral alumina to remove the catalyst. After removing the solvent, the product was precipitated with methanol as the precipitator to yield a white solid.

Synthesis of 21-arm Star-like Poly(Acrylic Acid)-block- Poly(styrene-co-acrylonitrile) (PAA-*b*-PSAN) by Hydrolysis. P*t*BA block in the star-like P*t*BA-*b*-PSAN was hydrolyzed into PAA block to yield amphiphilic star-like PAA-*b*-PSAN diblock copolymers. Typically, star-like P*t*BA-*b*-PSAN (0.4 g) was dissolved in $CHCl_3$ (40 mL), followed by the addition of TFA (3 mL). After stirring at room temperature for 24 h, the reaction mixture was dried, re-dissolved in DMF, and gradually precipitated in MeOH. The final product was washed with Hexanes and dried under vacuum to yield a white solid.

Synthesis of PSAN-capped MO Nanoparticles (MO/PAA@PSAN). MFe_2O_4 (M=Mn/Co/Ni/Cu/Zn) nanoparticles were synthesized by capitalizing on star-like PAA-*b*-PSAN diblock copolymers as nanoreactors. The strong coordination between the carboxyl groups and metal leads to selective absorption of metal precursors (e.g. $Co(ac)_2$, $Fe(acac)_3$) onto the PAA core. Meanwhile, the poor solubility of precursor in DPE due to its low polarity also pushed the precursors to the more polar PAA domain, which led to the

formation of PSAN capped MFe_2O_4 nanoparticles after thermolysis. In a typical procedure (taken $CoFe_2O_4$ as an example), star-like PAA-*b*-PSAN (10 mg) was dissolved in mixed solvents of DPE (9 mL) and BA (1 mL) under 50ºC, followed by the addition of $Co(ac)_2$ (76 mg) and $Fe(acac)_3$ (216 mg) and stirred overnight under Ar. BA was used to swell the PAA core which collapsed due to poor solubility in DPE. With the addition of BA, a more stable micelle was formed with outer PSAN dissolved in DPE and inner PAA stretched in BA. As mentioned above, the metal precursors also tended to stay in the core swelled with polar BA, leading to the nucleation and growth of more spherical nanoparticles. The reaction was heated to refluxing temperature (about 258 ºC) for 2 h, and gradually cooled down to RT, yielding a dark black solution. The nanoparticles were precipitated and washed with EtOH 4 times and dried under vacuum overnight. In case of synthesis of single component metal oxide nanoparticles (MO_x, e.g. CoO), single precursor was used under same reaction conditions.

Synthesis of Graphene oxide (GO). Graphene oxide (GO) was prepared from graphite flake using a modified Hummers method.[246] Graphite flake (5 g) and sodium nitrate (2.5 g) were added into a 1 L beaker containing 130 mL concentrated sulfur acid in an ice bath. The suspension was stirred by mechanical agitation for 2 h. Potassium permanganate (15 g) was added and stirred for another 2 h. Then, the beaker was transferred to a water bath and stirred at 35 ºC for 1 h. Ultrapure water (230 mL) was dropwise added into the beaker to keep the temperature of the solution below 40 ºC. After that, the beaker was immersed in 98ºC oil bath for 30 min under stirring, followed by adding 400 mL ultrapure water and 10 mL hydrogen peroxide at room temperature. Finally, the GO solution was centrifuged with ultrapure water until a neutral pH is achieved.

Synthesis of Nanoparticles/Graphene Nanocomposite (MO/PAA@PSAN-rGO). Metal oxide nanoparticles (MO NPs) was embedded in graphene to enhance the conductivity as anode material since the PSAN-surface is insulating. Typically, GO (10 wt% of MO NPs) was dispersed in DMF and added dropwise to the previous made crude MO NPs solution under RT and gradually heated to 120 ºC. The reaction was stirred under 120 ºC for 2 h, then purified by precipitation with ethanol. The nanoparticle-graphene composite was abstracted with magnet (or centrifugation) and washed with ethanol 2 more times. The residue was dried under vacuum overnight.

Control experiments:

Synthesis of $CoFe_2O_4$ Nanoparticles without Template. Same as the synthesis of PSAN-capped $CoFe_2O_4$ Nanoparticles but with no template added in the reaction (only solvent and precursor).

Synthesis of $CoFe_2O_4$ Nanoparticles with star-like PAA ($CoFe_2O_4$/PAA). Same as the synthesis of PSAN-capped $CoFe_2O_4$ Nanoparticles but with star-like PAA template (not PAA-PSAN) used in the reaction.

Synthesis of $CoFe_2O_4$@C ANPs. $CoFe_2O_4$/PAA@PSAN nanoparticles were calcinated in Air at 500 ºC for 2 h and then mixed with graphene in ethanol.

All the above control samples were made into particle/graphene nanocomposite by in-situ mixing with GO in DMF followed by heating at 120 ºC for 2h.

3.3 Results and Discussion

3.3.1 Anode material synthesis

A series of monodispersed MFe_2O_4 (M = Mn, Co, Ni, Cu, or Zn) nanoparticles with a defined diameter of ~8 nm was crafted with star-like poly(acrylic acid)-block-poly(styrene-co-acrylonitrile) copolymer (denoted star-like PAA-*b*-PSAN) as nanoreactors followed by homogeneously anchored on reduced graphene oxide (rGO) nanosheets (denoted MFe_2O_4/PAA@PSAN-rGO), as depicted by **Figure 3.1**.

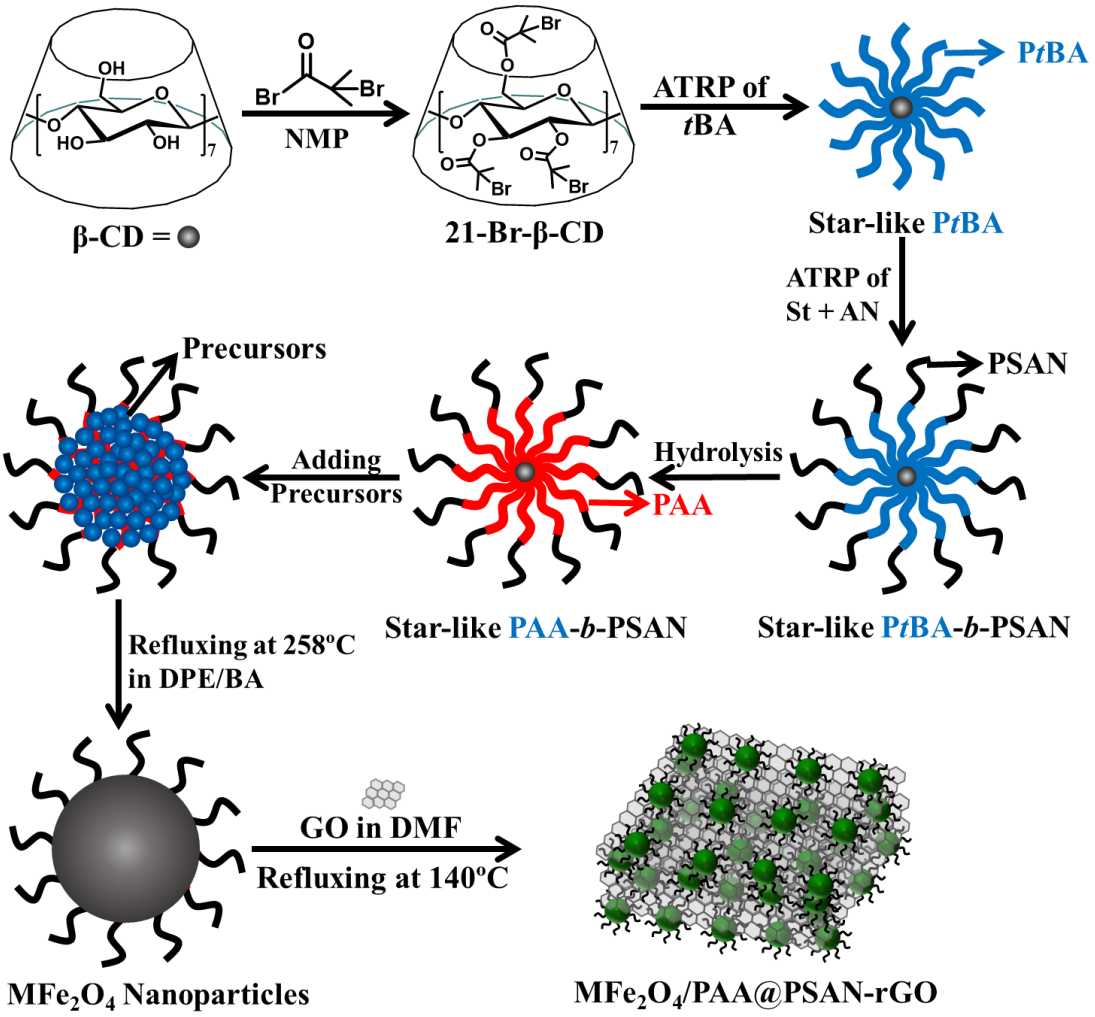

Figure 3.1. Synthetic scheme of MFe_2O_4/PAA@PSAN-rGO (M = Mn, Co, Ni, Cu, or Zn) nanocomposites.

Specifically, starting from the bromination of *β*-cyclodextrin (*β*-CD) into 21-Br-*β*-CD, a 21-arm macroinitiator, unimolecular star-like poly(*tert*-butyl acrylate)-block-poly(styrene-co acrylonitrile) (P*t*BA-*b*-PSAN) diblock copolymers were synthesized through sequential atom transfer radical polymerization (ATRP) of *tert*-butyl acrylate and a mixture of styrene and acrylonitrile. The successful synthesis of star-like P*t*BA and star-like P*t*BA-*b*-PSAN were confirmed by proton NMR (^{1}H NMR) spectra (**Figure 3.2a,b**). The diblock copolymers have well-defined molecular weight as well as low PDI evidenced by GPC (**Figure 3.2c**) after first and second step polymerization. The inner P*t*BA block of the diblock copolymer was subsequently hydrolyzed into hydrophilic poly(acrylic acid) (PAA) generating star-like PAA-*b*-PSAN, which was further capitalized as nanoreactors for nanoparticles synthesis. The chemical composition of the hydrolyzed product was also verified by FTIR characterization (**Figure 3.2d**) (-CN from PSAN: 2237 nm, -COOH from PAA: 1718 nm, -Ph from PSAN: 1493 nm; 1454 nm; 765 nm; 697 nm). An advantage of the nanoreactor strategy is that the core and shell diameter can be tuned by controlling the polymerization time of each block to generate nanoparticles of different sizes. Three star-like P*t*BA-*b*-PSAN block copolymers were synthesized with different molecular weight of PAA and PSAN as shown in **Table 3.1** (corresponding GPC results in **Figure 3.2c**).

Table 3.1. Number average molecular weight of PAA and PS block of three different star-like P*t*BA-*b*-PSAN copolymers and their corresponding estimated core size / synthesized particle size.

Nanoreactor	$M_{n,\,PAA}$[a]	$M_{n,\,PSAN}$[b]	Inner PAA size[c]	NPs size (ave.)
Sample A	6.5K	8K	6 nm	5 nm
Sample B	9K	10.5K	8 nm	8 nm
Sample C	17K	14K	15 nm	11 nm

a. Molecular weight of PAA was calculated from the molecular weight of PtBA acquired from GPC results. The single arm Mn was derived from the standard curve (Figure S4) built with 21-arm star-like PS and single arm PS after cleavage. All GPC results were calibrated with linear PS standards.
b. Molecular weight of PSAN was calculated from the 1H NMR spectra of star-like PtBA-b-PSAN with known Mn of PtBA.
c. The core PAA diameter is estimated from full stretched chains.

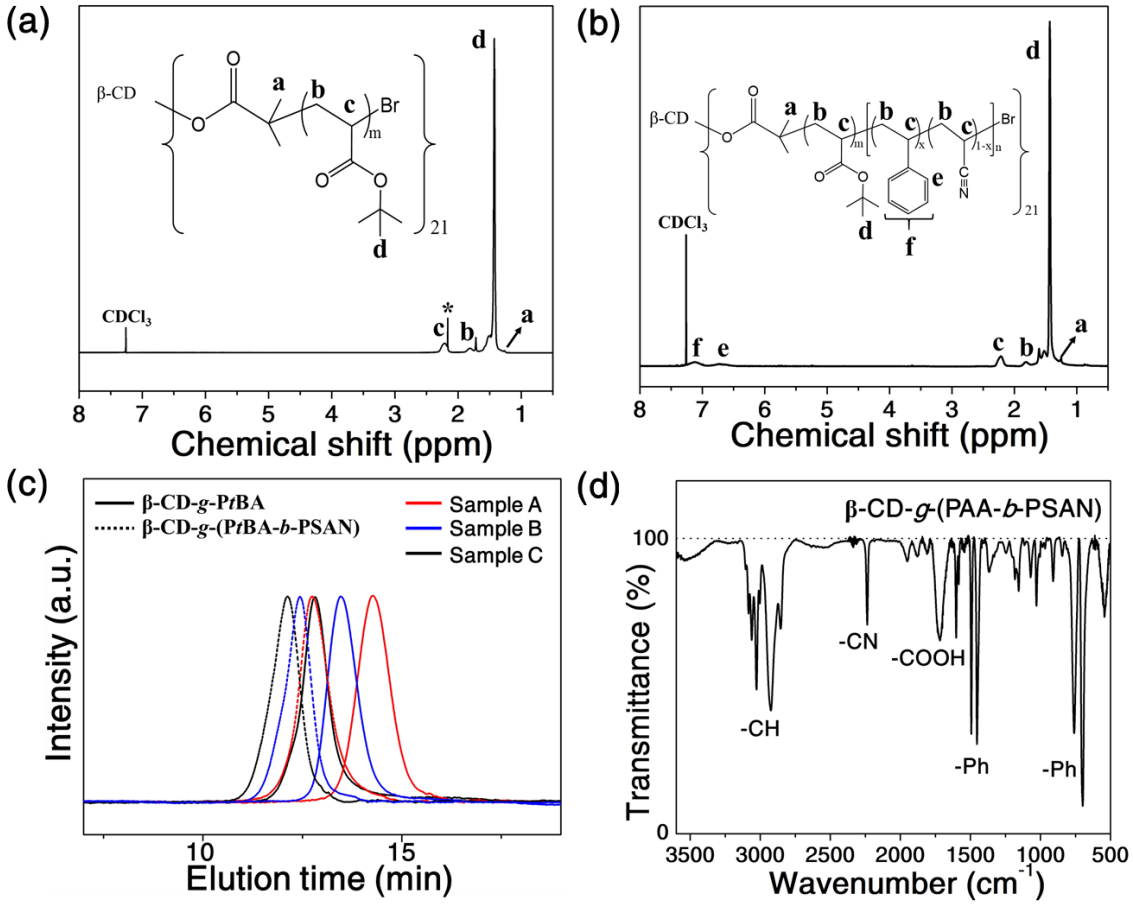

Figure 3.2. (a) ^{1}H NMR spectrum of star-like P*t*BA. (b) ^{1}H NMR spectrum of star-like P*t*BA-*b*-PSAN. (c) GPC curves of star-like P*t*BA (solid curve) and star-like P*t*BA-*b*-PSAN (dashed curve) for all three samples in Table 3.1 (sample A: red, sample B: blue, sample C: black). (d) FTIR of β-CD-*g*-(PAA-*b*-PSAN). (-CN from PSAN: 2237 nm, -COOH from PAA: 1718 nm, -Ph from PSAN: 1493 nm; 1454 nm; 765 nm; 697 nm).

It has been already demonstrated previously in our group that star-like block copolymers can serve as the nanoreactors for synthesis of plain, core-shell, and hollow nanoparticles.[22, 25, 210-212, 214-215, 247-248] The nanoparticle synthesis is carried out by premixing of polymeric nanoreactors and metal precursors followed by in-situ reduction or precipitation, leading to controlled growth of nanocrystals within the nanoreactor. In principle, the carboxyl groups (-COOH) of hydrophilic PAA blocks in the star-like nanoreactors have strong coordination interaction with metal moieties of metal precursors, which will preferentially situate within the PAA core. Previous researches are all based on DMF system which used DMF as the good solvent to dissolve both blocks of the star-like copolymers and BA as the bad solvent for only PS block which collapses the outer surface to confine the precursors inside the nanoreactors. However, the major drawback of this system is that DMF is the good solvent for both the polymeric nanoreactors and the precursors. With excess of precursors to ensure full loading of nanoreactors, there is no control of crystal growth outside the nanoreactors. Consequently, the synthesized product is a combination of both monodisperse nanoparticles grown from the nanoreactors and the big aggregates grown in solution. More effort is required to separate these two components to acquire pure nanoparticles, which always results in low yield with respect to precursor input.

To overcome this problem and increase the yield for battery application, Diphenyl ether (DPE) system was employed instead, in which DPE serves as the good solvent for only PSAN and poor solvent for PAA leading to a stretched PSAN shell and shrunk PAA core initially. In the meantime, organometallic precursors were used for coordinating instead of ionic precursors which were applied in DMF system because they are capable of undergoing thermolysis under refluxing temperature in DPE to form metal oxide. More importantly, the organometallic precursors have relatively low solubility in the less polar DPE and favor the hydrophilic PAA core, which serve as the driving force to push all precursors into the nanoreactors with minimal free precursors in solution. For all the metal ferrite as well as metal oxide nanoparticles synthesized with DPE as the solvent, the yield (precursor conversion) reached almost 100%. BA was also added in the DPE with the ratio of DPE/BA = 9/1. Apart from collapsing the PSAN shell, BA also has the function to swell the initially shrunk core into more spherical morphology due to its polar interactions with PAA chains. By staining the PAA domain within the nanoreactor, it is found that the PAA domain of the nanoreactor is enlarged with BA creating smoother surface. The synthesized nanoparticles after adding BA are consequently more uniform with respect to size and morphology. Meanwhile, to verify that precursors were selectively situated inside the nanoreactors, the nanoreactors were characterized by TEM after soaking with excess Fe precursors. It is found that the size of precursor-loaded nanoparticles (~15 nm) is larger than actual nanoparticles after crystal growth (~8 nm), which is due to volume contraction of metal moieties during crystal formation under thermolysis. The crystalline density of MFe_2O_4 is much higher than precursors.

The polymeric nanoreactors play an essential role in the formation of monodisperse nanoparticles. First, the inner PAA core serves as the template to direct the growth of nanocrystals and confine it just within the PAA domain. As a matter of fact, the -COOH groups in PAA can also catalyze the thermolysis of the organometallic precursors to reduce reaction time. For reaction with nanoreactors (star-like PAA-*b*-PSAN), conversion of metal precursors reached more than 90% in just a couple of hours. However, for same reaction without nanoreactor (precursor + solvent), similar conversion can only be achieved for almost a week. Second, the PSAN outer chains can provide good solubility in organic solvent such as DMF without the addition of extra surface ligands. Different from traditional synthesis strategies where acid or amine are used to provide surface capping, the PSAN chains on the NPs prepared from the nanoreactor are permanently attached on the particle surface. Therefore, they are capable of sustaining high temperature as well as extreme chemical conditions in batteries without detachment to mitigate aggregation of NPs which will lead to poor cycling performance in battery test. Control experiment where no nanoreactors were added in the reaction shows that only large aggregations of irregular clusters formed. Low yield (<10%) was also discovered in control experiment as mentioned earlier.

Five different transition metal ferrites (MFe_2O_4) were synthesized from sample B (8 nm nanoreactor) with M = Mn, Co, Ni, Cu, Zu. **Figure 3.3a** shows the TEM images of the as synthesized PSAN capped $CoFe_2O_4$, $NiFe_2O_4$, $MnFe_2O_4$, $CuFe_2O_4$, $ZnFe_2O_4$ nanoparticles with uniform size and shape. The nanoparticles were well-dispersed in DMF solution due to the PSAN capping on the surface, which is directly visualized through staining of PS by ruthenium tetroxide (the shell in **Figure 3.4**). All five different metal

ferrite nanoparticles have the same diameter as well as similar crystal lattice because of high resemblance of their crystal structures. An intrinsic drawback of MFe_2O_4 materials as well as capped polymers is that they have rather low electrical conductivity, which inhibit charge transfer during battery operations. Consequently, the battery anode can hardly reach the high theoretical capacity that MFe_2O_4 can bring. In order to increase conductivity and efficiently exploit the electrochemical potential of every nanoparticle in the electrode, graphene have been capitalized on previously by multiple researchers[249-254] as the holding matrix for nanoparticles deposition because of their high electrical conductivity and 2D morphology. More importantly, graphene offers the structure flexibility to accommodate the volume change of nanoparticles in Li insertion and desertion process. In the synthesis of MFe_2O_4 nanoparticle/graphene nanocomposite, graphene oxide was first dissolved in DMF and added to the post-reaction solution of MFe_2O_4 nanoparticles to ensure good mixing where nanoparticles can easily deposit onto the graphene sheets. Graphene oxide was chosen as the starting material because it offers good solubility in DMF and can be further reduced into reduced graphene oxide (rGO) under elevated temperature. Only 10% graphene oxide was incorporated with the nanoparticles to provide decent conductivity while maintaining the high capacity of MFe_2O_4 materials. Another role of rGO in the nanocomposite is to immobilize nanoparticles on the 2D sheets to enhance their cycling stability, which will be further discussed in battery performance. As can be seen from **Figure 3.3b**, after simple physical mixing of PSAN capped nanoparticles and graphene oxide, the nanoparticles were uniformly distributed onto the rGO sheets with few agglomerations. It is also found that even after ultrasonication, there were no detachment of NPs from rGO. This strong physical integration between NPs and rGO comes from the

π-π stacking between PSAN side chains and conjugate carbon network of graphene.[255] Meanwhile, the hydrophobic interaction between PS chains on nearby NPs drives them to self-assemble into close-packed monolayer on the graphene sheets, which contributes greatly to the high anode capacity and excellent cycling performance.

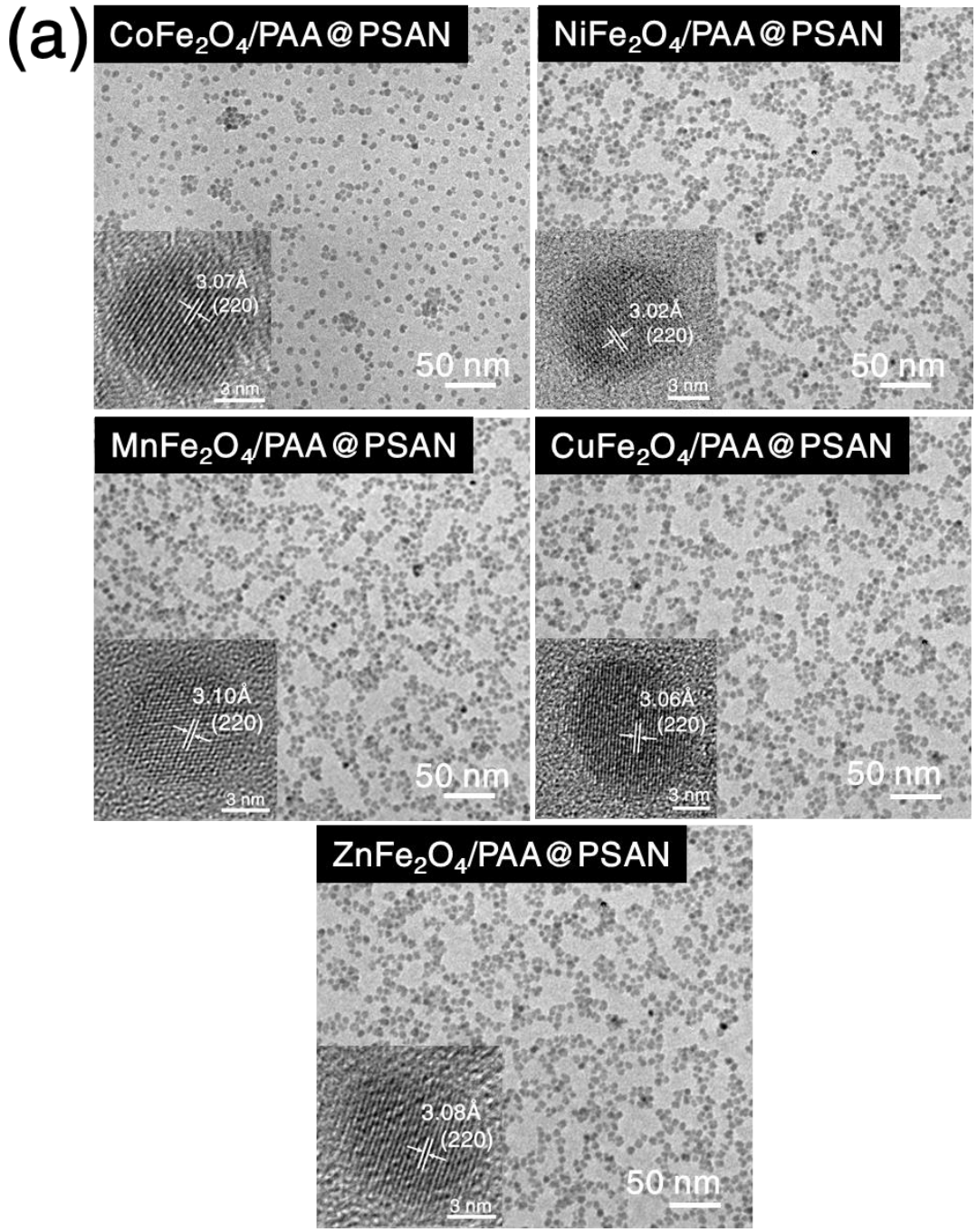

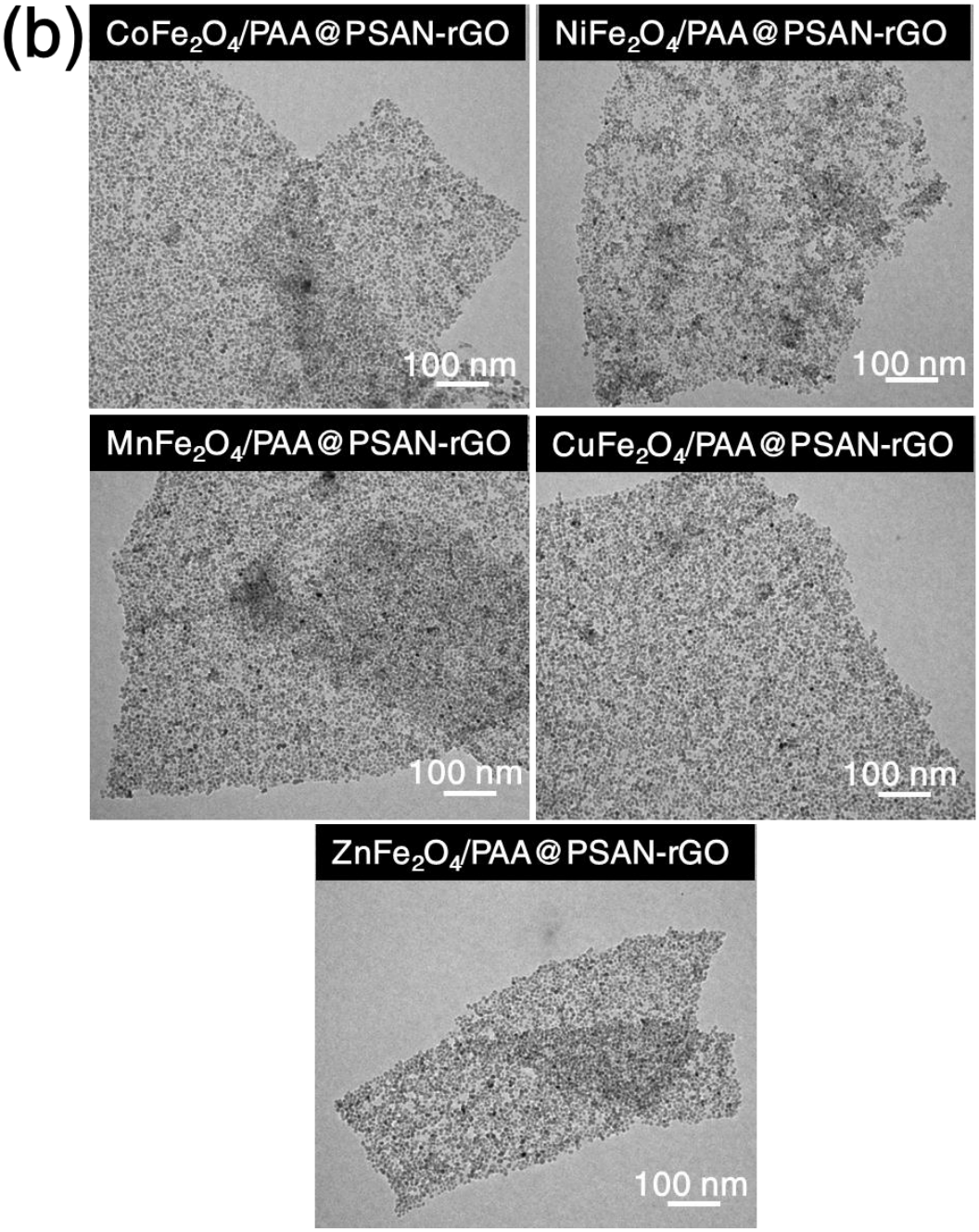

Figure 3.3. (a) TEM and HRTEM (insets) images of MFe_2O_4/PAA@PSAN nanoparticles. (b) TEM images of MFe_2O_4/PAA@PSAN-rGO nanocomposites

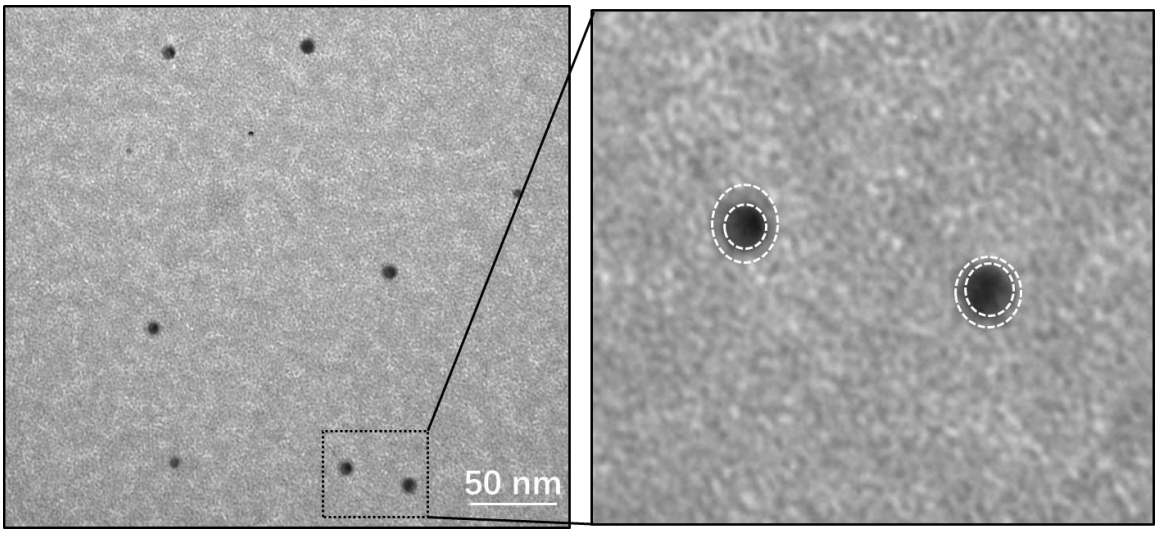

Figure 3.4. TEM of $CoFe_2O_4$ nanoparticles after staining with Ruthenium tetroxide vapor for 30min. The PS shell is selectively stained which can be directly visualized from the clear contrast to the $CoFe_2O_4$ core.

Moreover, to further demonstrate the size control of NPs via nanoreactor assisted strategy, we synthesized $CoFe_2O_4$ NPs of three different size (5 nm, 8 nm, 11 nm) with different MW of nanoreactors (**Figure 3.5** & **Table 3.1**). By comparing the sizes of the synthesized NPs with theoretical values estimated from PAA MW, it can be observed that the two smaller sizes correspond well with each other. However, for sample C which has much larger PAA, the synthesized NP is significantly smaller than nanoreactor size. As mentioned previously, the PAA chain tends to collapse in DPE and was therefore swelled with additional BA. However, as MW weight of PAA goes higher, the entropy barrier for stretching of PAA chains is even harder to overcome. Consequently, it is rather difficult to synthesize large NPs (>10 nm) with the currently applied nanoreactor strategy in DPE system. Nevertheless, it still offers adequate ability to precisely tune the size of NPs by simply controlling the PAA molecular weight.

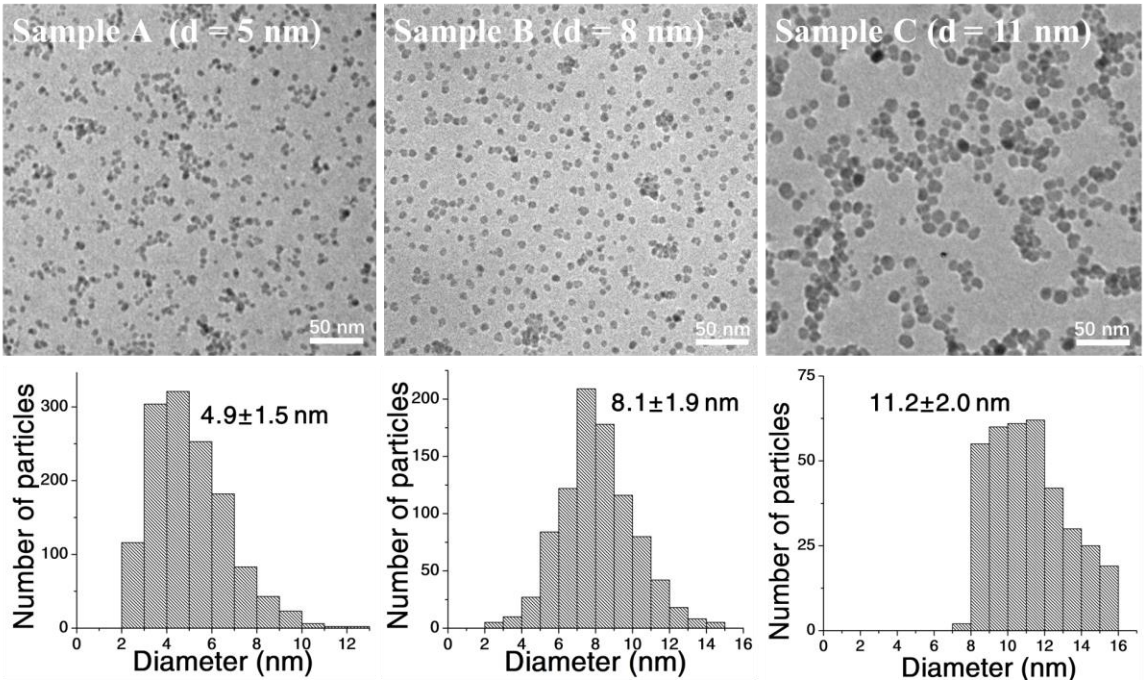

Figure 3.5. TEM of $CoFe_2O_4$ nanoparticles of three different sizes synthesized from sample A, B, C, respectively and their corresponding size distribution analysis.

The composition of MFe_2O_4 NPs were further characterized by XRD (shown in **Figure 3.6a**), All MFe_2O_4 crystals have the same lattice structure, the spinel structure, with slight variation in unit cell dimension ($NiFe_2O_4$: 0.834 nm, $CuFe_2O_4$: 0.838 nm, $CoFe_2O_4$: 0.839 nm, $ZnFe_2O_4$ 0.844 nm, $MnFe_2O_4$: 0.852 nm). According to Bragg's law, $2d \sin\theta = n\lambda$. Higher lattice dimension (d) results in lower 2θ for given facet. It can be clearly observed in the right panel of **Figure 3.6a** that the reflection angle of (311) facet decreases as the M in MFe_2O_4 changes from Ni to Mn due to increase in unit cell size. Meanwhile, according to the high-res TEM images of MFe_2O_4 NPs in **Figure 3.3a**, the lattice spacing of (220) facet also increases from 3.02 Å for $NiFe_2O_4$, 3.06 Å for $CuFe_2O_4$, 3.07 Å for $CoFe_2O_4$, 3.08 Å for $ZnFe_2O_4$, to 3.10 Å for $MnFe_2O_4$, which correspond well with the XRD data and theoretical lattice parameters. To further investigated the valence information of the bimetallic material, XPS was used to characterize

$CoFe_2O_4$/PAA@PSAN nanoparticles, which also reveals the PSAN composition. **Figure 3.6b** shows the C 1s binding energy in which the peak at 287 eV depicts the C-C bond in PS while the peak at 289.5 eV depicts the C≡N bond in PAN. The percentage of AN units within the PSAN copolymers is calculated from the integration to be 25%, which will offer moderate Li ion transportability. Co 2p spectra in **Figure 3.6c** reveals 3 distinct doublets originated from octahedral site, tetrahedral site, and satellite peaks of Co^{2+}, respectively[256]. All the peaks aligned well the peaks from CoO nanoparticles synthesized from the same strategy indicating the 2+ state of Co in $CoFe_2O_4$. Similarly, the 3 distinct doublets of Fe in **Figure 3.6d** were also identified accordingly to octahedral site, tetrahedral site, and satellite peak. The 3+ state of Fe in $CoFe_2O_4$ was also confirmed through comparison with the spectra of Fe_2O_3 nanoparticles. Both XRD and XPS demonstrated the successful synthesis of $CoFe_2O_4$ spinal nanoparticles via our nanoreactor strategy.

The Raman spectra of $CoFe_2O_4$/PAA@PSAN exhibit characteristic peaks of polystyrene (PS) and $CoFe_2O_4$ (synthesized in the absense of star-like PAA-*b*-PSAN). The Raman spectra of pristine GO, rGO (obtained after heat treatment of pristine GO in DMF) and $CoFe_2O_4$/PAA@PSAN-rGO exhibit characteristic G-band (1595 cm^{-1}) and D-band (1345 cm^{-1}) from GO (**Figure 3.6e**).[257] The higher D/G intensity ratios (I_D/I_G) of $CoFe_2O_4$/PAA@PSAN-rGO (I_D/I_G = 1.09) and rGO (1.11) than pristine GO (0.86) indicate the reduction of GO after 140 ºC heat treatment in DMF. The mass ratio of $CoFe_2O_4$ in $CoFe_2O_4$/PAA@PSAN-rGO are estimated to be 77.6 wt.% based on the TGA measurements of rGO, $CoFe_2O_4$/PAA@PSAN and $CoFe_2O_4$/PAA@PSAN-rGO in air (**Figure 3.6f**).

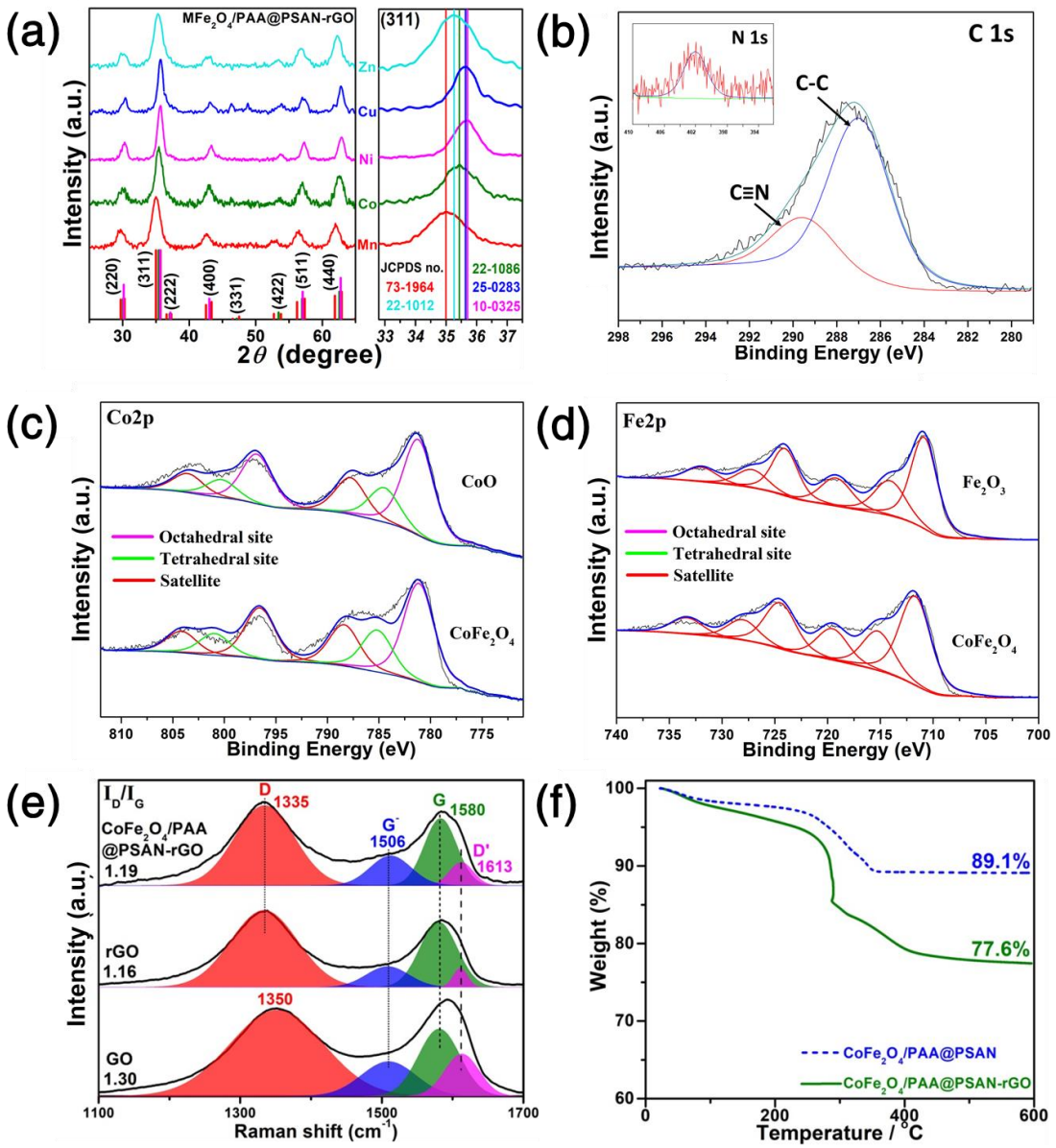

Figure 3.6. XRD patterns of the MFe_2O_4/PAA@PSAN-rGO (M = Mn, Co, Ni, Cu or Zn) nanocomposites. (b),(c),(d) XPS spectra of $CoFe_2O_4$@PSAN nanoparticles: (b) C 1s spectrum, (c) Co 2p spectrum, (d) Fe 2p spectrum. (e) Raman spectra of pristine GO, rGO (obtained after 140 ºC heat treatment in DMF in the absence of $CoFe_2O_4$/PAA@PSAN nanoparticles) and $CoFe_2O_4$/PAA@PSAN-rGO. (f) TGA results of $CoFe_2O_4$/PAA@PSAN and $CoFe_2O_4$/PAA@PSAN-rGO

As shown in the large scale SEM and TEM images (**Figure 3.7a-d**), the $CoFe_2O_4$/PAA@PSAN-rGO nanocomposites possess a graphite-like macrostructure constructed by layer-by-layer self-assembly of the $CoFe_2O_4$/PAA@PSAN nanoparticles

loaded rGO driven by the π-π stacking interaction of rGO.[258] Unform size distrubution of $CoFe_2O_4$/PAA@PSAN nanoparticles can be seen in High-res SEM (**Figure 3.7e**) with an average diameter of 8 nm. EDS mapping of single nanoparticle **(Figure 3.7f)** shows the uniform distribution of Co and Fe across entire nanocrystal as well as some N signal, which is a direct evidence for presence of PSAN on nanoparticle surface.

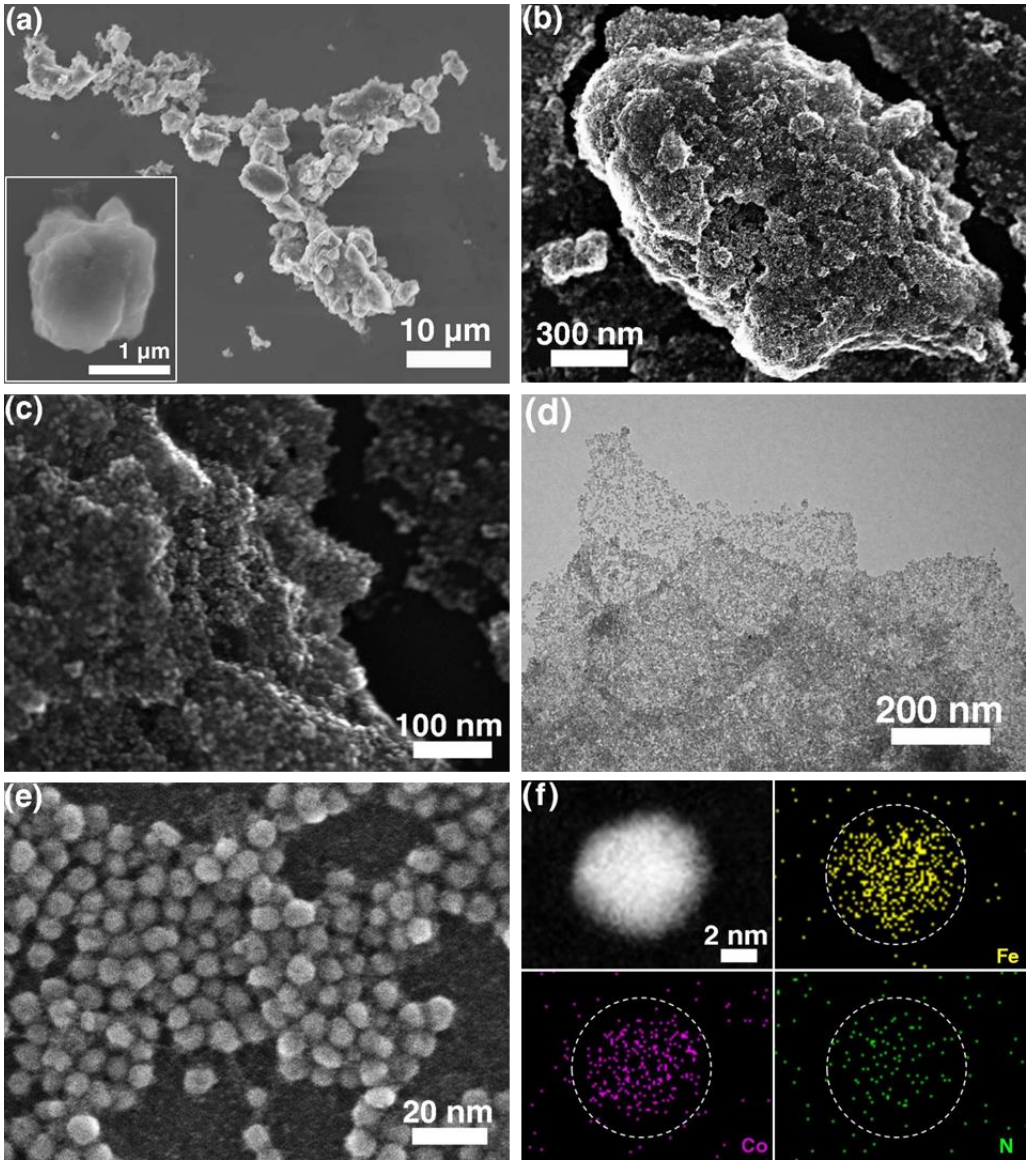

Figure 3.7. (a-c) SEM and (d) TEM images of the graphite-like macrostructure of $CoFe_2O_4$/PAA@PSAN-rGO formed by the layer-by-layer self-assembly of

$CoFe_2O_4$/PAA@PSAN nanoparticles loaded rGO nanosheets driven by the π-π stacking interaction of rGO. (e) High-res SEM images of assembly of $CoFe_2O_4$/PAA@PSAN nanoparticles. (f) EDS mapping of simgle $CoFe_2O_4$/PAA@PSAN nanoparticles.

In contrast, $CoFe_2O_4$ (**Figure 3.8a**) and $CoFe_2O_4$/PAA (**Figure 3.8b**) obtained in the absence of star-like PAA-*b*-PSAN and in the presence of star-like PAA, respectively, formed microparticles which are composed of aggregated irregular nanoparticles. Consequently, neither of them can be completely and uniformly encapsulated in rGO due to their large particle sizes and lack of surface π-π interaction (**Figure 3.8c-d**).

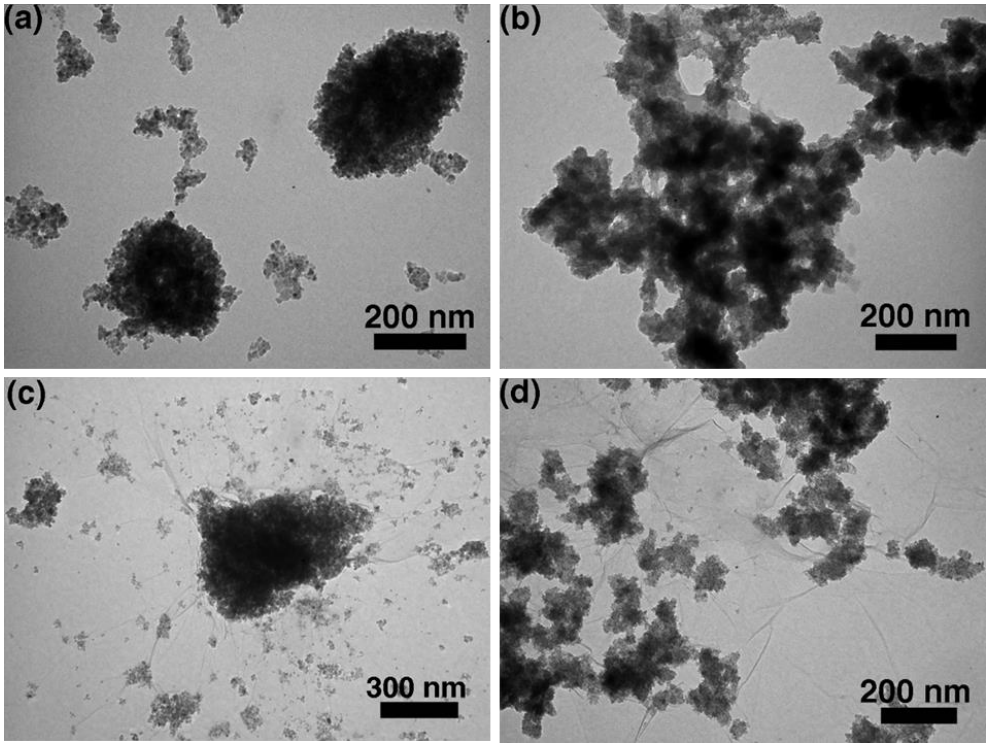

Figure 3.8. TEM images of (a) $CoFe_2O_4$ nanoparticle aggregates obtained in the absence of polymer template (b) $CoFe_2O_4$/PAA nanoparticle aggregates obtained with star-like PAA as nanoreactor (c) $CoFe_2O_4$-rGO composites and (d) $CoFe_2O_4$/PAA-rGO composites.

Additionally, $CoFe_2O_4$/PAA@PSAN nanoparticles were also annealed at 500ºC in N_2 to convert the surface PSAN polymers into graphite which will provide higher conductivity.

However, due to much higher phase mobility at the calcinating temperature and depletion of polymers between particles during the conversion, aggregation of particles began to occur resulting in aggregated nanoparticles (ANPs) with poor size distribution (**Figure 3.9a**) and surface coated carbon layer (**Figure 3.9b**). Raman spectra of the nanoparticles after calcination reveals the formation of graphite layer (**Figure 3.9e**). Evidently, the calcinated nanoparticles without the surface PSAN polymer cannot be absorbed onto rGO surface (**Figure 3.9c**). In order to maintain nanoparticles morphology, $CoFe_2O_4$/PAA@PSAN-rGO composite was calcinated where the nanoparticles were stabilized on graphene. It can be observed from **Figure 3.9d** that despite the disruption of layer-by-layer assembly of the composite strucutre, there is smaller morphological change in the nanoparticles than the ones without graphene, indicating that graphene can physically impede the motion of nanoparticles and prevent them from phase aggregation. The crystalinity of $CoFe_2O_4$ was also increased after calcination as evidented by XRD (**Figure 3.9f**).

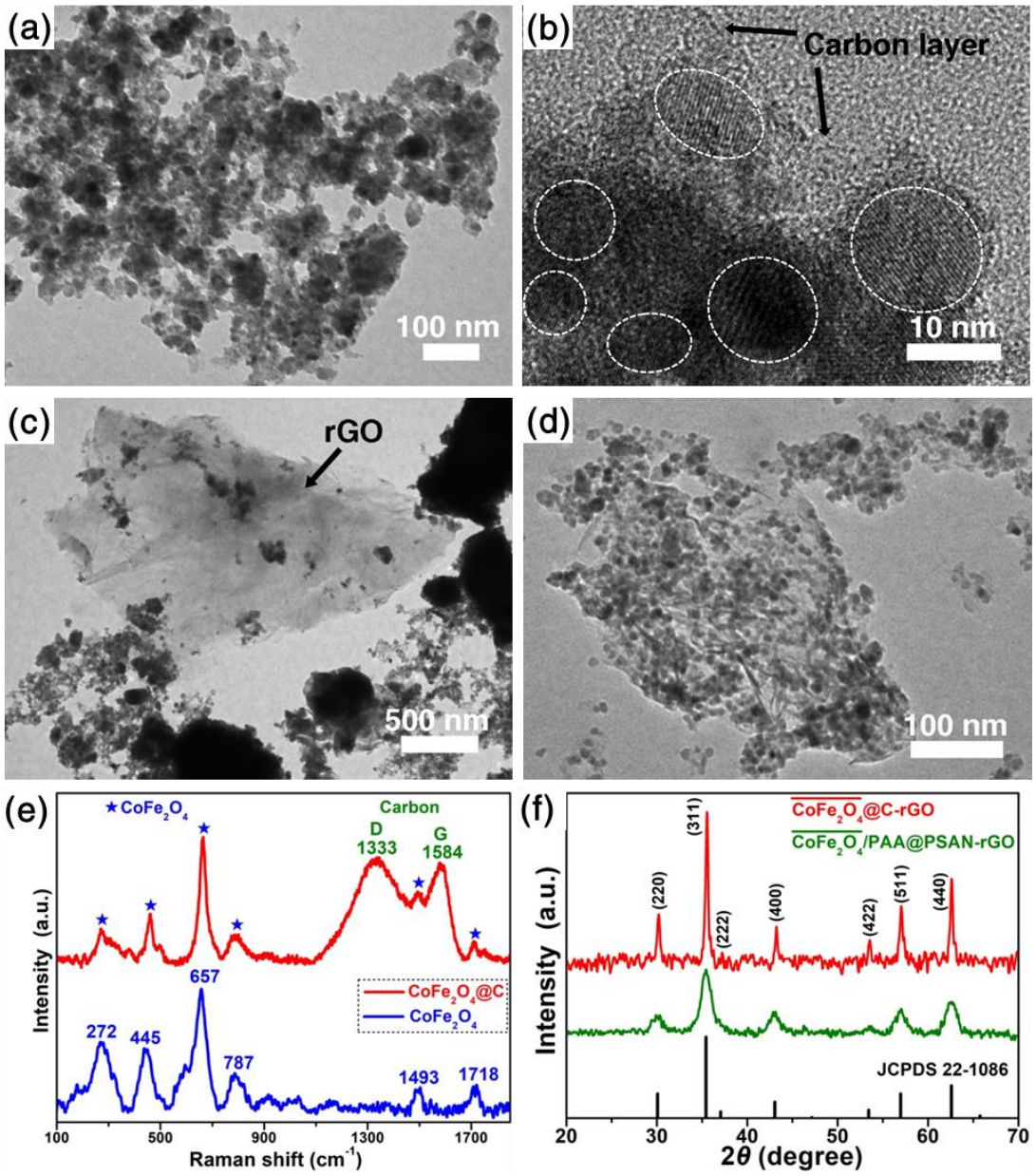

Figure 3.9. (a) TEM images of $CoFe_2O_4$@C aggregated nanoparticles (ANPs) obtained by calcination of $CoFe_2O_4$/PAA@PSAN nanoparticles in N_2 at 500 ºC for 2 h. (b) HRTEM image of $CoFe_2O_4$@C ANPs showing the presence of carbon layer on the $CoFe_2O_4$ NPs. (c) TEM images of $CoFe_2O_4$ ANPs-rGO nanocomposite. (d) TEM images of $CoFe_2O_4$@C-rGO obtained after annealing $CoFe_2O_4$/PAA@PSAN-rGO at 500 ºC for 2 h in N_2 atmosphere. (e) Raman spectra of $CoFe_2O_4$@C-rGO and $CoFe_2O_4$/PAA@PSAN-rGO. (f) XRD patterns of $CoFe_2O_4$@C-rGO and $CoFe_2O_4$/PAA@PSAN-rGO.

To further prove that the major contribution to particles-rGO interaction is the π-π interaction rather than hydrogen binding between N and remaining polar groups on rGO or metal-carboxyl coordination, $CoFe_2O_4$/PAA@PSAN nanoparticles were mixed with same account of pure graphene as GO but without the polar groups presented on GO. As shown in **Figure 3.10**, the nanoparticles can still be uniformed attached to the graphene surface demonstrating the importance of π-π interaction for assembly of $CoFe_2O_4$/PAA@PSAN nanoparticles.

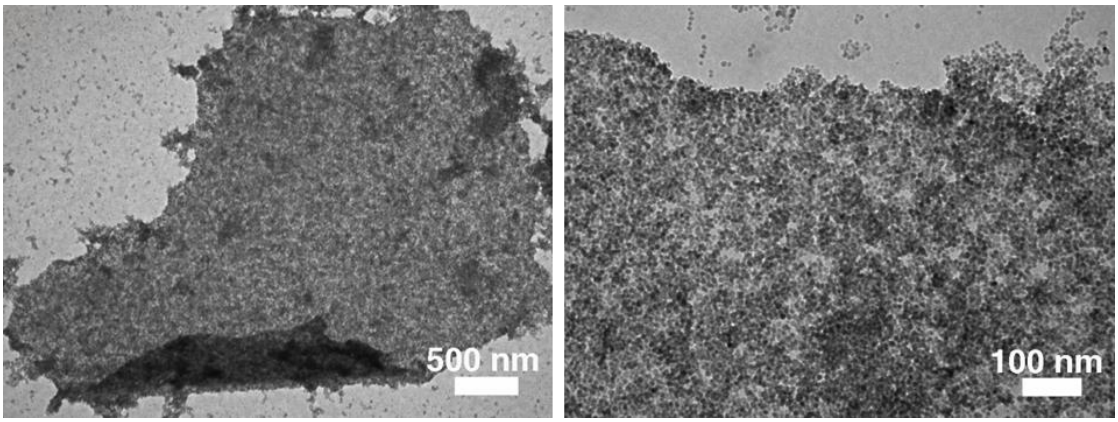

Figure 3.10. TEM images of $CoFe_2O_4$/PAA@PSAN-Gr nanocomposite obtained by physical mixing of $CoFe_2O_4$/PAA@PSAN NPs with graphene.

In order to demonstrate the importance of bimetallic composition in the improvement of the LIB capacity and cycling stability. A series of monometallic metal oxides nanoparticles (MO_x/PAA@PSAN) (M = Fe, Mn, Co) were synthesized by the same nanoreactor approach. Similar size distribution and assembly behavior on graphene were observed (**Figure 3.11**). Their crystal structures were further verified by XRD which matches with database (**Figure 3.12**). Specifical, the synthesized Fe_2O_3 nanoparticles are in gamma phase adopting a similar crystal lattice as spinel Fe_3O_4 cyrstals.

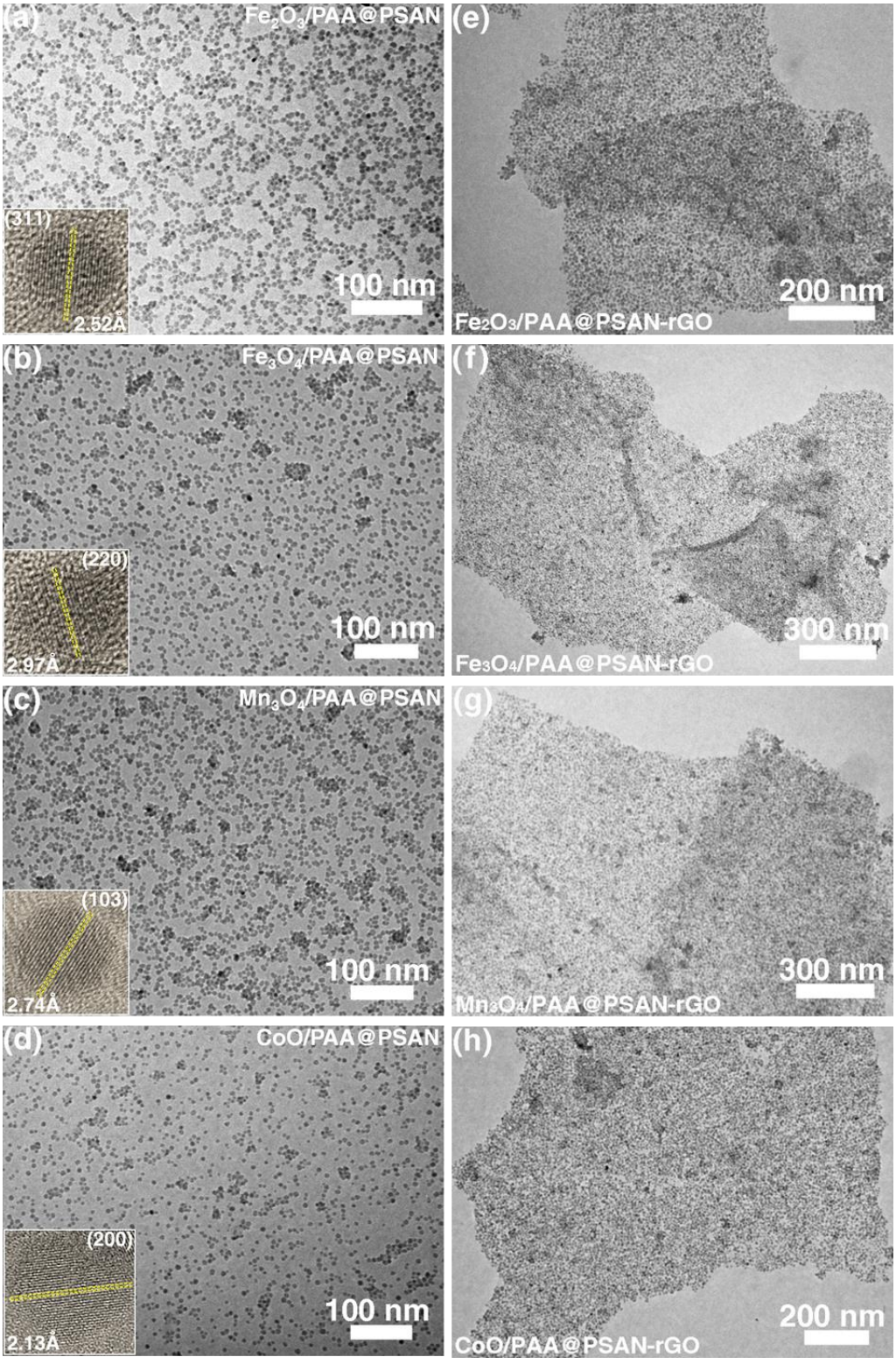

Figure 3.11. TEM images of the synthesized (a-d) MO_x/PAA@PSAN nanoparticles (inset: HRTEM) and (e-h) MO_x /PAA@PSAN-rGO (M = Fe, Mn, Co) nanocomposites with star-like PAA-*b*-PSAN as nanoreactor.

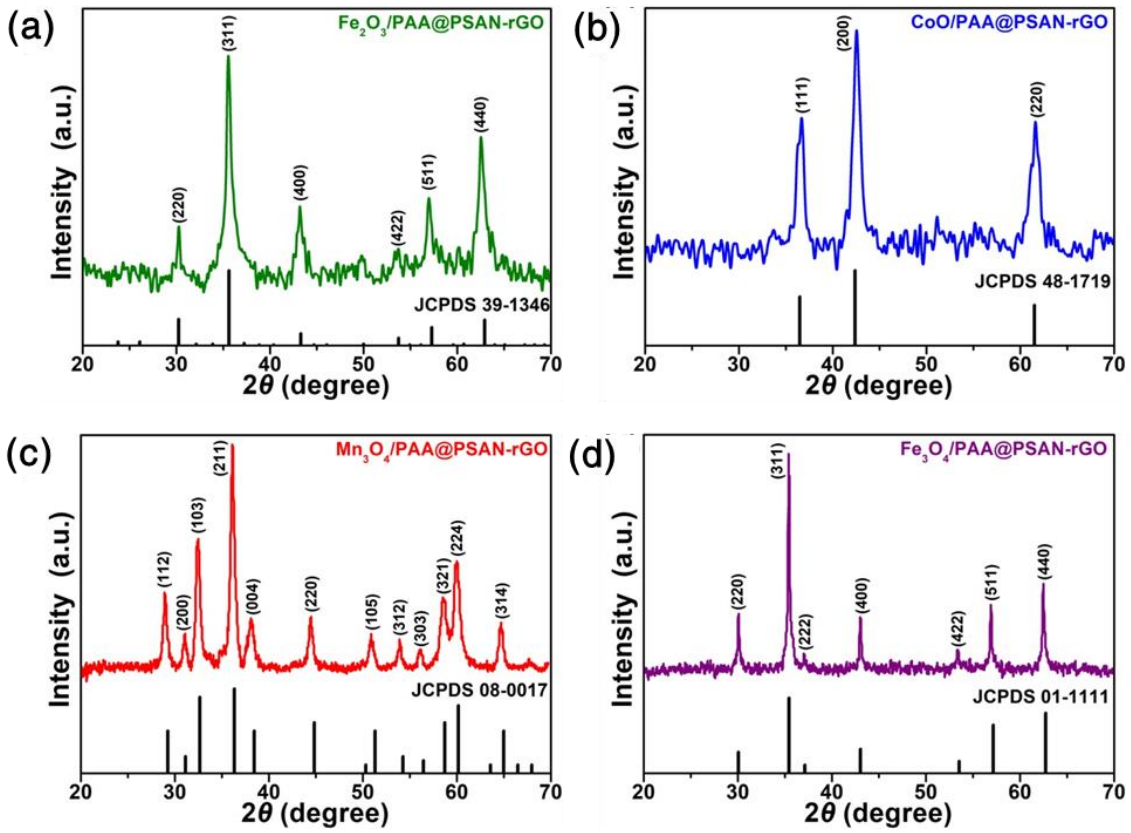

Figure 3.12. XRD spectra of MO_x/PAA@PSAN nanoparticles with MO_x = (a) Fe_2O_3, (b) CoO, (c) Mn_3O_4, (d) Fe_3O_4.

3.3.2 Battery performances

All synthesized materials were used as anodes to assemble into half-cell to test their battery performances. **Figure 3.13a-d** show the cycling stabilities and rate performances of MFe_2O_4/PAA@PSAN-rGO (M=Mn, Co, Ni, Cu or Zn) nanocomposites as anodes of lithium and sodium ion batteries. High capacities of 1200 mAh/g at 200 mA/g and 800 mAh/g at 1000 mA/g close to the theoretical capacities of MFe_2O_4 (i.e., ~889-930 mAh g^{-1}) were observed as anodes of LIBs. The extremely high capacities can be attributed to the nanosized morphology (small nanoparticles, diameter ~8 nm) of MFe_2O_4/PAA@PSAN NPs which shortens the ion and electron transfer distances and enhances the reaction

kinetics. Such high capacities were maintained even after hundreds of cycles, demonstrating high cycling stabilities. The surface PSAN chains can effectively protect the nanoparticles from aggregation rendering superior structure stability. Reduced graphene oxide (rGO) can firmly immobilize the nanoparticles and keep them well-separated during battery operation. High rate performances were also observed owing to the high electronic conductivity contributed by the three-dimensional conductive network constructed by the layer-by-layer self-assembled rGO nanosheets. Additionally, as anodes of SIBs, the MFe_2O_4/PAA@PSAN-rGO nanocomposites also showed outstanding cycling and rate performances, demonstrating that this strategy is versatile for performance improvement in alkaline ion battery. It is noticed that the sodium storage capacities of MFe_2O_4/PAA@PSAN-rGO nanocomposites are lower than expected theoretical capacities (i.e., ~889-930 mAh g^{-1}) due to the heavier mass and larger radius of Na^+ ion (22.99 g mol^{-1}, 1.02 Å) than Li^+ ion (6.94 g mol^{-1}, 0.76 Å) which leads to a lower diffusivity of Na^+ in MFe_2O_4, a more severe volume expansion, and a more sluggish reactivity. Nevertheless, the Li^+ and Na^+ insertion-extraction resulted volume changes of MFe_2O_4/PAA@PSAN nanoparticles can be effectively accommodated by the PSAN hairs and rGO nanosheets, resulting in high conversion reaction reversibility with outstanding cycling and rate performances of the MFe_2O_4/PAA@PSAN-rGO nanocomposites as anodes of LIBs and SIBs. The discharge-charge profiles of $CoFe_2O_4$/PAA@PSAN-rGO nanocomposites from 2nd to 30th cycles are almost overlapped with each other with constant discharge plateaus at 0.94 and 0.98 V as anodes of LIBs and SIBs (**Figure 3.13e&f**), respectively, confirming the ultrastable electrochemical reaction reversibility on the electrodes.

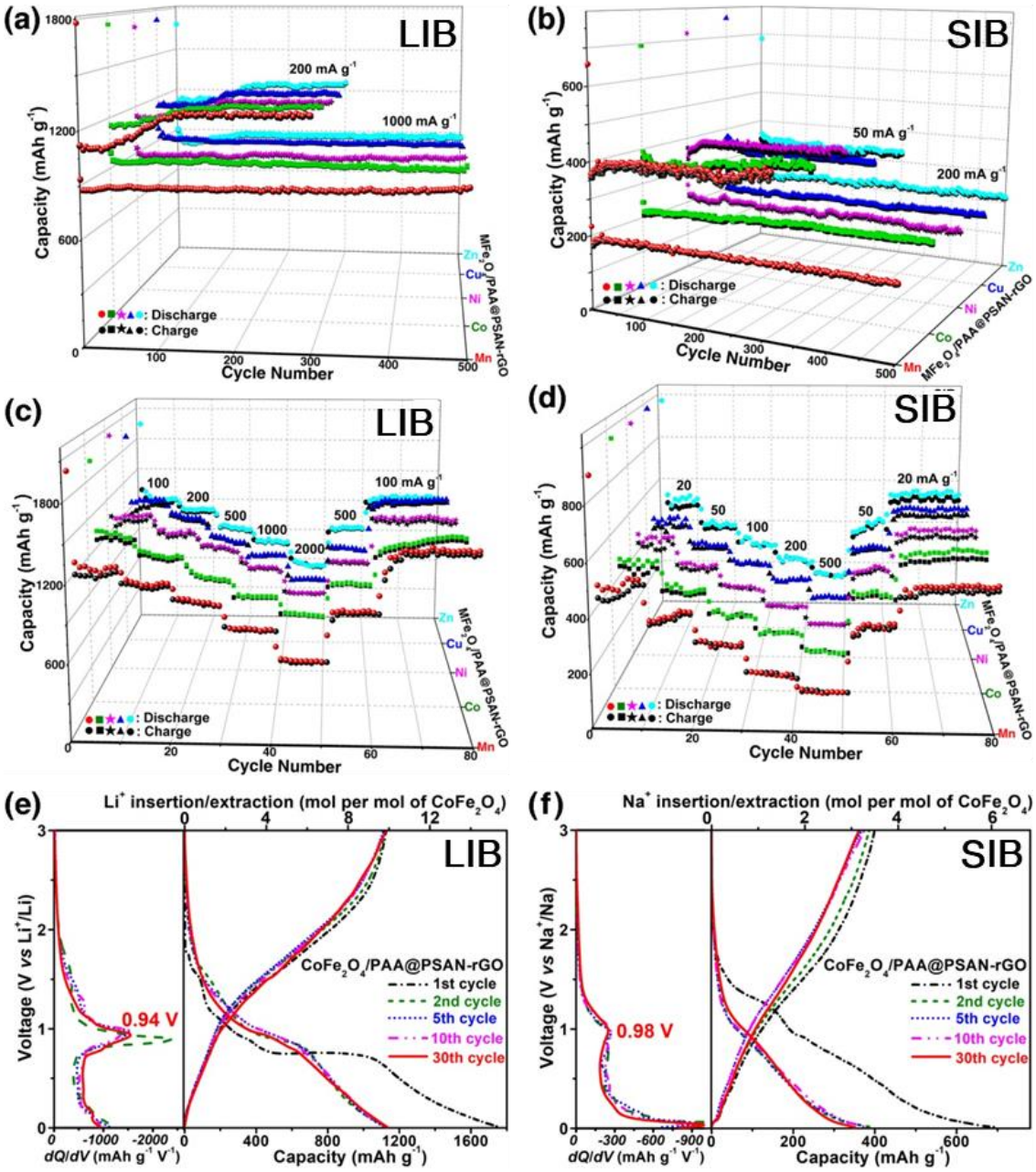

Figure 3.13. (a, b) Cycling stabilities, (c, d) rate performances and (e, f) charge-discharge profiles and corresponding *dQ*/*dV* curves of discharge profiles of MFe_2O_4/PAA@PSAN-rGO (M = Mn, Co, Ni, Cu or Zn) nanocomposites as anodes of (a, b, e) LIBs and (c, d, f) SIBs.

The contribution of polymer template and rGO support on the enhanced battery performance of MFe_2O_4/PAA@PSAN-rGO (M = Mn, Co, Ni, Cu or Zn) nanocomposites is systematically investigated by conducting control experiments of

$CoFe_2O_4$/PAA@PSAN-rGO nanocomposites where either GO or star-like PAA-*b*-PSAN was not used in the nanocomposite synthesis. As can be seen in the cycling stabilities of control samples as anodes of LIBs and SIBs in **Figure 3.14a&b**, respectively, the $CoFe_2O_4$/PAA@PSAN NPs exhibited the worst cycling performance due to the poor electronic conductivity of PSAN hair which results in a low electrochemical reactivity of $CoFe_2O_4$ with Li^+ and Na^+. $CoFe_2O_4$-rGO composite (**Figure 3.8c**) also performed poorly due to the large ionic and electronic transfer distance as well as severe volume changes of large-size $CoFe_2O_4$ particles induced by Li^+/Na^+ insertion-extraction. Notably, it is worth mentioning that the cycling stability of $CoFe_2O_4$/PAA-rGO composite (**Figure 3.8d**) is slightly better than the $CoFe_2O_4$-rGO composite although similar aggregation occurred due to absence of PSAN hairs. This slightly enhanced cycling stability of $CoFe_2O_4$/PAA-rGO composites can be potentially attributed to the stabilization effect of internally embedded PAA chains on the structure of aggregated $CoFe_2O_4$/PAA nanoparticles. On the other hand, the cycling stability of $CoFe_2O_4$@C-rGO nanocomposite (**Figure 3.9d**) is not as good at that of $CoFe_2O_4$/PAA@PSAN-rGO nanocomposite but obviously better than the other control samples. It is because that the carbon layer generated after the pyrolysis of PSAN in N_2 can still act as a protection layer on nanoparticles to prevent the aggregation of $CoFe_2O_4$@C NPs. Nevertheless, the localized aggregation of $CoFe_2O_4$@C NPs and partial disruption of the nanoparticle-rGO sandwich structures during calcination still lead to the poorer cycling stability than the original $CoFe_2O_4$/PAA@PSAN-rGO nanocomposite.

The performances of a series of monometallic metal oxides-based nanocomposites (i.e., MO_x/PAA@PSAN-rGO, MO_x = Fe_2O_3, Fe_3O_4, Mn_3O_4, CoO) were also tested to compare with the bimetallic compositions (MFe_2O_4/PAA@PSAN-rGO). Surprisingly, as

anodes of LIBs (**Figure 3.14c**), the capacities of all the MO_x/PAA@PSAN-rGO nanocomposites initially decreased, then slowly increased, and finally stabilized at high capacities close to the original values. In contrast, as anodes of SIBs, all the MO_x/PAA@PSAN-rGO nanocomposites exhibited continuous decreased capacities along with increased cycle numbers (**Figure 3.14d**). The divergent cycling stabilities of MFe_2O_4/PAA@PSAN-rGO and MO_x/PAA@PSAN-rGO nanocomposites with similar structure-function relationship indicate that some extraordinary performance enhancement mechanism exists in the MFe_2O_4/PAA@PSAN-rGO nanocomposites in spite of the positive effect of polymer template and rGO. As shown in the charge-discharge profiles of Fe_2O_3/PAA@PSAN-rGO nanocomposites, the capacity fading can be attributed to the gradual degradation of the charge-discharge plateaus (e.g., discharge plateaus at 0.96 and 0.71 V as anodes of LIBs and SIBs, respectively), corresponding to gradually decayed electrochemical reaction reversibility on the electrode of Fe_2O_3/PAA@PSAN-rGO nanocomposites.

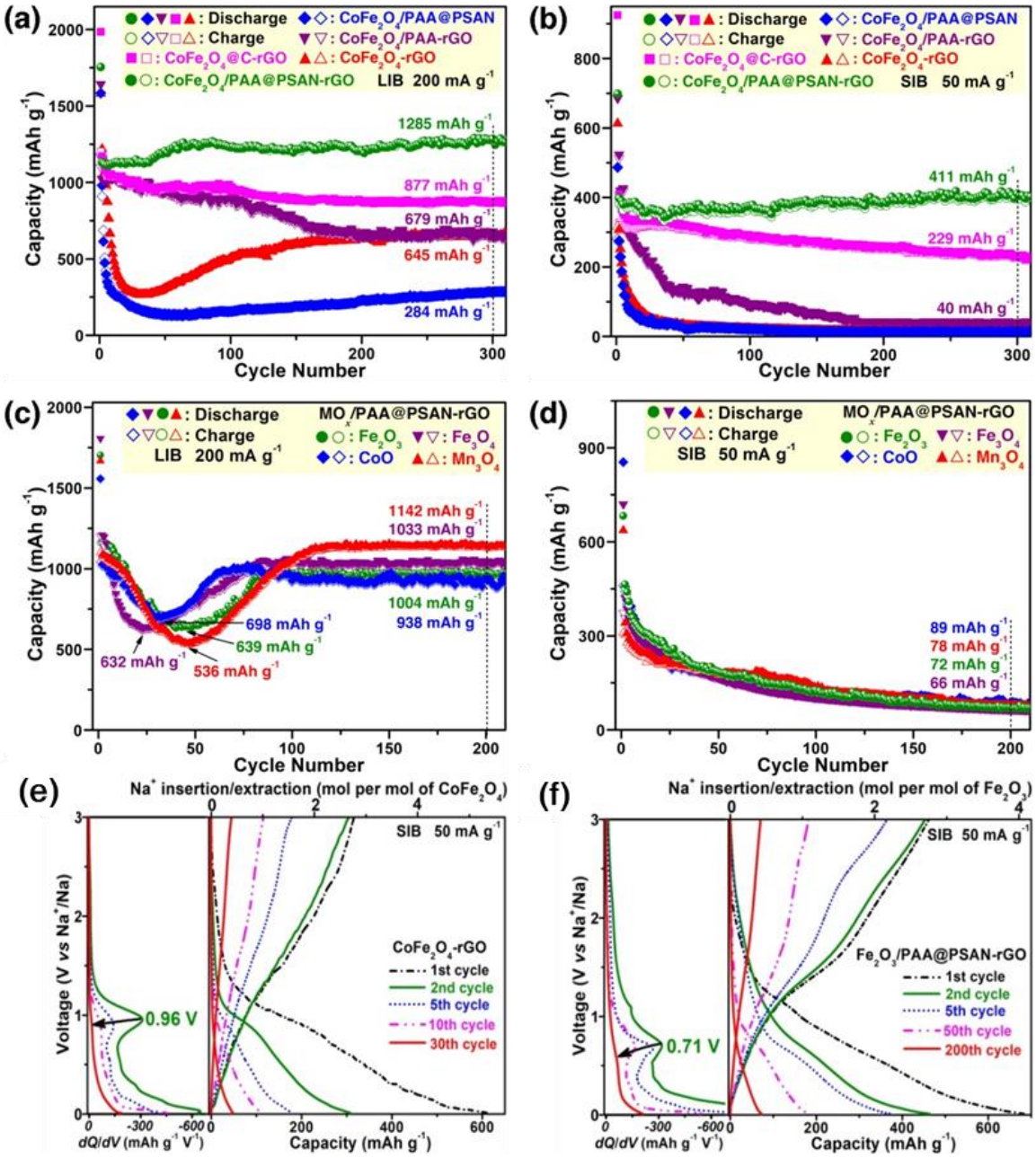

Figure 3.14. Cycling performances of (a,b) $CoFe_2O_4$/PAA@PSAN, $CoFe_2O_4$-rGO, $CoFe_2O_4$/PAA-rGO, $CoFe_2O_4$@C-rGO and (c,d) MO_x/PAA@PSAN-rGO (M = Mn, Co, Fe) as anodes of (a,c) LIBs and (b,d) SIBs. Charge-discharge profiles and corresponding *dQ*/*dV* curves of discharge profiles of (e) $CoFe_2O_4$-rGO and (f) Fe_2O_3/PAA@PSAN-rGO.

$$CoFe_2O_4 + 8A^+ + 8e^- \rightarrow Co + Fe + A_2O \qquad \textbf{(Equation 1)}$$

$$Co + A_2O \leftrightarrow CoO + 2A^+ + 2e^- \qquad \textbf{(Equation 2)}$$

$$2Fe + 3A_2O \leftrightarrow Fe_2O_3 + 6A^+ + 6e^- \quad \textbf{(Equation 3)}$$

To uncover the performance enhancement mechanism of MFe_2O_4/PAA@PSAN-rGO nanocomposites and the failure mechanism of MO_x/PAA@PSAN-rGO nanocomposites as anodes of LIBs and SIBs, the cycled electrodes of $CoFe_2O_4$/PAA@PSAN-rGO and Fe_2O_3/PAA@PSAN-rGO nanocomposites were comparatively investigated. The lithium and sodium storage in $CoFe_2O_4$ and Fe_2O_3 are based on the conversion reactions in **Equation 1-3** and **Equation 3**. Thus, extensive HRTEM and EDS characterizations of $CoFe_2O_4$ and Fe_2O_3 nanoparticles inside the cycled $CoFe_2O_4$/PAA@PSAN-rGO and Fe_2O_3/PAA@PSAN-rGO nanocomposites were carried out to uncover the phase changes to fully understand the fundamental mechanism for their divergent cycling stabilities. From the TEM image in **Figure 3.15a**, we can find that the nanoparticles morphology of $CoFe_2O_4$/PAA@PSAN-rGO anode is well-maintained after 300 cycles of discharge-charge process, illustrating an excellent structure stability of the $CoFe_2O_4$/PAA@PSAN-rGO nanocomposites in the reversible conversion reaction process (**Equation 2 and 3**) along with the repeated sodiation-desodiation. However, in stark contrast to the initial $CoFe_2O_4$ NPs which have perfect spinel lattice fringes (**Figure 3.3a**) and uniformly distributed Co and Fe elements (**Figure 3.7f**), the cycled $CoFe_2O_4$ NPs phase-separated into CoO and Fe_2O_3 domains after conversion reactions (**Equation 2-4**) as evidenced by lattice analysis and elemental mapping in **Figure 3.15b&c**. This is consistent with widely reported conversion reaction mechanism of spinal MFe_2O_4 materials as electrodes of LIBs and SIBs in the literature. Such microphase separation can introduce abundant heterophase interfaces inside and between the $CoFe_2O_4$/PAA@PSAN NPs which inhibit the homophase coarsening of Co, Fe and Na_2O crystal domains, therefore, keeping high conversion reaction reversibility with stable sodium storage capacity (**Figure 3.13b**). In stark contrast,

when monometallic nanoparticles such as Fe_2O_3/PAA@PSAN-rGO were used as anodes of SIBs, significant homophase coarsening of Fe and Na_2O among the adjacent Fe_2O_3/PAA@PSAN nanoparticles was observed after 200 cycles, resulting in the generation of large Fe and Na_2O crystal domains with low reactivity (**Figure 3.15d&e**). The XPS spectra of Fe2p3 of charged $CoFe_2O_4$/PAA@PSAN-rGO nanocomposites can be divided into three peaks at 710.7, 709.4 and 707.2 eV, corresponding to Fe^{3+}, Fe^{2+} and Fe^0 (**Figure 3.15f**). In addition, an obvious Na1s peak corresponding to the presence of Na_2O was observed in the charged $CoFe_2O_4$/PAA@PSAN-rGO nanocomposites. The presence of Fe^{2+}, Fe and Na_2O in the charged electrode of $CoFe_2O_4$/PAA@PSAN-rGO nanocomposites might correspond to the amorphous region in the cycled $CoFe_2O_4$/PAA@PSAN NPs (**Figure 3.15b**). This demonstrates that Fe and Na_2O cannot be fully recovered into Fe_2O_3 due to the sluggish reactivity of large sized Na^+ ion. In contrast, the cycled Fe_2O_3/PAA@PSAN-rGO electrode showed a much stronger XPS peak of Na1s and only one XPS peak of Fe2p3 at 707.2 eV corresponding to Fe^0. This indicates that the 200th cycled electrode of Fe_2O_4/PAA@PSAN-rGO nanocomposites were composed of only Na_2O and Fe^0 due to the homophase coarsening. Overall, it can be speculated that the homophase coarsening of M and A_2O (A = Li^+ or Na^+) in the cycling process of monometallic MO_x /PAA@PSAN-rGO nanocomposites is the essential reason for the degradation of conversion reaction reversibility of MO_x NPs. However, in the case of bimetallic MFe_2O_4/PAA@PSAN-rGO nanocomposites, the homophase coarsening of M, Fe and A_2O can be inhibited by the heterophase interfaces constructed by the phase separation of MFe_2O_4 into MO and Fe_2O_3 after cycles.

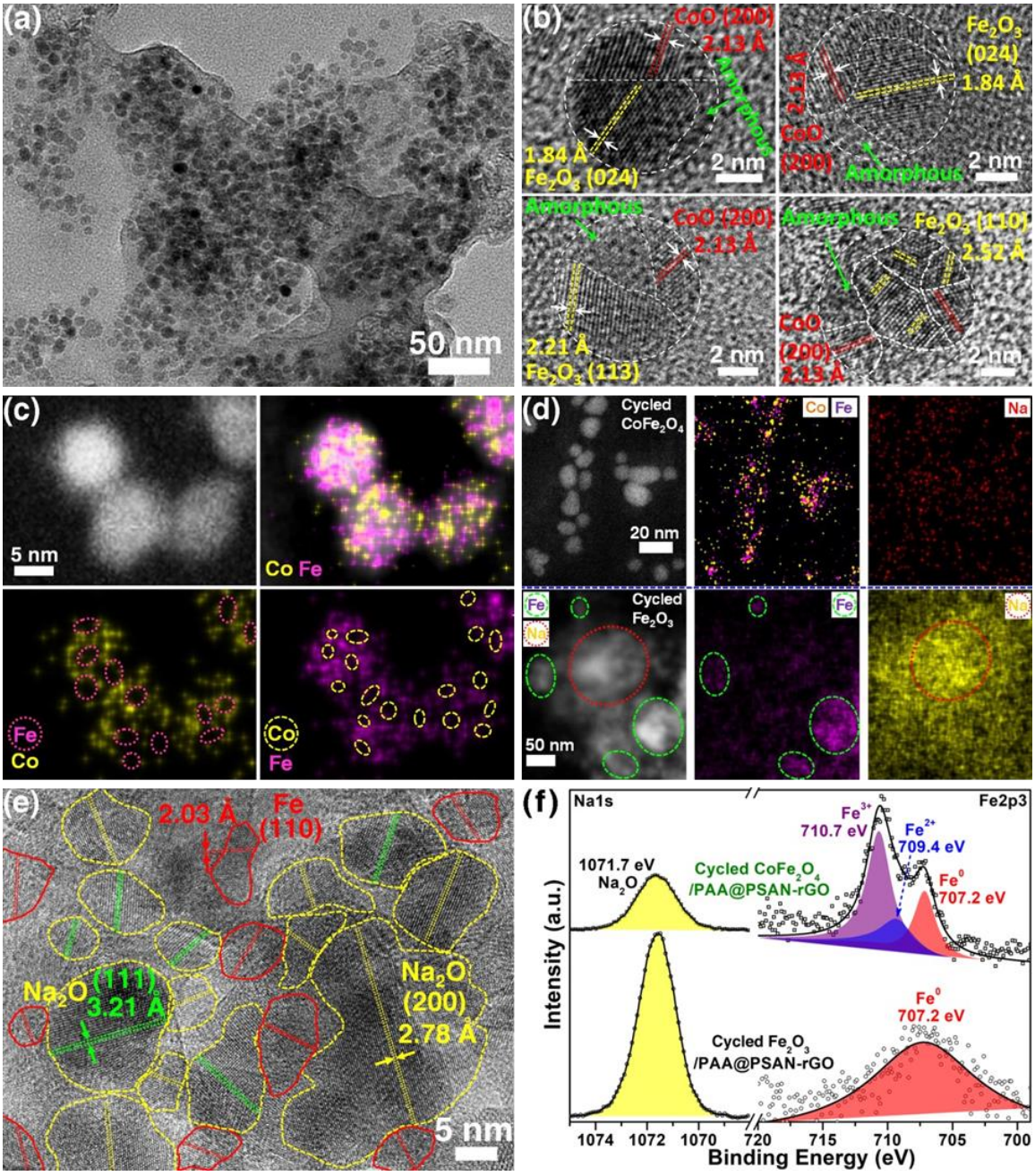

Figure 3.15. (a, b, e) (HR) TEM images, (c, d) HAADF-STEM-EDS images and (f) XPS spectra of Na1s and Fe2p3 of charged electrodes of (a-c and upper panels of d and f) $CoFe_2O_4$/PAA@PSAN-rGO nanocomposites and (e and lower panels of d and f) Fe_2O_3/PAA@PSAN-rGO nanocomposites after 300 and 200 cycles as anodes of SIBs at 50 mA g^{-1} (Figure 3.13b & 3.14d), respectively.

A comprehensive phase coarsening mechanism is proposed to explain the observed homophase coarsening failure phenomenon in conversion-type metal oxides as anodes of

LIBs or SIBs, as illustrated in **Figure 3.16**. First of all, when no physical barrier exists between NPs (e.g. $CoFe_2O_4$-rGO), the huge volume expansion of lithiated/sodiated NPs will lead to directed homophase contact and high chance of homophase coarsening among the adjacent NPs, ending up with much larger crystal domains of metals and A_2O (A = Li or Na) with poor conversion reaction reversibility due to low specific contact area between metal and A_2O crystal domains. On the other hand, in the case of Fe_2O_3/PAA@PSAN-rGO nanocomposites, there are indeed polymer barriers of PSAN hairs between nanoparticles which can prevent particle aggregation in some sense. However, the grafted PSAN hairs on the Fe_2O_3 NPs are not dense enough to ensure smooth transmission of electrons between rGO and Fe_2O_3 NPs. Moreover, as the Fe_2O_3 NPs are compactly packed on the rGO nanosheets (**Figure 3.11e**), there isn't enough space between them to tolerate the lithiation/sodiation induced volume expansion of the Fe_2O_3 NPs. Therefore, homophase coarsening will take place at the contact interfaces among adjacent Fe_2O_3/PAA@PSAN NPs, resulting in the degradation of conversion reaction reversibility and capacity decay. Conversely, in bimetallic $CoFe_2O_4$/PAA@PSAN-rGO nanocomposite, $CoFe_2O_4$ NPs will randomly phase separate into numerous domains of two different phases (CoO and Fe_2O_3) after the first cycle, creating abundant heterophase interfaces inside and among the $CoFe_2O_4$ NPs. The synergistic effect of the heterophase interfaces and the physical barriers of PSAN and rGO can robustly inhibit the homophase coarsening of Co, Fe and A_2O in the cycled $CoFe_2O_4$/PAA@PSAN-rGO nanocomposites for keeping a high conversion reaction reversibility with stable lithium and sodium storage capacity. Innovated by the mechanisms proposed above, two distinct strategies were established to overcome the capacity decrease of MO_x/PAA@PSAN-rGO anodes by eliminating homophase

coarsening in the system: (1) constructing robust physical barriers to accommodate the lithiation/sodiation induced volume expansion and minimizing the physical contact probability between MO_x NPs by increasing the amount of rGO or decreasing the particle size of MO_x NPs; (2) introducing abundant heterophase interfaces by artificially mixing different MO_x species with uniform distribution in anode material.

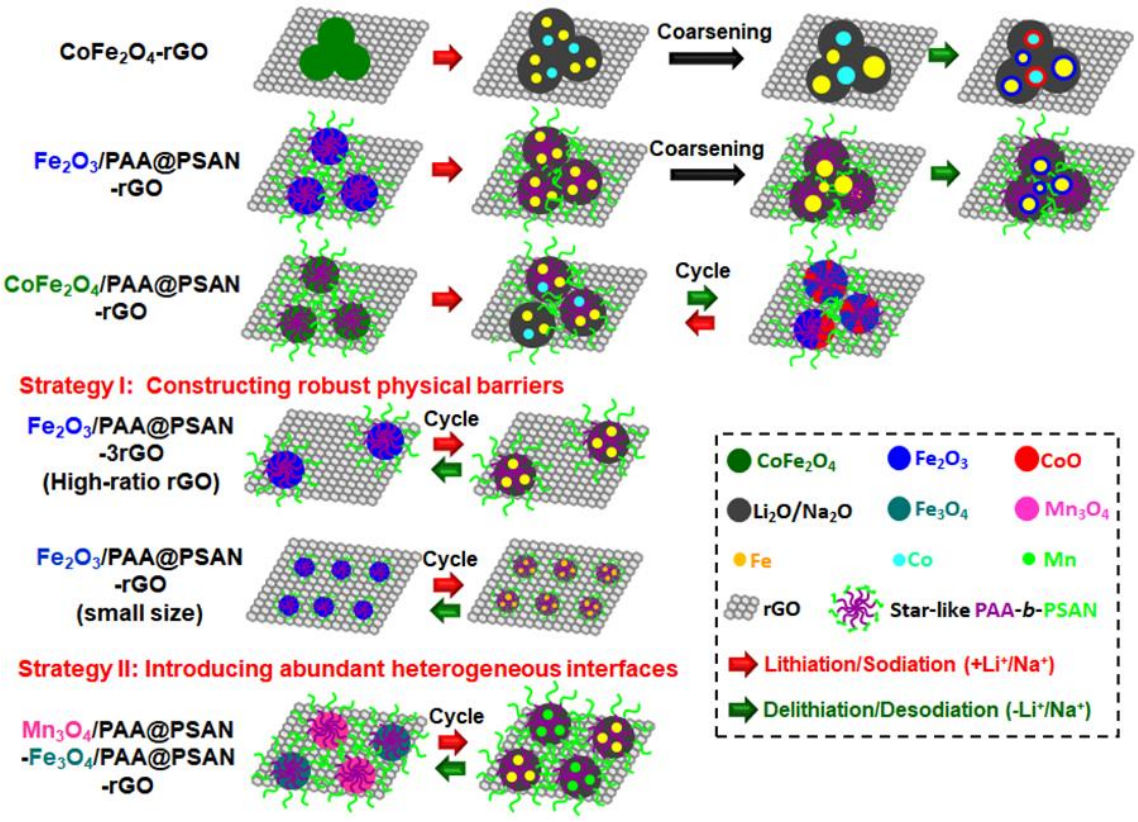

Figure 3.16. Schematic illustration of the phase coarsening capacity decay mechanism, enhanced cycling stability of $CoFe_2O_4$/PAA@PSAN-rGO, and proposed universal strategies for improving cycling stability of MOs as anodes of LIB/SIB.

For strategy 1, three times of GO amount was used to synthesize the Fe_2O_3/PAA@PSAN-3rGO nanocomposite. The inter-distance between nearby nanoparticles is therefore greatly increased as shown in **Figure 3.17a&b**. The larger distance makes the nanoparticles harder to get into physical contact with each other in order

to prevent the homophase coarsening among them in the cycling process. In contrast to the Fe_2O_3/PAA@PSAN-rGO nanocomposite, significantly improved cycling and rate performances were observed for Fe_2O_3/PAA@PSAN-3rGO nanocomposite as anodes of LIBs and SIBs (**Figure 3.17c&d**). On the other hand, Fe_2O_3/PAA@PSAN NPs with a smaller diameter of ~4 nm (**Figure 3.18a**) were used to substitute the ~8 nm Fe_2O_3/PAA@PSAN NPs in the nanocomposite synthesis. The smaller size of the ~4 nm Fe_2O_3/PAA@PSAN NPs will decrease the lithiation/sodiation induced volume expansion and comparatively enhance the stabilization effect of PSAN hairs and rGO on the NPs. As shown in **Figure 3.18b**, the cycling stabilities of ~4 nm Fe_2O_3/PAA@PSAN-rGO nanocomposites as anodes of LIBs and SIBs both significantly increased verifying the above hypothesis.

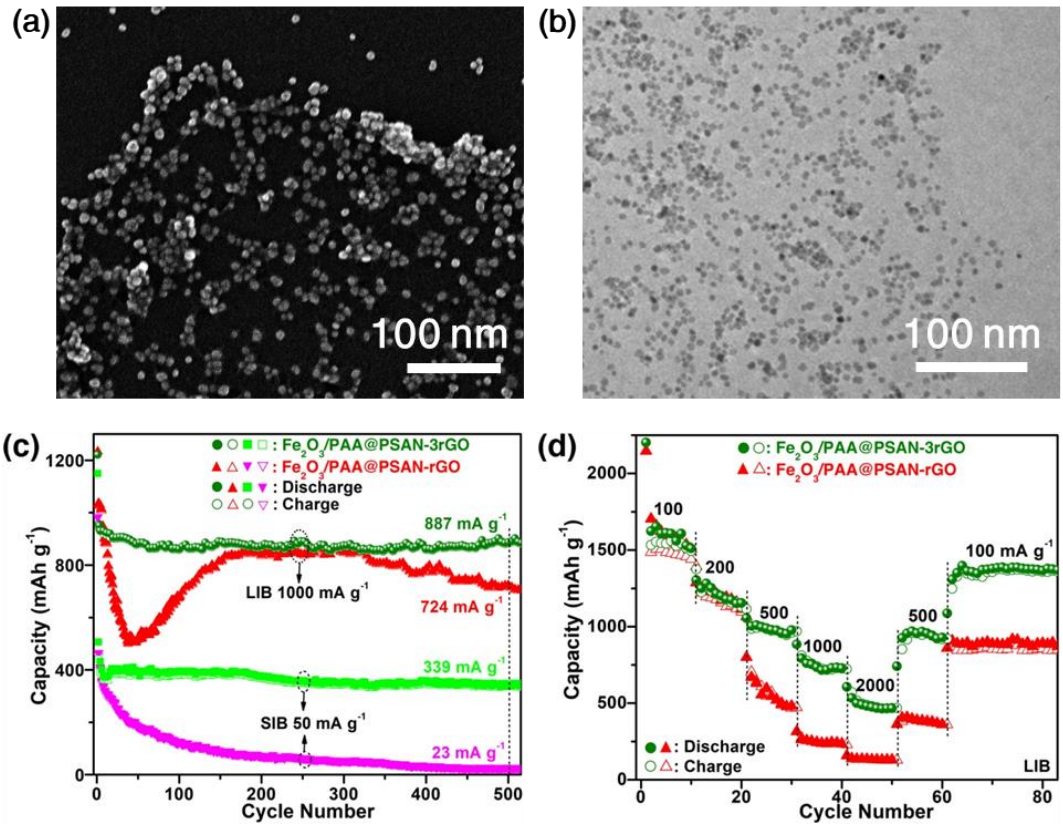

Figure 3.17. (a) SEM and (b) TEM images of Fe_2O_3/PAA@PSAN-3rGO nanocomposite. (c) Comparison of cycling performances of Fe_2O_3/PAA@PSAN-3rGO nanocomposite and Fe_2O_3/PAA@PSAN-rGO nanocomposite in LIB and SIB. (d) Comparison of rate performances of Fe_2O_3/PAA@PSAN-3rGO nanocomposite and Fe_2O_3/PAA@PSAN-rGO nanocomposite in LIB.

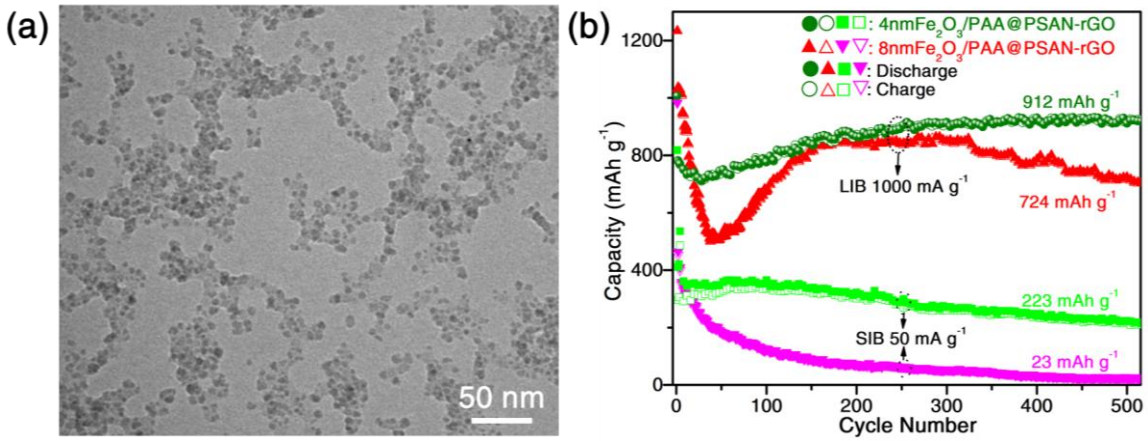

Figure 3.18. (a) TEM image of 4 nm Fe_2O_3/PAA@PSAN nanoparticles. (b) Cycling performance of 4 nm Fe_2O_3/PAA@PSAN-rGO as anode of LIB and SIB.

For strategy 2, an equal molar amount of Fe_3O_4/PAA@PSAN NPs and Mn_3O_4/PAA@PSAN NPs were uniformed mixed and then encapsulated in rGO. Raman spectrum (**Figure 3.19b)** shows both signals from Fe_3O_4 and Mn_3O_4 in the (Fe_3O_4/PAA@PSAN-Mn_3O_4/PAA@PSAN)-rGO nanocomposite. According to **Figure 3.19c**, the cycling performance of (Fe_3O_4/PAA@PSAN-Mn_3O_4/PAA@PSAN)-rGO nanocomposite is much better than Fe_3O_4 or Mn_3O_4 alone, reaching stable lithium and sodium storage capacities of 1239 and 330 mAh/g at 200 and 330 mA/g, respectively, which are close to the values of bimetallic MFe_2O_4/PAA@PSAN-rGO nanocomposites. After cycling, the morphology of both nanoparticles is well-maintained as shown in **Figure 3.19a**. It demonstrates that both intraparticle heterophase and interparticle heterophase can stabilize the anode materials by limiting homophase coarsening during conversion reaction and improve the battery performances. Additionally, the discharge (**Figure 3.19d**) and charge (**Figure 3.19e**) curves of (Fe_3O_4/PAA@PSAN-Mn_3O_4/PAA@PSAN)-rGO exhibit integrated characters of Fe_3O_4 and Mn_3O_4. Specifically, the two discharge plateaus exactly match the individual plateau of Fe_3O_4 and Mn_3O_4, indicating independent conversion reactions in Fe_3O_4/PAA@PSAN and Mn_3O_4/PAA@PSAN NPs in the mixture nanocomposites during the whole cycling processes. Together, they contributed to the high and stable capacity with strongly-inhibited homophase coarsening.

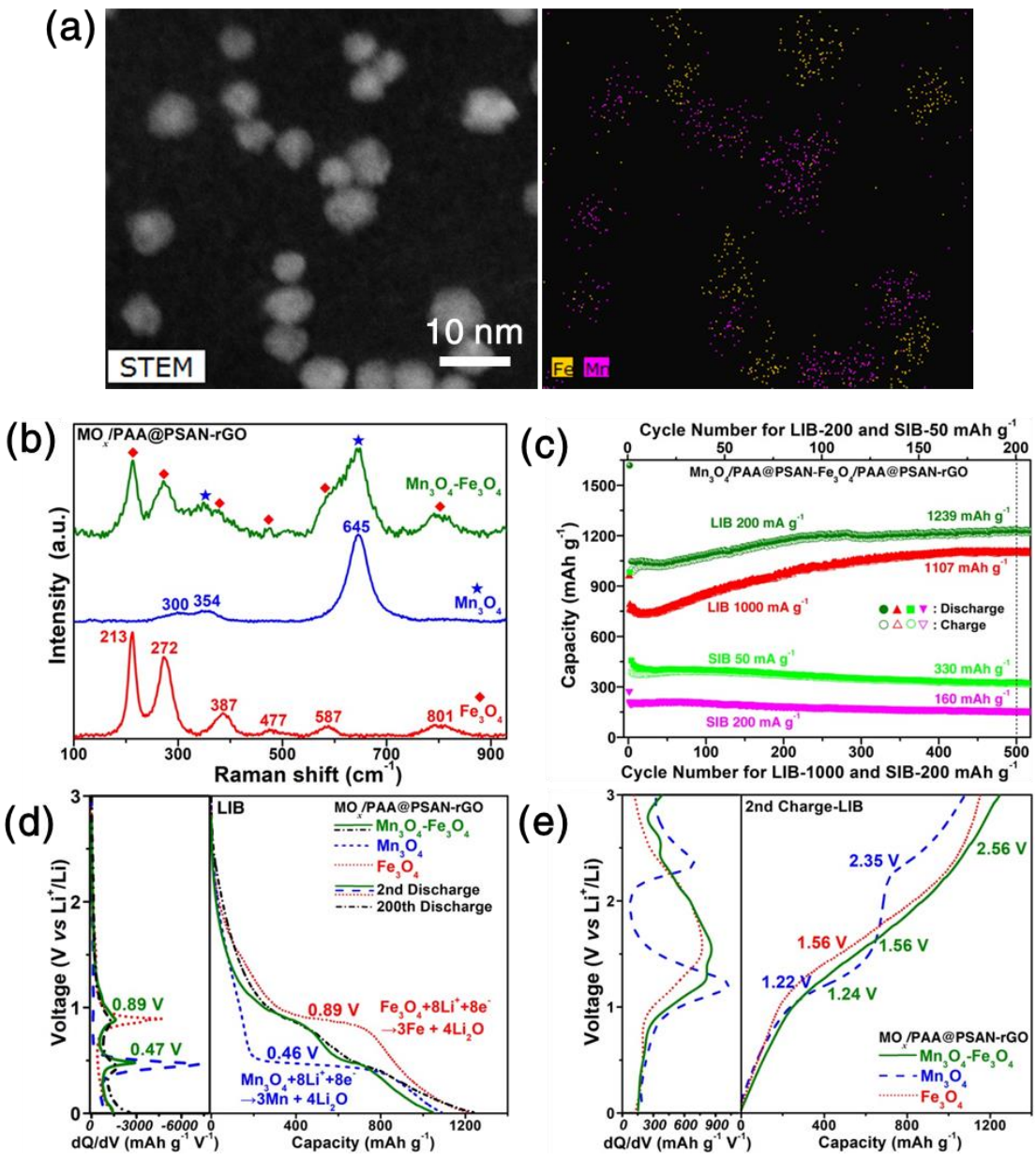

Figure 3.19. (Fe_3O_4/PAA@PSAN+Mn_3O_4/PAA@PSAN)-rGO nanocomposites. (a) HAADF-STEM-EDS images of the 200th charged electrode, (b) Raman spectrum, (c) cycling performance as anodes of LIBs and SIBs, (d) discharge and (e) charge curves as anodes of LIBs.

3.4 Conclusions

In summary, monodisperse MFe_2O_4 and MO_x nanoparticles of precisely controlled size were crafted with star-like PAA-*b*-PSAN block copolymers as nanoreactors, which

was then uniformly anchored on reduced graphene oxide nanosheets induced by the π-π stacking interaction between PSAN and rGO. As anodes of LIBs/SIBs, the MFe_2O_4/PAA@PSAN-rGO expressed outstanding cycling stabilities at various current rates. In stark contrast, Li^+ storage capacities of MO_x/PAA@PSAN-rGO decreased initially and then raised while Na^+ storage capacities continued to decay. Detailed HRTEM and EDS characterization of cycled electrodes revealed that for monometallic metal oxides such as Fe_2O_3, homophase coarsening occurred between Fe nanoparticles resulting in larger domains and thus the decrease of specific contact areas of Fe with Li_2O/Na_2O and the reduction of conversion reaction reversibility. Conversely, the bimetallic $CoFe_2O_4$ nanoparticles randomly phase-separate into CoO and Fe_2O_3 domains after the first cycle, creating abundant heterophase interfaces within the cycled $CoFe_2O_4$/PAA@PSAN-rGO nanocomposites. The heterophase interfaces together with physical barriers provided by rGO and PSAN hairs inhibit the large-scale homophase coarsening of Co and Fe nanoparticles stabilizing the electrochemical reaction reversibility. Finally, two key strategies to inhibit homophase metal coarsening are proposed and verified, which is essential for the enhancement of cycling stability of MO_x as anode of LIBs/SIBs. (1) constructing robust physical barriers to minimize physical contact between nanoparticles during volume expansion, and (2) introducing abundant heterogeneous interfaces by artificially increasing the number of metal species with uniform distribution in anode material. These strategies can be universally applied to all metal oxides anode materials to increase rate and cycling performances, therefore providing an important guideline for future battery research on electrode material design.

CHAPTER 4. ROBUST ROUTE TO MULTI-FUNCTIONAL CELLULOSE-BASED POLYMERIC BOTTLE-BRUSH COCOONS

This work will be published as: Z. Wang, Y. Liu, Y. Harn, S. Liang, and Z. Lin*, Robust Route to Multi-Functional Cellulose-Based Polymeric Bottle-Brush Cocoons. (Submitted)

4.1 Introduction

Bottlebrush polymers composed of a linear backbone and highly densely grafted side chains represent a classic anisotropic polymeric structure that is useful for various applications, including self-assembly for photonic crystals,[34, 259-260] super soft elastomers,[261-262] templates for generating nanowires,[41, 263] and drug delivery.[61, 264-265] Core-shell bottlebrush structures specifically attract more attention because of the different chemical environments in the core and shell which is beneficial for site-selective functionalization as well as for crafting non-spherical nano-objects.[46, 216] The most adopted synthetic strategies for making core-shell bottlebrush polymers is either via "grafting-though" norbornane-functionalized linear block copolymers,[266-267] or via "grafting from" linear polyacrylate backbones,[47, 74, 268] both of which having flexible carbon backbones. Alternatively, cellulose, a biodegradable natural polymer has been explored to be capitalized on as the backbone for the growth of bottlebrush polymers with much higher grafting density.[269-271] Precise size control of the bottlebrushs can be achieved by size selection of cellulose backbone and controlled living polymerization of side chain

monomers.[216] Clearly, cellulose-based bottlebrush polymers possess a significant advantage for more advanced applications[271].

Recently, there is enormous research to apply cylindrical bottlebrush polymers as nanocarriers for drug encapsulation and delivery because the cylindrical structure is advantageous for molecular retention and uptake as well as targeting of specific cells or tissues.[272-273] However, most of the nanocarrier function is achieved by covalently attaching the effective drug moieties onto the polymer chains and triggering the breakage through external stimuli,[274-278] which limits the drug loading level. Some encapsulation properties have been demonstrated with both unimolecular bottlebrush core-shell polymers,[279-280] and self-assembly of Janus-type bottlebrush polymers into large micellar nanocarriers.[281-283] Nevertheless, few of them worked with crosslinking of the surface polymer, which will undoubtedly increase drug loading and modulate release profile. Polymeric cocoons derived from crosslinked bottlebrush polymers are of great advantages to serve as unimolecular drug carriers. Up to now, there are several polymeric cocoons that have been prepared through post-polymerization crosslinking of the outer block of bottlebrush polymers with additional crosslinker. [47, 100, 284] However, none of them has demonstrated the encapsulation properties of the cocoons and both strategies impose limitations on the encapsulation objects which should not interact with external crosslinker. At the same time, it is hard to remove crosslinker itself which is usually bio-toxic.

Herein, we report a robust strategy for the synthesis of cellulose-based unimolecular core-shell bottlebrush block copolymers with a photo-crosslinkable outer block which can be readily converted to polymeric cocoons. The cellulose-based bottlebrush copolymers were synthesized by “grafting from” strategy on functionalized cellulose single-chain

backbone via sequential living radical polymerization of *tert*-butyl acrylate (*t*BA) and hydroxyethyl methacrylate (HEMA). The outer poly(hydroxyethyl methacrylate) (PHEMA) block was further functionalized with azide groups to provide crosslinking capability. UV triggered azide-azide coupling (nitrene coupling) reaction has been widely used as a robust, efficient strategy for crafting crosslinkable shell of core-shell polymer structures. Effective encapsulation of molecules within the inner compartment of core-shell polymer can be readily achieved by UV irritation after loading, which is applicable to both organic molecular and inorganic compound. The potential use of this versatile cellulose-derived polymeric cocoons as nanocarriers for drug delivery was elaborated by loading with fluorescent dyes, where the release behavior can be tracked by fluorescence spectroscopy. It is expected that the photo-crosslinking of the outer polymer block leads to enhanced dye encapsulation as well as modulated release rate.

Meanwhile, bottlebrush polymers have also been exploited as nanoreactors for nanorods and nanowires synthesis. Notably, conventional bottlebrush polymer bearing soft backbones are usually worm-like structures, ending up with nanowires of poorly confined shape.[41, 263] On the other hand, bottlebrush polymers with cellulose backbone have been successfully used for synthesis of monodisperse nanorods of various compositions because cellulose can provide much high grafting density, creating a bottlebrush polymer with rigid rod conformation.[216] There are three hydroxy groups in one repeating unit of cellulose which can be brominated in ionic liquid, leading to high population of radical initiation sites. After sequential ATRP polymerization of *t*BA and styrene (St), a core-shell bottlebrush block copolymer with rigid conformation was formed, which was then exploited as nanoreactor to synthesis inorganic nanorod. The longitudinal and lateral

dimension of the nanorod can be precisely tuned by controlling the molecular weight of cellulose as well as the grafted P*t*BA block. Similarly, by substituting polystyrene with poly(ethylene oxide), water soluble nanorod was created. More complex structures such as core-shell nanorod and nanotube were also synthesized by designing bottlebrush triblock copolymers.

The same methodology can be applied to the bottlebrush P*t*BA-*b*-PHEMA presented here. The inner P*t*BA can be readily hydrolyzed into PAA, which was able to form strong coordination interaction with metal precursors, enabling the selective loading of metal precursors such as CsBr, $PbBr_2$ into the inner compartment of the core-shell bottlebrush polymers. Perovskite $CsPbBr_3$ nanorods can be instantly formed after coprecipitation into toluene with outer polymer block permanently capped on the surface providing exceptional water, UV, and thermal stabilities. More importantly, the dimensions of the nanorods can be easily controlled through modulation of the molecular weight of cellulose and grafted polymer blocks. It is also worth mentioning that crosslinked cocoons as nanoreactors would provide even higher stability than the original bottlebrush polymer due to their higher polymer shell density which further depress molecular diffusion and structural decomposition. In general, these cellulosed-based polymeric cocoons possess great potential as (1) nanocarriers for drug delivery, and (2) nanoreactors for crafting inorganic nanorods.

4.2 Experimental Section

4.2.1 Materials

2-Bromoisobutyryl bromide (98%), 4-bromomethylbenzoyl bromide (BMBB, 96%), cellulose (microcrystalline, 342 g/mol), cesium bromide (CsBr, 99.9%), lead bromide ($PbBr_2$, 98%), anhydrous N,N-dimethylformamide (DMF, 99.9%), methyl ethyl ketone (MEK, 99.9%), anhydrous 1-methyl-2-pyrrolidinone (NMP, 99.5%), N,N,N′,N″,N″-pentamethyldiethylenetriamine (PMDETA, 99%), *n*-Propanol (*n*PA, 99%), sodium azide (NaN_3, 99%), trifluoroacetic acid (TFA, 99.9%). CuBr (98%) was stirred in acetic acid for 24 h, washed with ethanol and diethyl ether, and dried in a vacuum oven at room temperature. *tert*-Butyl acrylate (*t*BA, 98%) was distilled over CaH_2 under reduced pressure prior to use. 2-Hydroxyethyl methacrylate (HEMA, 97%) was passed through basic alumina prior to use.

4.2.2 Characterizations

The molecular weights of polymers were measured by gel permeation chromatography (GPC, shimazu) equipped with an LC20AD HPLC pump and a refractive index detector (RID-10A, 120 V). THF was used as the eluent with a flow rate of 1.0 mL/min and operation temperature of 35 °C. One Phenogel 5 μm linear column and one Phenogel 5 μm 10E4A mixed bed column were calibrated with polystyrene standards. Proton nuclear magnetic resonance (^{1}H NMR) spectra of organic samples were recorded on Varian VXR-300 spectroscope. Functionalization and crosslinking of polymers were tracked by Fourier Transform Infrared Spectrometer (FTIR, Shimadzu Prestige 21). The crystalline structures of $CsPbBr_3$ NRs were measured by powder X-ray diffraction (XRD, X'pert PRO, Netherlands). The size distribution and morphology of polymeric cocoons and $CsPbBr_3$ NRs were measured by transmission electron microscope (TEM, JEOL 100 CX-II; operated at 100 kV). Crystal lattice of $CsPbBr_3$ NRs were measured by high-res

transmission electron microscope (HRTEM, FEI Tecnai F30; operated at 300 kV). TEM samples were prepared by dropping a diluted solution containing cocoons and $CsPbBr_3$ NRs onto a carbon-coated copper TEM grid (300 mesh) and dried at room temperature. Cocoons were stained uranium tetroxide vapor for 30 min prior to the TEM imaging. The morphology of cocoons was also measured by atom force microscopy (AFM, XE-100, Park Systems). AFM samples were prepared by spin-coating dilute DMF solution onto Si substrate. The photoluminescence spectra of fluorescein solution and $CsPbPr_3$ solution were measured by spectrofluorophotometer (Shimadzu UV-2450 spectrometer and Shimadzu fluorescent RF-5301 PC spectrofluorophotometer). UV absorption of $CsPbBr_3$ were characterized by UV-vis.

4.2.3 Synthesis procedures

Synthesis of Brominated Cellulose (Cellulose-Br) as Macroinitiator. First, 1-allyl-3-methylimidazolium chloride (AMIMCl) as ionic liquid were prepared by published method[285]. Cellulose powder (2 g) was dried by azeotropic distillation with 40 ml toluene and fully dissolved with previously prepared ionic liquid (40 ml) at 60ºC overnight in a round-bottom flask. Anhydrous DMF (10 ml) and anhydrous NMP (20 ml) were then added to the solution and stirred at 60ºC under solution became homogeneous. After cooling down to room temperature, 2-bromoisobutyryl bromide (9 ml) was added dropwise to the solution and stirred for 24 h. The resulting brownish solution was precipitated in DI water (500 ml). The final product was purified by dissolution-precipitation with acetone and DI water for more than 5 times to yield brominated cellulose (cellulose-Br) as a white powder. Bromination efficiency was calculated from ^1H NMR. Second bromination is sometimes needed to reach 100% bromination efficiency. In second bromination, all

product from the first bromination was dissolved in anhydrous NMP (50 ml) and cooled in ice bath. 2-bromoisobutyryl bromide (9 ml) was added dropwise to the solution and stirred for 24 h. The purification of product followed the same procedure as first bromination.

Preparation of Cellulose-Br of Different Molecular Weight with Low PDI by Fractional Precipitation. Cellulose-Br (10 g) was dissolved in acetone (200 ml). Certain amount of DI water was added gradually into the solution until it became turbid. The solution was settled overnight, and bottom precipitate was collected as one fraction. More water was added to the top transparent solution to precipitate the second fraction and so forth. The fractions collected were from higher molecular weight to lower with low dispersity (PDI).

Synthesis of Cellulose Grafted Bottlebrush P*t*BA (Cellulose-*g*-P*t*BA). One fraction of the cellulose-Br of certain molecular weight was used as the macroinitiator for ATRP polymerization of *t*BA with three -Br initiation site in one backbone repeat unit. In a typical reaction, cellulose-Br (50 mg), CuBr (35.0 mg), PMDETA (85.0 mg), *t*BA (21 mL), and MEK (21 mL), (molar ratio: initiator/Cu/ligand/monomer = 1/1/2/800), were mixed in a pressure vessel, degassed by three freeze-pump-thaw cycles, and charged with argon. The vessel was sealed and immerged into oil bath at 60 ºC for a desired period. Then the reaction was quenched by dipping the vessel into liquid N_2, diluted with acetone, and passed through a column of neutral alumina to remove the catalyst. After removing the solvent, the product was precipitated with methanol/water (v/v = 1/1) as the precipitator to yield a white powder.

Synthesis of Cellulose Grafted Bottlebrush P*t*BA-block-PHEMA (Cellulose-*g*-(P*t*BA-*b*-PHEMA)). Cellulose-P*t*BA was used as the macroinitiator for ATRP polymerization of HEMA. In a typical reaction, cellulose-P*t*BA (100 mg), CuBr (10.0 mg), PMDETA (20.0 mg), HEMA (1 mL), MEK (7 ml), and *n*PA (3 mL), were mixed in a pressure vessel, degassed by three freeze-pump-thaw cycles, and charged with argon. The vessel was sealed and stirred at room temperature for a desired period. Then the reaction was quenched by dipping the vessel into liquid N_2, diluted with acetone, and passed through a column of neutral alumina to remove the catalyst. After removing the solvent, the product was precipitated with water as the precipitator to yield a white powder. All procedures were conducted in dark.

Synthesis of Azide-functionalized into Cellulose-*g*-(P*t*BA-*b*-(PHEMA-N_3)). Azide functionality was incorporated in to cellulose-*g*-(P*t*BA-*b*-PHEMA) through a two-step reaction of the -OH group on PHEMA: bromination and azidation. During bromination, cellulose-*g*-(P*t*BA-*b*-PHEMA) (0.2 g) was dissolved in anhydrous NMP (10 ml). Then BMBB (1 ml) was added dropwise into the solution in ice bath and stirred for 1 h. The reaction was continued under room temperature for 48 h and precipitated in water to yield a yellowish solid as cellulose-*g*-(P*t*BA-*b*-(PHEMA-Br)). In the second azidation step, the product from bromination was dissolved in anhydrous DMF (10 ml). NaN_3 (200 mg) was gradually added to the solution which was then vigorously stirred under ambient condition for 48h. The residue was precipitated in water and purified by dissolution-precipitation with THF/water 2 times. The product cellulose-*g*-(P*t*BA-*b*-(PHEMA-N_3)) was a white solid and stored away from light.

Encapsulation of Fluorescein in Cellulose-based Cocoons. Cellulose-*g*-(P*t*BA-*b*-(PHEMA-N_3)) (10 mg) and fluorescein (30 mg) was dissolved in $CHCl_3$ (10 ml) and stirred for 12 h. The solution was subjected to UV light (265 nm) in a dark container for 12 h to fully activate azide groups to form azo crosslinkers. The product was then precipitated and washed with methanol. Fluorescein was released by re-dissolving the product in $CHCl_3$. (Methanol is poor solvent and $CHCl_3$ is good solvent for dye encapsulated cocoons, see **Figure S7**)

Synthesis of Cellulose-*g*-(PAA-*b*-(PHEMA-N_3)) by Hydrolysis. P*t*BA block in the cellulose-*g*-(P*t*BA-*b*-(PHEMA-N_3)) was hydrolyzed into PAA block to yield amphiphilic cellulose-*g*-(PAA-*b*-(PHEMA-N_3)) bottlebrush copolymers. Typically, cellulose-*g*-(P*t*BA-*b*-(PHEMA-N_3)) (0.2 g) was dissolved in $CHCl_3$ (20 mL), followed by the addition of TFA (1 mL). After vigorous stirring at room temperature for 24 h, the reaction mixture was dried, re-dissolved in DMF, and gradually precipitated in MeOH. The final product was washed with Hexanes and dried under vacuum to yield a white solid.

Synthesis of Azide-functionalized PHEMA (PHEMA-N_3) capped $CsPbBr_3$ Nanorods. $CsPbBr_3$ nanorods were synthesized by capitalizing on cellulose-*g*-(P*t*BA-*b*-(PHEMA-N_3)) polymers as nanoreactors. The strong coordination between the carboxyl groups and metal leads to selective absorption of metal precursors (CsBr, $PbBr_2$) onto the PAA core. CsBr and $PbBr_2$ was coprecipitated in Toluene to form $CsPbBr_3$ within the core with PHEMA-N_3 permanently capped on the outside. In a typical reaction, CsBr and $PbBr_2$ (molar ratio 1.2:1) was dissolved in DMF with $PbBr_2$ at 0.01mol/L. Cellulose-*g*-(PAA-*b*-(PHEMA-N_3)) solution in DMF was prepared at 5 mg/ml. Precursor and polymer solution were mixed at 1:1 volume ratio to make stock solution and stirred overnight. Drops of stock

solution were added to 5-10 ml toluene under constant stirring yielding transparent fluorescent light-yellow solution. (Absorption max: 510 nm, PL max: 518 nm)

Surface crosslinking of $CsPbBr_3$ Nanorods. $CsPbBr_3$ nanorods solution or drop casted $CsPbBr_3$ nanorods film was subjected to UV irritation (265 nm) for 12 h before testing.

4.2.4 Stability test

Water stability test. For colloidal solution stability test, 5 ml $CsPbBr_3$ toluene solution was mixed with 5 ml H_2O and stirred under 1400 rpm. For film stability test, a film of $CsPbBr_3$ nanorods prepared by drop casting on a glass substrate were immersed into water directly.

UV stability test. 5 ml $CsPbBr_3$ toluene solution was irradiated 365 nm UV light under stirring in a dark container.

Thermal stability test. 5 ml $CsPbBr_3$ toluene solution was heated on a hot plate at 80ºC under stirring in a dark container.

4.3 Results and Discussion

The polymeric cocoons were capitalized from cellulosed-based bottlebrush block copolymers with crosslinkable outer shell, depicted in **Figure 4.1a**. The bottlebrush polymers were synthesized by sequential atom transfer radical polymerization (ATRP) of *t*BA and HEMA from brominated cellulose, which provides sufficient -Br groups to serve as the macroinitiator. After two step functionalization of PHEMA outer block, the -OH

groups were transferred into azide groups which are subjected to nitrene homocoupling under UV irradiation. The relative robust synthetic pathways make it a promising strategy for synthesis of a variety of cellulosed-based bottlebrush polymers with tailored composition and functionalities.

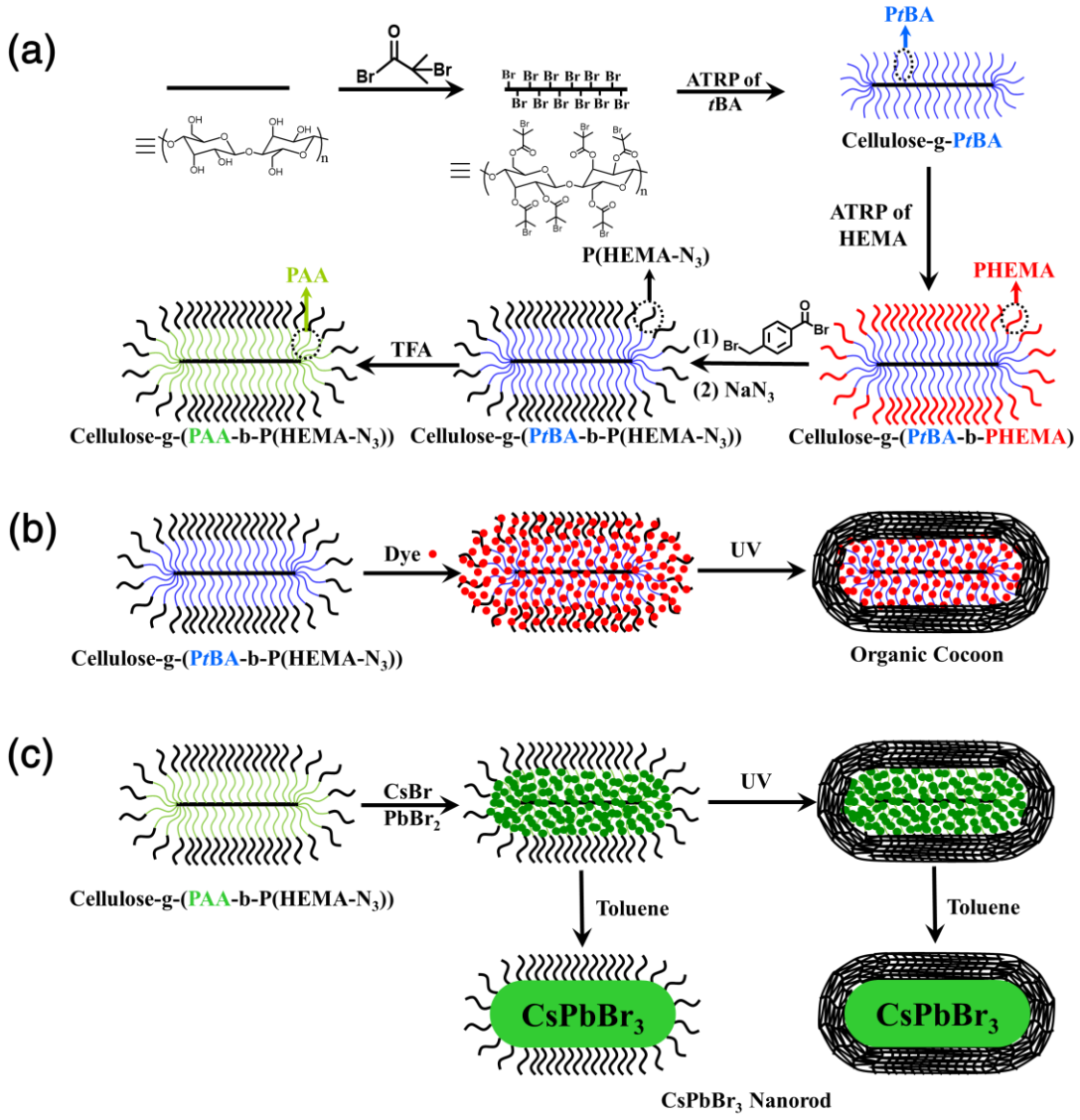

Figure 4.1. Synthetic strategy of (a) cellulosed-based bottlebrush polymers towards both (b) organic cocoons and (c) inorganic $CsPbBr_3$ nanorods.

4.3.1 Cellulose-based bottlebrush block copolymer

Cellulose was chosen as the backbone due to its high population of functional groups. Unlike worm-like traditional bottlebrush polymers where the backbone is typically synthetic flexible polymer chain, cellulose-based bottlebrush polymers morphologies are straight rod because cellulose can provide much higher grafting density creating a bottlebrush polymer with rigid rod conformation,[271] which is beneficial when it was capitalized on as nanoreactor for inorganic nanorods synthesis.

Cellulose was brominated in ionic liquid via previously established method[216]. The bromination efficiency was calculated to be 90% from ^{1}H NMR characterization (**Figure 4.2a**). The crude cellulose-Br macroinitiator has large size distribution because it came from natural resource. In order to grow bottlebrush polymers of finite length and width. Size selection of cellulose-Br was first conducted through manual fractional precipitation. The resulting fractions were of low dispersity (PDI) with their molecular weight shown in **Table 4.1**. The corresponding GPC traces were also shown in **Figure 4.2b**. In order to get monodisperse bottlebrush polymers, batch 4 with a PDI below 1.2, were selected as the backbone to prepare bottlebrush block copolymers corresponding to a theoretical length of 150 nm.

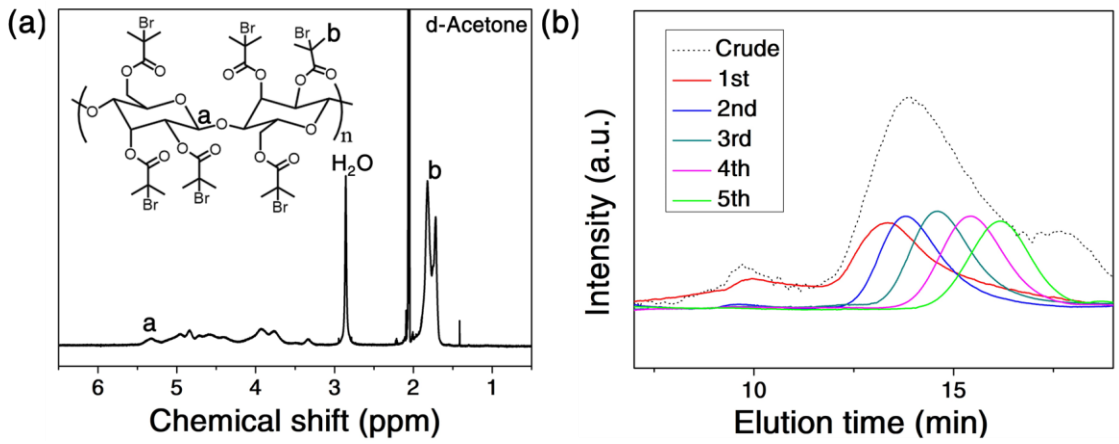

Figure 4.2. (a) ^{1}H NMR of brominated cellulose. (b) GPC traces of crude cellulose-Br and each fraction after fractional precipitation.

Table 4.1. Molecular weight data of each fraction of cellulose-Br after fractional precipitation.

Batch	*M_n**	*PDI**	*Yield*
2nd	85K	1.36	1.63g
3rd	58K	1.22	0.77g
4th	38K	1.19	0.48g
5th	27K	1.17	0.26g

*. Molecular weight and PDI of cellulose bromide were acquired from THF GPC calibrated by polystyrene standards.

ATRP, a living radical polymerization technique, was used for sequential polymerization of *t*BA and HEMA to generate bottlebrush polymers with low dispersity. The reaction time was precisely controlled to reach desired molecular weight of each block. The two-step polymerization was monitored by ^{1}H NMR which showed the successful synthesis of P*t*BA and PHEMA in **Figure 4.3a**. Molecular weight evolution was evidenced by GPC results after each step of polymerization with narrow distribution (**Figure 4.3d**). The molecular weight of P*t*BA block was calculated from GPC based on pre-established

calibration curve of bottlebrush PS with same backbone to be around 15K, corresponding to a theoretical length of 14 nm. Therefore, the diameter of the inner PAA domain is estimated to be 28 nm. The molecular weight of PHEMA is calculated then from ^{1}H NMR to be 14K corresponding to a length of 6 nm. In order to introduce crosslink functionality into the outer PHEMA shell, the abundant hydroxyl (-OH) groups on PHEMA were modified by a two-step reaction. First, bromide end groups (-Br) were introduced via esterification reaction, verified by ^{1}H NMR (**Figure 4.3b**). Next, the bromide end groups were converted into azide (-N_3) under nucleophilic substitution verified by ^{1}H NMR (**Figure 4.3c**) and FTIR (**Figure 4.3e**, red line). The complete shift of resonance peak at 4.5 ppm to 4.1 ppm in ^{1}H NMR suggests 100% conversion of Br to N_3. Azide groups have distinct absorption peak around 2100 cm^{-1} which appeared after azide substitutions. To demonstrate the homocoupling behavior of azide groups, prolong UV irradiation (265 nm) were conducted to the bottlebrush polymers in DMF solution. According to the FTIR result in **Figure 4.3e** blue line, the azide peaks at 2100 cm^{-1} completed disappeared after UV irradiation which suggested the outer functionalized PHEMA polymer shell was fully crosslinked to form cocoon structure. The detailed azide homocoupling (nitrene homocoupling) mechanism has been demonstrated in previous publications[286-288].

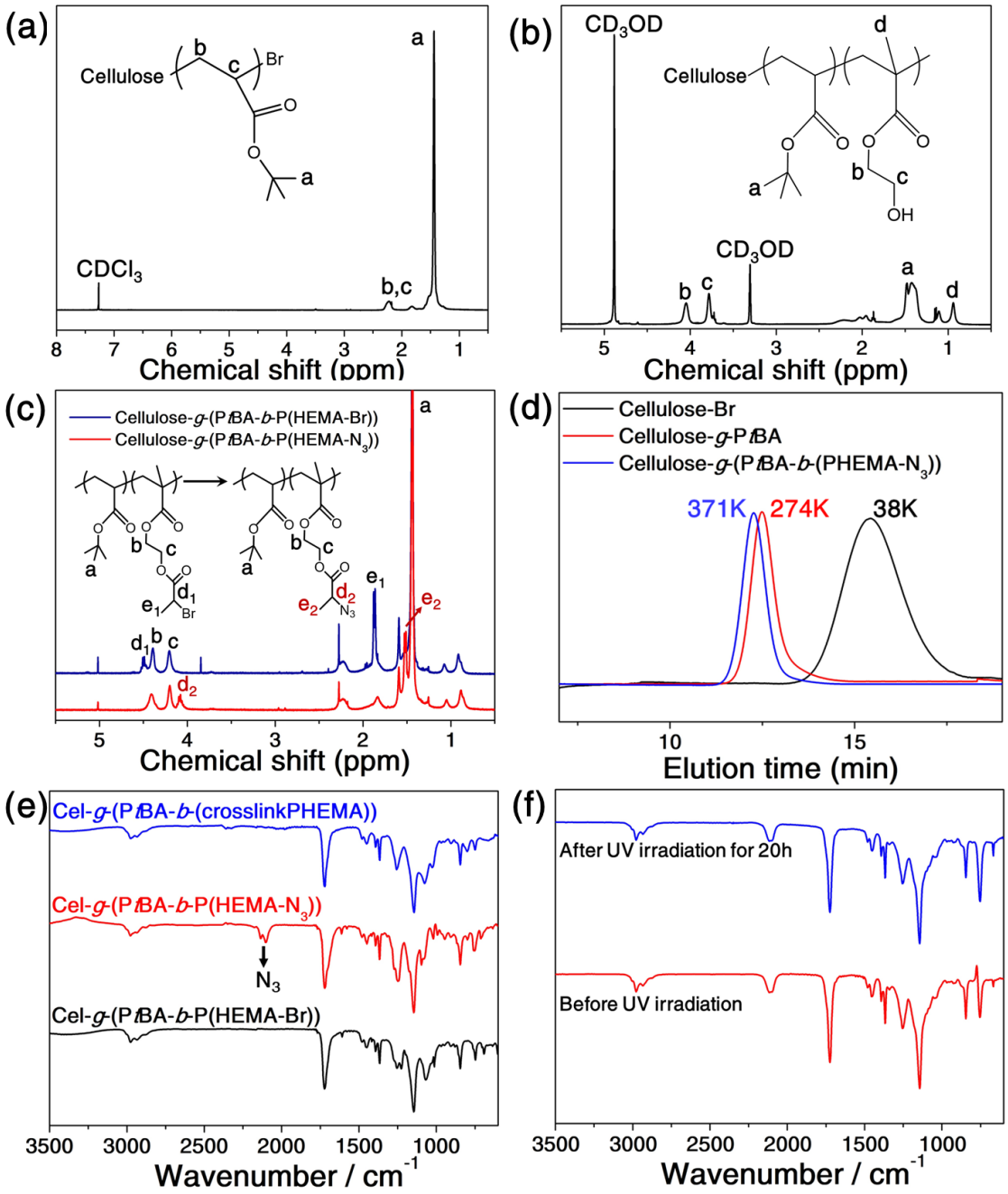

Figure 4.3. (a) ^{1}H NMR of cellulose-*g*-P*t*BA. (b) ^{1}H NMR of cellulose-*g*-(P*t*BA-*b*-P(HEMA-Br)). (c) ^{1}H NMR of cellulose-*g*-(P*t*BA-*b*-P(HEMA-N$_3$)). (d) GPC curves of cellulose-based bottlebrush polymers of two different length. (e) FT-IR spectra of cellulose-based bottlebrush polymers after each step of post-polymerization functionalization (from bottom to top: bromination, azidation, UV-crosslink) (f) FI-TR spectra of cellulose-*g*-(P*t*BA-*b*-P(HEMA2-N$_3$)) synthesized using 2-bromopropionyl bromide as the bromination agent before (red) and after (blue) 20h of UV irradiation (265 nm).

It is worth mentioning though that the azide has to be attached to methylbenzoyl groups to exhibit UV coupling activities. A different esterification agent, 2-bromopropionyl bromide, was also used for esterification of PHEMA followed by successful azidation. However, no weakening of azide peak was observed after extensive UV irradiation according to **Figure 4.3f**. It is probably because the benzene group provides lower activation energy for azide to be converted into active nitrene intermediate where homocoupling can happen under low intensity UV irradiation, while the one without benzene group requires UV source of much higher intensity.

4.3.2 Polymeric cocoons for controlled delivery

Bottlebrush polymers are a good candidate for drug encapsulation and delivery due to their densely grafting outer polymer chains which provide good shielding properties for their interior. Furthermore, crosslinking of the outer shell will create a much stronger barrier against molecular diffusion for enhancement of encapsulation and release properties. In this work, fluorescein, a commonly used fluorescent dye, was exploited as a model guest compound to track the release profile for the cellulose-based polymeric cocoons. The ease of UV crosslinking provides a robust and feasible way for encapsulation of dyes without possible contaminations from external crosslinking agent. The bottlebrush polymers cellulose-*g*-(P*t*BA-*b*-P(HEMA-N_3)) without crosslink were first loaded with fluorescein in $CHCl_3$, then subjected to prolonged UV irradiation (265 nm) to fully photo-crosslink the azide containing shell which seals fluorescein inside the P*t*BA domain (**Figure 4.1b**). After precipitating and sequential washing with excess ethanol to remove unencapsulated free dyes outside the cocoons, the precipitate was redissolved in $CHCl_3$. The release profile was characterized by changes in photoluminescence of the solution shown in **Figure 4.4a**. The

characteristic emission peak of fluorescein is 466 nm (exited at 430 nm). When trapped inside the cocoons, the fluorescence of dye is self-quenched due to π-π interaction between adjacent dyes under high local concentration. Upon release into solution, free dyes would exhibit much stronger fluorescence. A gradual increase of PL intensity can be seen with increasing release time, which indicates a gradual release of dyes from the cocoons into solution. To demonstrate the advantage of crosslinked shell, the release profile of uncrosslinked cocoons (without UV irradiation) was also tested as shown in **Figure 4.4b**. A continuous release of dyes can still be seen up to 6h, indicating the densely grafted PHEMA shell can still act as a barrier for dye encapsulation even without crosslink. By comparing the complete release profile of both crosslinked and uncrosslinked cocoons in **Figure 4.4c**, it can be found that the total release time of dye increased from 6h to 18h after the polymer shell was fully crosslinked. The final PL intensity after complete release increased from 350 to 1050. It is evident that both the encapsulation quantity and release duration was increased to 3 folds with crosslinked shell manifesting the superb performance of shell crosslinking in encapsulation and delivery. On the other hand, the release profile of dye for crosslinked cocoons is at a steady rate while there is a rapid release of dye in the first several minutes for uncrosslinked cocoons. The time of half-release is 15 min for uncrosslinked cocoons and 4.5 h for crosslinked cocoons, a notably 17 times increase. It is proposed that without crosslink, most of dyes trapped inside the cocoon would immediately diffuse out when it was dissolved in $CHCl_3$ while the remaining dyes far inside the core as well as those absorbed on the polymer chains began to slowly diffuse through the polymer shell. The initial release is primarily driven by concentration gradient of dyes inside the polymer and in solution. Therefore, the release profile of uncrosslinked

cocoons follows the typical concentration-driven diffusion dynamics. However, when the surface of the cocoons was completely crosslinked leading to an effective shielding of interior of cocoons, a high energy barrier for diffusion of dyes through the shell is created so that diffusion at the crosslinked surface became the rate limiting step leading to a semi-steady diffusion state (**Figure 4.4d**). Nevertheless, the diffusion is still driven by concentration gradient which will decrease during release resulting in a slow drop of release rate. Since both dye loading time and concentration are identical for crosslinked and uncrosslinked cocoons, the large difference in encapsulation quantity is suspected to come from washing of the cocoons with methanol where the uncrosslinked cocoons can be subjected to huge loss of dyes.

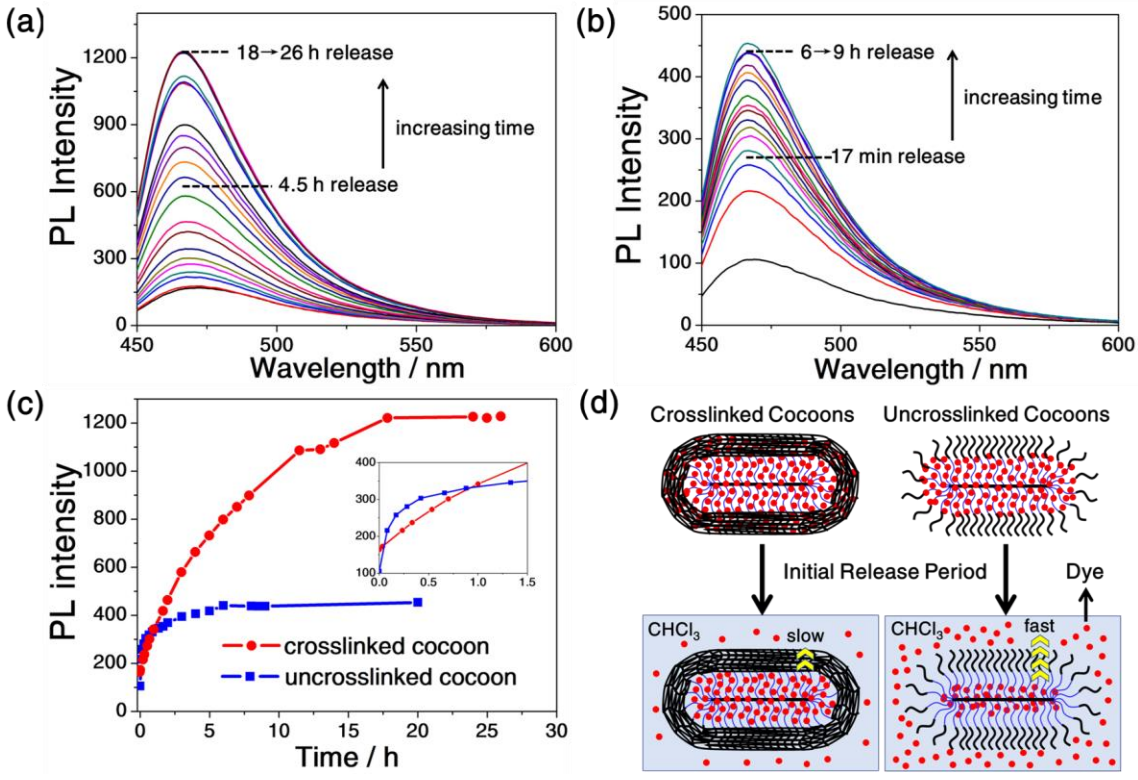

Figure 4.4. Encapsulation and release of dyes. (a) Fluorescence spectra of crosslinked cocoons loaded with fluorescein. Curve went from bottom to up with increasing time

with 4.5 h as the mid-release point. (b) Fluorescence spectra of uncrosslinked cocoons loaded with fluorescein. Curve went from bottom to up with increasing time with 15 h as the mid-release point. (c) Dye release profiles of crosslinked cocoons (red dots) and uncrosslinked cocoons (blue squares). Data collected at maximum emission intensity (466 nm) at each time. (d) Diffusion characteristics of dyes in crosslinked and uncrosslinked cocoons dissolved in $CHCl_3$. Red dots represent dyes (fluorescein).

4.3.3 Perovskite nanorods from cocoon nanoreactors

As mentioned earlier, bottlebrush polymers can be capitalized as nanoreactors for control growth of inorganic nanocrystals. Compared with cylindrical micelle structures formed by self-assembly of linear block copolymers which require specific condition to maintain the micellar structure, unimolecular cylindrical bottlebrush polymers with similar architecture are more robust and stable. They can tolerate the typical harsh synthesis condition of inorganic nanomaterials such as high temperature. The solvent composition may also change during reaction leading to the dis-assembly of self-assembly micelles. Additionally, cellulose backbone affords a rigid bottlebrush structure making it a good candidate for nanorod synthesis. This work is mainly focused the synthesis and stabilities investigation of perovskite nanorods, specifically $CsPbBr_3$ nanorod, because perovskite nanomaterials have become the rising star in optoelectronic application due to its high photoluminescence quantum yield. Up to now, there are limited reports on the controlled synthesis of $CsPbBr_3$ nanorod.[289-292] At the same time, instability has always been an issue for $CsPbBr_3$ NCs because of its high sensitivity to moisture, UV and heat. All precious reported $CsPbBr_3$ NRs were synthesis with oleic acid and oleylamine as the ligand which is highly unstable and easy to dissociate from the surface. It has also been demonstrated that surface polymer coating can improve the stability of perovskite NCs.[293] Therefore, the nanoreactor strategy is presented as the perfect synthetic approach for making $CsPbBr_3$

nanorods with enhanced stability. In this work, the $CsPbBr_3$ nanorods were in-situ grown inside the cocoon nanoreactors with outer polymer shell permanently attached on the surface serving as a protecting layer against crystal decomposition. Furthermore, even higher crystal stability is expected after the polymer shell is crosslinked to afford better barrier properties. In order for the bottlebrush cellulose-*g*-(P*t*BA-*b*-P(HEMA-N_3)) to be used as the nanoreactors, the inner P*t*BA block, which is inactive to precursor interaction, was first hydrolyzed by TFA into polyacrylic acid (PAA) bearing functional -COOH groups. The hydrolysis process was characterized by FTIR, clearly showing the emergence of -COOH absorption at 1700 nm^{-1} after hydrolysis (**Figure 4.5**).

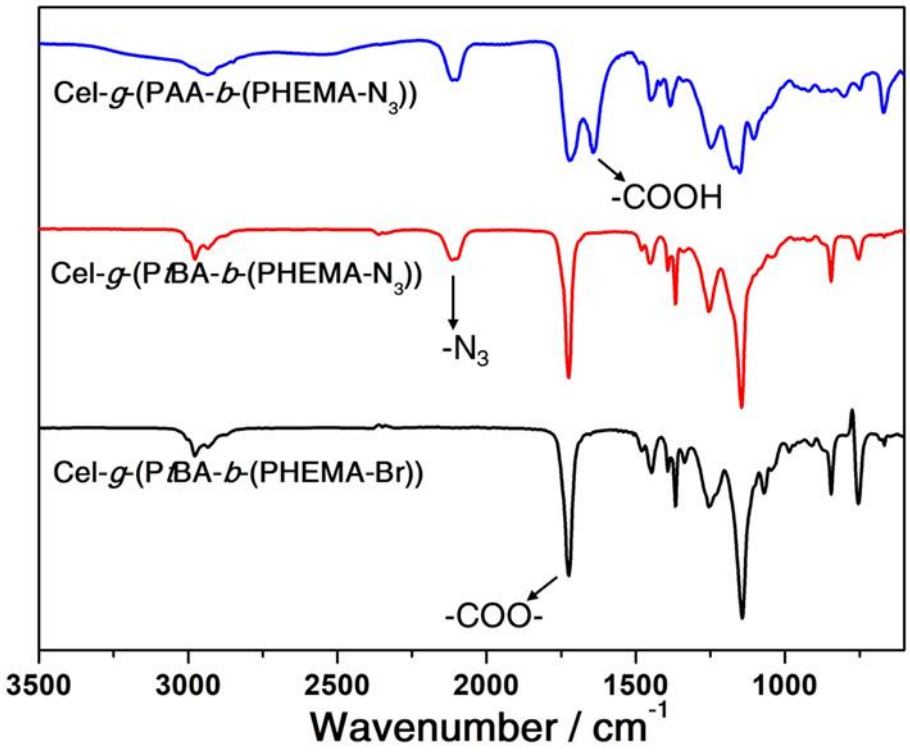

Figure 4.5. FITR spectra of cellulose-*g*-(P*t*BA-*b*-P(HEMA-Br)) (black), cellulose-*g*-(P*t*BA-*b*-P(HEMA-N_3)) (red), cellulose-*g*-(PAA-*b*-P(HEMA- N_3)) (blue).

The synthesis of $CsPbBr_3$ NRs was conducted in a two-step process (**Figure 4.1a**). First CsBr and $PbBr_2$ precursors were selectively loaded into the inner PAA domain of the bottlebrush cocoons based on strong coordination between metal precursors and the -COOH moieties situated on the PAA chains. The relatively low solubility of the precursors in DMF solvent also minimize the residue precursors outside the nanoreactors confining the formation of NCs only in the cocoons. The second step is the coprecipitation of CsBr and $PbBr_2$ in toluene (a poor solvent for both precursors) to form $CsPbBr_3$ nanorods. The precursor-polymer interaction is depicted in **Figure 4.6**.

$$\text{CsBr} + \text{-COOH (from PAA block)} \rightarrow \text{CsBr(COO)}$$
$$\text{PbBr}_2 + \text{-COOH (from PAA block)} \rightarrow \text{PbBr}_2\text{(COO)}$$
$$\text{CsBr(COO)} + \text{PbBr}_2\text{(COO)} \rightarrow \text{CsPbBr}_3\text{(COO)}_x$$

Figure 4.6. Chemical reaction mechanism for synthesis of $CsPbBr_3$ nanorods.

The functionalized PHEMA chains on the surface of the nanorods keep the them well-dispersed in toluene exhibiting strong photoluminescence. According **Figure 4.7a**, the UV-vis spectrum (red line) and the PL spectrum (green line) demonstrated a characteristic absorption peak at 510 nm and emission peak at 518 nm which is in accordance with previously reported $CsPbBr_3$ nanorods[292]. The crystal structure of $CsPbBr_3$ was further verified by X-ray diffraction (XRD) to be the patterns of orthorhombic perovskite phase (**Figure 4.7b**).[294]

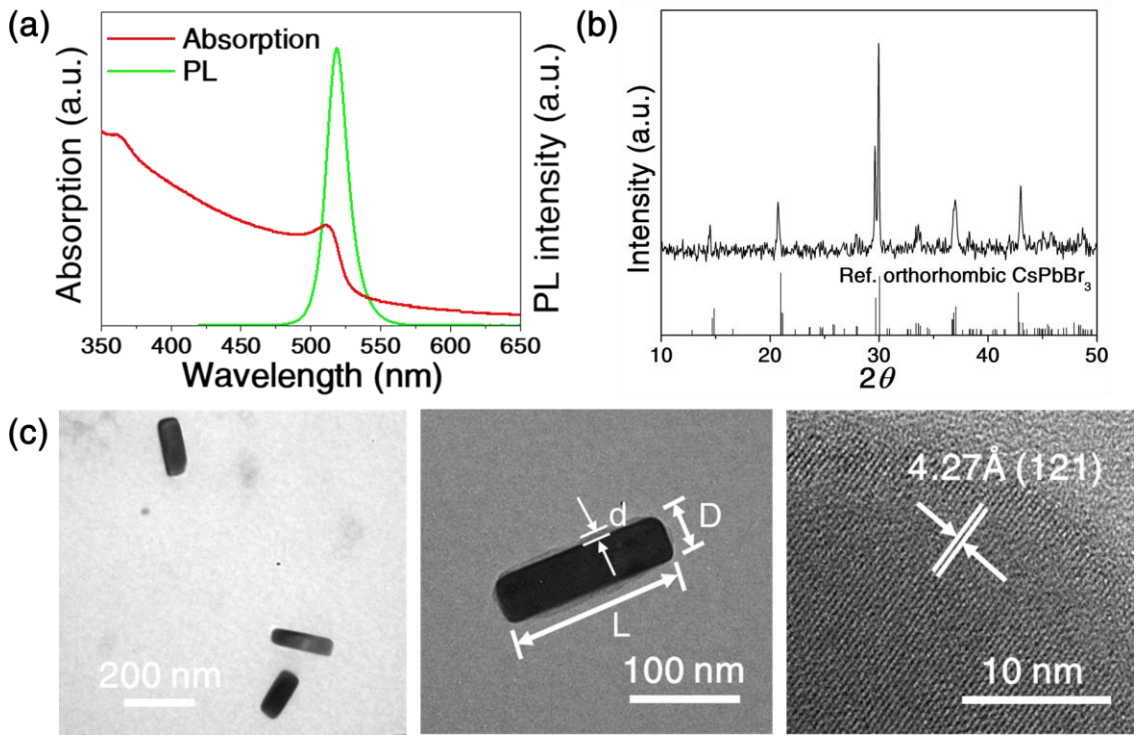

Figure 4.7. (a) Absorption and PL spectra of PHEMA-N_3 capped $CsPbBr_3$ NRs. (b) XRD spectrum of as-synthesized $CsPbBr_3$ nanorods from bottlebrush cocoons. ICSD No. 97851 is provided as the reference orthorhombic $CsPbBr_3$ XRD data. (c) TEM images of $CsPbBr_3$ nanorods.

$CsPbBr_3$ nanorods were synthesized from cocoons with a backbone length of 38K in **Figure 4.3d**. According to the TEM characterizations shown in **Figure 4.7c**, the length of synthesized $CsPbBr_3$ nanorods (L = 150 nm) closely matches with cellulose molecular weight and the diameter (D = 40 nm) matches with the PAA domain size of the cocoons. Additionally, the crosslinked PHEMA shell can also be visualized in TEM. The thickness (d = 6 nm) is the same with the estimated length of PHEMA. The perovskite crystal structure was further confirmed by HRTEM revealing a lattice parameter of 4.27Å corresponding to its (121) plane. The $CsPbBr_3$ nanorods solution possess excellent colloidal stability owing to the permanently tethered PHEMA chains on the surface which prevents the nanorods from aggregation. A unique property of $CsPbBr_3$ NCs is the ability

to tune the emission wavelength by anion exchange. As seen in **Figure 4.8**, after anion exchange with $ZnCl_2$ or ZnI_2, the initial green emitting $CsPbBr_3$ nanorods solution was tuned to emit light across a broad wavelength range, all the way from blue to red. Control experiment was also conducted in the absence of cocoon nanoreactor. When only precursor DMF solution was dropped into toluene, it is immediately quenched showing little fluorescence. Because there is no ligand to cap the NCs, only large particles (>500 nm) formed.

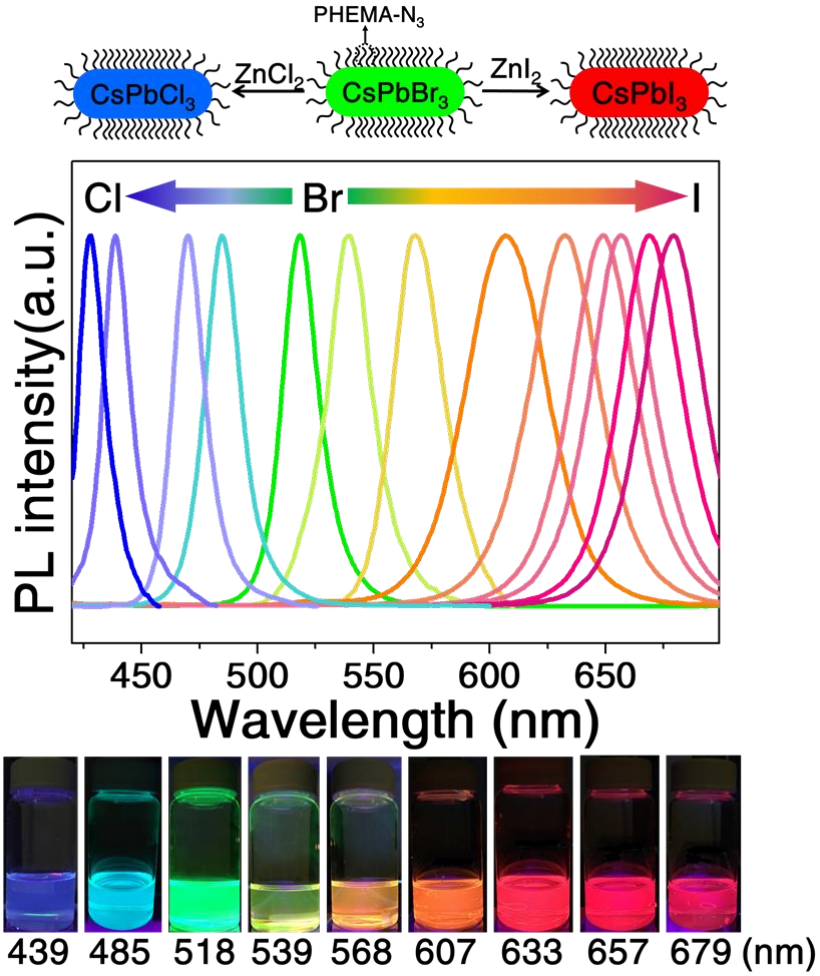

Figure 4.8. Anion exchange of PHEMA-N_3 capped $CsPbBr_3$ NRs.

Surface protection has always been an efficient strategy for improving the stability of perovskite materials. It has been reported that polymer capping on $CsPbBr_3$ quantum dots can effectively increase their moisture and long-term stability by serving as a water repulsion layer[293]. Herein, we kept on demonstrating that crosslinking of the capping polymers can further enhance the barrier properties provided by the surface polymers, leading to excelled water, UV, and thermal stabilities compared with uncrosslinked polymers. To prepared $CsPbBr_3$ nanorods capped with crosslink polymers (PHEMA), the stock solution (nanoreactor solution loaded with metal precursors) was first subjected to prolonger UV irradiation (265 nm) before dropping into toluene (**Figure 4.1c**). $CsPbBr_3$ nanorods formed instantly with crosslinked PHEMA capped on the surface. The water stability was tested by mixing the as-prepared $CsPbBr_3$ solution with equal amount of water under vigorous stirring. The gradual change in photoluminescence (under 365 nm) was tracked by video visualization (**Figure 4.9**).

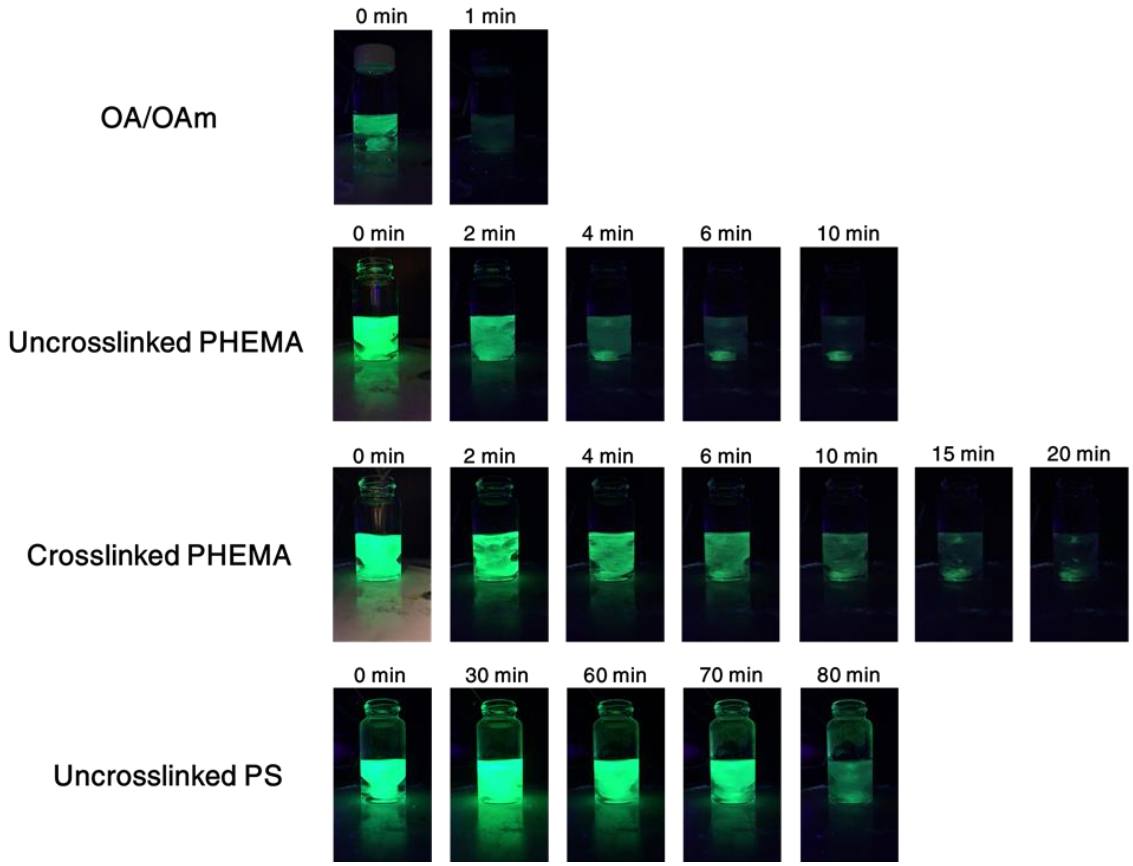

Figure 4.9. Representative photography of $CsPbBr_3$ NRs solution (5 mL) mixed with water (5 mL) under vigorous stirring at different time. $CsPbBr_3$ NRs were synthesized from (a) cellulose-*g*-(P*t*BA-*b*-P(HEMA-N_3)), (b) cellulose-*g*-(P*t*BA-*b*-crosslinkedP(HEMA)), (c) cellulose-*g*-(P*t*BA-*b*-PS), (d) oleic acid/ oleylamine as ligand.

Since the mixture was a two-phase solution and it is hard to extract the pure toluene phase for PL measurement, the relative emission intensity was calculated from the brightness (gray value) of the captured photo images of the solution. As can be seen from **Figure 4.10a**, without crosslink, the PHEMA capped $CsPbBr_3$ nanorods lost 80% photoluminescence after 7 min while the ones after crosslink can last up to 14 min, which demonstrated that crosslinked PHEMA can enhanced the water stability of $CsPbBr_3$ because it created a denser polymer surface. It is noticed that, the PL of conventional $CsPbBr_3$ nanorods synthesized with oleic acid and oleyl amine as the ligand were mostly

quenched after 1.5 min due to poor ligand protection. Conventional ligand is loosely attached onto $CsPbBr_3$ surface which can be easily washed off by water exposing the inner $CsPbBr_3$. We further investigated how surface polymer functionality affects the water stability. PS capped $CsPbBr_3$ NRs were prepared with bottlebrush cellulose-*g*-(PAA-*b*-PS) as the nanoreactors. With hydrophobic PS capping, $CsPbBr_3$ was stabilized until 95 min in water. The much more enhanced water stability of PS capped $CsPbBr_3$ NRs is due to extensive collapsing of the hydrophobic PS shell in water making it an even denser barrier than crosslinked PHEMA, demonstrating the importance of hydrophobicity in water resistance. The protection mechanism for polymer ligation on $CsPbBr_3$ NRs were illustrated in **Figure 4.11**. The UV stability test was also conducted for $CsPbBr_3$ nanorods with different capping by tracking the PL decay of $CsPbBr_3$ NRs solution under constant UV irradiation at 365 nm. As shown in **Figure 4.10b**, the UV stability of $CsPbBr_3$ nanorods were also increased after the surface PHEMA was crosslinked. The photoluminescence of uncrosslinked-PHEMA capped $CsPbBr_3$ nanorod dropped to 10% of its initial intensity after 4.6 h while crosslinked-PHEMA capped $CsPbBr_3$ nanorod extended the time to 9.6 h. It is suspected that the higher polymer density on the surface after crosslinking can effectively block UV light and stabilize perovskite structure. One the other hand, it took 5 h for the PL of PS capped $CsPbBr_3$ nanorod to decrease below 10% which is similar to uncrosslinked-PHEMA. There is no contribution from the UV absorption of PS because the absorption of PS is below 300 nm (i.e. no absorption at the applied 365 nm UV).[295] Additionally, since the absorption peak of PS is too weak to be seen from the UV-vis absorption spectrum of PS-capped $CsPbBr_3$ NRs, the relative influence of the UV adsorption of PS on UV stability of $CsPbBr_3$ NRs can be neglected. Therefore, PS capping

doesn't provide any enhancement in UV stability compared to PHEMA indicating the UV stability of $CsPbBr_3$ is not greatly affected by surface polymer type. Since PL decay of $CsPbBr_3$ NCs is mainly contributed by the formation of non-radioactive traps due to UV induced photo-oxidation of lead atoms,[296] UV intensity is the major factor in determining the PL decay rate under UV in case of PS and PHEMA capped $CsPbBr_3$ NCs. On the other hand, the conventional oleic acid/oleylamine capped $CsPbBr_3$ nanorods have extremely poor UV stability because such surface photo oxidation by UV light will lead to the detachment of small organic ligands resulting in particle aggregation and structure decomposition,[297] which won't happen with permanent polymer-ligated $CsPbBr_3$ NRs. Thermal stabilities were also compared for $CsPbBr_3$ NRs with different capping by constant stirring at 80ºC on a hot plate, as shown in **Figure 4.10c**. Unsurprisingly, $CsPbBr_3$ NRs with permanent polymer capping can maintain their PL at 80ºC for more than 3h, while OA/OAm capped $CsPbBr_3$ NRs completely lost PL after 1h because of detachment of OA/OAm ligand under high temperature leading to the aggregation of perovskite NCs. The gradual decrease of PL in case of PS capped $CsPbBr_3$ NRs is attributed to Ostwald ripening[298] of the crystals since no ligand detachment nor phase change will occur at 80ºC. Intriguingly, both uncrosslinked and crosslinked PHEMA showed excellent thermal stability. It is because azide groups can also undergo coupling reactions under elevated temperature. During heating of the solution, uncrosslinked PHEMA already became fully crosslinked.[299-300] The crosslinked shell is able to encapsulate the inner perovskite crystals preventing molecular diffusion. Therefore, Ostwald ripening cannot occur in the crosslinked polymer capped $CsPbBr_3$ NRs solutions. By comparing the influence of different capping on water and UV stability of $CsPbBr_3$ nanorods in **Figure 4.10d**, we can

conclude that permanent capping is important in maintaining high stability which affords great advantage in the nanoreactor strategy for prepared colloidal stable perovskite nanostructures. Secondly, hydrophobic polymer such as PS is subjected to collapsing when contacted with water greatly enhancing the water stability of perovskite NCs, while providing no additional UV protection because it is fully stretched in colloidal solution same with PHEMA. Finally, crosslinking can improve all water, UV, and thermal stabilities. The higher polymer density induced by crosslinking will serve as a stronger barrier against molecular diffusion. It can be potentially applied to all type of unstable perovskite NCs reaching for additional colloidal stabilities. Based on previous discussions, it is proposed that crosslinked PS capping would be the best choice for all-inclusive water, UV, and thermal stabilities, which will be the focus of our future research.

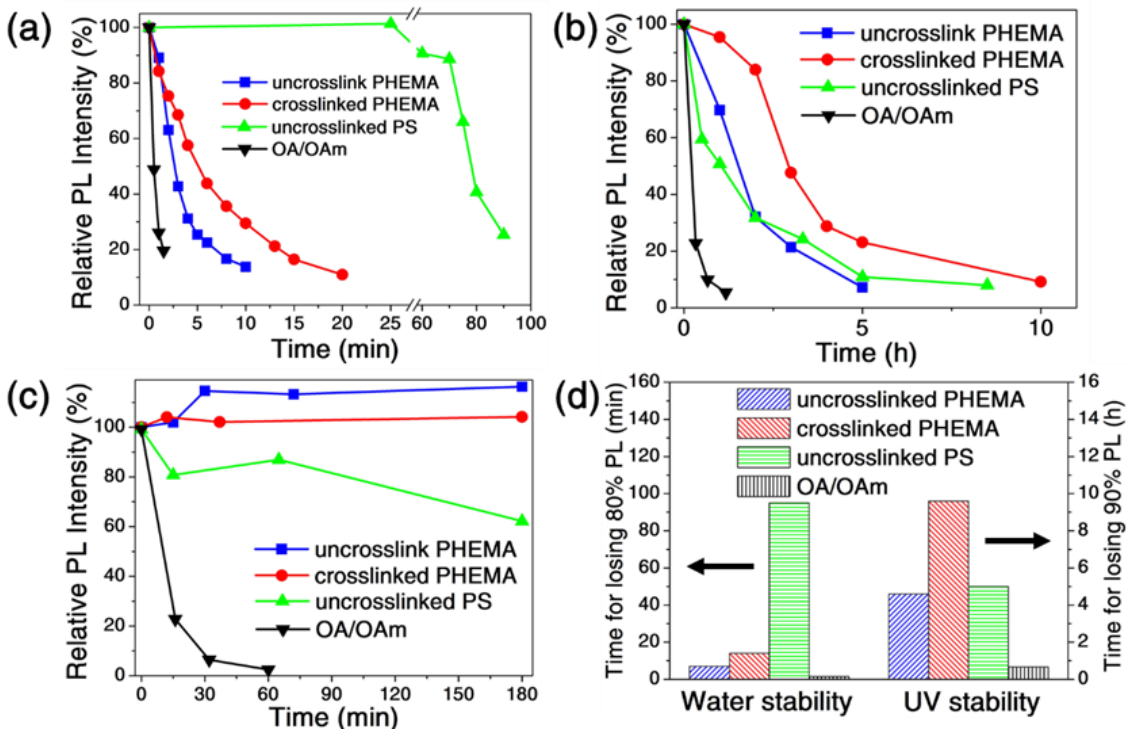

Figure 4.10. (a) PL decay of $CsPbBr_3$ NRs solution when mixed with equal amount of water under stirring. (b) PL decay $CsPbBr_3$ NRs solution under UV irradiation (365

nm). (c) Water and PL stability of $CsPbBr_3$ NRs with different polymer capping. (d) PL decay $CsPbBr_3$ NRs solution heated at 80 °C.

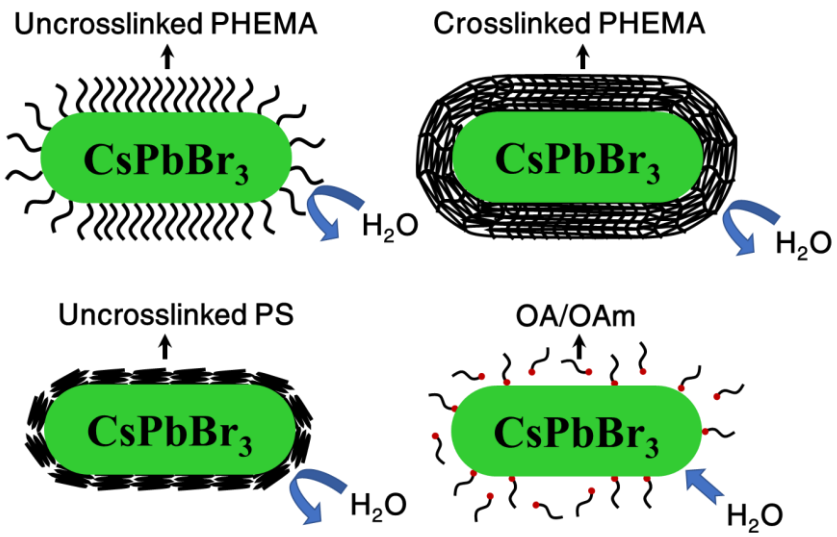

Figure 4.11. Water protection mechanism of $CsPbBr_3$ NRs with uncrosslinked PHEMA, crosslinked PHEMA, uncrosslinked PS, and OA/OAm respectively.

4.4 Conclusions

In summary, we developed a robust strategy to synthesize multifunctional cellulosed-based polymeric bottlebrush cocoons which serve as effective nanocarriers for drug delivery. Azide functionalities in the other block provide a simple encapsulation approach by UV irradiation. The total encapsulation amounts as well as release time was extended three-fold after surface crosslinking. Meanwhile, modulated release rate was achieved with the cocoons as the nanocarrier compared to uncrosslinked counterpart. Potentially, the inner P*t*BA can be substituted with other functional polymers that possess special interaction with biomedical compound such as drugs or peptides to achieve selective encapsulation for targeted drug delivery. The cellulose-based bottlebrush cocoons were also used as nanoreactors for the synthesis of monodisperse $CsPbBr_3$ nanorods with

enhanced water, UV, and thermal stabilities. Inorganic precursors were selectively loaded into the inner PAA domains due to strong coordination between -COOH groups on PAA and metal moieties, leading to the confined growth of $CsPbBr_3$ NCs. Therefore, the size and shape of $CsPbBr_3$ NCs can precisely controlled by tuning molecular weight of bottlebrush polymer. The outer polymer block was permanently tethered on the $CsPbBr_3$ surface providing superior water, UV, and thermal stabilities compared to conventional OA/OAm-capped $CsPbBr_3$ NCs. Additionally, by inducing crosslinking in the surface capped polymer via robust UV treatment, the stabilities were further improved due to higher polymer density on the surface serving as a more effective barrier. Specifically, water stability can be significantly improved by increase the hydrophobicity of the surface polymer. This multifunctional cellulosed-based bottlebrush cocoons have been demonstrated to be a new polymetric materials for effective drug delivery as well as crafting $CsPbBr_3$ nanorods with enhanced stability for the applications in optoelectronics.

CHAPTER 5. FROM JANUS STAR-SHAPED POLYMERS TO JANUS BIFUNCTIONAL NANOCRYSTALS

5.1 Introduction

Janus structures named after the ancient two-faced Roman god Janus are composed of two hemi-structures with different compositions and functionalities. The past decades have witnessed much research on Janus structures due to the intriguing properties and promising potential applications of these unusually shaped materials as sensors,[301-302] imaging,[125, 128] nanomotors,[136-138] drug delivery carriers,[303-304] multifunctional surfactants, [305-306] stabilizers,[134, 307] etc. Janus nanocrystals can be classified into spherical Janus particles, dumbbell-like, rod-like, disc-like, and sheet-like based on the architecture and dimensionality.[122] So far, there has been only one viable approach to synthesize strictly spherical Janus nanoparticles, that is, by surface deposition (e.g. ALD, CVD) of noble metal or metal oxide onto a monolayer assembly of nanoparticles of a different composition also known as masking.[138] However, such nanoshells display much different nanoscale properties than nanoparticles and there is strong limitation of materials that is suitable for surface deposition. Masking is also different to perform on small nanoparticles below 10 nm. It has been well-established that the nanoreactor strategy for synthesis of nanocrystals is applicable to a much broader range of materials.[210, 216] Additionally, lattice mismatch which is detrimental in synthesis Janus crystals by heterogeneous nucleation can be overcome by confined crystal growth in the nanoreactor. Up till now, no researchers have been able to synthesize strictly biphasic Janus nanoparticles comprised of two distinct hemispheres. Nanoreactor strategy might be the only solution to this grade challenge.

Moreover, Au-TiO_2 heterodimers have been demonstrated to have superior photocatalytic performance compared with novel Au-TiO_2 core-shell nanocomposites.[139-140] The asymmetric structure leads to strong localized-surface-plasmon-resonance (LSPR) at Au-TiO_2 interface, where enhanced optical absorption and electron-hole generation is observed. Therefore, it is important to be able to produce Au/TiO_2 Janus structures with much different interfacial interaction to further strengthen its photocatalytic performances.

In general, there is great demand for an innovative approach to incorporate well-established nanoreactor strategy into Janus nanoparticle synthesis. Herein, we developed a general and robust synthetic strategy for strictly biphasic Janus nanoparticles with controlled size and shape. To this end, amphiphilic Janus star-like block copolymer is first synthesized via the combination of reversible addition-fragmentation chain transfer polymerization (RAFT) and atom transfer radical polymerization (ATRP). These Janus amphiphilic star-like block copolymers are then utilized as nanoreactors for in-situ synthesis of Janus nanoparticles with two hemispheres consisting of two dissimilar inorganic functional materials (e.g., plasmonic/magnetic, plasmonic/semiconducting, amorphous/crystalline, tetragonal/cubic, etc.). The size of each hemisphere can be precisely tuned by controlling the length of the corresponding block in Janus amphiphilic star-like block copolymers. These Janus nanoparticles is proposed to exhibit unique self-assembly behaviors as well as superior properties in energy related applications such as solar cells, photocatalysis, etc. his unprecedented structure will also provide the platform for fundamental study of interfacial interaction between nanomaterials.

5.2 Experimental Section

5.2.1 Materials

Azobisisobutyronitrile (AIBN, 97%), anhydrous N,N-dimethylformamide (DMF, 99.9%), anhydrous acetone ($CH_3CO\ CH_3$, 99.5-100.5%), anhydrous dichloromethane (CH_2Cl_2, 99.8%), benzyl alcohol (BA, 98%), 2-bromoisobutyryl bromide (BIBB, 98%), N,N,N′,N″,N″-pentamethyldiethylenetriamine (PMDETA, 99%), tris[2-(dimethylamino)ethyl]amine (Me6TREN, 99%), anhydrous 1-methyl-2-pyrrolidinone (NMP, 99.5%), trifluoroacetic acid (TFA, 99.9%), tripotassium orthophosphate (K_3PO_4, 97%), dodecane thiol ($C_{12}H_{26}S$, 98%), carbon disulphide (CS_2, 99.9%), 2-bromoisobutyric acid (BIBA, 98%), hydrazine (N_2H_4, 98%), tris(2-carboxyethyl)phosphine hydrochloride (TCEP HCl, 98%), borane tert-butylamine (BTBA, 97%), gold(III) chloride trihydrate ($HAuCl_4 \cdot 3H_2O$, 99.9%). All above chemicals were used as received. β-Cyclodextrin (β-CD, Sigma-Aldrich) was dried in a vacuum oven at 80 °C overnight prior to use. CuCl (98%, Sigma-Aldrich) was stirred in acetic acid for 24 h, washed with ethanol and diethyl ether, and dried in a vacuum oven at room temperature. 4-Vinylpyridine (4VP, Alfa Aesar, 97%), Styrene (St, Alfa Aesar, ≥99%), and *tert*-butyl acrylate (*t*BA, Alfa Aesar, 98%) were distilled over CaH_2 under reduced pressure prior to use.

5.2.2 Characterizations

The molecular weights of polymers were measured by gel permeation chromatography (GPC, shimazu) equipped with an LC20AD HPLC pump and a refractive index detector (RID-10A, 120 V). THF was used as the eluent with a flow rate of 1.0 mL/min and operation temperature of 35 °C. One Phenogel 5 μm linear column and one Phenogel 5 μm 10E4A mixed bed column were calibrated with polystyrene standards.

Proton nuclear magnetic resonance (^{1}H NMR) spectra of organic samples were recorded on Varian VXR-300 spectroscope.

5.2.3 Synthesis procedures

5.2.3.1 Synthesis and characterization of Janus macroinitiator (DDMAT$_7$-β-CD-Br$_{14}$)

Synthesis of DDMAT. RAFT agent, specifically (dodecylthiocarbonothioylthio)-2-methylpropanoic acid (DDMAT) was synthesized according to Skey's method.[308] In a typical procedure, K_3PO_4 (4.08 g) was dispersed in anhydrous acetone (80 mL) under RT and stirred for 1 h. Dodecane thiol (5.36 g) was added dropwise into the solution and stirred for 1 h. Carbon disulphide (CS_2) (5.48 g) was then added dropwise into the solution and stirred for 1 h. Solution became yellow. Finally, 2-bromoisobutyric acid (4.0 g) in acetone (20 mL) was added dropwise into the solution and stirred for 20 h. After solvent was removed by rotary evaporator, the product was extracted with 300 mL CH_2Cl_2 from 200 mL 1M HCl and washed three times with DI water. After removing CH_2Cl_2, the residue was recrystalized with Hexanes three times to yield an orange crystal.

Synthesis of DDMAT$_7$-β-CD-Br$_{14}$ macroinitiator. 21-arm Bifunctional macroinitiator was synthesized by first selective esterification of the 7-primary alcohol with RAFT agent (DDMAT), followed by esterification of the other 14 secondary alcohol with bromination agent (BIBB). In a typical reaction, RAFT agent (DDMAT, 2.5 g) was dissolved in anhydrous CH_2Cl_2 (50 mL) followed by the addition of oxalyl chloride (6 mL) and stirred at RT under Ar flow for 12 h. The residue was rotavaped to removed solvent and re-dissolve with anhydrous NMP. The solution was added dropwise to the β-CD (1.0 g) solution in anhydrous NMP (30 mL) dissolved separately in ice bath. After stirring for 24 h, 2-bromoisobutyryl bromide (BIBB, 8 mL) was added dropwise into the solution and

continue stirred at RT for 48 h. Crude solution is washed with $NaHCO_3$ aq. solution and DI water, then precipitated in water and extracted with methanol. The obtained orange solid was dried in vacuum.

5.2.3.2 Synthesis of Janus amphiphilic star-like polymer as nanoreactor (PS-b-P4VP-g_{L7}-β-CD-g_{R8}-PtBA-b-PS)

Synthesis of P4VP-g_{L7}-β-CD half-star polymer. $DDMAT_7$-β-CD-Br_{14} was used as the macroinitiator to first growth P4VP on one side of β-CD (7 arms) via RAFT polymerization. In a typical reaction, $DDMAT_7$-β-CD-Br_{14}, AIBN, 4VP and DMF were mixed in a pressure vessel and degassed by N_2 bubbling. The vessel was then put into oil bath and stirred at 70℃. Polymerization is terminated by immersing into liquid N_2. The solution was precipitated in Hexanes three times. Product was then dried in vacuum. Molecular weight (length) of P4VP block was controlled by reaction time.

Synthesis of PS-*b*-P4VP-g_{L7}-β-CD half-star polymer. PS was continued to grow on the end of P4VP block from P4VP-g_{L7}-β-CD half-star polymer via RAFT polymerization resulting in a 7-arm diblock PS-*b*-P4VP half-star polymer with the other 14 arm unpolymerized. In a typical reaction, P4VP-g_{L7}-β-CD, AIBN, styrene and DMF were mixed in a pressure vessel and degassed by N_2 bubbling. The vessel was then put into oil bath and stirred at 70℃. Polymerization is terminated by immersing into liquid N_2. The solution was precipitated in hexanes three times. Product was then dried in vacuum. Molecular weight (length) of PS block was controlled by reaction time.

Cleavage of RAFT end groups. The RAFT functional end groups on 7 PS-P4VP block polymer arms was cleaved by hydrazine into -SH because RAFT functionalities can also participate in ATRP reactions disrupting the polymerization on the other 14 arms. In

a typical reaction, PS-*b*-P4VP-g_{L7}-β-CD half-star polymer was dissolved in DMF. Hydrazine and TCEP (2 mg) were added to the solution. After stirring at RT under Ar for 3 h, the product was precipitated in hexanes three times and dried under vacuum.

Synthesis of PS-*b*-P4VP-g_{L7}-β-CD-g_{R8}-P*t*BA star-like polymer. PS-*b*-P4VP-g_{L7}-β-CD half-star polymer after cleavage was used as the macroinitiator for ATRP polymerization of *t*BA on 14 -Br initiating site on the other half of the Janus star-like initiator. In a typical reaction, PS-*b*-P4VP-g_{L7}-β-CD, CuCl, $CuCl_2$, tris[2-(dimethylamino)ethyl]amine (Me_6TREN), tert-butyl acrylate (*t*BA) and DMF were mixed in a pressure vessel and degassed by N_2 bubbling. The vessel was then put into oil bath and stirred at 60℃. Polymerization is terminated by immersing into liquid N_2. The solution was passed through basic alumina column and precipitated in methanol/water (1:1) mixture. Product was then dried in vacuum. Molecular weight (length) of P*t*BA block was controlled by reaction time.

Synthesis of PS-*b*-P4VP-g_{L7}-β-CD-g_{R8}-P*t*BA-*b*-PS star-like polymer. PS was continued to grow on the end of P*t*BA block from PS-*b*-P4VP-g_{L7}-β-CD-g_{R8}-P*t*BA star-like polymer via ATRP polymerization to form a 21-arm Janus star-like tetrablock copolymer with amphiphilic inner core and PS outer shell. In a typical reaction, PS-*b*-P4VP-g_{L7}-β-CD-g_{R8}-P*t*BA, CuCl, $CuCl_2$, Me_6TREN, styrene and DMF were mixed in a pressure vessel and degassed by N_2 bubbling. The vessel was then put into oil bath and stirred at 90℃. Polymerization is terminated by immersing into liquid N_2. The solution was passed through basic alumina column and precipitated in methanol. Product was then dried in vacuum. Molecular weight (length) of new PS block was controlled by reaction time.

5.2.3.3 Synthesis of strictly biphasic Janus nanoparticles

The synthesized star-shaped Janus block copolymer is used as the nanoreactor for in-situ production of Janus Au/TiO_2 nanoparticles.

Synthesis of Au hemisphere with PS-*b*-P4VP-g_{L7}-β-CD-g_{R8}-P*t*BA-*b*-PS star-like Janus nanoreactor. Au precursor was selectively loaded into the P4VP domain which was then in-situ reduced into Au hemisphere. In a typical reaction, PS-*b*-P4VP-g_{L7}-β-CD-g_{R8}-P*t*BA-*b*-PS was dissolved in DMF followed by adding certain amount of precursor ($HAuCl_4 \cdot 3H_2O$). The mixture was subjected to prolonged stirring before adding certain amount of benzyl alcohol (BA). The reaction was carried out at elevated temperature under Ar flow with borane tert-butylamine (BTBA) added dropwise. The product was purified by dissolution−precipitation with toluene and methanol.

Hydrolysis of P*t*BA block on the other side of Au hemisphere. The inactive P*t*BA block was hydrolysis with TFA into active PAA which can coordinate with metal precursors. In a typical reaction, Au hemisphere was dissolved in diphenyl ether (DPE) and refluxed at 200℃ for 2h. The product was then precipitated in methanol several times and re-dispersed in DMF.

Synthesis of Au/TiO_2 Janus nanoparticles. TiO_2 precursor was selectively loaded into the PAA domain which was then in-situ hydrolyzed into TiO_2 hemisphere alongside Au hemisphere creating Au/TiO_2 Janus nanoparticles. In a typical reaction, certain amount of precursor (TTIP) was added to Au-β-CD-g_{R8}-PAA-*b*-PS solution in DMF. The mixture was subjected to prolonged stirring before adding certain amount of benzyl alcohol (BA). The reaction was carried out at elevated temperature under Ar flow with ammonium

hydroxide aq. solution added dropwise. The product was purified by dissolution−precipitation with toluene and methanol.

5.3 Results and Discussion

Janus nanoparticles were synthesized by capitalizing on star-shaped Janus amphiphilic block copolymers as nanoreactors. The synthetic scheme is depicted in **Figure 5.1**. β-CD was used as the initiator due to its bowl-shaped core and bifunctional nature. The 21 hydroxyl groups on β-CD can be divided into 7 primary alcohol groups on up-side of the bowl and 14 secondary alcohol groups on down-side of the bowl, providing the possibility for site-selective functionalization to craft a bifunctional macroinitiator capable of carrying out two different types of polymerization (ATRP and RAFT) on each side of the bowl. The as-synthesized Janus initiator termed DDMAT$_7$-β-CD-Br$_8$ has 7 (dodecylthiocarbonothioylthio)-2-methylpropanoic acid (DDMAT) groups on one side and 8 bromide (-Br) group on the other side. Sequential RAFT polymerization of 4-vinyl pyridine (4VP) and styrene (St) was first initiated from DDMAT, a RAFT agent, to create half of the Janus star-shaped polymer. Because RAFT functional groups can also participate in ATRP polymerization and disturbed the pre-designed structure, it was cleaved off the polymer before sequential ATRP of *t*BA and St initiated from -Br groups on the other side of the Janus initiator. The Janus star-shaped block copolymers were then loaded with the precursor of material A into the P4VP blocks due to strong coordination interactions of pyridine groups with metal moieties in the precursor. Hemisphere of material A was formed after in-situ crystal formation with the other half of the Janus star-shaped polymer (P*t*BA-*b*-PS) still exposed. The P*t*BA blocks were first hydrolysed into PAA which can coordinates with precursors of material B to direct the crystal growth the

hemisphere B in the same fashion as hemisphere A. The synthesized spherical Janus nanoparticles are composed of two hemispheres of two different materials with a distinct planar phase boundary as well as permanently capped PS hair providing excellent colloidal stability.

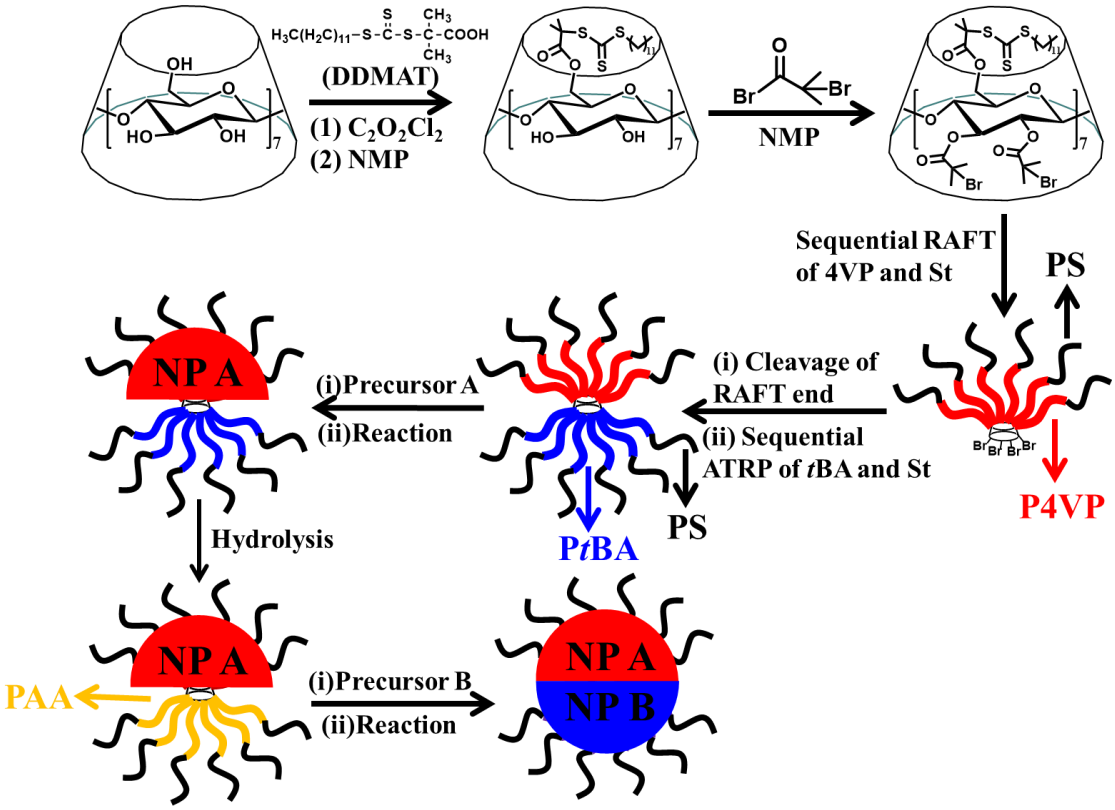

Figure 5.1. Synthetic scheme of spherical Janus nanoparticles from star-shaped Janus block copolymers.

5.3.1 Janus initiator

RAFT functionality and Br functionality were induced into β-CD sequentially. The selective functionalization (esterification) of the 21 -OH groups in β-CD is based on the difference of reactive of primary and secondary -OH groups as well as the steric hindrance between secondary -OH and bulky RAFT agent (DDMAT). Primary alcohols tend to have

much higher esterification rate than secondary alcohols. It is also evident that the 14 secondary -OH groups are more closely packed creating huge steric hindrance for insertion of DDMAT.

First, RAFT agent (DDMAT) was synthesized according to Skey's method.[308] The ^{1}H NMR of product was shown in **Figure 5.2** demonstrating the successful synthesis of DDMAT.

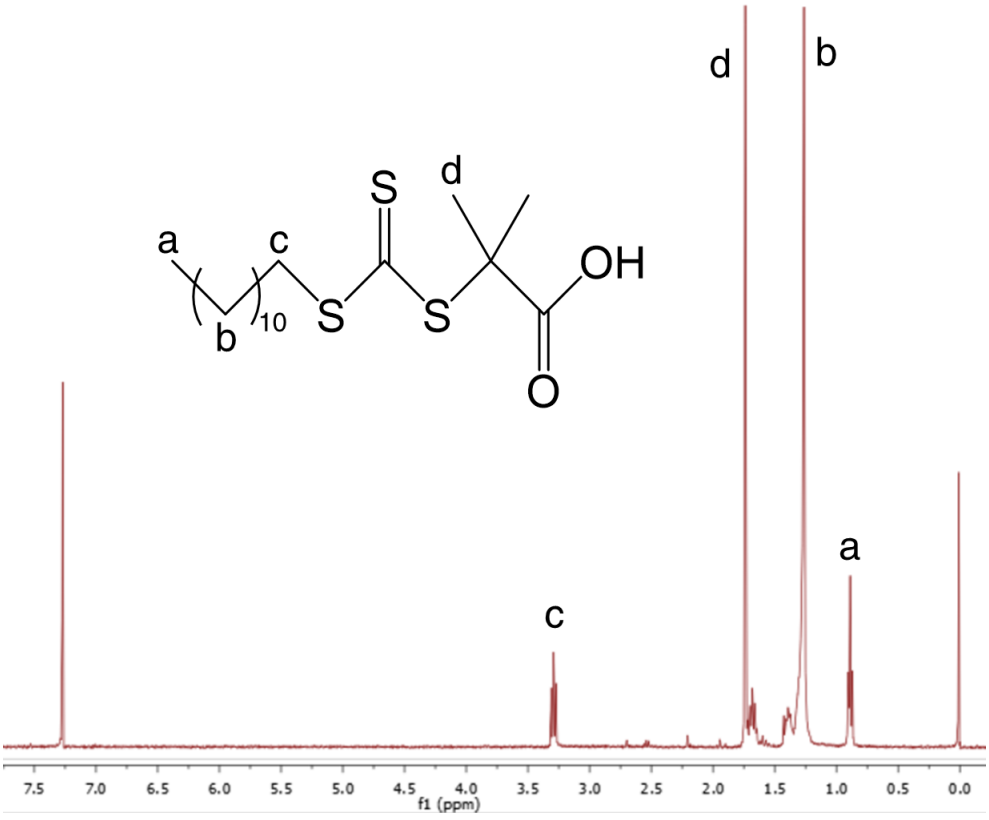

Figure 5.2. ^{1}H NMR of DDMAT.

Then, Janus initiator $DDMAT_7$-β-CD-Br_8 was synthesized by two-step esterification process, that is, first esterification of primary -OH with DDMAT and second esterification

of secondary -OH with BIBB. Each esterification was verified by ^{1}H NMR (**Figure 5.3a&b**). The esterification efficiency for RAFT functionalization was calculated from **Figure 5.3a** to be 100% by comparing the peaks from β-CD backbone (2.5ppm-6.0ppm excluding peak *c*) and peak *a* from DDMAT, which means all 7 primary alcohols were functionalized with DDMAT. The esterification efficiency for bromide (or ATRP) functionalization was calculated from **Figure 5.3b** to be 57.5% by comparing peak *a* of DDMAT functionality versus peak *e* of bromide functionality, which means 8 of the 14 secondary alcohols were functionalized with Br, producing a Janus initiator with almost equal amount of initiating site on both side of β-CD. The reason for having similar number of initiating sites is that it will produce Janus star-shaped polymer with similar number of arms on both side of the initiator which is more conformational symmetric, providing the ability to generate hemispherical rather than cone-like structures. Molecular weight of the Janus initiator was characterization by GPC (**Figure 5.3c**). THF GPC showed a number average molecular weight of 3.7K and a PDI of 1.06 demonstrating a near unimolecular distribution, which means all β-CDs were functionalized equally. The slight lower molecular weight than theoretical value is because the GPC is calibrated by linear PS while the Janus initiator is star-shaped.

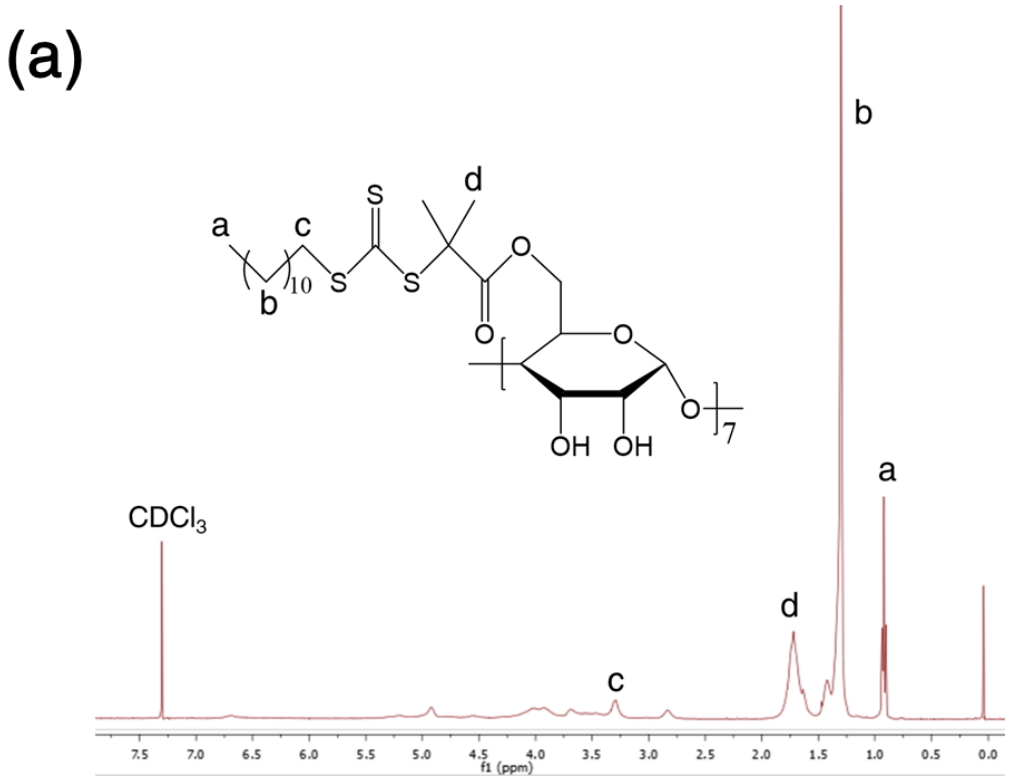
(a)
a
b
c
d
S
S
S
O
O
O
O
O
10
7
OH
OH
CDCl3
b
a
d
c
7.5
7.0
6.5
6.0
5.5
5.0
4.5
4.0
3.5
3.0
2.5
2.0
1.5
1.0
0.5
0.0
f1 (ppm)

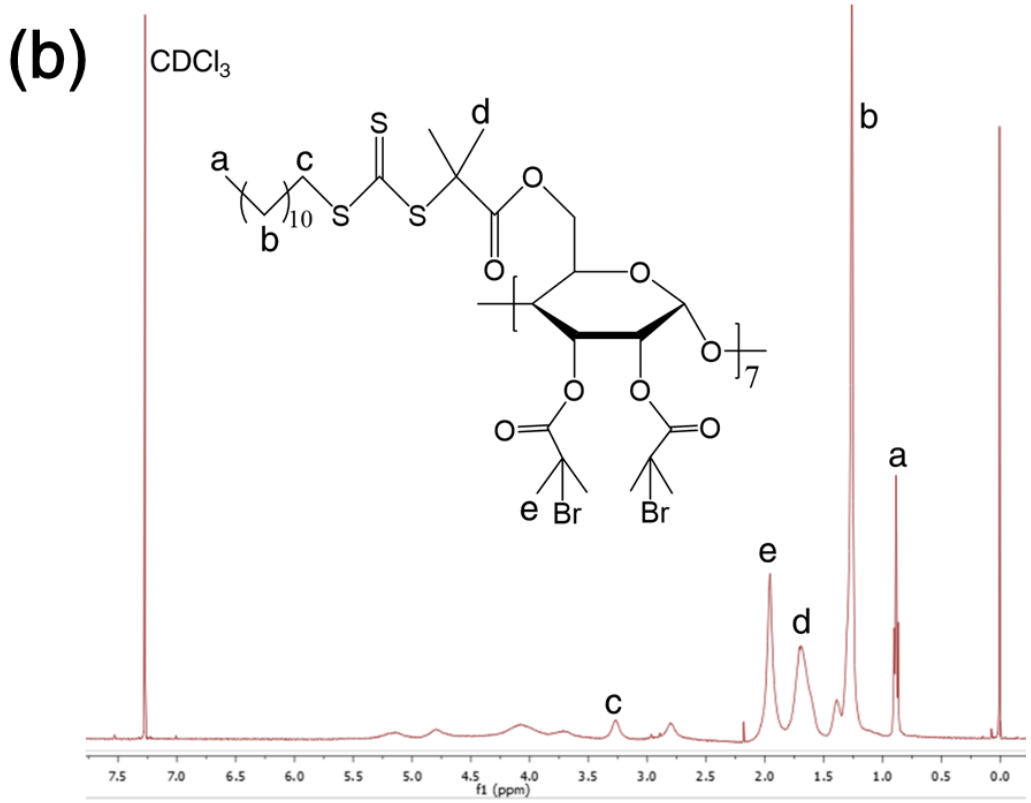
(b)
CDCl3
a
b
c
d
e
S
S
S
O
O
O
O
O
O
O
O
10
7
Br
Br
b
a
e
d
c
7.5
7.0
6.5
6.0
5.5
5.0
4.5
4.0
3.5
3.0
2.5
2.0
1.5
1.0
0.5
0.0
f1 (ppm)

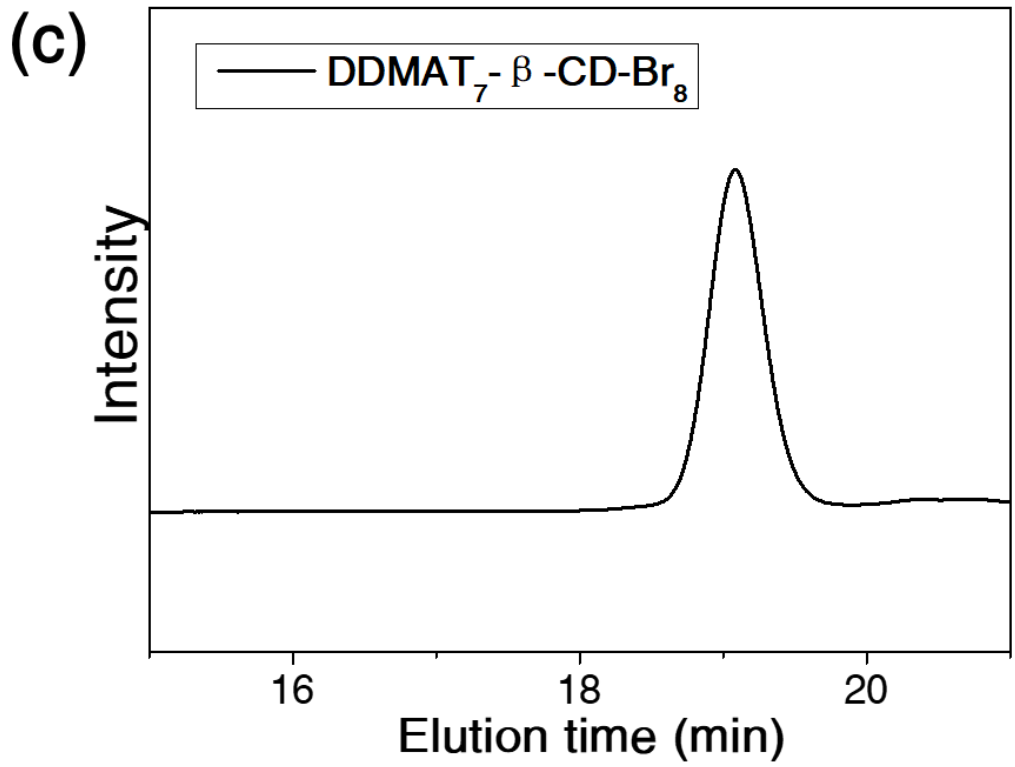

Figure 5.3. (a) ^{1}H NMR of DDMAT$_7$-β-CD. (b) ^{1}H NMR of DDMAT$_7$-β-CD-Br$_8$. (c) GPC spectrum of ^{1}H NMR of DDMAT$_7$-β-CD-Br$_8$ (THF mobile phase).

5.3.2 Janus star-shaped polymers

Half Janus star-shaped polymers PS-*b*-P4VP-g_{L7}-β-CD was first synthesized by sequential RAFT polymerization of 4VP and St. ^{1}H NMR in **Figure 5.4 a&b** demonstrated the successful synthesis of P4VP and PS. Molecular weight evolution was characterized by GPC in **Figure 5.5**. Low PDI was observed after each step of polymerization due to controlled nature of RAFT polymerization.

(a)

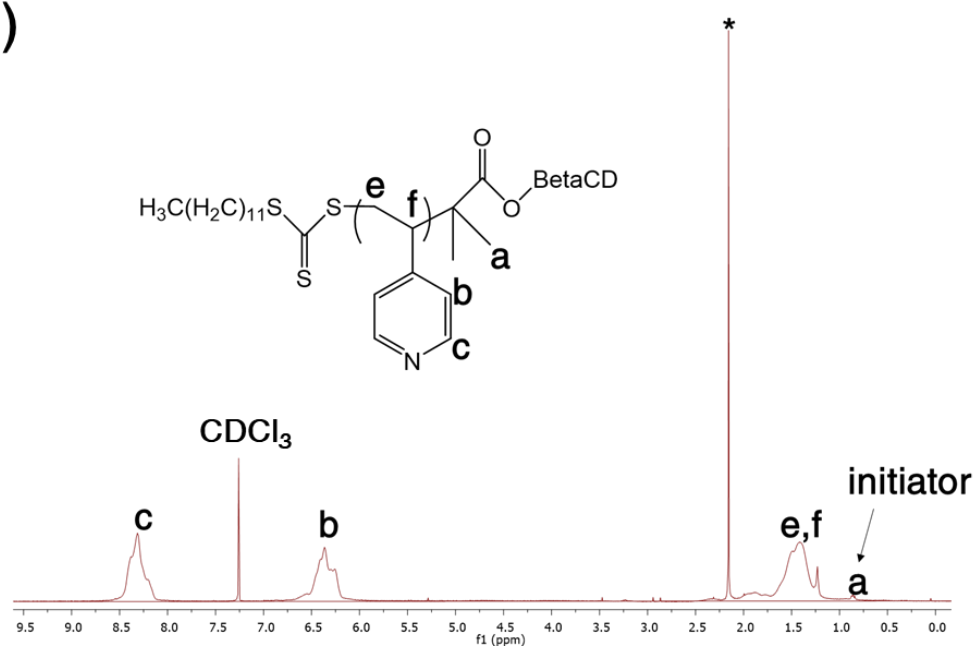
*
O
BetaCD
O
H3C(H2C)11S
S
e
f
a
S
b
c
N
CDCl3
initiator
c
b
e,f
a
9.5 9.0 8.5 8.0 7.5 7.0 6.5 6.0 5.5 5.0 4.5 4.0 3.5 3.0 2.5 2.0 1.5 1.0 0.5 0.0
f1 (ppm)

(b)

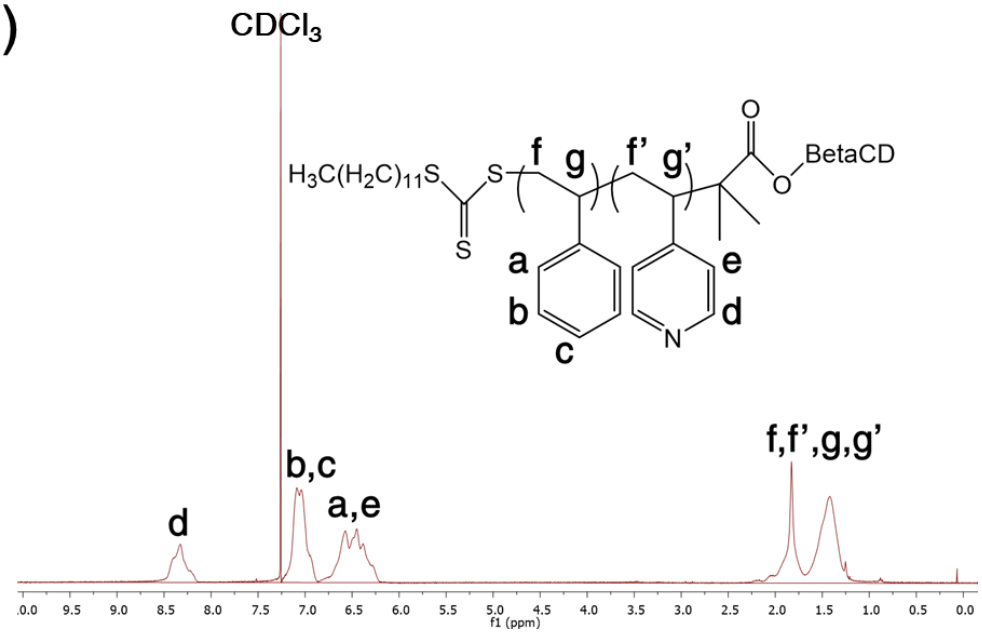
CDCl3
O
BetaCD
H3C(H2C)11S
S
f
g
f'
g'
O
S
a
e
b
d
c
N
f,f',g,g'
b,c
a,e
d
.0.0 9.5 9.0 8.5 8.0 7.5 7.0 6.5 6.0 5.5 5.0 4.5 4.0 3.5 3.0 2.5 2.0 1.5 1.0 0.5 0.0
f1 (ppm)

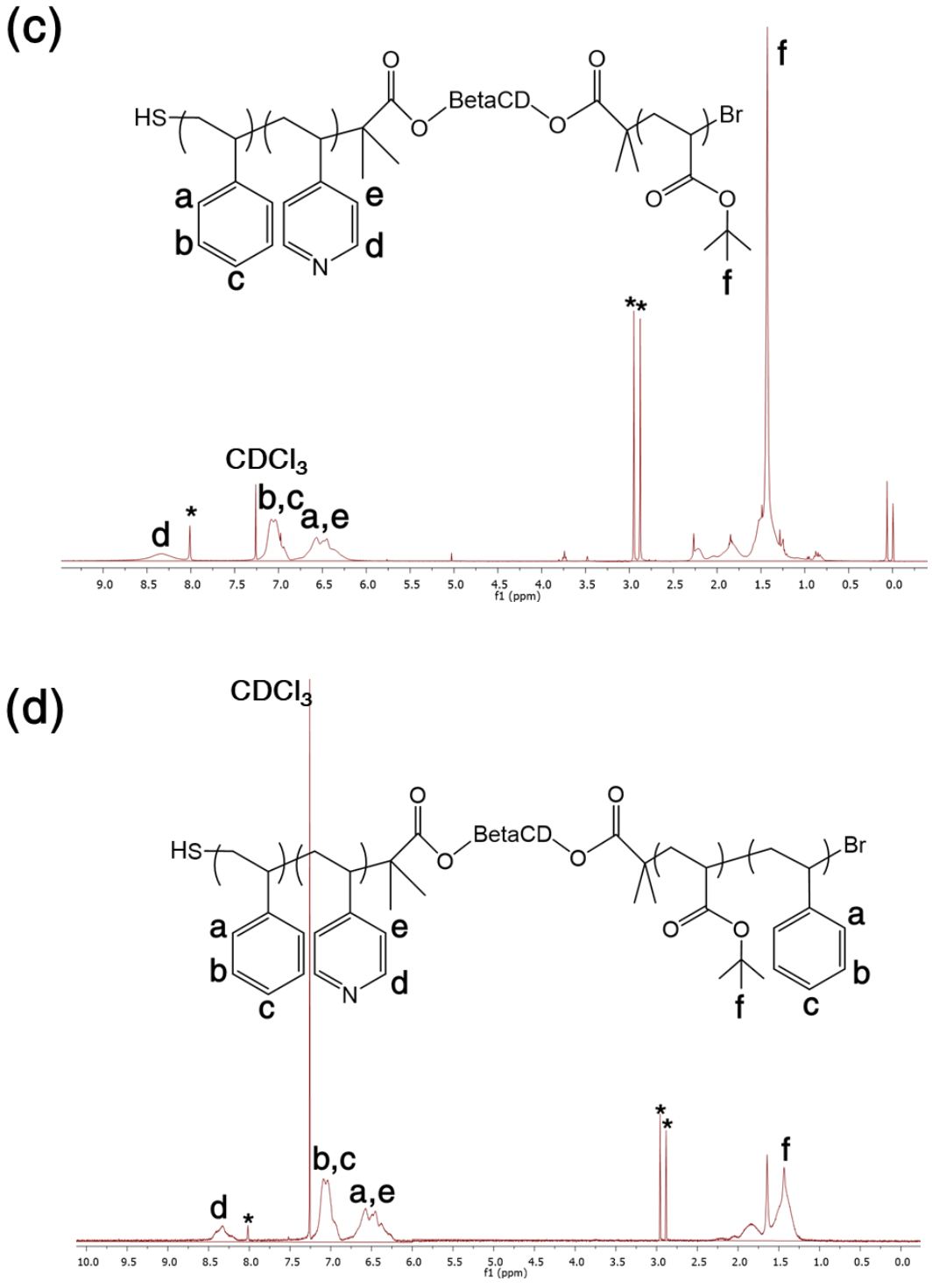

Figure 5.4. ^{1}H NMR of (a) P4VP-*g*$_{L7}$-β-CD, (b) PS-*b*-P4VP-*g*$_{L7}$-β-CD, (c) PS-*b*-P4VP-*g*$_{L7}$-β-CD-*g*$_{R8}$-P*t*BA, (d) PS-*b*-P4VP-*g*$_{L7}$-β-CD-*g*$_{R8}$-P*t*BA-*b*-PS.

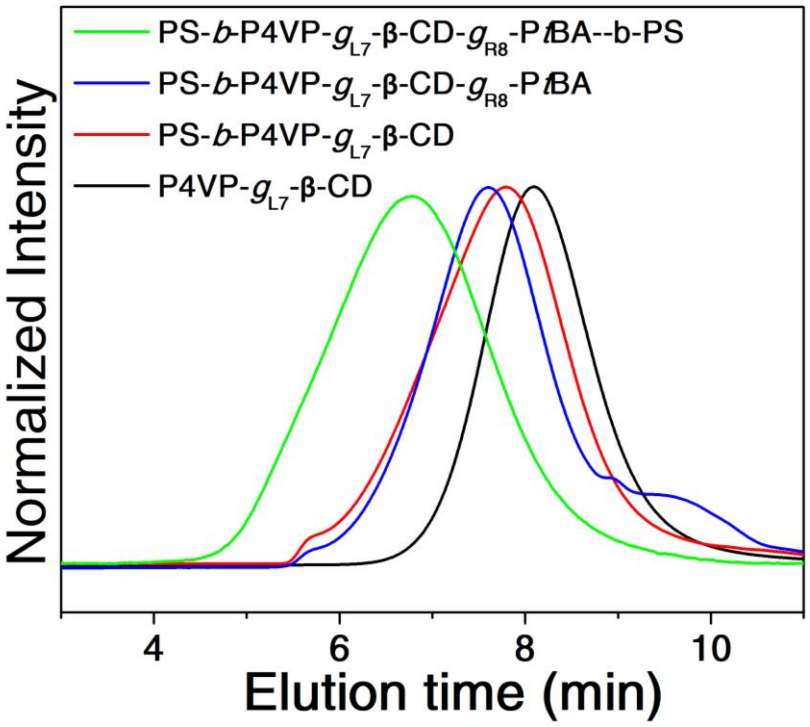

Figure 5.5. GPC curves of star-like Janus block copolymers after each step of polymerization to growth (1) P4VP (2) PS (3) P*t*BA (4) PS.

The initially synthesized PS-*b*-P4VP-g_{L7}-β-CD was terminated with DDMAT which will participate in all radical polymerizations including ATRP. Therefore, the DDMAT groups have to be cleaved off before ATRP can be conducted on the 8 -Br groups. Typical cleavage was conduct by reacting with hydrazine which can reduce the trisulfide bonds into thiol (-SH) groups. A trace amount of tris(2-carboxyethyl) phosphine (TCEP) was also added during cleavage to prevent potential disulfide (-S-S-) bond formation. UV-vis absorption of the polymer after cleavage reaction confirmed the complete cleavage of the RAFT groups. Trisulfide groups have distinct UV absorption at 310 nm which completely disappeared after hydrazine cleavage (**Figure 5.6a**). Additionally, as shown in **Figure 5.6b**, the GPC peaks of PS-*b*-P4VP-g_{L7}-β-CD before and after cleavage are identical indicating that polymer structure is not influenced by cleavage reaction.

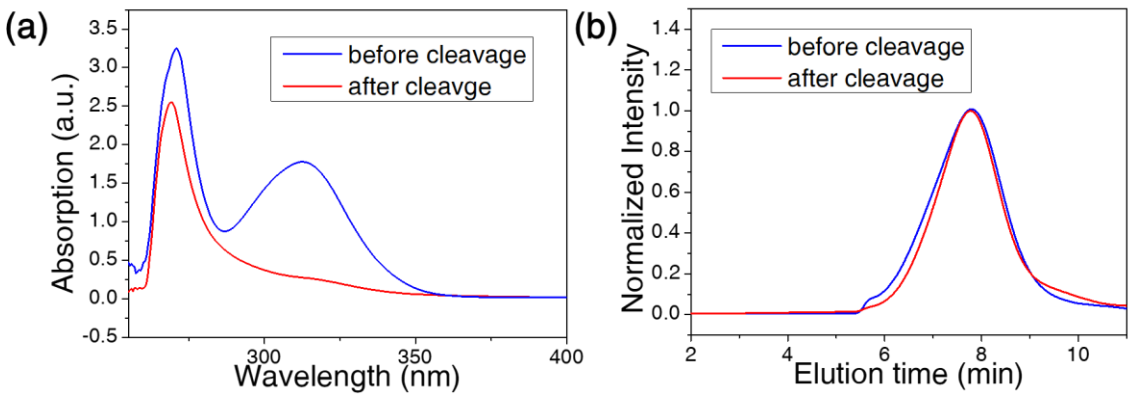

Figure 5.6. (a) UV-vis absorption and (b) GPC spectra of PS-*b*-P4VP-g_{L7}-β-CD before and after cleavage.

The third and fourth block were grafted onto the other side the Janus initiator through sequential ATRP of *t*BA and St. The successful synthesis of the Janus star-shaped block copolymers was verified by ^{1}H NMR (**Figure 5.4 c&d**) and GPC (**Figure 5.5**). To get the molecular weight of P4VP block, P4VP-g_{R7}-β-CD was first cleaved in basic condition to get single P4VP chain, which was then measured by DMF GPC. The molecular weight of all other blocks can be calculated from ^{1}H NMR respectively, which is summarized in **Table 5.1**.

Table 5.1. Molecular weight of each block of PS-*b*-P4VP-g_{L7}-β-CD-g_{R8}-P*t*BA-*b*-PS.

Block	P4VP	PS(L)	P*t*BA(PAA)	PS(R)
Sample A	14K	27K	2.7K(1.5K)	5K
Sample B	14K	14K	23.5K(13K)	31K

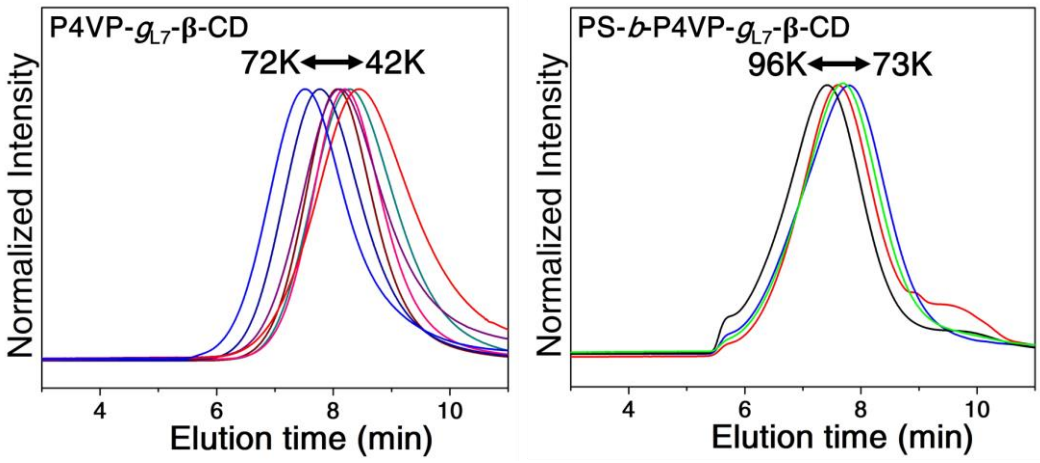

Figure 5.7. P4VP-g_{L7}-β-CD (left) and PS-*b*-P4VP-g_{L7}-β-CD (left) with a range of molecular weight.

In practice, there is more kinetic control in RAFT polymerization of 4VP and St from Janus initiator to generate half of the Janus star-shaped polymer because little steric hindrance exists and P4VP coupling is negligible in RAFT polymerization. P4VP-g_{L7}-β-CD and PS-*b*-P4VP-g_{L7}-β-CD of a wide range of molecular weight with low PDI have been successfully synthesized as shown in **Figure 5.7**. A P4VP block length of 12K to 20K and a PS block length of 6K to 14K can be easily achieved by tuning polymerization time. However, due to steric hindrance induced by P4VP-b-PS chains that wrap around to cover the other side of the initiator, the initiating and propagation of *t*BA and St by ATRP is very much inhibited making polymerization rate extremely slow. Low reproducibility is therefore observed under same polymerization condition. Additionally, it has been found that significant P4VP coupling can happen in ATRP polymerization of star-like polymer but not in RAFT polymerization due to pyridine-halogen interaction. Extensive shouldering is observed in ATRP of 4VP with 21-Br functionalized β-CD initiator. Therefore, it is expected that more coupling is likely to happen when the reaction time of ATRP polymerization of *t*BA (3-step in the Janus polymer synthesis) is prolonged. As a

result, few complete Janus block copolymers with 4 blocks have been synthesized especially with desired molecular weight, which can be used in the later stage for inorganic Janus nanoparticle synthesis.

5.3.3 Janus nanoparticles-Au hemisphere

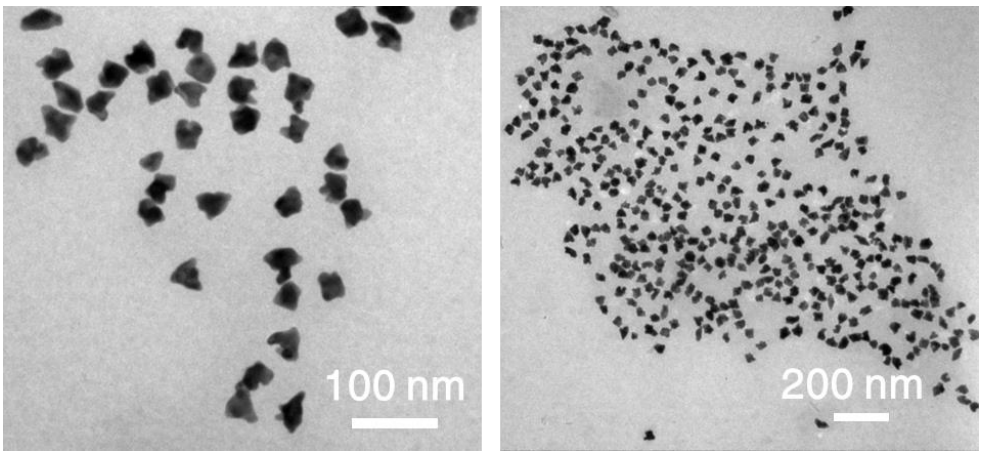

Figure 5.8. TEM images of irregular Au nanoparticles synthesized from Janus polymers with low P*t*BA-*b*-PS length.

Au hemisphere was synthesized by loading Au precursor selectively into the hydrophilic P4VP domain via strong coordination between Au and pyridine groups following by in-situ reduction. However, the structure of the Janus block copolymers (i.e. ratio between all the blocks) is critical in generating Au nanocrystals with desired morphology. Incomparable polymer length between P4VP-*b*-PS and P*t*BA-*b*-PS will not fulfil the Janus polymer's functional as nanoreactor, rather as multi-arm macro-ligands. For example, when P*t*BA-*b*-PS is relatively small due to slow growth rate (sample A in **Table 5.1**), the synthesized Au nanoparticles were around 30 nm (larger then nanoreactor) and adopted a non-uniform rippled structure shown in **Figure 5.8**. It is suspected that the Janus polymers served as capping agents in Au synthesis where the P4VP blocks were

attached on Au surface due to the lack of protection from the short chains on the other side. The complex amphiphilic structure of the Janus polymers forced the growth of Au nanocrystals into a highly irregular morphology.

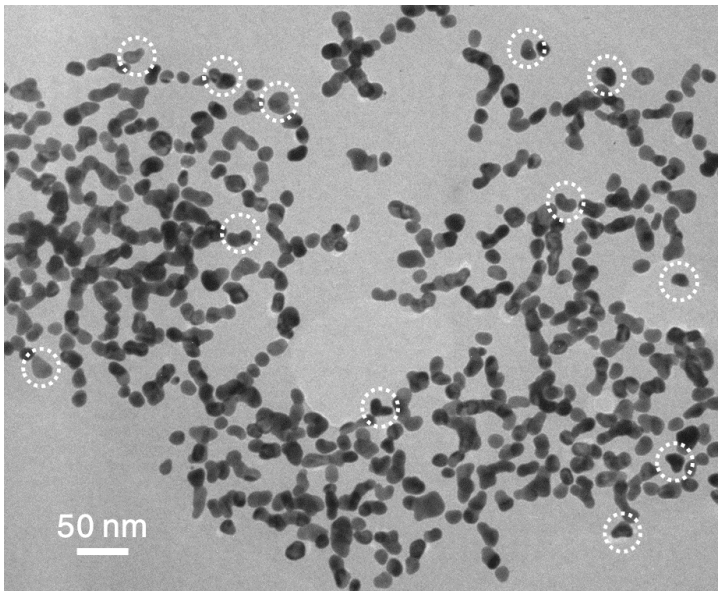

Figure 5.9. TEM image of Au hemisphere synthesized from Janus star-shaped block copolymers of proper molecular weight.

Figure 5.9 shows the Au hemispheres synthesized from Janus block copolymers with proper molecular weight (sample B in **Table 5.1)**. Multiple hemispherical particles can be clearly observed together with other unwanted structures which is probably due to poor quality of polymer nanoreactors as well as un-optimized synthetic conditions. The average length of Au hemispheres is about 25 nm, corresponding well with the length of P4VP block (14K). The complete Janus nanoparticles haven't been successfully synthesized yet. However, this preliminary result demonstrates that the proposed Janus nanoreactor strategy for the synthesis of strictly biphasic Janus nanoparticles is feasible. With further optimization of the polymer molecular weight and the inorganic synthesis condition, Janus nanoparticles with more uniform size and morphology can be achieved eventually.

5.4 Conclusions

In summary, we rationally designed and synthesized a type of Janus star-shaped block polymers using bifunctional bowl-shaped initiator, β-CD. Site-selective functionalization of β-CD was achieved by controlling the esterification reactivity of primary and secondary alcohol groups. RAFT functionalities and ATRP functionalities were attached separately to two different sides of the bowl-shaped β-CD, generating a bifunctional initiator capable of conducing two different polymerizations. The Janus block copolymers were produced by sequential 4-step polymerization of different monomers including RATF of 4VP and St and ATRP of *t*BA and St. The controlled living characteristic of RAFT and ATRP contributes to the well-defined molecular weight and low PDI during all polymerization steps, yielding monodisperse soft Janus polymer micelles. However, the size of the Janus polymer that can successfully synthesized is limited because the first polymerized long P4VP-*b*-PS chains will coil up to completely, thereby covering the other side of the initiator and thus preventing the following initiation and growth of P*t*BA-*b*-PS. Star-shaped PS-*b*-P4VP-g_{L7}-β-CD-g_{R8}-P*t*BA-*b*-PS P4VP was then employed as nanoreactors for the synthesis of strictly biphasic Janus nanoparticles. The P4VP domain comprising half the core of Janus polymer was first converted into Au hemisphere via strong coordination between pyridine groups on P4VP and Au precursors. The other half of the core, P*t*BA, will also be hydrolyzed into PAA for TiO_2 hemisphere synthesis. However, due to the difficulty in the purification of Au hemisphere and hydrolysis, Au/TiO_2 Janus nanoparticles haven't yet been successfully synthesized. Continuing effort will be made in the Janus nanoparticles synthesis as well as the investigation of their photocatalytic properties.

CHAPTER 6. GENERAL CONCLUSIONS AND BROADER IMPACTS

6.1 General conclusions

Architectured amphiphilic block copolymers with complex molecular structures have garnered much attention in recent years due to their distinct chemical and physical properties compared to the linear counterparts. The amphiphilic chemical environment provides a robust platform for site selective functionalization as well as molecular interactions. Notably, architectured amphiphilic block copolymers can be employed as nanoreactors for crafting polymer-ligated nanocrystals. Specifically, the hydrophilic blocks of architectured amphiphilic block copolymers can be selectively loaded with metal precursors to achieve confined growth of inorganic nanocrystals. The size and shape of as-synthesized polymer-ligated nanocrystals can be precisely tailored via architectural design and controlling the reaction time of architectured amphiphilic block copolymers.

First, MFe_2O_4 (M = Mn, Co, Ni, Cu, Zn) and MO_x (M = Mn, Co, Fe) nanoparticles with a desired size were precisely crafted by capitalizing on star-like polyacrylic acid-*block*-polystyrene-acrylonitrile (star-like PAA-*b*-PSAN) copolymers as nanoreactors, which was then uniformly anchored on reduced graphene oxide nanosheets induced by the π-π stacking interaction between PSAN and rGO (denoted MFe_2O_4/PAA@PSAN-rGO and MO_x/PAA@PSAN-rGO). As anodes of LIBs/SIBs, the MFe_2O_4/PAA@PSAN-rGO expressed outstanding cycling stabilities at various current rates. In stark contrast, Li^+ storage capacities of MO_x/PAA@PSAN-rGO decreased initially and then raised while Na^+

storage capacities continued to decay. According to the HRTEM observations of cycled Fe_2O_3/PAA@PSAN-rGO electrodes, the coarsening of small Fe nanoparticles into larger domains leads to the decrease of specific contact areas of Fe with Li_2O/Na_2O, finally resulting in the reduction of conversion reaction reversibility. Notably, the $CoFe_2O_4$/PAA@PSAN nanoparticles randomly phase-separate into CoO and Fe_2O_3 domains after the first cycle creating abundant heterophase interfaces inside the cycled $CoFe_2O_4$/PAA@PSAN-rGO nanocomposites. The heterophase interfaces together with physical barriers provided by rGO and PSAN hairs inhibit the large-scale homophase coarsening of Co and Fe nanoparticles stabilizing the electrochemical reaction reversibility. Therefore, two key strategies to inhibit homophase metal coarsening are proposed and verified which are essential for the enhancement of cycling stability of MO_x as anode of LIBs/SIBs: (1) establishing robust physical barriers on the surfaces of MO_x nanoparticles by homogeneously coating carbonaceous materials or polymers; and (2) introducing abundant heterophase interfaces in the cycled MO_x electrodes by fabricating polymetallic oxides or uniform mixture of different MO_x nanoparticles.

Second, a robust route to synthesize unimolecular organic bottle-brush cocoons with crosslinked shell was developed where the interior was occupied by judiciously designed polymer chains (i.e., poly(acrylic acid); PAA) to provide preferential anchoring points for organic and inorganic molecules. The azide functionalized outer block of the bottle-brush polymer can be readily crosslinked upon UV irradiation presenting an efficient and robust route for post-loading encapsulation. As a result, the polymeric cocoons showed excellent encapsulation and delivery properties with 3-fold encapsulation amount and 3-fold total delivery period over uncrosslinked bottle-brush polymers. Different from previous

approaches for making worm-like bottle-brush polymers, cellulose was used as the backbone giving the cocoons a straight nanorod morphology. This type of bottle-brush cocoons can be directly capitalized as nanoreactors to produce monodisperse inorganic nanorod with controlled size and composition. The crosslinked outer layer on the nanorod provide additional barrier protection to enhance its stability. $CsPbBr_3$ nanorods as a promising perovskite material has been known to have extremely poor stability. Remarkably, the $CsPbBr_3$ nanorods synthesized from the polymeric cocoons exhibited much enhanced UV, water, and thermal stabilities when the outer polymer block was crosslinked after nanorods synthesis, providing them with great potential in application of optoelectronics. This unique cocoon strategy provides an innovating approach towards the development of new-generation nanocarrier for drug delivery and nanoreactor for the synthesis of nanocrystals with superior stabilities.

Third, an innovative synthetic strategy for star-shaped Janus block polymers was developed by employing bifunctional β-CD as the macroinitiator. The bowl shaped β-CD is composed of 7 primary -OH groups on one side of the bowl and 14 secondary -OH groups on the other, which can be selectively functionalized based on the difference in reactivity and steric hindrance. 7 -COOH terminated RAFT agent (DDMAT) was first coupled to the primary alcohols by esterification with the other 8 out of 14 secondary alcohols esterified by bromination agent, producing a multifunctional macroinitiator with 7 RAFT initiating sites and 8 ATRP initiating sites on different side of the bowl-shaped β-CD. After sequential 4-step polymerization (2-steps RAFT of 4VP and St, 2-steps ATRP of *t*BA and St), star-shaped Janus core-shell polymers were synthesized with an amphiphilic core and hydrophobic PS shell. Strictly biphasic Janus nanoparticles can be

synthesized using the above Janus polymer as the nanoreactor. The amphiphilic core consists of an activated P4VP half, which can be incorporated with Au precursor for the synthesis of Au hemisphere, and a deactivated P*t*BA half which can be hydrolyzed into PAA to incorporate with TiO_2 precursor for the synthesis of the other TiO_2 hemisphere, together yielding a spherical Au/TiO_2 Janus nanoparticle with two hemispheres comprising different materials. So far, Au hemispheres have been synthesized with ongoing effort for synthesis of the other TiO_2 hemisphere.

6.2 Broader impacts

This work provides a general strategy to craft core-shell type architectured block copolymers with controlled morphology by combining well-developed controlled living polymerization technique such as ATRP and RAFT with highly functionalized initiator. Nanocrystals of different size and shape can be readily synthesized by using rationally designed block copolymers noted above as nanoreactors. Additionally, the nanocrystals synthesized via this strategy are highly advantageous over conventionally synthesized nanocrystals. The former nanocrystals are permanently capped with functional polymers which provide superior colloidal stabilities as well as barrier properties, while the latter nanocrystals are typically dynamically capped with small organic ligand resulting in poor long-term stability. The unique properties of the architectured block copolymers as well as highly stable nanocrystals manifest great potential in the biochemical and energy applications including drug delivery, bioimaging, lithium ion battery, light emitting diode, electrocatalysis, photocatalysis, etc.

The first project presented in Chapter 3 developed a novel metal oxides anode material with high capacity and magnificent cycling stability. Though detailed mechanism investigation, the major cause for the decrease of conversion reaction reversibility of metal oxide nanoparticles is discovered to be the homophase coarsening of metal during charge-discharge process, which makes the particles grower bigger in size. Two effective strategies have been proposed and demonstrated to significantly increase the particle structural stability and boost its cycling performance: (1) surface protection and (2) polymetallic composition. This significant finding will provide important guideline for the development and research of metal oxides-based anode materials in LIB to overcome the currently faced stability issue and eventually towards commercialization. Moreover, it is suspected that such reaction mechanism is not limited to metal oxide nanoparticles, instead applicable to all anode materials that encounter high volume change in battery operation including SnO_2 and SiO_2. Therefore, this work will have broad impact in the development of next-generation lithium-ion batteries.

Despite the significant contribution in lithium ion batteries, these metal ferrite nanoparticles can also find wide applications in electrocatalysis due to high surface area which has been demonstrated to exhibit excellent ORR performances, especially with the incorporation of the lanthanum (La) metal. Due to the precise size and composition control of nanoreactor strategy, it provides the opportunity for fundamental understanding of size- and composition-dependent electrochemical properties of metal oxide materials.

The second project presented in Chapter 4 provides a new approach to synthesize polymeric cocoons with biodegradable cellulose. It is presented as a novel nanocarrier for drug delivery. It demonstrated that surface crosslinking is essential in higher encapsulation

value as well as more modulated release rate, which should be widely adopted in crafting unimolecular micelles as drug delivery vehicles. Due to robust ATRP polymerization technique, a variety of different functional polymer can be directly synthesized to be the inner or outer block to suit for different drug delivery system. For example, specific host molecular can be attached to the inner core for selective encapsulation of certain guest drugs, proteins, even DNA. Stimuli-responsive properties can be induced into the outer block by special polymeric design to internally modulate the crosslink structure and control the release rate in-vivo, which should be the future direction for drug delivery research. This project also provides a new strategy to synthesize perovskite nanorods which has superior colloidal stabilities than previously reported nanorods. The major weakness of perovskite materials such as $CsPbBr_3$ is poor stability especially to moisture and UV, which hinders their commercial application in photoelectronic devices. The permanent polymer capping impart much more enhanced water, UV, thermal stabilities that cannot be achieved through conventional methods.

More importantly, in boarder aspect, the cellulosed-based bottlebrush core-shell copolymers can be exploited as nanoreactors to synthesize all types of nanorods with tunable size, aspect ratio, and composition. It presents as a newly developed advanced nanorod synthesis technique which enables the crafting of specifically designed nanorod structure with much higher precision than other synthesis strategies.

The third project presented in Chapter 5 developed a novel strategy to synthesize Janus star-shaped block copolymers, which has been rarely investigated due to limited synthetic approaches available. A bifunctional Janus initiator is crucial in this strategy in order to have different polymers grow on the opposite sides of the initiator. A major

contribution of this project is the development of selective functionalization of β-CD, a biocompound with intriguing Janus structure and abundant functional groups. Janus star-shaped polymer was synthesized by adopting two different polymerization techniques that can be carried out independently. It provides a general guideline for the design of other types of Janus polymers with more complicated and precisely controlled structures by combining rational initiator design with multiple controlled living polymerization techniques. More importantly, these Janus star-shaped block copolymers can be used to synthesize strictly biphasic inorganic Janus nanoparticles comprising two hemispheres, which has never been synthesized before. This first attempt has broad impact in many ways. First, it demonstrates that highly anisotropic structures can be achieved through nanoreactor strategy. Second, unique physical properties will arise with strictly biphasic Janus particles which are different from the traditionally synthesized dumbbell-shaped Janus nanoparticles. For example, the photocatalytic properties will be different due to different interfacial integration. Strictly biphasic Janus particles have large planar interface while dumbbell Janus nanoparticles have small curved interface. Not only will it open a new door for fundamental study of biphasic interactions in Janus nanoparticles including self-assembly behavior, the bifunctional physical and chemical properties originated from the combination of two different nanomaterials will bring immerse potential in the application of nanomotors, bioimaging, photocatalysis, etc.

In general, this dissertation aims to establish a general methodology for the design and synthesis of block copolymers with complex architectures and subsequently use them as nanoreactors to produce nanocrystals of precisely defined size and shape. Going beyond the star-shaped, bottlebrush-shaped, and Janus star-shaped morphologies that were

investigated here, much more sophisticated structures ,both polymeric and inorganic could, be developed via the combination of modern polymer synthesis techniques such as living polymerization, click chemistry, host-guest interaction, polymer functionalization, and even ionic or hydrogen bonding. In the meantime, nanoreactor strategy for nanocrystal synthesis also enables the possibility for precision nanofabrication of artificially designed nanostructures with no limitation.

DISSEMINATION OF WORK

This work has been disseminated to the broader researcher community in the following publications and presentations.

Publications

1. **Z. Wang**, Y. Harn, S. Liang, Y. Liu, and Z. Lin*, Robust Route to Multi-Functional Cellulose-Based Polymeric Bottle-Brush Cocoons. (Submitted)

2. S. Zhao†, **Z. Wang†**, H. Zhang, Y. Harn, and Z. Lin*, Homophase Metal Coarsening: an Essential Reason for the Capacity Decay of Conversion Type Metal Oxide Anodes for Lithium/Sodium Ion Batteries. (In preparation)

3. S. Zhao, **Z. Wang**, Y. He, H. Jiang, Y. Harn, X. Liu, C. Su, H. Jin, Y. Li*, S. Wang*, Q. Shen*, and Z. Lin*, A Robust Route to $Co_2(OH)_2CO_3$ Ultrathin Nanosheets with Superior Lithium Storage Capability Templated by Aspartic Acid-Functionalized Graphene Oxide. *Advanced Energy Materials*. **2019**, 9, 1901093

4. Y. Chen, **Z. Wang**, Y. Harn, S. Pan, Z. Li, S. Lin, J. Peng, G. Zhang, and Z. Lin*, Resolving Optical and Catalytic Activities in Thermoresponsive Nanoparticles by Permanent Ligation with Temperature-Sensitive Polymers. *Angewandte Chemie International Edition*. **2019**, 58, 11910.

5. Y. Chen, **Z. Wang**, Y. He, Y. J. Yoon, J. Jung, G. Zhang*, and Z. Lin*, Light-Enabled Reversible Self-Assembly and Tunable Optical Properties of Stable Hairy Nanoparticles. *Proceedings of the National Academy of Sciences of the United State of America*. **2018**, 115, E1391.

6. S. Zhao, **Z. Wang**, Y. He, B. Jiang, Y. Harn, X. Liu, F. Yu, F. Feng, Q. Shen, and Z. Lin*, Interconnected $Ni(HCO_3)_2$ Hollow Spheres Enabled by Self-Sacrificial Templating with Enhanced Lithium Storage Properties. *ACS Energy Letters*. **2017**, 2, 111.

7. Y. Yoon, Y. Chang, S. Zhang, M. Zhang, S. Pan, Y. He, C. Lin, S. Yu, Y. Chen, **Z. Wang**, Y. Ding, J. Jung, N. Thadhani, V. V. Tsukruk, Z. Kang, and Z. Lin*, Enabling Tailorable Optical Properties and Markedly Enhanced Stability of Perovskite Quantum Dots by Permanently Ligating with Polymer Hairs. *Advanced Materials*. **2019**, 31, 1901602.

8. X. Meng, X. Cui, M. Rager, S. Zhang, **Z. Wang**, J. Yu, Y. Harn, Z. Kang, B. K. Wagner, Y. Liu, C. Yu, J. Qiu,* and Z. Lin*, Cascade Charge Transfer Enabled by Incorporating Edge-Enriched Graphene Nanoribbons for Mesostructured Perovskite Solar Cells with Enhanced Performance. *Nano Energy*. **2018**, 52, 123.

9. Y. Chang, Y. Yoon, G. Li, E. Xu, S. Yu, C. Lu, **Z. Wang**, Y. He, C. Lin, B. K. Wagner, V. V. Tsukruk, Z. Kang, N. Thadhani, Y. Jiang*, and Z. Lin*, All-Inorganic Perovskite Nanocrystals with a Stellar Set of Stabilities and Their Use in White Light-Emitting Diodes. *ACS Applied Materials & Interfaces*. **2018**, 10, 37267.

10. Y. Chen, D. Yang, Y. J. Yoon, X. Pang, **Z. Wang**, J. Jung, Y. He, Y. W. Harn, M. He, S. Zhang, G. Zhang*, and Z. Lin*, Hairy Uniform Permanently-Ligated Hollow Nanoparticles with Precise Dimension Control and Tunable Optical Properties. *Journal of the American Chemical Society*. **2017**, 139, 12956.

11. X. Cui, P. Xiao, J. Wang, M. Zhou, W. Guo, Y. Yang, Y. He, **Z. Wang**, Y. Yang, Y. Zhang*, and Z. Lin*, Highly Branched Metal Alloy Networks with Superior Activities for Methanol Oxidation Reaction. *Angewandte Chemie International Edition*. **2017**, 56, 4488.

Presentations

1. **Z. Wang**, S. Zhao, H. Zhang, Z. Lin*, "Crafting mono-disperse bimetallic oxide nanoparticles via polymeric nanoreactors with enhanced lithium storage properties", American Chemical Society Fall National Meeting, Boston, 2018.

2. **Z. Wang**, Z. Lin*, "Robust route to multi-functional cellulose-based polymeric bottle-brush cocoons", American Chemical Society Southeastern Regional Meeting, Savannah, 2019.

REFERENCES

1. Zheng, Y. C.; Li, S. P.; Weng, Z. L.; Gao, C., Hyperbranched polymers: advances from synthesis to applications. *Chem. Soc. Rev.* **2015,** *44* (12), 4091-4130.

2. Matyjaszewski, K.; Xia, J. H., Atom transfer radical polymerization. *Chem. Rev.* **2001,** *101* (9), 2921-2990.

3. Chiefari, J.; Chong, Y. K.; Ercole, F.; Krstina, J.; Jeffery, J.; Le, T. P. T.; Mayadunne, R. T. A.; Meijs, G. F.; Moad, C. L.; Moad, G.; Rizzardo, E.; Thang, S. H., Living free-radical polymerization by reversible addition-fragmentation chain transfer: The RAFT process. *Macromolecules* **1998,** *31* (16), 5559-5562.

4. Hadjichristidis, N.; Pitsikalis, M.; Pispas, S.; Iatrou, H., Polymers with complex architecture by living anionic polymerization. *Chem. Rev.* **2001,** *101* (12), 3747-3792.

5. Nguyen, S. T.; Johnson, L. K.; Grubbs, R. H.; Ziller, J. W., Ring-Opening Metathesis Polymerization (Romp) of Norbornene by a Group-Viii Carbene Complex in Protic Media. *J. Am. Chem. Soc.* **1992,** *114* (10), 3974-3975.

6. Liberman-Martin, A. L.; Chu, C. K.; Grubbs, R. H., Application of Bottlebrush Block Copolymers as Photonic Crystals. *Macromol. Rapid. Comm.* **2017,** *38* (13), 1700058.

7. Ren, J. M.; McKenzie, T. G.; Fu, Q.; Wong, E. H. H.; Xu, J. T.; An, Z. S.; Shanmugam, S.; Davis, T. P.; Boyer, C.; Qiao, G. G., Star Polymers. *Chem. Rev.* **2016,** *116* (12), 6743-6836.

8. Jesberger, M.; Barner, L.; Stenzel, M. H.; Malmstrom, E.; Davis, T. P.; Barner-Kowollik, C., Hyperbranched polymers as scaffolds for multifunctional reversible addition-fragmentation chain-transfer agents: A route to polystyrene-core-polyesters and polystyrene-block-poly(butyl acrylate)-core-polyesters. *J. Polym. Sci. Pol. Chem* **2003,** *41* (23), 3847-3861.

9. Kreutzer, G.; Ternat, C.; Nguyen, T. Q.; Plummer, C. J. G.; Manson, J. A. E.; Castelletto, V.; Hamley, I. W.; Sun, F.; Sheiko, S. S.; Herrmann, A.; Ouali, L.; Sommer, H.; Fieber, W.; Velazco, M. I.; Klok, H. A., Water-soluble, unimolecular containers based on amphiphilic multiarm star block copolymers. *Macromolecules* **2006,** *39* (13), 4507-4516.

10. Iocozzia, J.; Lin, Z. Q., Solution-Stable Colloidal Gold Nanoparticles via Surfactant-Free, Hyperbranched Polyglycerol-b-polystyrene Unimolecular Templates. *Langmuir*. **2016,** *32* (28), 7180-7188.

11. Hao, X. J.; Nilsson, C.; Jesberger, M.; Stenzel, M. H.; Malmstrom, E.; Davis, T. P.; Ostmark, E.; Barner-Kowollik, C., Dendrimers as scaffolds for multifunctional reversible addition-fragmentation chain transfer agents: Syntheses and polymerization. *J. Polym. Sci. Pol. Chem* **2004,** *42* (23), 5877-5890.

12. Hedrick, J. L.; Trollsas, M.; Hawker, C. J.; Atthoff, B.; Claesson, H.; Heise, A.; Miller, R. D.; Mecerreyes, D.; Jerome, R.; Dubois, P., Dendrimer-like star block and amphiphilic copolymers by combination of ring opening and atom transfer radical polymerization. *Macromolecules* **1998,** *31* (25), 8691-8705.

13. Li, X. J.; Qian, Y. F.; Liu, T.; Hu, X. L.; Zhang, G. Y.; You, Y. Z.; Liu, S. Y., Amphiphilic multiarm star block copolymer-based multifunctional unimolecular micelles for cancer targeted drug delivery and MR imaging. *Biomaterials.* **2011,** *32* (27), 6595-6605.

14. Prabaharan, M.; Grailer, J. J.; Pilla, S.; Steeber, D. A.; Gong, S. Q., Amphiphilic multi-arm-block copolymer conjugated with doxorubicin via pH-sensitive hydrazone bond for tumor-targeted drug delivery. *Biomaterials.* **2009,** *30* (29), 5757-5766.

15. Li, J. S.; Xiao, H. N.; Kim, Y. S.; Lowe, T. L., Synthesis of water-soluble cationic polymers with star-like structure based on cyclodextrin core via ATRP. *J. Polym. Sci. Pol. Chem* **2005,** *43* (24), 6345-6354.

16. Plamper, F. A.; Becker, H.; Lanzendorfer, M.; Patel, M.; Wittemann, A.; Ballauff, M.; Muller, A. H. E., Synthesis, characterization and behavior in aqueous solution of star-shaped poly(acrylic acid). *Macromol. Chem. Phys.* **2005,** *206* (18), 1813-1825.

17. Karaky, K.; Reynaud, S.; Billon, L.; Francois, J.; Chreim, Y., Organosoluble star polymers from a cyclodextrin core. *J. Polym. Sci. Pol. Chem* **2005,** *43* (21), 5186-5194.

18. Pang, X. C.; Zhao, L.; Akinc, M.; Kim, J. K.; Lin, Z. Q., Novel Amphiphilic Multi-Arm, Star-Like Block Copolymers as Unimolecular Micelles. *Macromolecules* **2011,** *44* (10), 3746-3752.

19. Feng, C. W.; Pang, X. C.; He, Y. J.; Li, B.; Lin, Z. Q., Robust Route to Unimolecular Core-Shell and Hollow Polymer Nanoparticles. *Chem. Mater.* **2014,** *26* (20), 6058-6067.

20. Xu, J.; Liu, S. Y., Synthesis of Well-Defined 7-Arm and 21-Arm Poly (N-isopropylacrylamide) Star Polymers with beta-Cyclodextrin Cores via Click Chemistry and Their Thermal Phase Transition Behavior in Aqueous Solution. *J. Polym. Sci. Pol. Chem* **2009,** *47* (2), 404-419.

21. Pang, X. C.; Zhao, L.; Feng, C. W.; Lin, Z. Q., Novel Amphiphilic Multiarm, Starlike Coil-Rod Diblock Copolymers via a Combination of Click Chemistry with Living Polymerization. *Macromolecules* **2011,** *44* (18), 7176-7183.

22. He, Y. J.; Pang, X. C.; Jiang, B. B.; Feng, C. W.; Harn, Y. W.; Chen, Y. H.; Yoon, Y. J.; Pan, S.; Lu, C. H.; Chang, Y. J.; Zebarjadi, M.; Kang, Z. T.; Thadhani, N.; Peng, J.; Lin, Z. Q., Unconventional Route to Uniform Hollow Semiconducting Nanoparticles with Tailorable Dimensions, Compositions, Surface Chemistry, and Near-Infrared Absorption. *Angew. Chem. Int. Ed.* **2017,** *56* (42), 12946-12951.

23. Jiang, B. B.; Pang, X. C.; Li, B.; Lin, Z. Q., Organic-Inorganic Nanocomposites via Placing Monodisperse Ferroelectric Nanocrystals in Direct and Permanent Contact with Ferroelectric Polymers. *J. Am. Chem. Soc.* **2015,** *137* (36), 11760-11767.

24. Xu, H.; Pang, X. C.; He, Y. J.; He, M.; Jung, J. H.; Xia, H. P.; Lin, Z. Q., An Unconventional Route to Monodisperse and Intimately Contacted Semiconducting Organic-Inorganic Nanocomposites. *Angew. Chem. Int. Ed.* **2015,** *54* (15), 4636-4640.

25. Yang, D.; Pang, X. C.; He, Y. J.; Wang, Y. Q.; Chen, G. X.; Wang, W. Z.; Lin, Z. Q., Precisely Size-Tunable Magnetic/Plasmonic Core/Shell Nanoparticles with Controlled Optical Properties. *Angew. Chem. Int. Ed.* **2015,** *54* (41), 12091-12096.

26. Wintermantel, M.; Gerle, M.; Fischer, K.; Schmidt, M.; Wataoka, I.; Urakawa, H.; Kajiwara, K.; Tsukahara, Y., Molecular bottlebrushes. *Macromolecules* **1996,** *29* (3), 978-983.

27. Joannopoulos, J. D.; Johnson, S. G.; Winn, J. N.; Meade, R. D., *Photonic crystals: molding the flow of light*. Princeton university press: 2011.

28. Kang, Y.; Walish, J. J.; Gorishnyy, T.; Thomas, E. L., Broad-wavelength-range chemically tunable block-copolymer photonic gels. *Nat. Mater.* **2007,** *6* (12), 957.

29. Miyake, G. M.; Weitekamp, R. A.; Piunova, V. A.; Grubbs, R. H., Synthesis of isocyanate-based brush block copolymers and their rapid self-assembly to infrared-reflecting photonic crystals. *J. Am. Chem. Soc.* **2012,** *134* (34), 14249-14254.

30. Phillips, C. L.; Glotzer, S. C., Effect of nanoparticle polydispersity on the self-assembly of polymer tethered nanospheres. *J. Chem. Phys.* **2012,** *137* (10), 104901.

31. Piunova, V. A.; Miyake, G. M.; Daeffler, C. S.; Weitekamp, R. A.; Grubbs, R. H., Highly ordered dielectric mirrors via the self-assembly of dendronized block copolymers. *J. Am. Chem. Soc.* **2013,** *135* (41), 15609-15616.

32. Runge, M. B.; Bowden, N. B., Synthesis of high molecular weight comb block copolymers and their assembly into ordered morphologies in the solid state. *J. Am. Chem. Soc.* **2007,** *129* (34), 10551-10560.

33. Rzayev, J., Synthesis of polystyrene− polylactide bottlebrush block copolymers and their melt self-assembly into large domain nanostructures. *Macromolecules* **2009,** *42* (6), 2135-2141.

34. Sveinbjornsson, B. R.; Weitekamp, R. A.; Miyake, G. M.; Xia, Y.; Atwater, H. A.; Grubbs, R. H., Rapid self-assembly of brush block copolymers to photonic crystals. *Proceedings of the National Academy of Sciences of the United States of America* **2012,** *109* (36), 14332-14336.

35. Xia, Y.; Olsen, B. D.; Kornfield, J. A.; Grubbs, R. H., Efficient synthesis of narrowly dispersed brush copolymers and study of their assemblies: the importance of side chain arrangement. *J. Am. Chem. Soc.* **2009,** *131* (51), 18525-18532.

36. Sun, G.; Cho, S.; Clark, C.; Verkhoturov, S. V.; Eller, M. J.; Li, A.; Pavía-Jiménez, A.; Schweikert, E. A.; Thackeray, J. W.; Trefonas, P., Nanoscopic cylindrical dual concentric and lengthwise block brush terpolymers as covalent preassembled high-resolution and high-sensitivity negative-tone photoresist materials. *J. Am. Chem. Soc.* **2013,** *135* (11), 4203-4206.

37. Cho, S.; Yang, F.; Sun, G.; Eller, M. J.; Clark, C.; Schweikert, E. A.; Thackeray, J. W.; Trefonas, P.; Wooley, K. L., Directing Self‐Assembly of Nanoscopic Cylindrical Diblock Brush Terpolymers into Films with Desired Spatial Orientations: Expansion of Chemical Composition Scope. *Macromol. Rapid. Comm.* **2014,** *35* (4), 437-441.

38. Sun, G.; Cho, S.; Yang, F.; He, X.; Pavía‐Sanders, A.; Clark, C.; Raymond, J. E.; Verkhoturov, S. V.; Schweikert, E. A.; Thackeray, J. W., Advanced photoresist technologies by intricate molecular brush architectures: Diblock brush terpolymer‐based positive‐tone photoresist materials. *Journal of Polymer Science Part A: Polymer Chemistry* **2015,** *53* (2), 193-199.

39. Xu, H.; Sun, F. C.; Shirvanyants, D. G.; Rubinstein, M.; Shabratov, D.; Beers, K. L.; Matyjaszewski, K.; Sheiko, S. S., Molecular pressure sensors. *Adv. Mater.* **2007,** *19* (19), 2930-2934.

40. Nese, A.; Lebedeva, N. V.; Sherwood, G.; Averick, S.; Li, Y.; Gao, H.; Peteanu, L.; Sheiko, S. S.; Matyjaszewski, K., pH-responsive fluorescent molecular bottlebrushes prepared by Atom Transfer Radical polymerization. *Macromolecules* **2011,** *44* (15), 5905-5910.

41. Djalali, R.; Li, S. Y.; Schmidt, M., Amphipolar core-shell cylindrical brushes as templates for the formation of gold clusters and nanowires. *Macromolecules* **2002,** *35* (11), 4282-4288.

42. Zhang, M.; Estournes, C.; Bietsch, W.; Müller, A., Superparamagnetic hybrid nanocylinders. *Adv. Funct. Mater.* **2004,** *14* (9), 871-882.

43. Xu, Y.; Yuan, J.; Fang, B.; Drechsler, M.; Müllner, M.; Bolisetty, S.; Ballauff, M.; Müller, A. H., Hybrids of Magnetic Nanoparticles with Double‐Hydrophilic Core/Shell Cylindrical Polymer Brushes and Their Alignment in a Magnetic Field. *Adv. Funct. Mater.* **2010,** *20* (23), 4182-4189.

44. Zhang, M.; Drechsler, M.; Müller, A. H., Template-controlled synthesis of wire-like cadmium sulfide nanoparticle assemblies within core− shell cylindrical polymer brushes. *Chem. Mater.* **2004,** *16* (3), 537-543.

45. Yuan, J.; Drechsler, M.; Xu, Y.; Zhang, M.; Müller, A. H., Cadmium selenide nanowires within core–shell cylindrical polymer brushes: Synthesis, characterization and the double-loading process. *Polymer* **2008,** *49* (6), 1547-1554.

46. Yuan, J. Y.; Xu, Y. Y.; Walther, A.; Bolisetty, S.; Schumacher, M.; Schmalz, H.; Ballauff, M.; Muller, A. H. E., Water-soluble organo-silica hybrid nanowires. *Nat. Mater.* **2008,** *7* (9), 718-722.

47. Huang, K.; Rzayev, J., Well-Defined Organic Nanotubes from Multicomponent Bottlebrush Copolymers. *Journal of the American Chemical Society* **2009,** *131* (19), 6880-6885.

48. Huang, K.; Johnson, M.; Rzayev, J., Synthesis of degradable organic nanotubes by bottlebrush molecular templating. *ACS Macro Letters* **2012,** *1* (7), 892-895.

49. Huang, K.; Canterbury, D. P.; Rzayev, J., Synthesis of segmented polylactide molecular brushes and their transformation to open-end nanotubes. *Macromolecules* **2010,** *43* (16), 6632-6638.

50. Huang, K.; Jacobs, A.; Rzayev, J., De novo synthesis and cellular uptake of organic nanocapsules with tunable surface chemistry. *Biomacromolecules* **2011,** *12* (6), 2327-2334.

51. Zou, J.; Jafr, G.; Themistou, E.; Yap, Y.; Wintrob, Z. A.; Alexandridis, P.; Ceacareanu, A. C.; Cheng, C., pH-Sensitive brush polymer-drug conjugates by ring-opening metathesis copolymerization. *Chem. Commun.* **2011,** *47* (15), 4493-4495.

52. Li, Y.; Zou, J.; Das, B. P.; Tsianou, M.; Cheng, C., Well-defined amphiphilic double-brush copolymers and their performance as emulsion surfactants. *Macromolecules* **2012,** *45* (11), 4623-4629.

53. Yang, Y. Q.; Guo, X. D.; Lin, W. J.; Zhang, L. J.; Zhang, C. Y.; Qian, Y., Amphiphilic copolymer brush with random pH-sensitive/hydrophobic structure: synthesis and self-assembled micelles for sustained drug delivery. *Soft Matter* **2012,** *8* (2), 454-464.

54. Johnson, J. A.; Lu, Y. Y.; Burts, A. O.; Xia, Y.; Durrell, A. C.; Tirrell, D. A.; Grubbs, R. H., Drug-loaded, bivalent-bottle-brush polymers by graft-through ROMP. *Macromolecules* **2010,** *43* (24), 10326-10335.

55. Sheiko, S. S.; Sumerlin, B. S.; Matyjaszewski, K., Cylindrical molecular brushes: Synthesis, characterization, and properties. *Prog. Polym. Sci.* **2008,** *33* (7), 759-785.

56. Ito, K.; Kawaguchi, S., PMs: Homo-and Copolymeriztion. *Adv. Polym. Sci* **1999,** *142*, 128.

57. Hadjichristidis, N.; Pitsikalis, M.; Iatrou, H.; Pispas, S., The strength of the macromonomer strategy for complex macromolecular architecture: molecular characterization, properties and applications of polymacromonomers. *Macromol. Rapid. Comm.* **2003,** *24* (17), 979-1013.

58. Mijović, J.; Sun, M.; Pejanović, S.; Mays, J. W., Effect of molecular architecture on dynamics of multigraft copolymers: combs, centipedes, and barbwires. *Macromolecules* **2003,** *36* (20), 7640-7651.

59. Lee, H.-i.; Pietrasik, J.; Sheiko, S. S.; Matyjaszewski, K., Stimuli-responsive molecular brushes. *Prog. Polym. Sci.* **2010,** *35* (1), 24-44.

60. Feng, C.; Li, Y.; Yang, D.; Hu, J.; Zhang, X.; Huang, X., Well-defined graft copolymers: from controlled synthesis to multipurpose applications. *Chem. Soc. Rev.* **2011,** *40* (3), 1282-1295.

61. Mullner, M.; Muller, A. H. E., Cylindrical polymer brushes - Anisotropic building blocks, unimolecular templates and particulate nanocarriers. *Polymer* **2016,** *98*, 389-401.

62. Stupp, S. I.; LeBonheur, V.; Walker, K.; Li, L.-S.; Huggins, K. E.; Keser, M.; Amstutz, A., Supramolecular materials: self-organized nanostructures. *Science* **1997,** *276* (5311), 384-389.

63. Ruokolainen, J.; Tanner, J.; Ten Brinke, G.; Ikkala, O.; Torkkeli, M.; Serimaa, R., Poly (4-vinyl pyridine)/zinc dodecyl benzene sulfonate mesomorphic state due to coordination complexation. *Macromolecules* **1995,** *28* (23), 7779-7784.

64. Antonietti, M.; Conrad, J.; Thuenemann, A., Polyelectrolyte-surfactant complexes: a new type of solid, mesomorphous material. *Macromolecules* **1994,** *27* (21), 6007-6011.

65. Schappacher, M.; Deffieux, A., New polymer chain architecture: synthesis and characterization of star polymers with comb polystyrene branches. *Macromolecules* **2000,** *33* (20), 7371-7377.

66. Uhrig, D.; Mays, J. W., Synthesis of combs, centipedes, and barbwires: poly (isoprene-graft-styrene) regular multigraft copolymers with trifunctional, tetrafunctional, and hexafunctional branch points. *Macromolecules* **2002,** *35* (19), 7182-7190.

67. Iatrou, H.; Mays, J. W.; Hadjichristidis, N., Regular comb polystyrenes and graft polyisoprene/polystyrene copolymers with double branches ("centipedes"). Quality of (1, 3-phenylene) bis (3-methyl-1-phenylpentylidene) dilithium initiator in the presence of polar additives. *Macromolecules* **1998,** *31* (19), 6697-6701.

68. Gao, H.; Matyjaszewski, K., Synthesis of molecular brushes by "grafting onto" method: combination of ATRP and click reactions. *J. Am. Chem. Soc.* **2007,** *129* (20), 6633-6639.

69. Hou, C.; Hu, J.; Liu, G.; Wang, J.; Liu, F.; Hu, H.; Zhang, G.; Zou, H.; Tu, Y.; Liao, B., Synthesis and bulk self-assembly of well-defined binary graft copolymers. *Macromolecules* **2013,** *46* (10), 4053-4063.

70. Schappacher, M.; Deffieux, A., From combs to comb-g-comb centipedes. *Macromolecules* **2005,** *38* (17), 7209-7213.

71. Lanson, D.; Ariura, F.; Schappacher, M.; Borsali, R.; Deffieux, A., Comb copolymers with polystyrene and polyisoprene branches: effect of block topology on film morphology. *Macromolecules* **2009,** *42* (12), 3942-3950.

72. Chen, P.; Li, C.; Liu, D.; Li, Z., DNA-grafted polypeptide molecular bottlebrush prepared via ring-opening polymerization and click chemistry. *Macromolecules* **2012,** *45* (24), 9579-9584.

73. Gerle, M.; Fischer, K.; Roos, S.; Müller, A. H.; Schmidt, M.; Sheiko, S. S.; Prokhorova, S.; Möller, M., Main chain conformation and anomalous elution behavior of cylindrical brushes as revealed by GPC/MALLS, light scattering, and SFM. *Macromolecules* **1999,** *32* (8), 2629-2637.

74. Cheng, G. L.; Boker, A.; Zhang, M. F.; Krausch, G.; Muller, A. H. E., Amphiphilic cylindrical core-shell brushes via a "grafting from" process using ATRP. *Macromolecules* **2001,** *34* (20), 6883-6888.

75. Tsukahara, Y.; Kohjiya, S.; Tsutsumi, K.; Okamoto, Y., On the intrinsic viscosity of poly (macromonomer) s. *Macromolecules* **1994,** *27* (6), 1662-1664.

76. Tsukahara, Y.; Tsutsumi, K.; Yamashita, Y.; Shimada, S., Radical polymerization behavior of macromonomers. 2. Comparison of styrene macromonomers having a methacryloyl end group and a vinylbenzyl end group. *Macromolecules* **1990,** *23* (25), 5201-5208.

77. Wintermantel, M.; Schmidt, M.; Tsukahara, Y.; Kajiwara, K.; Kohjiya, S., Rodlike combs. *Macromol. Rapid. Comm.* **1994,** *15* (3), 279-284.

78. Hatada, K.; Kitayama, T.; Masuda, E.; Kamachi, M., Electron paramagnetic resonance observation of propagating radicals in the polymerization of highly syndiotactic ω - (p - vinylbenzyl) poly (methyl methacrylate) macromonomer. *Macromol. Rapid. Comm.* **1990,** *11* (2), 101-107.

79. Masuda, E.; Kishiro, S.; Kitayama, T.; Hatada, K., Radical polymerization of highly isotactic and syndiotactic poly (methyl methacrylate) macromonomers. *Polym. J.* **1991,** *23* (7), 847-857.

80. Sheiko, S.; Gerle, M.; Fischer, K.; Schmidt, M.; Möller, M., Wormlike polystyrene brushes in thin films. *Langmuir.* **1997,** *13* (20), 5368-5372.

81. Dziezok, P.; Fischer, K.; Schmidt, M.; Sheiko, S. S.; Möller, M., Cylindrical molecular brushes. *Angew. Chem. Int. Ed.* **1997,** *36* (24), 2812-2815.

82. Wintermantel, M.; Fischer, K.; Gerle, M.; Ries, R.; Schmidt, M.; Kajiwara, K.; Urakawa, H.; Wataoka, I., Lyotropic phases formed by "molecular bottlebrushes". *Angew. Chem. Int. Ed.* **1995,** *34* (13 - 14), 1472-1474.

83. Tsukahara, Y.; Ohta, Y.; Senoo, K., Liquid crystal formation of multibranched polystyrene induced by molecular anisotropy associated with its high branch density. *Polymer* **1995,** *36* (17), 3413-3416.

84. Ito, K.; Tanaka, K.; Tanaka, H.; Imai, G.; Kawaguchi, S.; Itsuno, S., Poly (ethylene oxide) macromonomers. 7. Micellar polymerization in water. *Macromolecules* **1991,** *24* (9), 2348-2354.

85. Nomura, E.; Ito, K.; Kajiwara, A.; Kamachi, M., Radical polymerization kinetics of poly (ethylene oxide) macromonomers. *Macromolecules* **1997,** *30* (10), 2811-2817.

86. Ishizu, K.; Yukimasa, S.; Saito, R., Organized ‐ polymerization in micelle formed by diblock macromonomers. *Journal of Polymer Science Part A: Polymer Chemistry* **1993,** *31* (12), 3073-3080.

87. Ishizu, K.; Tsubaki, K.-i.; Ono, T., Synthesis and dilute solution properties of poly (diblock macromonomer) s. *Polymer* **1998,** *39* (13), 2935-2939.

88. Grassl, B.; Rempp, S.; Galin, J. C., New super ‐ hairy semi ‐ rigid polymers. *Macromol. Chem. Phys.* **1998,** *199* (2), 239-246.

89. Mendrek, A.; Mendrek, S.; Trzebicka, B.; Kuckling, D.; Walach, W.; Adler, H. J.; Dworak, A., Polyether Core ‐ Shell Cylinder ‐ Polymerization of Polyglycidol Macromonomers. *Macromol. Chem. Phys.* **2005,** *206* (20), 2018-2026.

90. Ishizu, K.; Kakinuma, H.; Ochi, K.; Uchida, S.; Hayashi, M., Encapsulation of silver nanoparticles within double ‐ cylinder ‐ type copolymer brushes as templates. *Polym. Advan. Technol.* **2005,** *16* (11 ‐ 12), 834-839.

91. Deng, G.; Chen, Y., Preparation of novel macromonomers and study of their polymerization. *Journal of Polymer Science Part A: Polymer Chemistry* **2004,** *42* (15), 3887-3896.

92. Grubbs, R. H.; Tumas, W., Polymer synthesis and organotransition metal chemistry. *Science* **1989,** *243* (4893), 907-915.

93. Schrock, R. R., Living ring-opening metathesis polymerization catalyzed by well-characterized transition-metal alkylidene complexes. *Acc. Chem. Res.* **1990,** *23* (5), 158-165.

94. Cheng, C.; Khoshdel, E.; Wooley, K. L., ATRP from a norbornenyl-functionalized initiator: Balancing of complementary reactivity for the preparation of α-norbornenyl macromonomers/ω-haloalkyl macroinitiators. *Macromolecules* **2005,** *38* (23), 9455-9465.

95. Heroguez, V.; Breunig, S.; Gnanou, Y.; Fontanille, M., Synthesis of α-norbornenylpoly (ethylene oxide) macromonomers and their ring-opening metathesis polymerization. *Macromolecules* **1996,** *29* (13), 4459-4464.

96. Allcock, H. R.; de Denus, C. R.; Prange, R.; Laredo, W. R., Synthesis of norbornenyl telechelic polyphosphazenes and ring-opening metathesis polymerization reactions. *Macromolecules* **2001,** *34* (9), 2757-2765.

97. Mecerreyes, D.; Dahan, D.; Lecomte, P.; Dubois, P.; Demonceau, A.; Noels, A. F.; Jérôme, R., Ring‐opening metathesis polymerization of new α‐norbornenyl poly (ε‐caprolactone) macromonomers. *Journal of Polymer Science Part A: Polymer Chemistry* **1999,** *37* (14), 2447-2455.

98. Jha, S.; Dutta, S.; Bowden, N. B., Synthesis of ultralarge molecular weight bottlebrush polymers using Grubbs' catalysts. *Macromolecules* **2004,** *37* (12), 4365-4374.

99. Cheng, C.; Qi, K.; David, S. G.; Khoshdel, E.; Wooley, K. L. In *Crosslinked polymeric nanoparticles via brush copolymers*, The 2007 Annual Meeting, 2007.

100. Cheng, C.; Qi, K.; Khoshdel, E.; Wooley, K. L., Tandem synthesis of core-shell brush copolymers and their transformation to peripherally cross-linked and hollowed nanostructures. *J. Am. Chem. Soc.* **2006,** *128* (21), 6808-6809.

101. Cheng, C.; Khoshdel, E.; Wooley, K. L., One-Pot Tandem Synthesis of a Core− Shell Brush Copolymer from Small Molecule Reactants by Ring-Opening Metathesis and Reversible Addition− Fragmentation Chain Transfer (Co) polymerizations. *Macromolecules* **2007,** *40* (7), 2289-2292.

102. Yamada, K.; Miyazaki, M.; Ohno, K.; Fukuda, T.; Minoda, M., Atom transfer radical polymerization of poly (vinyl ether) macromonomers. *Macromolecules* **1999,** *32* (2), 290-293.

103. Sumerlin, B. S.; Neugebauer, D.; Matyjaszewski, K., Initiation efficiency in the synthesis of molecular brushes by grafting from via atom transfer radical polymerization. *Macromolecules* **2005,** *38* (3), 702-708.

104. Neugebauer, D.; Sumerlin, B. S.; Matyjaszewski, K.; Goodhart, B.; Sheiko, S. S., How dense are cylindrical brushes grafted from a multifunctional macroinitiator? *Polymer* **2004,** *45* (24), 8173-8179.

105. Wang, J.-S.; Matyjaszewski, K., Controlled/" living" radical polymerization. Atom transfer radical polymerization in the presence of transition-metal complexes. *J. Am. Chem. Soc.* **1995,** *117* (20), 5614-5615.

106. Tsarevsky, N. V.; Matyjaszewski, K., "Green" atom transfer radical polymerization: from process design to preparation of well-defined environmentally friendly polymeric materials. *Chem. Rev.* **2007,** *107* (6), 2270-2299.

107. Braunecker, W. A.; Matyjaszewski, K., Controlled/living radical polymerization: Features, developments, and perspectives. *Prog. Polym. Sci.* **2007,** *32* (1), 93-146.

108. Pietrasik, J.; Sumerlin, B. S.; Lee, R. Y.; Matyjaszewski, K., Solution Behavior of Temperature‐Responsive Molecular Brushes Prepared by ATRP. *Macromol. Chem. Phys.* **2007,** *208* (1), 30-36.

109. Beers, K. L.; Gaynor, S. G.; Matyjaszewski, K.; Sheiko, S. S.; Möller, M., The synthesis of densely grafted copolymers by atom transfer radical polymerization. *Macromolecules* **1998,** *31* (26), 9413-9415.

110. Zhang, A.; Barner, J.; Göessl, I.; Rabe, J. P.; Schlüter, A. D., A Covalent‐Chemistry Approach to Giant Macromolecules and Their Wetting Behavior on Solid Substrates. *Angew. Chem. Int. Ed.* **2004,** *43* (39), 5185-5188.

111. Börner, H. G.; Beers, K.; Matyjaszewski, K.; Sheiko, S. S.; Möller, M., Synthesis of molecular brushes with block copolymer side chains using atom transfer radical polymerization. *Macromolecules* **2001,** *34* (13), 4375-4383.

112. Zhang, M.; Breiner, T.; Mori, H.; Müller, A. H., Amphiphilic cylindrical brushes with poly (acrylic acid) core and poly (n-butyl acrylate) shell and narrow length distribution. *Polymer* **2003,** *44* (5), 1449-1458.

113. Qin, S.; Matyjaszewski, K.; Xu, H.; Sheiko, S. S., Synthesis and visualization of densely grafted molecular brushes with crystallizable poly (octadecyl methacrylate) block segments. *Macromolecules* **2003,** *36* (3), 605-612.

114. Grubbs, R. B.; Hawker, C. J.; Dao, J.; Fréchet, J. M., A tandem approach to graft and dendritic graft copolymers based on “living” free radical polymerizations. *Angew. Chem. Int. Ed.* **1997,** *36* (3), 270-272.

115. Venkatesh, R.; Yajjou, L.; Koning, C. E.; Klumperman, B., Novel brush copolymers via controlled radical polymerization. *Macromol. Chem. Phys.* **2004,** *205* (16), 2161-2168.

116. Khelfallah, N.; Gunari, N.; Fischer, K.; Gkogkas, G.; Hadjichristidis, N.; Schmidt, M., Micelles Formed by Cylindrical Brush‐Coil Block Copolymers. *Macromol. Rapid. Comm.* **2005,** *26* (21), 1693-1697.

117. Xia, Y.; Kornfield, J. A.; Grubbs, R. H., Efficient synthesis of narrowly dispersed brush polymers via living ring-opening metathesis polymerization of macromonomers. *Macromolecules* **2009,** *42* (11), 3761-3766.

118. Zhang, M. F.; Drechsler, M.; Muller, A. H. E., Template-controlled synthesis of wire-like cadmium sulfide nanoparticle assemblies within core-shell cylindrical polymer brushes. *Chem. Mater.* **2004,** *16* (3), 537-543.

119. Moughton, A. O.; Sagawa, T.; Gramlich, W. M.; Seo, M.; Lodge, T. P.; Hillmyer, M. A., Synthesis of block polymer mikto brushes. *Polym. Chem.* **2013,** *4* (1), 166-173.

120. Runge, M. B.; Yoo, J.; Bowden, N. B., Synthesis of Comb Tri - and Tetrablock Copolymers Catalyzed by the Grubbs First Generation Catalyst. *Macromol. Rapid. Comm.* **2009,** *30* (16), 1392-1398.

121. Degennes, P. G., Soft Matter. *Science* **1992,** *256* (5056), 495-497.

122. Walther, A.; Muller, A. H. E., Janus Particles: Synthesis, Self-Assembly, Physical Properties, and Applications. *Chem. Rev.* **2013,** *113* (7), 5194-5261.

123. Yan, J.; Han, M.; Zhang, J.; Xu, C.; Luijten, E.; Granick, S., Reconfiguring active particles by electrostatic imbalance. *Nat. Mater.* **2016,** *15* (10), 1095.

124. Takei, H.; Shimizu, N., Gradient sensitive microscopic probes prepared by gold evaporation and chemisorption on latex spheres. *Langmuir.* **1997,** *13* (7), 1865-1868.

125. Hu, S. H.; Gao, X. H., Nanocomposites with Spatially Separated Functionalities for Combined Imaging and Magnetolytic Therapy. *J. Am. Chem. Soc.* **2010,** *132* (21), 7234.

126. Glaser, N.; Adams, D. J.; Boker, A.; Krausch, G., Janus particles at liquid-liquid interfaces. *Langmuir.* **2006,** *22* (12), 5227-5229.

127. Ruhland, T. M.; Groschel, A. H.; Wather, A.; Muller, A. H. E., Janus Cylinders at Liquid-Liquid Interfaces. *Langmuir.* **2011,** *27* (16), 9807-9814.

128. Xu, C.; Xie, J.; Ho, D.; Wang, C.; Kohler, N.; Walsh, E. G.; Morgan, J. R.; Chin, Y. E.; Sun, S., Au-Fe3O4 dumbbell nanoparticles as dual-functional probes. *Angew. Chem. Int. Ed.* **2008,** *47* (1), 173-176.

129. Isojima, T.; Lattuada, M.; Vander Sande, J. B.; Hatton, T. A., Reversible clustering of pH- and temperature-responsive Janus magnetic nanoparticles. *ACS Nano* **2008,** *2* (9), 1799-1806.

130. Gangwal, S.; Cayre, O. J.; Velev, O. D., Dielectrophoretic Assembly of Metallodielectric Janus Particles in AC Electric Fields. *Langmuir.* **2008,** *24* (23), 13312-13320.

131. Zhao, N.; Gao, M. Y., Magnetic Janus Particles Prepared by a Flame Synthetic Approach: Synthesis, Characterizations and Properties. *Adv. Mater.* **2009,** *21* (2), 184.

132. Anker, J. N.; Behrend, C.; Kopelman, R., Aspherical magnetically modulated optical nanoprobes (MagMOONs). *J. Appl. Phys.* **2003,** *93* (10), 6698-6700.

133. Anker, J. N.; Behrend, C. J.; Huang, H. M.; Kopelman, R., Magnetically-modulated optical nanoprobes (MagMOONs) and systems. *J. Magn. Magn. Mater.* **2005,** *293* (1), 655-662.

134. Walther, A.; Hoffmann, M.; Muller, A. H. E., Emulsion polymerization using Janus particles as stabilizers. *Angew. Chem. Int. Ed.* **2008,** *47* (4), 711-714.

135. Walther, A.; Matussek, K.; Muller, A. H. E., Engineering nanostructured polymer blends with controlled nanoparticle location using Janus particles. *ACS Nano* **2008,** *2* (6), 1167-1178.

136. Xuan, M. J.; Wu, Z. G.; Shao, J. X.; Dai, L. R.; Si, T. Y.; He, O., Near Infrared Light-Powered Janus Mesoporous Silica Nanoparticle Motors. *J. Am. Chem. Soc.* **2016,** *138* (20), 6492-6497.

137. Xuan, M. J.; Shao, J. X.; Lin, X. K.; Dai, L. R.; He, Q., Self-Propelled Janus Mesoporous Silica Nanomotors with Sub-100 nm Diameters for Drug Encapsulation and Delivery. *Chemphyschem* **2014,** *15* (11), 2255-2260.

138. Dong, R. F.; Zhang, Q. L.; Gao, W.; Pei, A.; Ren, B. Y., Highly Efficient Light-Driven TiO2-Au Janus Micromotors. *ACS Nano* **2016,** *10* (1), 839-844.

139. Pradhan, S.; Ghosh, D.; Chen, S. W., Janus Nanostructures Based on Au-TiO2 Heterodimers and Their Photocatalytic Activity in the Oxidation of Methanol. *ACS Appl. Mater. Interfaces* **2009,** *1* (9), 2060-2065.

140. Seh, Z. W.; Liu, S. H.; Low, M.; Zhang, S. Y.; Liu, Z. L.; Mlayah, A.; Han, M. Y., Janus Au-TiO2 Photocatalysts with Strong Localization of Plasmonic Near-Fields for Efficient Visible-Light Hydrogen Generation. *Adv. Mater.* **2012,** *24* (17), 2310-2314.

141. Erhardt, R.; Boker, A.; Zettl, H.; Kaya, H.; Pyckhout-Hintzen, W.; Krausch, G.; Abetz, V.; Muller, A. H. E., Janus micelles. *Macromolecules* **2001,** *34* (4), 1069-1075.

142. Ma, R. J.; Wang, B. L.; Xu, Y. L.; An, Y. L.; Zhang, W. Q.; Li, G. Y.; Shi, L. Q., Surface phase separation and morphology of stimuli responsive complex micelles. *Macromol. Rapid. Comm.* **2007,** *28* (9), 1062-1069.

143. Zubarev, E. R.; Xu, J.; Sayyad, A.; Gibson, J. D., Amphiphilicity-driven organization of nanoparticles into discrete assemblies. *J. Am. Chem. Soc.* **2006,** *128* (47), 15098-15099.

144. Vilain, C.; Goettmann, F.; Moores, A.; Le Floch, P.; Sanchez, C., Study of metal nanoparticles stabilised by mixed ligand shell: a striking blue shift of the surface-plasmon band evidencing the formation of Janus nanoparticles. *J. Mater. Chem.* **2007,** *17* (33), 3509-3514.

145. Jakobs, R. T. M.; van Herrikhuyzen, J.; Gielen, J. C.; Christianen, P. C. M.; Meskers, S. C. J.; Schenning, A. P. H. J., Self-assembly of amphiphilic gold nanoparticles decorated with a mixed shell of oligo(p-phenylene vinylene)s and ethyleneoxide ligands. *J. Mater. Chem.* **2008,** *18* (29), 3438-3441.

146. Chen, T.; Chen, G.; Xing, S. X.; Wu, T.; Chen, H. Y., Scalable Routes to Janus Au-SiO2 and Ternary Ag-Au-SiO2 Nanoparticles. *Chem. Mater.* **2010,** *22* (13), 3826-3828.

147. Percebom, A. M.; Giner-Casares, J. J.; Claes, N.; Bals, S.; Loh, W.; Liz-Marzan, L. M., Janus gold nanoparticles obtained via spontaneous binary polymer shell segregation. *Chem. Commun.* **2016,** *52* (23), 4278-4281.

148. Xu, X. Y.; Rosi, N. L.; Wang, Y. H.; Huo, F. W.; Mirkin, C. A., Asymmetric functionalization of gold nanoparticles with oligonucleotides. *J. Am. Chem. Soc.* **2006,** *128* (29), 9286-9287.

149. Pradhan, S.; Xu, L. P.; Chen, S. W., Janus nanoparticles by interfacial engineering. *Adv. Funct. Mater.* **2007,** *17* (14), 2385-2392.

150. Sardar, R.; Shumaker-Parry, J. S., Asymmetrically functionalized gold nanoparticles organized in one-dimensional chains. *Nano Lett.* **2008,** *8* (2), 731-736.

151. Lattuada, M.; Hatton, T. A., Preparation and controlled self-assembly of janus magnetic nanoparticles. *J. Am. Chem. Soc.* **2007,** *129* (42), 12878-12889.

152. Suzuki, D.; Tsuji, S.; Kawaguchi, H., Janus microgels prepared by surfactant-free pickering emulsion-based modification and their self-assembly. *J. Am. Chem. Soc.* **2007,** *129* (26), 8088.

153. Lenis, J.; Razavi, S.; Cao, K. D.; Lin, B. H.; Lee, K. Y. C.; Tu, R. S.; Kretzschmar, I., Mechanical Stability of Polystyrene and Janus Particle Mono layers at the Air/Water Interface. *J. Am. Chem. Soc.* **2015,** *137* (49), 15370-15373.

154. Gu, H. W.; Yang, Z. M.; Gao, J. H.; Chang, C. K.; Xu, B., Heterodimers of nanoparticles: Formation at a liquid-liquid interface and particle-specific surface modification by functional molecules. *J. Am. Chem. Soc.* **2005,** *127* (1), 34-35.

155. Wang, B. B.; Dong, B.; Li, B.; Zhao, B.; Li, C. Y., Janus gold nanoparticle with bicompartment polymer brushes templated by polymer single crystals. *Polymer* **2010,** *51* (21), 4814-4822.

156. Ho, C. C.; Chen, W. S.; Shie, T. Y.; Lin, J. N.; Kuo, C., Novel fabrication of Janus particles from the surfaces of electrospun polymer fibers. *Langmuir.* **2008,** *24* (11), 5663-5666.

157. Ma, X.; Hahn, K.; Sanchez, S., Catalytic Mesoporous Janus Nanomotors for Active Cargo Delivery. *J. Am. Chem. Soc.* **2015,** *137* (15), 4976-4979.

158. Lin, C. C.; Liao, C. W.; Chao, Y. C.; Kuo, C. S., Fabrication and Characterization of Asymmetric Janus and Ternary Particles. *ACS Appl. Mater. Interfaces* **2010,** *2* (11), 3185-3191.

159. Maye, M. M.; Nykypanchuk, D.; Cuisinier, M.; van der Lelie, D.; Gang, O., Stepwise surface encoding for high-throughput assembly of nanoclusters. *Nat. Mater.* **2009,** *8* (5), 388-391.

160. Cao, W.; Huang, R. L.; Qi, W.; Su, R. X.; He, Z. M., Self-Assembly of Amphiphilic Janus Particles into Monolayer Capsules for Enhanced Enzyme Catalysis in Organic Media. *ACS Appl. Mater. Interfaces* **2015,** *7* (1), 465-473.

161. Qiang, W.; Wang, Y.; He, P.; Xu, H.; Gu, H.; Shi, D., Synthesis of asymmetric inorganic/polymer nanocomposite particles via localized substrate surface modification and miniemulsion polymerization. *Langmuir.* **2008,** *24* (3), 606-608.

162. Pardhy, N. P.; Budhlall, B. M., Pickering Emulsion as a Template to Synthesize Janus Colloids with Anisotropy in the Surface Potential. *Langmuir.* **2010,** *26* (16), 13130-13141.

163. Li, Y. B.; Song, L. L.; Qiao, Y. S., Spontaneous assembly and synchronous scan spectra of gold nanoparticle monolayer Janus film with thiol-terminated polystyrene. *Rsc Advances* **2014,** *4* (101), 57611-57614.

164. Jung, C. Y.; Kim, J. S.; Kim, H. S.; Ha, J. M.; Kim, S. T.; Lim, H. J.; Koo, S. M., Selective surface reactions for Janus ORMOSIL particles with multiple functional groups using an ordered monolayer film at liquid-liquid interface. *J. Colloid Interf. Sci* **2012,** *367*, 257-263.

165. Wang, Y. Z.; Fan, D. Q.; He, J. P.; Yang, Y. L., Silica nanoparticle covered with mixed polymer brushes as Janus particles at water/oil interface. *Colloid Polym. Sci.* **2011,** *289* (17-18), 1885-1894.

166. Casavola, M.; Buonsanti, R.; Caputo, G.; Cozzoli, P. D., Colloidal strategies for preparing oxide-based hybrid nanocrystals. *Eur. J. Inorg. Chem.* **2008,** (6), 837-854.

167. Carbone, L.; Cozzoli, P. D., Colloidal heterostructured nanocrystals: Synthesis and growth mechanisms. *Nano Today* **2010,** *5* (5), 449-493.

168. Wei, Y. H.; Klajn, R.; Pinchuk, A. O.; Grzybowski, B. A., Synthesis, Shape Control, and Optical Properties of Hybrid Au/Fe3O4 "Nanoflowers". *Small* **2008,** *4* (10), 1635-1639.

169. Yu, H.; Chen, M.; Rice, P. M.; Wang, S. X.; White, R. L.; Sun, S., Dumbbell-like bifunctional Au-Fe3O4 nanoparticles. *Nano Lett.* **2005,** *5* (2), 379-82.

170. Pellegrino, T.; Fiore, A.; Carlino, E.; Giannini, C.; Cozzoli, P. D.; Ciccarella, G.; Respaud, M.; Palmirotta, L.; Cingolani, R.; Manna, L., Heterodimers based on CoPt3-Au nanocrystals with tunable domain size. *J. Am. Chem. Soc.* **2006,** *128* (20), 6690-6698.

171. Jiang, J.; Gu, H. W.; Shao, H. L.; Devlin, E.; Papaefthymiou, G. C.; Ying, J. Y., Manipulation Bifunctional Fe3O4-Ag Heterodimer Nanoparticles for Two-Photon Fluorescence Imaging and Magnetic Manipulation. *Adv. Mater.* **2008,** *20* (23), 4403-4407.

172. Kwon, K. W.; Shim, M., gamma-Fe2O3/II-VI sulfide nanocrystal heterojunctions. *J. Am. Chem. Soc.* **2005,** *127* (29), 10269-10275.

173. Franchini, I. R.; Bertoni, G.; Falqui, A.; Giannini, C.; Wang, L. W.; Manna, L., Colloidal PbTe-Au nanocrystal heterostructures. *J. Mater. Chem.* **2010,** *20* (7), 1357-1366.

174. Yang, J.; Ying, J. Y., Diffusion of Gold from the Inner Core to the Surface of Ag2S Nanocrystals. *J. Am. Chem. Soc.* **2010,** *132* (7), 2114.

175. Morehead, F.; Stolwijk, N. A.; Meyberg, W.; Gosele, U., Self-Interstitial and Vacancy Contributions to Silicon Self-Diffusion Determined from the Diffusion of Gold in Silicon. *Appl. Phys. Lett.* **1983,** *42* (8), 690-692.

176. Wang, D. S.; Li, Y. D., One-Pot Protocol for Au-Based Hybrid Magnetic Nanostructures via a Noble-Metal-Induced Reduction Process. *J. Am. Chem. Soc.* **2010,** *132* (18), 6280.

177. Cozzoli, P. D.; Pellegrino, T.; Manna, L., Synthesis, properties and perspectives of hybrid nanocrystal structures. *Chem. Soc. Rev.* **2006,** *35* (11), 1195-1208.

178. Tao, A. R.; Habas, S.; Yang, P. D., Shape control of colloidal metal nanocrystals. *Small* **2008,** *4* (3), 310-325.

179. Li, X.; Iocozzia, J.; Chen, Y. H.; Zhao, S. Q.; Cui, X.; Wang, W.; Yu, H. F.; Lin, S. L.; Lin, Z. Q., From Precision Synthesis of Block Copolymers to Properties and Applications of Nanoparticles. *Angew. Chem. Int. Ed.* **2018,** *57* (8), 2046-2070.

180. Liang, H. W.; Liu, S.; Yu, S. H., Controlled Synthesis of One-Dimensional Inorganic Nanostructures Using Pre-Existing One-Dimensional Nanostructures as Templates. *Adv. Mater.* **2010,** *22* (35), 3925-3937.

181. Fuertes, A. B.; Sevilla, M.; Alvarez, S.; Valdes-Solis, T.; Tartaj, P., Templated synthesis of mesoporous superparamagnetic polymers. *Adv. Funct. Mater.* **2007,** *17* (14), 2321-2327.

182. Jia, H.; Schmitz, D.; Ott, A.; Pich, A.; Lu, Y., Cyclodextrin modified microgels as "nanoreactor" for the generation of Au nanoparticles with enhanced catalytic activity. *J. Mater. Chem. A* **2015,** *3* (11), 6187-6195.

183. Zhu, H. B.; Li, Y. X.; Qiu, R. Q.; Shi, L.; Wu, W. T.; Zhou, S. Q., Responsive fluorescent Bi2O3@PVA hybrid nanogels for temperature-sensing, dual-modal imaging, and drug delivery. *Biomaterials.* **2012,** *33* (10), 3058-3069.

184. Xu, S. Q.; Zhang, J. G.; Paquet, C.; Lin, Y. K.; Kumacheva, E., From hybrid microgels to photonic crystals. *Adv. Funct. Mater.* **2003,** *13* (6), 468-472.

185. Suzuki, D.; Nagase, Y.; Kureha, T.; Sato, T., Internal Structures of Thermosensitive Hybrid Microgels Investigated by Means of Small-Angle X-ray Scattering. *J. Phys. Chem. B* **2014,** *118* (8), 2194-2204.

186. Shi, S.; Wang, Q. M.; Wang, T.; Ren, S. P.; Gao, Y.; Wang, N., Thermo-, pH-, and Light-Responsive Poly(N-isopropylacrylamide-co-methacrylic acid)-Au Hybrid Microgels Prepared by the in Situ Reduction Method Based on Au-Thiol Chemistry. *J. Phys. Chem. B* **2014,** *118* (25), 7177-7186.

187. Akamatsu, K.; Shimada, M.; Tsuruoka, T.; Nawafune, H.; Fujii, S.; Nakamura, Y., Synthesis of pH-Responsive Nanocomposite Microgels with Size-Controlled Gold Nanoparticles from Ion-Doped, Lightly Cross-Linked Poly(vinylpyridine). *Langmuir.* **2010,** *26* (2), 1254-1259.

188. Han, J.; Liu, Y.; Guo, R., Reactive Template Method to Synthesize Gold Nanoparticles with Controllable Size and Morphology Supported on Shells of Polymer Hollow Microspheres and Their Application for Aerobic Alcohol Oxidation in Water. *Adv. Funct. Mater.* **2009,** *19* (7), 1112-1117.

189. Ding, J. H.; Gin, D. L., Catalytic Pd nanoparticles synthesized using a lyotropic liquid crystal polymer template. *Chem. Mater.* **2000,** *12* (1), 22.

190. Rosler, A.; Vandermeulen, G. W. M.; Klok, H. A., Advanced drug delivery devices via self-assembly of amphiphilic block copolymers. *Adv. Drug Deliver. Rev* **2012,** *64*, 270-279.

191. Moffitt, M.; Khougaz, K.; Eisenberg, A., Micellization of ionic block copolymers. *Acc. Chem. Res.* **1996,** *29* (2), 95-102.

192. Zhang, L. F.; Eisenberg, A., Multiple Morphologies of Crew-Cut Aggregates of Polystyrene-B-Poly(Acrylic Acid) Block-Copolymers. *Science* **1995,** *268* (5218), 1728-1731.

193. Antonietti, M.; Wenz, E.; Bronstein, L.; Seregina, M., Synthesis and characterization of noble metal colloids in block copolymer micelles. *Adv. Mater.* **1995,** *7* (12), 1000.

194. Kastle, G.; Boyen, H. G.; Weigl, F.; Lengl, G.; Herzog, T.; Ziemann, P.; Riethmuller, S.; Mayer, O.; Hartmann, C.; Spatz, J. P.; Moller, M.; Ozawa, M.; Banhart, F.; Garnier, M. G.; Oelhafen, P., Micellar nanoreactors - Preparation and characterization of hexagonally ordered arrays of metallic nanodots. *Adv. Funct. Mater.* **2003,** *13* (11), 853-861.

195. Moffitt, M.; Mcmahon, L.; Pessel, V.; Eisenberg, A., Size Control of Nanoparticles in Semiconductor-Polymer Composites .2. Control Via Sizes of Spherical Ionic Microdomains in Styrene-Based Diblock Ionomers. *Chem. Mater.* **1995,** *7* (6), 1185-1192.

196. Moffitt, M.; Vali, H.; Eisenberg, A., Spherical assemblies of semiconductor nanoparticles in water-soluble block copolymer aggregates. *Chem. Mater.* **1998,** *10* (4), 1021-1028.

197. Moffitt, M.; Eisenberg, A., Scaling relations and size control of block ionomer microreactors containing different metal ions. *Macromolecules* **1997,** *30* (15), 4363-4373.

198. Bronstein, L. H.; Sidorov, S. N.; Valetsky, P. M.; Hartmann, J.; Colfen, H.; Antonietti, M., Induced micellization by interaction of poly(2-vinylpyridine)-block-poly(ethylene oxide) with metal compounds. Micelle characteristics and metal nanoparticle formation. *Langmuir.* **1999,** *15* (19), 6256-6262.

199. Bronstein, L. M.; Sidorov, S. N.; Gourkova, A. Y.; Valetsky, P. M.; Hartmann, J.; Breulmann, M.; Colfen, H.; Antonietti, M., Interaction of metal compounds with 'double-hydrophilic' block copolymers in aqueous medium and metal colloid formation. *Inorg. Chim. Acta* **1998,** *280* (1-2), 348-354.

200. Qi, L. M.; Colfen, H.; Antonietti, M., Synthesis and characterization of CdS nanoparticles stabilized by double-hydrophilic block copolymers. *Nano Lett.* **2001,** *1* (2), 61-65.

201. Tarasov, K.; Houssein, D.; Destarac, M.; Marcotte, N.; Gerardin, C.; Tichit, D., Stable aqueous colloids of ZnS quantum dots prepared using double hydrophilic block copolymers. *New J. Chem.* **2013,** *37* (2), 508-514.

202. Mai, Y. Y.; Eisenberg, A., Self-assembly of block copolymers. *Chem. Soc. Rev.* **2012,** *41* (18), 5969-5985.

203. Seregina, M. V.; Bronstein, L. M.; Platonova, O. A.; Chernyshov, D. M.; Valetsky, P. M.; Hartmann, J.; Wenz, E.; Antonietti, M., Preparation of noble-metal colloids in block copolymer micelles and their catalytic properties in hydrogenation. *Chem. Mater.* **1997,** *9* (4), 923-931.

204. Spatz, J. P.; Roescher, A.; Moller, M., Gold nanoparticles in micellar poly(styrene)-b-poly(ethylene oxide) films-size and interparticle distance control in monoparticulate films. *Adv. Mater.* **1996,** *8* (4), 337-340.

205. Caruso, F.; Caruso, R. A.; Mohwald, H., Nanoengineering of inorganic and hybrid hollow spheres by colloidal templating. *Science* **1998,** *282* (5391), 1111-1114.

206. Hu, J.; Chen, M.; Fang, X. S.; Wu, L. W., Fabrication and application of inorganic hollow spheres. *Chem. Soc. Rev.* **2011,** *40* (11), 5472-5491.

207. Sasidharan, M.; Liu, D.; Gunawardhana, N.; Yoshio, M.; Nakashima, K., Synthesis, characterization and application for lithium-ion rechargeable batteries of hollow silica nanospheres. *J. Mater. Chem.* **2011,** *21* (36), 13881-13888.

208. Aizawa, M.; Buriak, J. M., Nanoscale patterning of two metals on silicon surfaces using an ABC triblock copolymer template. *J. Am. Chem. Soc.* **2006,** *128* (17), 5877-5886.

209. Koh, H. D.; Park, S.; Russell, T. P., Fabrication of Pt/Au Concentric Spheres from Triblock Copolymer. *ACS Nano* **2010,** *4* (2), 1124-1130.

210. Pang, X. C.; Zhao, L.; Han, W.; Xin, X. K.; Lin, Z. Q., A general and robust strategy for the synthesis of nearly monodisperse colloidal nanocrystals. *Nat. Nanotechnol.* **2013,** *8* (6), 426-431.

211. Chen, Y. H.; Yoon, Y. J.; Pang, X. C.; He, Y. J.; Jung, J. H.; Feng, C. W.; Zhang, G. Z.; Lin, Z. Q., Precisely Size-Tunable Monodisperse Hairy Plasmonic Nanoparticles via Amphiphilic Star-Like Block Copolymers. *Small* **2016,** *12* (48), 6714-6723.

212. Wang, M. Y.; Pang, X. C.; Zheng, D. J.; He, Y. J.; Sun, L.; Lin, C. J.; Lin, Z. Q., Nonepitaxial growth of uniform and precisely size-tunable core/shell nanoparticles and their enhanced plasmon-driven photocatalysis. *J. Mater. Chem. A* **2016,** *4* (19), 7190-7199.

213. Chen, Y. H.; Wang, Z. W.; Harn, Y. W.; Pan, S.; Li, Z. L.; Lin, S. L.; Peng, J.; Zhang, G. Z.; Lin, Z. Q., Resolving Optical and Catalytic Activities in Thermoresponsive Nanoparticles by Permanent Ligation with Temperature-Sensitive Polymers. *Angew. Chem. Int. Ed.* **2019,** *58* (34), 11910-11917.

214. Chen, Y. H.; Wang, Z. W.; He, Y. J.; Yoon, Y. J.; Jung, J. H.; Zhang, G. Z.; Lin, Z. Q., Light-enabled reversible self-assembly and tunable optical properties of stable hairy nanoparticles. *Proceedings of the National Academy of Sciences of the United States of America* **2018,** *115* (7), E1391-E1400.

215. Chen, Y. H.; Yang, D.; Yoon, Y. J.; Pang, X. C.; Wang, Z. W.; Jung, J. H.; He, Y. J.; Harn, Y. W.; He, M.; Zhang, S. G.; Zhang, G. Z.; Lin, Z. Q., Hairy Uniform Permanently Ligated Hollow Nanoparticles with Precise Dimension Control and Tunable Optical Properties. *J. Am. Chem. Soc.* **2017,** *139* (37), 12956-12967.

216. Pang, X. C.; He, Y. J.; Jung, J. H.; Lin, Z. Q., 1D nanocrystals with precisely controlled dimensions, compositions, and architectures. *Science* **2016,** *353* (6305), 1268-1272.

217. Yang, C. Y.; Chen, J.; Ji, X.; Pollard, T. P.; Lu, X. J.; Sun, C. J.; Hou, S.; Liu, Q.; Liu, C. M.; Qing, T. T.; Wang, Y. Q.; Borodin, O.; Ren, Y.; Xu, K.; Wang, C. S., Aqueous Li-ion battery enabled by halogen conversion-intercalation chemistry in graphite. *Nature* **2019,** *569* (7755), 245.

218. Berecibar, M., Accurate predictions of lithium-ion battery life. *Nature* **2019,** *568* (7752), 325-326.

219. Xia, C.; Kwok, C. Y.; Nazar, L. F., A high-energy-density lithium-oxygen battery based on a reversible four-electron conversion to lithium oxide. *Science* **2018,** *361* (6404), 777-781.

220. Service, R. F., Advances in flow batteries promise cheap backup power Upstart technology could enable widespread adoption of renewables. *Science* **2018,** *362* (6414), 508-509.

221. Turcheniuk, K.; Bondarev, D.; Singhal, V.; Yushin, G., Ten years left to redesign lithium-ion batteries Reserves of rare metals used in electric-vehicle cells are dwindling, so boost research on iron and silicon alternatives, urge Kostiantyn Turcheniuk and colleagues. *Nature* **2018,** *559* (7715), 467-470.

222. Wang, J. Y.; Tang, H. J.; Zhang, L. J.; Ren, H.; Yu, R. B.; Jin, Q.; Qi, J.; Mao, D.; Yang, M.; Wang, Y.; Liu, P. R.; Zhang, Y.; Wen, Y. R.; Gu, L.; Ma, G. H.; Su, Z. G.; Tang, Z. Y.; Zhao, H. J.; Wang, D., Multi-shelled metal oxides prepared via an anion-adsorption mechanism for lithium-ion batteries. *Nat. Energy* **2016,** *1*, 16050.

223. Ko, M.; Chae, S.; Ma, J.; Kim, N.; Lee, H.; Cui, Y.; Cho, J., Scalable synthesis of silicon-nanolayer-embedded graphite for high-energy lithium-ion batteries. *Nat. Energy* **2016,** *1*, 16113.

224. Lee, M.; Hong, J.; Lopez, J.; Sun, Y. M.; Feng, D. W.; Lim, K.; Chueh, W. C.; Toney, M. F.; Cui, Y.; Bao, Z. N., High-performance sodium-organic battery by realizing four-sodium storage in disodium rhodizonate. *Nat. Energy* **2017,** *2* (11), 861–868

225. Vaalma, C.; Buchholz, D.; Weil, M.; Passerini, S., A cost and resource analysis of sodium-ion batteries. *Nat. Rev. Mater.* **2018,** *3* (4), 18013.

226. Li, L.; Zheng, Y.; Zhang, S. L.; Yang, J. P.; Shao, Z. P.; Guo, Z. P., Recent progress on sodium ion batteries: potential high-performance anodes. *Energy Environ. Sci.* **2018,** *11* (9), 2310-2340.

227. Wang, P. F.; You, Y.; Yin, Y. X.; Guo, Y. G., Layered Oxide Cathodes for Sodium-Ion Batteries: Phase Transition, Air Stability, and Performance. *Adv. Energy Mater.* **2018,** *8* (8), 1701912.

228. Barpanda, P.; Lander, L.; Nishimura, S.; Yamada, A., Polyanionic Insertion Materials for Sodium-Ion Batteries. *Adv. Energy Mater.* **2018,** *8* (17), 1703055.

229. Xie, H. Z.; Tan, X. H.; Luber, E. J.; Olsen, B. C.; Kalisvaart, W. P.; Jungjohann, K. L.; Mitlin, D.; Buriak, J. M., beta-SnSb for Sodium Ion Battery Anodes: Phase Transformations Responsible for Enhanced Cycling Stability Revealed by In Situ TEM. *ACS Energy Lett.* **2018,** *3* (7), 1670-1676.

230. Ou, X.; Cao, L.; Liang, X. H.; Zheng, F. H.; Zheng, H. S.; Yang, X. F.; Wang, J. H.; Yang, C. H.; Liu, M. L., Fabrication of SnS2/Mn2SnS4/Carbon Heterostructures for Sodium-Ion Batteries with High Initial Coulombic Efficiency and Cycling Stability. *ACS Nano* **2019,** *13* (3), 3666-3676.

231. Ma, D. T.; Li, Y. L.; Mi, H. W.; Luo, S.; Zhang, P. X.; Lin, Z. Q.; Li, J. Q.; Zhang, H., Robust SnO2-x Nanoparticle-Impregnated Carbon Nanofibers with Outstanding Electrochemical Performance for Advanced Sodium-Ion Batteries. *Angew. Chem. Int. Ed.* **2018,** *57* (29), 8901-8905.

232. Jiang, B. B.; He, Y. J.; Li, B.; Zhao, S. Q.; Wang, S.; He, Y. B.; Lin, Z. Q., Polymer-Templated Formation of Polydopamine-Coated SnO2 Nanocrystals: Anodes for Cyclable Lithium-Ion Batteries. *Angew. Chem. Int. Ed.* **2017,** *56* (7), 1869-1872.

233. Zhao, S. Q.; Wang, Z. W.; He, Y. J.; Jiang, B. B.; Harn, Y. W.; Liu, X. Q.; Yu, F. Q.; Feng, F.; Shen, Q.; Lin, Z. Q., Interconnected Ni(HCO3)(2) Hollow Spheres Enabled by Self-Sacrificial Templating with Enhanced Lithium Storage Properties. *ACS Energy Lett.* **2017,** *2* (1), 111-116.

234. Zhao, S.; Wang, Z.; He, Y.; Jiang, H.; Harn, Y. W.; Liu, X.; Su, C.; Jin, H.; Li, Y.; Wang, S.; Shen, Q.; Lin, Z., A Robust Route to Co2(OH)2CO3 Ultrathin Nanosheets with Superior Lithium Storage Capability Templated by Aspartic Acid-Functionalized Graphene Oxide. *Adv. Energy Mater.* **2019**, 1901093.

235. Sun, J.; Lee, H. W.; Pasta, M.; Yuan, H. T.; Zheng, G. Y.; Sun, Y. M.; Li, Y. Z.; Cui, Y., A phosphorene-graphene hybrid material as a high-capacity anode for sodium-ion batteries. *Nat. Nanotechnol.* **2015,** *10* (11), 980-U184.

236. Poizot, P.; Laruelle, S.; Grugeon, S.; Dupont, L.; Tarascon, J. M., Nano-sized transition-metaloxides as negative-electrode materials for lithium-ion batteries. *Nature* **2000,** *407* (6803), 496-499.

237. Lu, Y.; Yu, Y.; Lou, X. W., Nanostructured Conversion-type Anode Materials for Advanced Lithium-Ion Batteries. *Chem* **2018,** *4* (5), 972-996.

238. Hu, Y. Y.; Liu, Z. G.; Nam, K. W.; Borkiewicz, O. J.; Cheng, J.; Hua, X.; Dunstan, M. T.; Yu, X. Q.; Wiaderek, K. M.; Du, L. S.; Chapman, K. W.; Chupas, P. J.; Yang, X. Q.; Grey, C. P., Origin of additional capacities in metal oxide lithium-ion battery electrodes. *Nat. Mater.* **2013,** *12* (12), 1130-1136.

239. Wang, Z. Y.; Zhou, L.; Lou, X. W., Metal Oxide Hollow Nanostructures for Lithium-ion Batteries. *Adv. Mater.* **2012,** *24* (14), 1903-1911.

240. Zhou, L.; Zhao, D. Y.; Lou, X. W., Double-Shelled CoMn2O4 Hollow Microcubes as High-Capacity Anodes for Lithium-Ion Batteries. *Adv. Mater.* **2012,** *24* (6), 745.

241. Liu, Y. C.; Zhang, N.; Yu, C. M.; Jiao, L. F.; Chen, J., MnFe2O4@C Nanofibers as High-Performance Anode for Sodium-Ion Batteries. *Nano Lett.* **2016,** *16* (5), 3321-3328.

242. Kollu, P.; Kumar, P. R.; Santosh, C.; Kim, D. K.; Grace, A. N., A high capacity MnFe2O4/rGO nanocomposite for Li and Na-ion battery applications. *Rsc Advances* **2015,** *5* (78), 63304-63310.

243. Li, T.; Qin, A. Q.; Yang, L. L.; Chen, J.; Wang, Q. F.; Zhang, D. H.; Yang, H. X., In Situ Grown Fe2O3 Single Crystallites on Reduced Graphene Oxide Nanosheets as High Performance Conversion Anode for Sodium-Ion Batteries. *ACS Appl. Mater. Interfaces* **2017,** *9* (23), 19900-19907.

244. Zhao, Y. J.; Wang, F. X.; Wang, C.; Wang, S.; Wang, C. Y.; Zhao, Z. W.; Duan, L. L.; Liu, Y. P.; Wu, Y. P.; Li, W.; Zhao, D. Y., Encapsulating highly crystallized mesoporous Fe3O4 in hollow N-doped carbon nanospheres for high-capacity long-life sodium-ion batteries. *Nano Energy* **2019,** *56*, 426-433.

245. Pang, X. C.; Wan, C. S.; Wang, M. Y.; Lin, Z. Q., Strictly Biphasic Soft and Hard Janus Structures: Synthesis, Properties, and Applications. *Angew. Chem. Int. Ed.* **2014,** *53* (22), 5524-5538.

246. Meng, X. T.; Yu, C.; Song, X. D.; Iocozzia, J.; Hong, J. F.; Rager, M.; Jin, H. L.; Wang, S.; Huang, L. L.; Qiu, J. S.; Lin, Z. Q., Scrutinizing Defects and Defect Density of Selenium-Doped Graphene for High-Efficiency Triiodide Reduction in Dye-Sensitized Solar Cells. *Angew. Chem. Int. Ed.* **2018,** *57* (17), 4682-4686.

247. He, M.; Pang, X. C.; Liu, X. Q.; Jiang, B. B.; He, Y. J.; Snaith, H.; Lin, Z. Q., Monodisperse Dual-Functional Upconversion Nanoparticles Enabled Near-Infrared Organolead Halide Perovskite Solar Cells. *Angew. Chem. Int. Ed.* **2016,** *55* (13), 4280-4284.

248. Zheng, D. J.; Pang, X. C.; Wang, M. Y.; He, Y. J.; Lin, C. J.; Lin, Z. Q., Unconventional Route to Hairy Plasmonic/Semiconductor Core/Shell Nanoparticles with Precisely Controlled Dimensions and Their Use in Solar Energy Conversion. *Chem. Mater.* **2015,** *27* (15), 5271-5278.

249. Ayhan, I. A.; Li, Q.; Meduri, P.; Oh, H.; Bhimanapati, G. R.; Yang, G.; Robinson, J. A.; Wang, Q., Effect of Mn3O4 nanoparticle composition and distribution on graphene as a potential hybrid anode material for lithium-ion batteries. *Rsc Advances* **2016,** *6* (39), 33022-33030.

250. Chang, J. B.; Huang, X. K.; Zhou, G. H.; Cui, S. M.; Hallac, P. B.; Jiang, J. W.; Hurley, P. T.; Chen, J. H., Multilayered Si Nanoparticle/Reduced Graphene Oxide Hybrid as a High-Performance Lithium-Ion Battery Anode. *Adv. Mater.* **2014,** *26* (5), 758-764.

251. Huang, X.; Chen, J.; Yu, H.; Cai, R.; Peng, S. J.; Yan, Q. Y.; Hng, H. H., Carbon buffered-transition metal oxide nanoparticle-graphene hybrid nanosheets as high-performance anode materials for lithium ion batteries. *J. Mater. Chem. A* **2013,** *1* (23), 6901-6907.

252. Li, X.; Sun, X. H.; Gao, Z. W.; Hu, X. D.; Ling, R.; Cai, S.; Zheng, C. M.; Hu, W. B., A Simple One-Pot Strategy for Synthesizing Ultrafine SnS2 Nanoparticle/Graphene Composites as Anodes for Lithium/Sodium-Ion Batteries. *Chemsuschem* **2018,** *11* (9), 1549-1557.

253. Shao, Q. G.; Tang, J. E.; Sun, Y. G.; Li, J.; Zhang, K.; Yuan, J. S.; Zhu, D. M.; Qin, L. C., Unique interconnected graphene/SnO2 nanoparticle spherical multilayers for lithium-ion battery applications. *Nanoscale* **2017,** *9* (13), 4439-4444.

254. Yuan, F. W.; Tuan, H. Y., Scalable Solution-Grown High-Germanium-Nanoparticle-Loading Graphene Nanocomposites as High-Performance Lithium-Ion Battery Electrodes: An Example of a Graphene-Based Platform toward Practical Full-Cell Applications. *Chem. Mater.* **2014,** *26* (6), 2172-2179.

255. Zhang, W. L.; Liu, Y. D.; Choi, H. J., Graphene oxide coated core-shell structured polystyrene microspheres and their electrorheological characteristics under applied electric field. *J. Mater. Chem.* **2011,** *21* (19), 6916-6921.

256. Wang, W. P.; Yang, H.; Xian, T.; Jiang, J. L., XPS and Magnetic Properties of CoFe2O4 Nanoparticles Synthesized by a Polyacrylamide Gel Route. *Mater. Trans.* **2012,** *53* (9), 1586-1589.

257. Jorio, A.; Souza, A. G., Raman Studies of Carbon Nanostructures. *Annual Review of Materials Research, Vol 46* **2016,** *46*, 357-382.

258. Georgakilas, V.; Tiwari, J. N.; Kemp, K. C.; Perman, J. A.; Bourlinos, A. B.; Kim, K. S.; Zboril, R., Noncovalent Functionalization of Graphene and Graphene Oxide for Energy Materials, Biosensing, Catalytic, and Biomedical Applications. *Chem. Rev.* **2016,** *116* (9), 5464-5519.

259. Macfarlane, R. J.; Kim, B.; Lee, B.; Weitekamp, R. A.; Bates, C. M.; Lee, S. F.; Chang, A. B.; Delaney, K. T.; Fredrickson, G. H.; Atwater, H. A.; Grubbs, R. H., Improving Brush Polymer Infrared One-Dimensional Photonic Crystals via Linear Polymer Additives. *J. Am. Chem. Soc.* **2014,** *136* (50), 17374-17377.

260. Miyake, G. M.; Piunova, V. A.; Weitekamp, R. A.; Grubbs, R. H., Precisely Tunable Photonic Crystals From Rapidly Self-Assembling Brush Block Copolymer Blends. *Angew. Chem. Int. Ed.* **2012,** *51* (45), 11246-11248.

261. Daniel, W. F. M.; Burdynska, J.; Vatankhah-Varnoosfaderani, M.; Matyjaszewski, K.; Paturej, J.; Rubinstein, M.; Dobrynin, A. V.; Sheiko, S. S., Solvent-free, supersoft and superelastic bottlebrush melts and networks. *Nat. Mater.* **2016,** *15* (2), 183.

262. Mukumoto, K.; Averick, S. E.; Park, S.; Nese, A.; Mpoukouvalas, A.; Zeng, Y. K.; Koynov, K.; Leduc, P. R.; Matyjaszewski, K., Phototunable Supersoft Elastomers using Coumarin Functionalized Molecular Bottlebrushes for Cell-Surface Interactions Study. *Macromolecules* **2014,** *47* (22), 7852-7857.

263. Raguzin, I.; Stamm, M.; Ionov, L., Conductive Nanowires Templated by Molecular Brushes. *ACS Appl. Mater. Interfaces* **2015,** *7* (41), 23305-23309.

264. Verduzco, R.; Li, X.; Pesek, S. L.; Stein, G. E., Correction: Structure, function, self-assembly, and applications of bottlebrush copolymers. *Chem. Soc. Rev.* **2015,** *44* (21), 7916.

265. Rzayev, J., Molecular Bottlebrushes: New Opportunities in Nanomaterials Fabrication. *Acs Macro Letters* **2012,** *1* (9), 1146-1149.

266. Kim, J. G.; Coates, G. W., Synthesis and Polymerization of Norbornenyl-Terminated Multiblock Poly(cyclohexene carbonate)s: A Consecutive Ring-Opening Polymerization Route to Multisegmented Graft Polycarbonates. *Macromolecules* **2012,** *45* (19), 7878-7883.

267. Li, Z.; Ma, J.; Lee, N. S.; Wooley, K. L., Dynamic Cylindrical Assembly of Triblock Copolymers by a Hierarchical Process of Covalent and Supramolecular Interactions. *J. Am. Chem. Soc.* **2011,** *133* (5), 1228-1231.

268. Huang, K.; Rzayev, J., Charge and Size Selective Molecular Transport by Amphiphilic Organic Nanotubes. *J. Am. Chem. Soc.* **2011,** *133* (42), 16726-16729.

269. Ostmark, E.; Harrisson, S.; Wooley, K. L.; Malmstrom, E. E., Comb polymers prepared by ATRP from hydroxypropyl cellulose. *Biomacromolecules* **2007,** *8* (4), 1138-1148.

270. Sui, X. F.; Yuan, J. Y.; Zhou, M.; Zhang, J.; Yang, H. J.; Yuan, W. Z.; Wei, Y.; Pan, C. Y., Synthesis of Cellulose-graft-Poly(N,N-dimethylamino-2-ethyl methacrylate) Copolymers via Homogeneous ATRP and Their Aggregates in Aqueous Media. *Biomacromolecules* **2008,** *9* (10), 2615-2620.

271. Roy, D.; Semsarilar, M.; Guthrie, J. T.; Perrier, S., Cellulose modification by polymer grafting: a review. *Chem. Soc. Rev.* **2009,** *38* (7), 2046-2064.

272. Geng, Y.; Dalhaimer, P.; Cai, S. S.; Tsai, R.; Tewari, M.; Minko, T.; Discher, D. E., Shape effects of filaments versus spherical particles in flow and drug delivery. *Nat. Nanotechnol.* **2007,** *2* (4), 249-255.

273. Venkataraman, S.; Hedrick, J. L.; Ong, Z. Y.; Yang, C.; Ee, P. L. R.; Hammond, P. T.; Yang, Y. Y., The effects of polymeric nanostructure shape on drug delivery. *Adv. Drug Deliver. Rev* **2011,** *63* (14-15), 1228-1246.

274. Johnson, J. A.; Lu, Y. Y.; Burts, A. O.; Lim, Y. H.; Finn, M. G.; Koberstein, J. T.; Turro, N. J.; Tirrell, D. A.; Grubbs, R. H., Core-Clickable PEG-Branch-Azide Bivalent-Bottle-Brush Polymers by ROMP: Grafting-Through and Clicking-To. *J. Am. Chem. Soc.* **2011,** *133* (3), 559-566.

275. Sowers, M. A.; McCombs, J. R.; Wang, Y.; Paletta, J. T.; Morton, S. W.; Dreaden, E. C.; Boska, M. D.; Ottaviani, M. F.; Hammond, P. T.; Rajca, A.; Johnson, J. A., Redox-responsive branched-bottlebrush polymers for in vivo MRI and fluorescence imaging. *Nat. Commun.* **2014,** *5*, 5460.

276. Yu, Y.; Chen, C. K.; Law, W. C.; Mok, J.; Zou, J.; Prasad, P. N.; Cheng, C., Well-Defined Degradable Brush Polymer-Drug Conjugates for Sustained Delivery of Paclitaxel. *Molecular Pharmaceutics* **2013,** *10* (3), 867-874.

277. Lu, X. G.; Tran, T. H.; Jia, F.; Tan, X. Y.; Davis, S.; Krishnan, S.; Amiji, M. M.; Zhang, K., Providing Oligonucleotides with Steric Selectivity by Brush-Polymer-Assisted Compaction. *J. Am. Chem. Soc.* **2015,** *137* (39), 12466-12469.

278. Zhang, H.; Xiong, L. F.; Liao, X. J.; Huang, K., Controlled-Release System of Small Molecules Triggered by the Photothermal Effect of Polypyrrole. *Macromol. Rapid. Comm.* **2016,** *37* (2), 149-154.

279. Zhao, P.; Liu, L. X.; Feng, X. Q.; Wang, C.; Shuai, X. T.; Chen, Y. M., Molecular Nanoworm with PCL Core and PEO Shell as a Non-spherical Carrier for Drug Delivery. *Macromol. Rapid. Comm.* **2012,** *33* (16), 1351-1355.

280. Tu, X. Y.; Meng, C.; Wang, Y. F.; Ma, L. W.; Wang, B. Y.; He, J. L.; Ni, P. H.; Ji, X. L.; Liu, M. Z.; Wei, H., Fabrication of Thermosensitive Cyclic Brush Copolymer with Enhanced Therapeutic Efficacy for Anticancer Drug Delivery. *Macromol. Rapid. Comm.* **2018,** *39* (5), 1700744.

281. Fenyves, R.; Schmutz, M.; Horner, I. J.; Bright, F. V.; Rzayev, J., Aqueous Self-Assembly of Giant Bottlebrush Block Copolymer Surfactants as Shape-Tunable Building Blocks. *J. Am. Chem. Soc.* **2014,** *136* (21), 7762-7770.

282. Unsal, H.; Onbulak, S.; Calik, F.; Er-Rafik, M.; Schmutz, M.; Sanyal, A.; Rzayev, J., Interplay between Molecular Packing, Drug Loading, and Core Cross-Linking in Bottlebrush Copolymer Micelles. *Macromolecules* **2017,** *50* (4), 1342-1352.

283. Yao, Q.; Gutierrez, D. C.; Hoang, N. H.; Kim, D.; Wang, R. N.; Hobbs, C.; Zhu, L., Efficient Codelivery of Paclitaxel and Curcumin by Novel Bottlebrush Copolymer-based Micelles. *Molecular Pharmaceutics* **2017,** *14* (7), 2378-2389.

284. Ostmark, E.; Nystrom, D.; Malmstrom, E., Unimolecular nanocontainers prepared by ROP and subsequent ATRP from hydroxypropylcellulose. *Macromolecules* **2008,** *41* (12), 4405-4415.

285. Zhang, H.; Wu, J.; Zhang, J.; He, J. S., 1-Allyl-3-methylimidazolium chloride room temperature ionic liquid: A new and powerful nonderivatizing solvent for cellulose. *Macromolecules* **2005,** *38* (20), 8272-8277.

286. Yoo, M.; Kim, S.; Lim, J.; Kramer, E. J.; Hawker, C. J.; Kim, B. J.; Bang, J., Facile Synthesis of Thermally Stable Core-Shell Gold Nanoparticles via Photo-Cross-Linkable Polymeric Ligands. *Macromolecules* **2010,** *43* (7), 3570-3575.

287. Abramovitch, R. A.; Kyba, E. P., Photodecomposition of Alkyl Azides - Absence of Freedom of Choice and Nonnitrene Mechanism. *J. Am. Chem. Soc.* **1971,** *93* (6), 1537.

288. Iocozzia, J.; Lin, Z. Q., Clean and Simple Route to Soft, Biocompatible Nanocapsules via UV-Cross-Linkable Azido-Hyperbranched Polyglycerol. *Macromolecules* **2017,** *50* (13), 4906-4912.

289. Wang, X. X.; Zhou, H.; Yuan, S. P.; Zheng, W. H.; Jiang, Y.; Zhuang, X. J.; Liu, H. J.; Zhang, Q. L.; Zhu, X. L.; Wang, X.; Pan, A. L., Cesium lead halide perovskite triangular nanorods as high-gain medium and effective cavities for multiphoton-pumped lasing. *Nano Research* **2017,** *10* (10), 3385-3395.

290. He, J.; Towers, A.; Wang, Y. A.; Yuan, P. S.; Jiang, Z.; Chen, J. S.; Gesquiere, A. J.; Wu, S. T.; Dong, Y. J., In situ synthesis and macroscale alignment of CsPbBr3 perovskite nanorods in a polymer matrix. *Nanoscale* **2018,** *10* (33), 15436-15441.

291. Jing, Q.; Su, Y. C.; Xing, X.; Lu, Z. D., Highly luminescent CsPbBr3 nanorods synthesized by a ligand-regulated reaction at the water-oil interface. *J. Mater. Chem. C* **2019,** *7* (7), 1854-1858.

292. Yang, D.; Li, P. L.; Zou, Y. T.; Cao, M. H.; Hu, H. C.; Zhong, Q. X.; Hu, J. X.; Sun, B. Q.; Duhm, S.; Xu, Y.; Zhang, Q., Interfacial Synthesis of Monodisperse CsPbBr3 Nanorods with Tunable Aspect Ratio and Clean Surface for Efficient Light-Emitting Diode Applications. *Chem. Mater.* **2019,** *31* (5), 1575-1583.

293. Cai, Y. T.; Wang, L.; Zhou, T. L.; Zheng, P.; Li, Y.; Xie, R. J., Improved stability of CsPbBr3 perovskite quantum dots achieved by suppressing interligand proton transfer and applying a polystyrene coating. *Nanoscale* **2018,** *10* (45), 21441-21450.

294. Zhang, D. D.; Yang, Y. M.; Bekenstein, Y.; Yu, Y.; Gibson, N. A.; Wong, A. B.; Eaton, S. W.; Kornienko, N.; Kong, Q.; Lai, M. L.; Alivisatos, A. P.; Leone, S. R.; Yang, P. D., Synthesis of Composition Tunable and Highly Luminescent Cesium Lead Halide Nanowires through Anion-Exchange Reactions. *J. Am. Chem. Soc.* **2016,** *138* (23), 7236-7239.

295. Li, T.; Zhou, C. L.; Jiang, M., Uv Absorption-Spectra of Polystyrene. *Polym. Bull.* **1991,** *25* (2), 211-216.

296. Li, J.; Wang, L.; Yuan, X.; Bo, B. X.; Li, H. B.; Zhao, J. L.; Gao, X., Ultraviolet light induced degradation of luminescence in CsPbBr3 perovskite nanocrystals. *Mater. Res. Bull.* **2018,** *102*, 86-91.

297. Moyen, E.; Jun, H.; Kim, H. M.; Jang, J., Surface Engineering of Room Temperature-Grown Inorganic Perovskite Quantum Dots for Highly Efficient Inverted Light-Emitting Diodes. *ACS Appl. Mater. Interfaces* **2018,** *10* (49), 42647-42656.

298. Koolyk, M.; Amgar, D.; Aharon, S.; Etgar, L., Kinetics of cesium lead halide perovskite nanoparticle growth; focusing and de-focusing of size distribution. *Nanoscale* **2016,** *8* (12), 6403-6409.

299. Neumann, S.; Bengtson, G.; Meis, D.; Filiz, V., Thermal Cross Linking of Novel Azide Modified Polymers of Intrinsic Microporosity-Effect of Distribution and the Gas Separation Performance. *Polymers* **2019,** *11* (8).

300. Schuh, K.; Prucker, O.; Ruhe, J., Surface Attached Polymer Networks through Thermally Induced Cross-Linking of Sulfonyl Azide Group Containing Polymers. *Macromolecules* **2008,** *41* (23), 9284-9289.

301. Yin, S. N.; Wang, C. F.; Yu, Z. Y.; Wang, J.; Liu, S. S.; Chen, S., Versatile Bifunctional Magnetic-Fluorescent Responsive Janus Supraballs Towards the Flexible Bead Display. *Adv. Mater.* **2011,** *23* (26), 2915.

302. Wu, L. Y.; Ross, B. M.; Hong, S.; Lee, L. P., Bioinspired Nanocorals with Decoupled Cellular Targeting and Sensing Functionality. *Small* **2010,** *6* (4), 503-507.

303. Xie, H.; She, Z. G.; Wang, S.; Sharma, G.; Smith, J. W., One-Step Fabrication of Polymeric Janus Nanoparticles for Drug Delivery. *Langmuir.* **2012,** *28* (9), 4459-4463.

304. Wang, F.; Pauletti, G. M.; Wang, J. T.; Zhang, J. M.; Ewing, R. C.; Wang, Y. L.; Shi, D. L., Dual Surface-Functionalized Janus Nanocomposites of Polystyrene/Fe3O4@SiO2 for Simultaneous Tumor Cell Targeting and Stimulus-Induced Drug Release. *Adv. Mater.* **2013,** *25* (25), 3485-3489.

305. Tu, F. Q.; Lee, D., Shape-Changing and Amphiphilicity-Reversing Janus Particles with pH-Responsive Surfactant Properties. *J. Am. Chem. Soc.* **2014,** *136* (28), 9999-10006.

306. Tanaka, T.; Okayama, M.; Minami, H.; Okubo, M., Dual Stimuli-Responsive "Mushroom-like" Janus Polymer Particles as Particulate Surfactants. *Langmuir.* **2010,** *26* (14), 11732-11736.

307. Faria, J.; Ruiz, M. P.; Resasco, D. E., Phase-Selective Catalysis in Emulsions Stabilized by Janus Silica-Nanoparticles. *Adv. Synth. Catal.* **2010,** *352* (14-15), 2359-2364.

308. Skey, J.; O'Reilly, R. K., Facile one pot synthesis of a range of reversible addition-fragmentation chain transfer (RAFT) agents. *Chem. Commun.* **2008,** (35), 4183-4185.